A New Methodology based on First Passage Times for Structural Health Monitoring in Civil Engineering

by

Kevin Theunissen

A thesis submitted in partial fulfillment of the requirements for the degree of Doctor of Philosophy in Engineering Sciences

May 2024

Members of the Jury

President	Prof. Philippe RIGO University of Liège
Advisor	Prof. Vincent DENOËL University of Liège
	Prof. Francesco Lo IACONO University of Enna
	Prof. Stefan MAAS University of Luxembourg
	Prof. Boyan MIHAYLOV University of Liège
	Dr. Ir. Edouard VERSTRAELEN V2i

À ma petite famille,

Abstract

Structural Health Monitoring refers to the process of implementing a damage identification strategy for infrastructures. As the global population continues to grow, urbanisation expands and the age of existing infrastructure is also increasing. Therefore, the field of Structural Health Monitoring has gained in popularity. A wide variety of methods have already been developed with vibration-based methods being among the most prevalent.

The concept of early damage detection is crucial. In the absence of apparent damage to a structure, the common and basic technique of visual inspection, which is employed for damage detection, is ineffective. The objective of detecting damage as early as possible is to reduce the costs and time required for repairs, as well as to enhance the safety and reliability of existing structures.

This thesis presents a novel method, located within the vibration-based methods. Unlike the modal-based methods, such as those tracking the degradation of eigenfrequencies, the proposed approach hinges on the concept of First Passage Time. This concept is applied for the first time to Structural Health Monitoring and refers to the time required by a dynamical system to reach a particular state for the first time, while starting from a known initial condition.

Although the mathematical study of First Passage Times has been well-established, there has been a lack of efficient algorithms for computing First Passage Times from experimental data. Therefore, a new and optimised algorithm is developed. As the First Passage Time is the keystone of this thesis, this algorithm benefits from fast computation time to extract the First Passage Times from any given time signal. For any random signal, First Passage Time is a random variable. The distribution of First Passage Times is shown to be a good candidate for the early damage detection. A novel methodology is proposed. It is based on the pre-processing of the input data and on the comparison of the distributions of First Passage Times. The latter relies on a new proposed statistical test, which is based on the sampling distribution of First Passage Times, and various existing two-sample tests, such as the Kolmogorov-Smirnov and the Anderson-Darling tests.

Finally, the sensitivity of the methodology is initially evaluated through numerical examples before being applied to two experimental setups: a small-scale laboratory test under control conditions and a large-scale outdoor test submitted to environmental effects. It is demonstrated that the First Passage Time is sufficiently sensitive to detect minor structural changes, thereby enabling damage detection at an early stage.

Acknowledgements

Ma thèse de doctorat constitue le fil conducteur d'une expérience de vie. Au seuil de ce travail, je souhaite remercier chaleureusement mon Promoteur Vincent Denoël pour sa proposition de doctorat. Durant ces quatre belles années, ma passion pour la recherche n'a cessé de grandir à ses côtés. Il a su attiser ma curiosité pour ces domaines de recherche que sont le Structural Health Monitoring, la dynamique des structures et les processus stochastiques. Merci Vincent pour nos discussions enrichissantes tant au bureau que lors de nos déplacements. Tes conseils avisés m'ont toujours été précieux et grâce à toi, j'ai découvert une passion devenant au fil du temps une vocation.

C'est ainsi que je me suis retrouvé embarqué dans ce projet ambitieux, nommé D-DAB et octroyé par le F.R.S.-FNRS (the Belgian Fund for Scientific Research) que je remercie vivement pour le financement accordé. Ce projet, en collaboration avec l'Université du Luxembourg, m'a permis de rencontrer des collègues formidables, dont le Professeur Maas et Khatereh, que je souhaite remercier cordialement pour les nombreux bons moments partagés lors des journées de test.

Merci également à la société V2i, en particulier Edouard et Sébastien, pour l'aide apportée lors des tests menés à l'Université de Liège. Je me souviens également lors de ma première conférence à Louvain où vous avez su m'entourer pour mieux aborder cette nouvelle expérience professionnelle.

Mes remerciements s'adressent aussi à tous mes collègues avec qui j'ai partagé d'agréables moments et sur qui j'ai toujours pu compter. Merci à tous d'avoir participé à ces si nombreuses éditions du Goodminton. Cet événement reste pour moi inoubliable. En particulier, je souhaite remercier la team SSD pour tous nos instants de complicité. Vous êtes, nous sommes, une team géniale !

Je remercie également mes amis qui m'ont toujours encouragé tout au long de ma thèse et malgré la distance, vous avez toujours été présents. Merci pour ces escapades mémorables, en particulier ce magnifique voyage au Japon qui m'a permis de me ressourcer et d'entamer ma fin de doctorat avec brio.

Mes remerciements ne peuvent s'achever sans une pensée pour ma petite famille comme je les appelle : mes Grands-Parents, mes Parents et essentiellement ma petite Sœur sans qui je n'en serais certainement pas là aujourd'hui. Notre complicité nous a toujours permis d'œuvrer dans le même direction, en se soutenant et en s'encourageant, pour mener à bien tous nos projets d'étude et d'avenir. Ma petite famille, vous êtes, à mes yeux, les personnes qui maintiennent tendu ce filet de trampoline sur lequel je rebondis et m'envole toujours plus haut. Vous êtes mes fondations, sur qui je pourrai toujours compter. Un tout Grand Merci !

La thèse n'est peut-être pas un long fleuve tranquille, mais le bateau se manœuvre toujours plus facilement quand on est bien accompagné.

List of Figures

Nomenclature

AD	Anderson-Darling
CDF	Cumulative Density Function
CVM	Cramer-Von Mises
DOF	Degree-of-freedom
DS	Damaged Scenario
ECDF	Empirical Cumulative Density Function
FPT	First Passage Time
GBM	Geometric Brownian Motion
K	Kuiper
KS	Kolmogorov-Smirnov
MAC	Modal Assurance Criterion
O-U	Ornstein-Uhlenbeck
PDF	Probability Density Function
PSD	Power Spectral Density
RMS	Root Mean Square
SHM	Structural Health Monitoring
STD	Standard Deviation
W	Wasserstein
WAD	Wasserstein-Anderson-Darling

Contents

Chapter 1

Introduction

1.1 Structural Health Monitoring

Structural Health Monitoring (SHM) refers to the process of implementing a damage identification strategy for aerospace, civil and mechanical engineering infrastructures [1]. It represents an approach in ensuring the safety, reliability, and longevity of infrastructures thanks to a wide variety of techniques, methodologies, and technologies that aim at monitoring the condition of structures to detect, assess, and mitigate potential damages [2]. With the increase of the global population, urbanisation grows [3] and existing infrastructures age [4]. SHM has gained in popularity with its applications spanning across civil infrastructures as bridges [5, 6], buildings [7], dams [8], pipelines [9], offshore structures [10, 11], and more.

The objective of SHM lies in its proactive approach to maintenance and risk management. By implementing SHM systems, stakeholders can transition from reactive responses to structural failures to a proactive stance, wherein potential issues are identified and addressed before they escalate into catastrophic events [12]. This goal allows greater safety and reliability of infrastructure but also leads to significant cost savings [13] by optimising maintenance schedules, extending the service life of structures, and minimising downtime associated with repairs [14, 15].

Moreover, SHM is the keystone in the evolution towards smart and resilient infrastructure systems [16]. By integrating advanced sensing technologies [17], wireless smart sensor networks [18], high-dimensional data analytics [19], and decision-making algorithms [20], SHM offers a large volume of data from different sources that contains essential information about the well-being of the structure itself. Combinations of data from various sensing techniques, called data fusion [21], makes SHM systems more resilient and robust to diverse effects that can affect a structure, such as environmental effects, material aging, and human-induced factors.

1.1.1 Fundamentals

Definition and basic principles

SHM involves the deployment of sensors and measurement devices to collect data regarding the structural response to environmental stresses and potential anomalies. This data is then analysed using various techniques that require the comparison of two states of the structure: the *healthy state*, also known as the *reference state*, and the *current state* that can become a *damaged state*, if a damage is detected [22]. To compare two states of the same structure, different techniques can be used, relying on, for example, the waves velocity inside the material [23], the modal curvature [24], the inverse of the structural stiffness matrix [25] or some modal parameters [26, 27], such as eigenfrequencies, eigenmodes, and damping ratios. Finally, based on data analysis, stakeholders can take decisions concerning the maintenance and repair of the structure if a damage was detected.

Components of an SHM system

The SHM system is made of different components, each playing an important role in the overall functionality and effectiveness of the monitoring process:

- **Sensors**: Sensors are devices that capture the data related to structural behaviour, including accelerations, strains, displacements, and environmental parameters. Common sensor types include accelerometers [28], strain gauges [29], displacement transducers [30], and temperature sensors [31].
- **Data acquisition systems**: These systems are responsible for collecting, processing, and storing data in real-time.
- **Data analysis algorithms**: Algorithms are employed to analyse the collected data and extract meaningful insights regarding the structural health condition. Techniques such as signal processing [32], statistical analysis [33], pattern recognition [34], and machine learning [35] are commonly used to identify anomalies.
- **Decision-making tools**: Based on the results of data analysis, decision-making tools facilitate informed decision-making regarding maintenance actions, structural repairs, and risk mitigation strategies. These tools integrate data from SHM systems with structural performance models, cost-benefit analyses, and risk assessments to optimise resource allocation and prioritise interventions [36, 37].

Common sensing techniques

Among the various sensors that can be used to capture different aspects of structural behaviour, the most common ones are:

- **Acoustic emission sensors**: Acoustic Emission (AE) is a technique that captures transient stress waves due to the release of localised internal energy, such as micro-fracture in elastic material. AE is particularly adept at detecting active damage, such as crack initiation and propagation, in a wide range of materials including metals, composites, and concrete [38, 39].

- **Accelerometers**: Vibration-based monitoring relies on analysing the dynamic response of structures to external forces or ambient vibrations. By measuring changes in eigenfrequencies, eigenmodes, and damping ratios, this technique can detect structural anomalies such as cracks, delamination, material degradation, and the loss of axial force in cables [40]. Recent advances include the integration of wireless sensor networks [41] and machine learning algorithms for enhanced data analysis and predictive maintenance [42].

- **Strain gauges**: Strain gauges are fundamental sensors used to measure the deformation or strain in structural components. These sensors are bonded to critical elements of a structure, allowing for the monitoring of strain variations induced by external loads or structural changes [43]. Modern strain gauge technology includes wireless technology, enabling the installation of strain monitoring on complex structures [44].

- **Ultrasonic testing**: Ultrasonic Testing (UT) uses high-frequency sound waves to inspect the internal structure of materials for defects, such as cracks, voids, and disbonds. UT is a versatile technique employed in various industries, including aerospace, automotive, and civil engineering, and is particularly appreciated for its high resolution and depth penetration capabilities [45].

- **Fiber optic sensors**: Fiber optic sensors use optical fibers to measure parameters such as strain, temperature, and displacement. These sensors offer several advantages, including immunity to electromagnetic interference and high sensitivity. Fiber optic sensing systems are extensively used in harsh environments and critical infrastructure for continuous and distributed monitoring [46, 47].

- **Electrical resistivity measurement**: Electrical resistivity measurement is a technique that assesses changes in the electrical resistivity of materials, which can indicate the presence of cracks, corrosion, or moisture ingress. This technique is particularly relevant for concrete structures, where monitoring the resisitivity of profile provides insights into the condition and durability of the material. Recent advancements include the integration of embedded sensors, automated data acquisition systems for in-situ monitoring of concrete structures, and new algorithms based on experimental databases [48].

- **Thermography**: Thermography involves the use of infrared cameras to capture thermal images of a structure surface. By analysing temperature variations, thermography can detect defects such as delamination, moisture ingress, and thermal anomalies [49].

- **Ground-Based Radar (GBR)**: GBR is a remote sensing technique used to monitor large structures, such as bridges, dams, tunnels, and buildings. GBR measures the displacement of structures over time, providing valuable insights into structural stability and integrity. Recent developments in GBR technology include interferometric radar systems and synthetic aperture radar techniques, enabling high-resolution monitoring over large areas [50].

- **Electromagnetic**: Electromagnetic methods such as eddy current testing [51] and magnetic flux leakage [52] are employed to detect changes in the electromagnetic properties of materials caused by structural damage. These techniques are particularly effective for inspecting metallic structures for cracks, corrosion, material loss, and also for detecting defects in repaired concrete slabs [53].

- **Crack width measurements**: Crack width on concrete members can also be used as an insightful data for damage assessment and residual capacity, see e.g. [54].

Each sensing technique has its own limitations, and the selection of sensors depends on factors, such as the type of structure, the monitoring objectives, the environmental conditions, and the budget constraints.

Sensor placement and optimisation

The sensor placement plays an important and critical role in the effectiveness of an SHM system. Optimal sensor placement ensures adequate coverage of critical structural components, maximises the sensitivity to potential damage locations, and minimises the number of sensors required [55]. Various optimisation techniques, such as numerical simulations [56], sensitivity analyses [57], and heuristic algorithms [58], can be employed to determine the optimal sensor locations based on factors such as structural geometry, loading conditions, and expected damage mechanisms.

Additionally, sensor calibration, maintenance, and recalibration are essential considerations to ensure the accuracy and reliability of sensor measurements over time [59]. Calibration procedures should be performed regularly to verify sensor accuracy and correct any drift or calibration error that may arise due to environmental factors or aging.

Levels of damage assessment

Rytter identified four different levels of damage identification [60]. These levels are reported in Figure 1.1.

The first level corresponds to damage detection. In this level, the goal is to extract insightful information from the collected data in the *current state* and to compare it with the corresponding data in the *healthy state*. Focusing on damage detection only is still a trend that is followed at the current stage of SHM [61, 62, 63].

The second level is the damage location, which is accessed after damage has been detected. The methods used to locate a damage can be based on measured data only [64] or on a comparison between experimental data and a digital twin model [65].

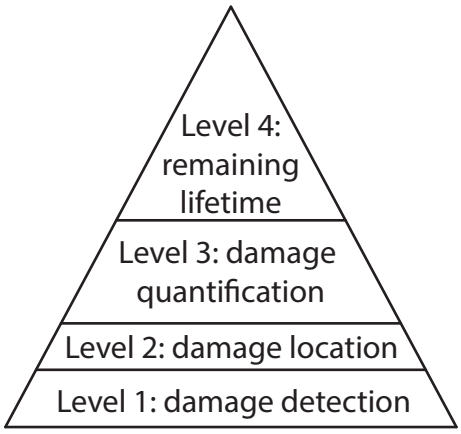

FIGURE 1.1: Levels of damage assessment. Adapted from Rytter.

The third level refers to damage quantification. Once the damage has been localised, it is important to assess the severity of this damage [66].

Finally, the fourth level deals with the remaining lifetime of a structure. Nowadays, this level seems unreachable as many challenges are still present, such as the creation of high-fidelity numerical models and the filtering of all environmental effects, which pollute the measured data.

The objective of this thesis is to achieve level 2 with a novel methodology.

1.1.2 Some SHM vibration-based methods

SHM vibration-based methods are among the most popular SHM methods. These methods rely on the vibrations of the structure under investigation, which can be measured by using accelerometers or lasers, for example. The vibration data can be classified as either acceleration, velocity, or displacement. The dynamic response of the system is obtained by means of dynamic tests such as free or forced vibration tests (impact hammer or shaker) and ambient vibration tests, which use the vibrations of the structure under operational loading. Moreover, the vibration-based methods can be either output-only methods, which rely solely on the measured vibrations, or input-output methods. The latter also requires the measurement of the input force.

Modal-based methods are the most common vibration-based methods. They rely on the extraction of modal parameters, such as the eigenfrequency. The eigenfrequency is the simplest of the modal parameters and is one of the earliest to be applied to SHM [67]. However, eigenfrequencies provide limited information about the state of a given structure or are sometimes only slightly affected by local structural changes. Therefore, the use of additional modal parameters, like damping ratios [68], mode shapes, and their curvature [69], has gained considerable interest. Great efforts have also been invested in the development of automated techniques for the tracking of modal parameters under environmental loading [70]. When environmental loading is employed, the method is designated as the Operational Modal Analysis (OMA).

The following is a non-exhaustive list of some commonly used methods to extract these modal parameters.

- **Time domain methods**:

In the case of time domain methods, the features in question are extracted directly from the measured time series. Simple methods, such as the statistical analysis of the time series, can be used to compute the average, the standard deviation, or even higher statistical moments, such as the kurtosis [71]. Other methods, like Auto-Regressive (AR) models, can be used for the purpose of damage detection. The coefficients of these AR models are identified from observed times series in the healthy and current states. By catching changes in the coefficients of these AR models, damage detection can be performed. This comparison can be made with two distinct (discrete) states [72] or continuously in time.

- **Frequency domain methods**:

Frequency domain methods rely on the transformation of time series into the frequency domain through the use of the Fourier Transform. These methods can either be based on the output-only of the structure, as exemplified by the Fast Fourier Transform [73], or on the input-ouput, such as the Frequency Response Function [74].

- **Time-frequency analysis methods**:

Methods based on the time-frequency analysis have also attracted considerable interest. These methods are well suited for the analysis of nonstationary data. In particular, tracking the time evolution of eigenfrequencies is a way to observe the apparition of damage on structures. Among the available methods, two of the most popular ones are the Wavelet transform [75] and the Hilbert-Huang Transform [76], which have demonstrated excellent performances in the context of SHM.

- **Machine learning**:

Over the past two decades, the quantity of data collected from SHM systems has increased. Long-term monitoring of environmental conditions and real-time damage detection have gained in popularity. Similarly, the monitoring of large structures, such as bridges or buildings, also requires the deployment of a considerable number of sensors. Consequently, novel advanced data processing methods have emerged, including deep learning algorithms [77], which appear to be promising candidates for extracting features and recognising data patterns. Among the deep learning algorithms, the Convolutional Neural Network (CNN) [78] and the Recurrent Neural Network (RNN) [79] have already been applied to SHM. These methods allow to extend detection techniques way beyond classical modal-based methods as they are able to deal with large structural models.

1.2 Motivation

The objective of this thesis is to develop a new methodology for early damage detection. Damage detection is said to be "early" when no visual change can be observed on the studied structure, rendering visual inspection ineffective. The motivation behind this challenge is a reduction in repair costs and an improvement in structural safety. Many safety issues can arise without any alarming visual signs, such as the corrosion of steel bars inside reinforced concrete structures. Indeed, prior to the observation of corrosion traces on the concrete surface, the corrosion process may have already significantly reduced the steel bar sections, resulting in an imminent failure. Therefore, early damage detection requires a sensitive technique that is able to address this problem.

Typically, local techniques, such as ultrasonic testing and electromagnetic methods, can be employed to tackle this problem. These techniques can be considered for small infrastructures or small areas where the damage is expected. In the case of large structures, such as buildings or bridges, global techniques are prefered as it is not possible to cover each element of a large structure with sensors. Therefore, choices must be made, such as placing sensors only on critical members regions or relying on vibrations of the whole structure. For the latter case, the methods are often referred to as vibration-based methods.

However, with respect to early damage detection, these features lack sensitivity. For example, temperatures impact the eigenfrequencies and this influence has the same order of magnitude as damage. In addition, the eigenfrequencies and mode shapes are scalar values and vectors respectively. The information provided by these mathematical tools is limited, and the introduction of new techniques involving matrices or even 3-D matrices could highlight more insightful characteristics of the studied structure. Consequently, the proposal of a novel and sensitive methodology for the early detection of damage was put forth.

1.3 The First Passage Time

The proposed method for early damage detection relies on the concept of First Passage Time (FPT). This method is located inside the vibration-based methods in time domain. This concept refers to the time required by a dynamical system to reach a particular state for the first time, while starting from a known initial condition. Figure 1.2(a) shows a random signal and identifies the first passage time corresponding to passage by the final state X_f, starting from the initial state X_0.

In many cases, the system dynamics can be the result of changes in loading conditions, but it could also result from aging of the structure. It is important to distinguish them. For instance, in the first case, a well-known textbook example [80] in structural dynamics is the response of an undamped mass-spring system (with mass m and stiffness k) subjected to a harmonic loading $p\sin(\omega_0 t)$ tuned on the natural frequency of the system, $\omega_0 = \sqrt{k/m}$. Assuming initial conditions at rest, $X_0 = 0$ and $\dot{X}_0 = 0$, the displacement of the mass reads

$$X(t) = \frac{p}{k}\left(\frac{1}{2}\sin(\omega_0 t) - \frac{\omega_0 t}{2}\cos(\omega_0 t)\right).$$

This response is sketched in Figure 1.2(b). The quantity p/k is the static displacement of the mass under load p. The second term in the parenthesis indicates an unbounded growth at resonance. As time goes by, the term in *cos* grows and it is possible to reach several times the static displacement. The first passage time corresponding to the occurrence of a large displacement $X_f = n \cdot p/k$ with $n \gg 1$, corresponds to the time t for which $X(t)$ exceeds the *final state* X_f for the first time. In this simple introductory example, the first passage time is approximately equal to $2n/\omega_0$, starting from the initial state $X_0 = 0$, until reaching the final state X_f.

This example illustrates that, for a given perfectly determined dynamical system subjected to a deterministic loading, the FPT can be calculated exactly for any given state based on standard time marching algorithms [81].

However, in real-life applications where environmental conditions influence observations, and where measurement errors contaminate data collection, external loads are stochastic processes. Similarly, the state of a structure can be modeled with usual techniques, such as the finite element method [82] or with other simpler kinematic methods [83], with slowly varying parameters to model their aging. In such cases, the FPT is a random variable. It is characterised by a probability distribution, and in particular its statistical moments (average, variance, etc.). In this work, both the loading and the state of the structure will be considered as stochastic processes. Therefore, the FPT will be considered as a random variable.

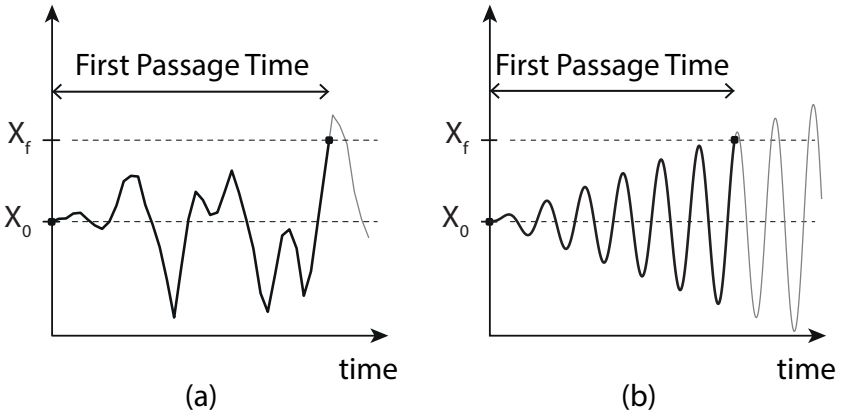

FIGURE 1.2: First Passage Time of a signal: (a) random signal and (b) response of an undamped mass-spring system.

1.3.1 Omnipresence of First Passage Times

Following its definition, a specific First Passage Time answers a question under the format : "How much time does it take for ... to (happen)". As such the concept of First Passage Time is therefore present everywhere in daily life. Without drifting into a philosophical discourse, time and space are the two basic independent variables in physics. Time, as read from the clock or on a calendar, plays a central role in human lives, which are regulated by 24h-days. First passage time problems refer to the first occurrence of a particular issue, or a particular event. Simple applications encompass transportation schedules. For instance, knowing that a morning train left the station Liège-Guillemins at 6:45AM, how much time will it take for this train to pass by the platform in Namur? How much time does it take for a kid to grow higher than 140 cm? How much time does it take for a baseball player to hit a home run for the first time (maybe never)? Or for wild flowers having been seeded on a 1-inch square area to cover a whole field? In all these applications, and the many more, one could just imagine based on his/her own life experience, FPTs are omnipresent. They are also random variables.

In structural engineering, FPTs could also relate to the first occurrence of a specific failure within a system. Structural design can be seen as how long it takes for a structure to reach failure [84], i.e. for the first time. This approach is particularly important in seismic engineering, where the earthquake loading can be seen as a Poisson loading process. In this case, the question addressed in the design can also be asked as : "How much time does it take for a structure to not be able to withstand the seismic action anymore?". Aging and health monitoring issues follow naturally the same logic.

Recently, the Baltimore Bridge collapsed after a cargo ship collision. This bridge opened in 1977 and during more than 40 years, many ships crossed under

the bridge. The design (or the failure) answers the question: how much time was necessary to observe this failure mode for the first time? Another example is related to tower cranes. Such structures are subjected to wind forces and during a period of high wind speeds, the rotation of tower cranes is permitted. However, after a given period of time, the accumulated energy in the structure may exceed the threshold limit. This has already been studied in the context of FPT [85].

In other cases, the system parameters may vary over time, resulting in an earlier degradation of the structure than anticipated. As an example, corrosion results in a slow, and random, decrease of the structural resistance. In this case, the failure condition is time-varying and again, the design answers the question of how much time it would take for the corrosion to diminish the strength for the first time below the loading, resulting in a failure.

Beside these domains of interest for the structural engineer, the concept of FPT can be found in other contexts, including chemistry [86], biology [87], wind engineering [88], sensor design [89], financial applications [90], and the modeling of global warming [91].

1.3.2 Mathematical context

Let consider $\mathcal{D}$, a closed domain in the phase plane of a dynamical system evolving from initial condition $x_0 \in \mathcal{D}$. The FPT corresponding to the first passage through the boundary $\partial\mathcal{D}$ of the domain is defined as [92]

$$t_f = \inf\{t > 0 \,|\, x(t) \in \partial\mathcal{D} \,\&\, x(0) = x_0\} \tag{1.1}$$

Under stochastic excitations, the FPT is a random variable and can be defined by either its Probability Density Function (PDF) p_f or its Cumulative Density Function (CDF) P_f. Its complement, $P = 1 - P_f$, is called the *reliability function*, or *survival probability*, and gives the probability that the system has not yet left the domain $\mathcal{D}$ over the time interval $[0, t]$,

$$P(t; x_0) = \text{prob}(t_f > t) = 1 - P_f(t; x_0) \tag{1.2}$$

The intuitive meaning of $P(t; x_0)$ is the probability of the FPT t_f being greater than t. Therefore, the PDF of the FPT is given by

$$p_f(t; x_0) = \frac{\partial P_f(t; x_0)}{\partial t} = -\frac{\partial P(t; x_0)}{\partial t} \tag{1.3}$$

The CDF of the FPT, $P_f(t; x_0)$, is defined as a function of the transition probability function $p(x, t \,|\, x_0, t_0 = 0)$

$$P_f(t; x_0) = \int_{\mathcal{D}} p(x, t \,|\, x_0, 0)\, dx \tag{1.4}$$

The computation of the FPT through this high-dimensional integral has been tackled in many mathematical problems with the following challenge: given a known dynamical system modelled by a stochastic differential equation, and given a random input to this system, determine the distribution of the FPT of any output of this system [92, 93]. Closed form solutions or their asymptotic behaviour are determined in some very specific cases only [92]. When analytical solutions are not available, the distribution of the FPT is obtained with numerical techniques dedicated to solving the backward Fokker-Planck-Kolmogorov equation [94, 95] or path integral methods [84]. An alternative approach consists in computing the moments of FPT by solving a Pontryagin equation [92]. These methods are not further discussed since the current work is aimed at identifying damage on structures without basing the decision on a fixed mathematical model.

1.3.3 Numerical computation of the First Passage Time

After solving partial differential equations governing the distribution of the FPT, mathematicians like to validate their analytical solutions or their numerical solutions of adjoint problems [96]. To do so, the standard approach is to use a Monte Carlo simulation method to generate samples of the dynamical system. They represent signals, as if they were measured in a random experience. For a given signal, the first passage time can be determined in a direct manner by travelling along the signal until the desired crossing of the final state X_f occurs. Repeating the same operations for another synthetic signal provides another sample of the FPT. After a large number of repetitions, the collection of FPTs obtained from each sample can be used to estimate the desired statistical distribution.

On the right, Figure 1.3 shows this way to the statistics of the FPT: from a theoretical description of a (usually academic) problem, the mathematician develops analytical solutions for the FPT which are validated by means of a Monte Carlo method. For each sample of the state of the system, the FPT is determined by means of a specific algorithm aiming at finding the first occurrence, then returning the corresponding time.

Since this Monte Carlo approach is used for validation purposes only, it appears that direct methods are generally used to obtain this time. For instance, the function *find* which is implemented in common programming languages is able to stop and return after the first occurrence of a condition. It is noticed however, that multiple final states would require several calls to this function, which makes it ineffective. An improved Monte Carlo algorithm has been proposed in [96] by considering multiple levels with different time steps to compute the FPT for various final states X_f. This ad hoc implementation of the algorithm significantly reduces the computation time.

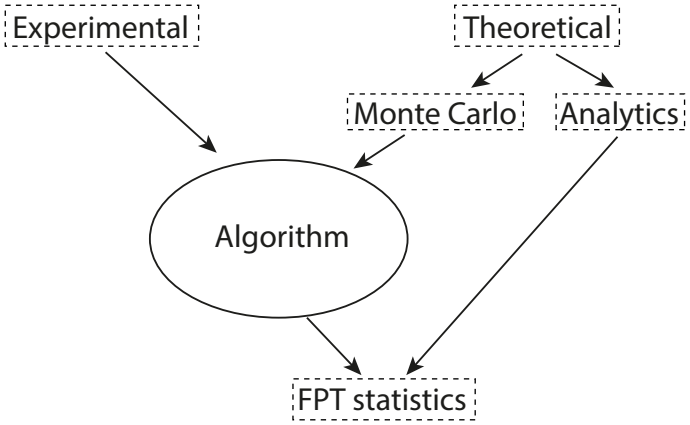

FIGURE 1.3: FPT computation from two different approaches.

In fact, for a given signal, it is possible to determine the FPT from any initial state X_0 to any final state X_f. In some sense, this signal could be a synthetic realisation, or any signal collected from experiments, see the left part of Figure 1.3. The same algorithm as the one used in the Monte Carlo approach is applicable. It turns out that this is a very recent practice to apply this type of statistical processing to experimental data [88, 97, 98].

The objective of this thesis is to go beyond the data processing stage and examine the possibility to detect changes in structures based on FPTs.

1.3.4 First Passage Time map

In this thesis, a novel health monitoring framework is built on the concept of *FPT map*. A map signifies that FPTs are computed for many combinations of initial and finale states (X_0, X_f). Figure 1.4(a) shows a signal sample together with one combination of initial and final states (X_0, X_f). Each crossing of the signal with level X_0 provides the occurrence in time of an initial state, and the corresponding final state needs to be found as the first later occurrence of X_f. Once the level X_f encountered, the FPT is simply the time difference between the two intersections, resulting in the difference between the time when the level X_f is crossed and the time when the level X_0 is encountered. These occurrences are indicated as FPT_1, FPT_2, FPT_3, and FPT_4. In figure, only 4 of the 8 initial states are shown since there are in fact 8 crossings of the signal with level X_0. In principle, the signal should be long enough to collect a large amount of such crossings, so that statistics of the FPT can be performed.

For a given signal, various combinations (X_0, X_f) can be taken into account, which leads to a matrix (*the map*), see Figure 1.4. The columns and rows of the FPT map respectively represent X_0 and X_f. Hence, each cell of the FPT

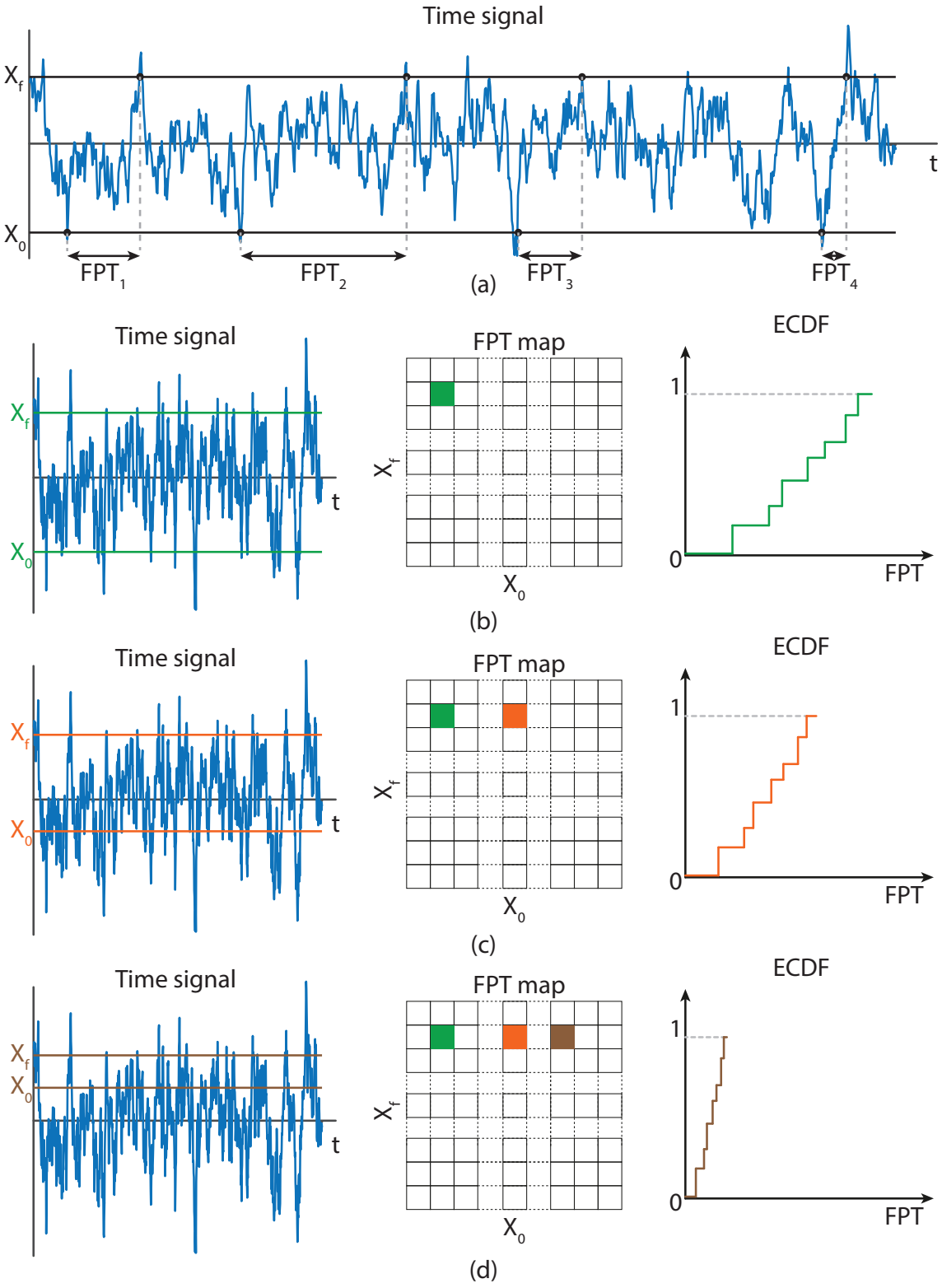

FIGURE 1.4: (a) FPT computation for a given (X_0, X_f) of a sample signal, and (b,c,d) FPT maps for various combinations (X_0, X_f) when X_0 becomes closer to X_f.

map corresponds to a particular combination of (X_0, X_f). In Figure 1.4(b), the levels X_0 and X_f are far from each other. Consequently, it is expected that the FPTs are long for this combination, at least on average. For this measured (or synthetic) signal, all FPTs contained in 1 cell can be statistically processed. Their histogram provides a first estimation of their statistical distribution. An alternative representation is the Empirical Cumulative Density Function (ECDF), which corresponds to the cumulative histogram. The ECDF plays the same role as the CDF in the theory of probabilistics with the difference that it is associated with a sample of a random variable, not with the variable itself. In Figure 1.4(c), the combination (X_0, X_f) is different: the level X_0 is closer to the level X_f. On average, the FPT becomes shorter, compared to the case depicted in Figure 1.4(b). When X_0 and X_f are really close to each other, the FPTs are even smaller, as sketched in Figure 1.4(d).

In these examples and for clarity in the explanations, only the level X_0 has been modified. However, all combinations of (X_0, X_f) are taken into account. The cases where X_0 is greater than X_f are also considered and are located in the lower half of the map, right below the main diagonal. They are associated to the time required to transition from an initial state, which is higher than the final state.

In Figure 1.5, some other important features of the FPT map are illustrated. If the signal is symmetrical, see Figures 1.5(a) and (b), the ECDF of FPT remains unchanged when X_0 and X_f are swapped. This is not the case if the signal is non-symmetrical, in which case the top and bottom halves of the FPT map can be significantly different. The last particular case is shown in Figure 1.5(c). It corresponds to the case where $X_0 = X_f$. In this case, the FPT is deterministic and equal to zero, as it takes no time for the process to reach X_f (equal to X_0). Therefore, on the main diagonal of the FPT map, all computed FPTs are null.

The rest of the FPT map is filled for each combination (X_0, X_f), as explained above. In the most complete description, each square of the map contains an ECDF, but it can also be attributed to any degenerated quantity, for instance, the average or the standard deviation of the FPT. In Figure 1.5(d), the average FPT map is shown for a symmetrical signal. The colored lines represent the contours of equal average of FPT, starting from zero along the main diagonal, and increasing towards the upper and lower edges.

The maps of the first and second statistical moments of the FPT were mentioned for the first time in 2017 [99, 100]. In this work, the maps of the ECDF of FPTs will be exclusively used. Indeed, it was found that a more comprehensive and detailed information was necessary for damage detection purposes.

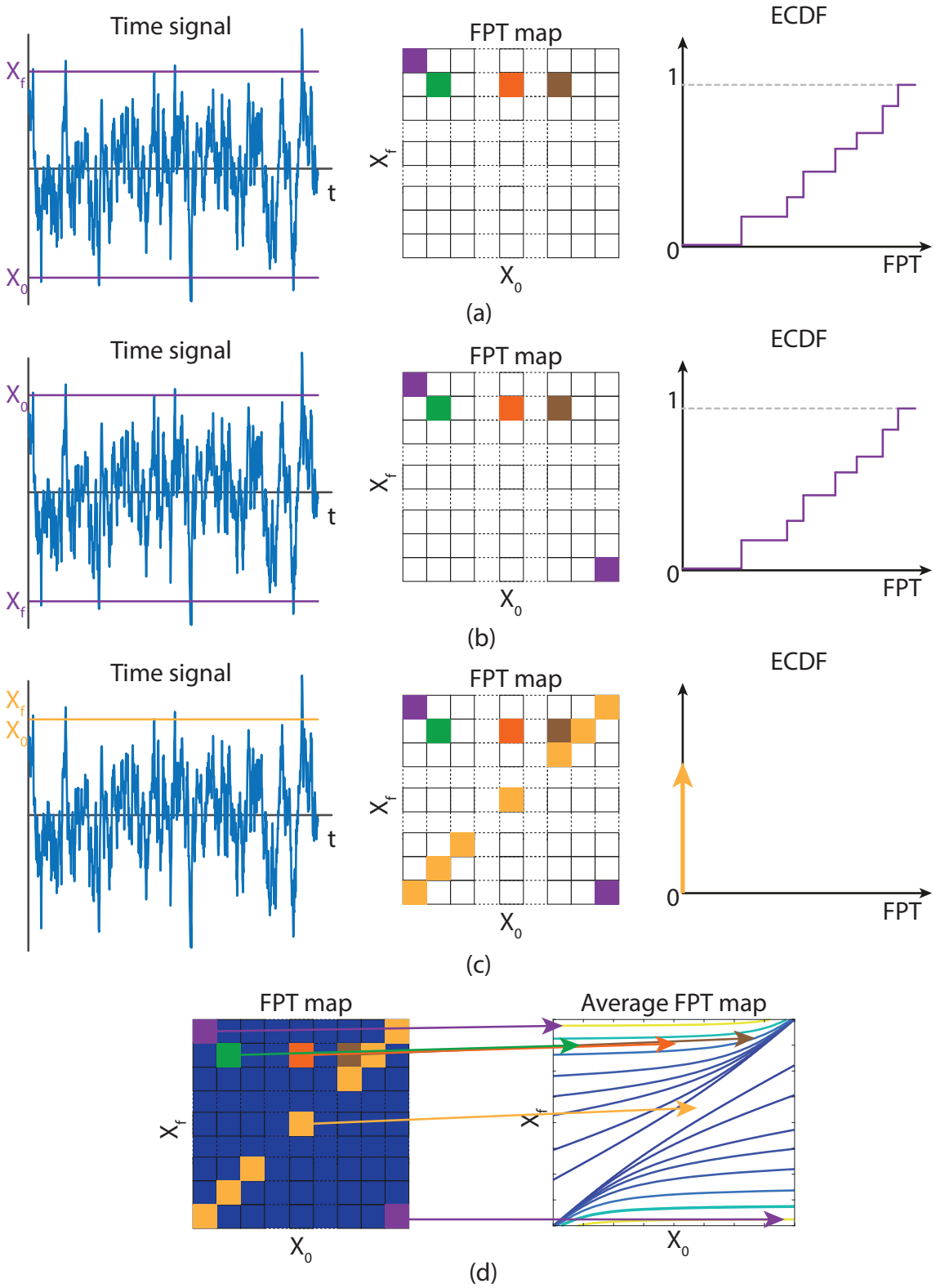

FIGURE 1.5: Particular cases in FPT maps: (a) and (b) if the signal is symmetrical, (c) if $X_0 = X_f$ and (d) average FPT map.

1.4 Outline of the thesis

The law of contraposition says that a conditional statement is true if, and only if, its contrapositive is true

$$(A \Rightarrow B) \quad \Leftrightarrow \quad (\sim B \Rightarrow \sim A)\,.$$

For instance, "rain (A) implies clouds (B)" is equivalent to "no cloud (~B) implies no rain (~A)". This law is at the basis of damage detection and, later, localisation. Indeed, if two structures are the same (A), they have the same response to given input (B). Damage can be inferred if they don't have the same response to given input (~B), in which case the two structures are logically different (~A).

The response to given input could be any mechanical property of the structure that can be easily monitored, for instance natural frequencies, flexibility or other quantities obtained with the technologies summarised in Section 1.1. It could also be the FPT map of the structural response under a given input, a novel approach that is developed in this thesis. No matter the observed response which is used to detect changes, a comprehensive study needs to be developed to analyse the detectability of damage, which is closely related to the sensitivity of FPT maps to small changes in the structure. The larger this sensitivity, the more reactive the method to detect changes, and consequently be a good candidate for early damage detection.

With this objective in mind, and knowing that the concept of First Passage Time is applied to SHM for the first time, the work provided in the thesis was a fresh exploration of the playground. In Figure 1.6, the outline of the thesis is depicted and follows the fundamentals of SHM evoked at the beginning of the introduction. **Chapters 4** and **5** report investigations on two experimental campaigns that were conducted during this thesis. In **Chapter 4**, a small-scale experimental setup made of a steel strip was used to assess and validate the proposed methodology for the first time. Then in **Chapter 5**, the experiment is a main beam of a prestressed concrete bridge coming from a demolished bridge in Luxembourg. This beam was deliberately damaged by progressively cutting the prestressing tendons, one-by-one, over the course of this project, from 21/07/2022 to 16/06/2023. This experiment served as a second test bed for the proposed method, making it more challenging owing to unavoidable environmental effects, such as humidity and temperature variations. Damage detection and localisation are discussed with these two final experimental campaigns, based on the methodology described in **Chapter 3**. This method hinges of the FPT maps of their complete distributions, more precisely on their cumulated histograms (or ECDFs). For the method to be efficient, it was necessary to have access to a fast, efficient and reliable algorithm for the computation of these FPT maps. This algorithm is presented in **Chapter 2**. Among other possible outputs, the

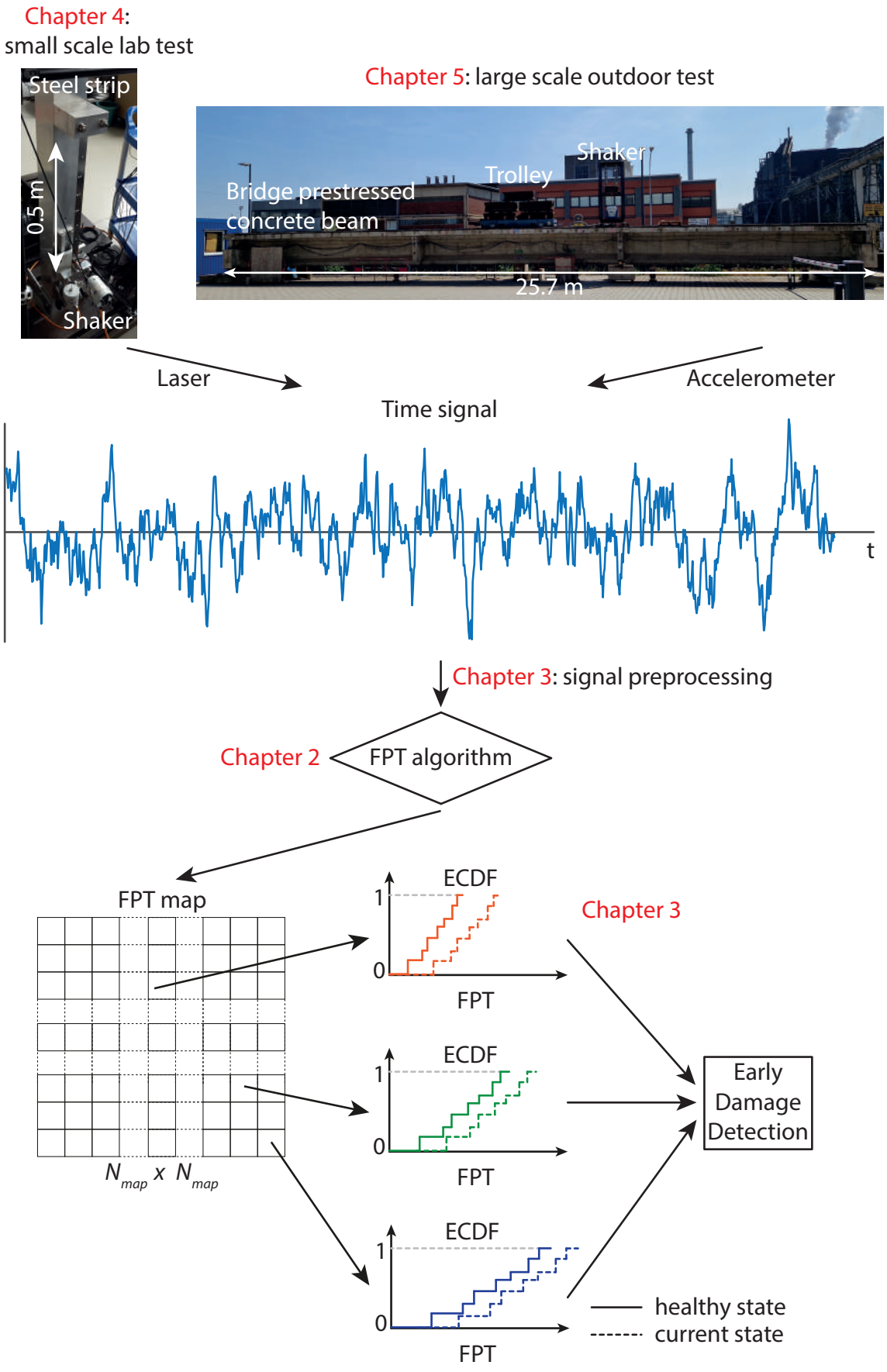

FIGURE 1.6: Outline of the thesis.

algorithm returns the ECDFs of the FPTs associated with the input signal. The comparison of the FPT maps obtained from signals collected on the structure in a reference state and in the current state is used to infer damage. The proposed method is also extended to localise damage whenever detected.

1.5 Personal contributions

The first contribution is the development of a fast and memory-efficient algorithm [101]. The creation of a new algorithm to compute FPTs was motivated by its repeated use to experimental signals. The algorithm has been written in MATLAB and uses, therefore, the vectorization allowed in this programming language to achieve much faster computation than existing alternatives. As described in Chapter 2, the key idea of the new algorithm is to process the signal backward; this allows to go through the signal only once to build the entire FPT map.

The second contribution is the proposed methodology for SHM, which belongs to the family of the vibration-based methods. It consists of several steps : choice of an appropriate loading, vibration measurement and standard pre-processing, computation of the FPT maps at various ages of the structure, comparison of the corresponding first passage time maps and decision on whether the structure is damaged or not. More precisely, beside loading and vibration measurement, which follow classical approaches,

- it was found that a good detectability was obtained when data pre-processing was relying on the envelope, obtained with the Hilbert transform, and two filters: a bandpass filter and a frequency content adjustment. These filters remove the unwanted frequency content from the signal and compensate for the slight differences in reproducing the same loads with a shaker, when it is operated in open loop configuration,

- since FPT maps are a rather young concept, it was necessary to develop an approach to compare two FPT maps coming from two different measurements. This was done by designing and developing a new hypothesis testing for the comparison of two collections of Empirical CDFs (ECDFs).

Last but not least, the proposed methodology was applied to a small-scale structure in lab conditions and to a large civil structure in environmental conditions. In the first experiment, damage detection and localisation were studied based on velocity measurements acquired by a laser. The second experimental setup was a prestressed concrete beam submitted to environmental loads on top of the deliberate damage incurred to the structure and the random passage of nearby trains. In this case, damage detection was partly successful and recommendations on how to improve the quality of damage detection could be identified.

1.6 List of Publications

Journal papers

- K. Theunissen and V. Denoël (2024). An efficient algorithm for the computation of the first passage time maps of a given signal. *Mechanical Systems and Signal Processing*, 207:110884 [101]
- K. Theunissen, E. Verstraelen, and V. Denoël (under internal review). Damage detection and localisation based on First Passage Time histograms. *Mechanical Systems and Signal Processing*
- K. Theunissen and V. Denoël (under preparation). Influence of noise on First Passage Time maps and their use for early damage detection. *Probabilistic Engineering Mechanics*

Conference papers

- K. Theunissen, E. Verstraelen, J.-C. Golinval, and V. Denoël (2022). Influence of structural damages on first passage time maps. In *ISMA-USD Noise and Vibration Engineering Conference 2022 [102]*
- K. Theunissen, E. Verstraelen, J.-C. Golinval, and V. Denoël (2024). Localization of structural damage based on first passage times for a prtheestressed steel strip. In Hae Young Noh, Matthew Whelan, and P. Scott Harvey, editors, *Dynamics of Civil Structures, Volume 2*, pages 99–101, Cham, 2024. Springer Nature Switzerland [103]
- K. Theunissen and V. Denoël (2022). Fractional derivatives model of aeroelastic derivatives of bridge decks. In *Proceedings of the 8th European-African Conference on Wind Engineering 2022 [104]*

Chapter 2

A Novel Algorithm for the computation of First Passage Times

This chapter focuses on a new efficient algorithm that has been developed in order to compute First Passage Times.

First, the algorithm is described, before assessing its efficiency with realisations of three stochastic processes: an Ornstein-Uhlenbeck process, a Geometric Brownian Motion, and a narrowband signal. Second, for the Ornstein-Uhlenbeck process, the algorithm is validated by comparing the numerical results, obtained with the algorithm, to the theoretical results. Finally, FPT maps and histograms of FPTs are computed to illustrate the application of the algorithm to selected experimental data.

2.1 Algorithm

2.1.1 Generalities

Let X_i, $(i = 1, ..., n)$ a discrete-time signal, which can be seen as a realisation of a random process. A novel algorithm for computing the First Passage Time maps is presented. These maps represent some selected centred statistical moments and histograms of the FPT for various combinations of the initial and final values, X_0 and X_f. The k^{th} centred statistical moment is given by

$$m_k = \mathbb{E}\left[\left(\text{FPT}\left(X_0, X_f\right) - \mathbb{E}\left[\text{FPT}\left(X_0, X_f\right)\right]\right)^k\right]. \tag{2.1}$$

The first two centred moments are the average first passage time ($k = 1$) and its variance ($k = 2$). In general, the first passage time maps of the first few centred moments $k = 1, ..., p$ are computed. Since the standard error of the estimators increases with p, it is customary to opt for $p = 2$. However, it is not forbidden to use the proposed algorithm for much larger values.

The maps are computed for N_{map} values of X_0 and X_f which are uniformly spaced between two levels, $L_{\min}$ and $L_{\max}$. These values are set to default at the 10^{th} and the 90^{th} percentiles of the given signal, as shown in Figure 2.1(a). The N_{map} equally spaced and ordered levels are noted L_{iL}, with $iL \in \{1, 2, ..., N_{\text{map}}\}$, $L_1 = L_{\min}$ and $L_{N_{\text{map}}} = L_{\max}$.

Beside centred moments, the proposed algorithm also optionally computes histograms of the FPT for the same combinations of X_0 and X_f, or less if some data storage needs to be saved. Indeed, these histograms are recursively computed as explained next by counting the number of occurrences of first passage times in small predetermined bins ($b = 1, ..., n_{\text{bins}}$) which are allocated at the beginning of the signal processing. These bins can then be aggregated in order to reach some optimality in the density estimator [105, 106]. Ultimately, the fundamentals of the SHM method presented in Chapter 3 will hinge on the Empirical Cumulative Density Function (ECDF), which corresponds to the cumulative of these histograms.

For centred moments, each of the FPT maps can therefore be seen as an $N_{\text{map}} \times N_{\text{map}}$ array gathering the statistics of the FPT for the different combinations of X_0 and X_f, and for $k = 1, \cdots, p$. The FPT map of the histogram, however, is a $N_{\text{map}} \times N_{\text{map}} \times n_{\text{bins}}$ array.

Since the same crossing levels are used for both X_0 and X_f, the main diagonal of an FPT map is omitted because, there, $X_0 = X_f$, and it takes no time to reach level $X_f = X_0$, starting from X_0. Also, the FPT values above and below this diagonal respectively correspond to $X_f > X_0$ and $X_f < X_0$. The latter case may be less intuitive but is not irrelevant (e.g. [96]); it has practical applications in dissipative systems.

A naive implementation would entail iterating through the varying initial and final values, leading to reprocessing of the signal for every new combination of X_0 and X_f, and possibly for every other centred moment of interest. This would result in at least 2 nested loops. Instead, a new algorithm was developed in order to efficiently compute FPT maps of a given signal. The conceptual idea is the same as the algorithm presented in [85, 88], in which the statistics of the FPT are computed for all combinations of X_0 and X_f simultaneously. This algorithm can be described as a variant of the rainflow algorithm [107]. By virtually rotating the time signal by 90°, one can visualise a water droplet falling and its trajectory defines the main envelope, which is stored. Subsequently, a partial envelope can be constructed for every point of the time signal utilising the same process until the water droplet meets the path of the main envelope. Once the main envelope is reached, the partial envelope aligns with it until the end of the time signal. Afterwards, the FPTs are derived from the computed envelopes.

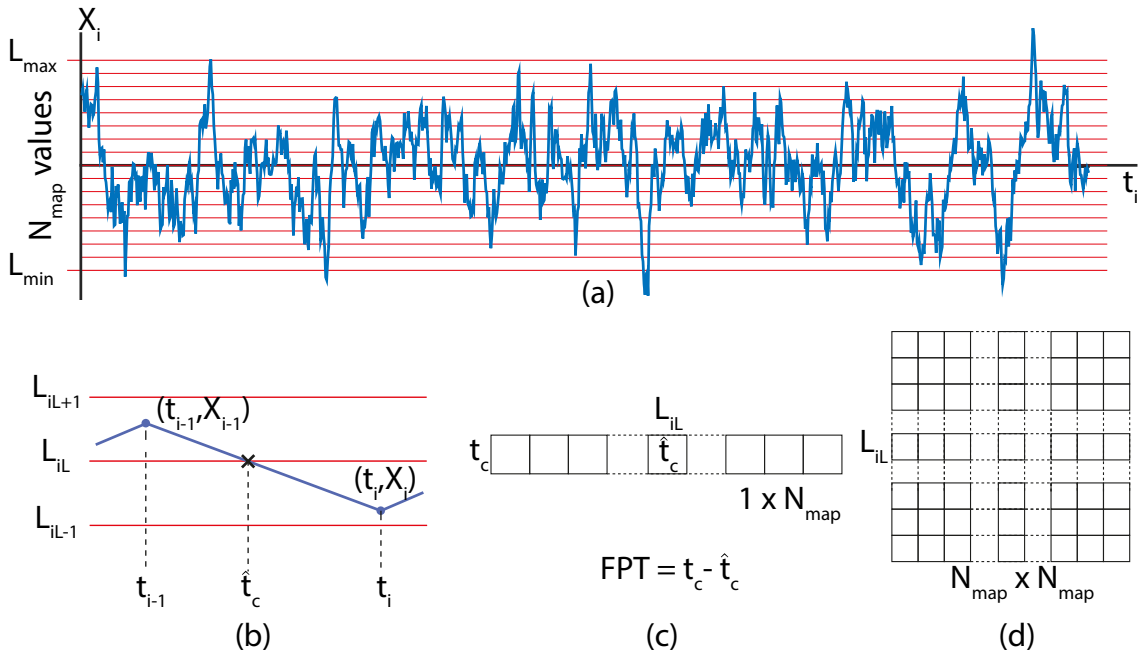

FIGURE 2.1: General overview of the proposed algorithm: (a) definition of levels, spanning a pre-defined value of the minimum and of the maximum, (b) linear interpolation to compute the crossing time $\hat{t}_c$, (c) storage of $\hat{t}_c$ into the vector t_c and FPT calculation (d) storage of FPT into the iL^{th} row of a map of a raw moment.

Another implementation has also been developed [108]. However, before computing the centred statistical moments of FPTs, all FPTs are stored inside a 3-D matrix, whose rows and columns correspond to the number of X_0 and X_f while its height is the number of FPTs computed for the considered combination (X_0, X_f). This reduces the algorithm efficiency and all computed FPTs must be stored.

Therefore, a novel algorithm is proposed. It differs as the signal is analysed backward and does not rely on a variant of the rainflow algorithm anymore. As a first advantage, only the last encountered time for each level is required to calculate the FPTs so that, in the reverse analysis process, only those crossing times are temporarily stored. This considerably reduces the memory storage. Also, the specific algorithmic arrangements presented in detail later ensure that the signal is processed only once, which significantly reduces the CPU time for the signal processing.

For a compact view, three pseudo-codes are provided. The main function of the algorithm is 1. Algorithms 2 and 3, used by `FPT_map()`, correspond to the functions `isALevelCrossed()` and `isAnotherLevelCrossed()`. They are related to the detection of crossed levels. These three functions are described in more detail later in this document.

In essence, the proposed algorithm is based on two different parts operating in cycle over each time step. The first part is the detection of level crossing and the second part is, if a level has been crossed, the computation of the FPT.

Firstly, the algorithm aims at keeping track of time instants where levels L_{iL} are crossed, while rewinding the signal. The level crossing detection hinges on two main functions aiming at efficiently finding a crossed level: `isALevelCrossed()` and `isAnotherLevelCrossed()`. These functions require the sign of the slope of the previous and current crossed levels L_{iL}. The slope is said to be *null* if $(X_{i-1} = X_i)$, positive if $X_{i-1} < X_i$ and negative otherwise. The first crossed level L_{iL} is determined based on the last point of the signal. Once the first crossed level has been determined, a pointer is used to move backward through the signal, point by point. The function isALevelCrossed() is always used first in order to check if at least one level is crossed. The efficiency of this function is based on a fast detection of level crossing, and if so, which level(s) has(have) been crossed. Thanks to simple if/else statements, the sign of the current slope and the sign of the slope of the last crossed level, only one level has to be checked in order to detect if a level is crossed. If the checked level is not crossed then no other test has to be performed. In the case of a null slope, the algorithm simply checks if the current level L_{iL} is equal to X_{i-1}.

There might be several level crossings over one time step, when the gradient of the signal is large. Therefore, the function `isAnotherLevelCrossed()` is used. This function is a lighter version of the function `isALevelCrossed()` which improves the speed of the algorithm. The function `isAnotherLevelCrossed()` will

be called while it detects a level crossing after each FPT calculation.

When a level is crossed, say level iL, a crossing time $\hat{t}_c$ is calculated by linear interpolation between t_i and t_{i-1},

$$\hat{t}_c = \frac{L_{iL} - X_{i-1}}{X_i - X_{i-1}} (t_i - t_{i-1}) + t_{i-1} \tag{2.2}$$

to provide a refined estimation, see Figure 2.1(b).

This time $\hat{t}_c$ is stored at the iL^{th} entry of a $1 \times N_{\text{map}}$ vector t_c, possibly replacing information previously stored at the same location, to indicate that level L_{iL} has been crossed at that time, see Figure 2.1(c). The vector t_c, initialised with `empty` values, is used to store the last value $\hat{t}_c$ for each level L_{iL}. In addition, a logical vector $1\text{x}N_{\text{map}}$ called L_{met}, initialised with `false` values, is used to track which level has already been encountered since the beginning of the signal processing; $L_{\text{met}}(iL)$ is therefore set to `true`. This vector is useful as it enables the vectorial programming capabilities of the MATLAB language [109].

Then, the FPT of all encountered levels is simply the difference $t_c - \hat{t}_c$.

These values are samples of the random variables corresponding to the first passage times. The integer powers $k = 1, \cdots, p$ of the differences $t_c - \hat{t}_c$ are added to the maps of raw moments which will be ultimately used to compute the centred moments of the first passage times, see Figure 2.1(d).

The centred moments are then updated inside matrices. Different centred moments can also be calculated by changing the power k. The histograms are also updated. These FPT histograms are calculated for all or some combinations (X_0, X_f) of a FPT map. The bin width can be determined based on the chosen accuracy and is a multiple (`coef_dt`) of the time step. A posteriori, the FPT histograms are post-processed using different formulas [105, 106] in order to reduce the number of bins. Before moving the pointer onwards, `isAnotherLevelCrossed()` checks if another level L is crossed. If this is the case, the FPT calculation is performed once again until the function `isAnotherLevelCrossed()` returns `false`, i.e. that no level crossing has been detected. Once the pointer has reached the first data point in the signal, the processing is complete. The algorithm returns numerical values of the FPT maps which can then be independently graphically represented.

`FPT_map()`

Input: t_i, X_i, $\forall i = 1, ..., N$
Output: FPT maps of centred moments and histograms of FPT

Discretisation of $X(t)$ into N_{map} equidistant levels L
Determination of the bin width and the number of bins based on the input coef_dt
Initialisation of the last crossed level and its slope based on $X(N)$
for $i \leftarrow N$ **to** 1

    Save of the slope for the last crossed level L_{iL}
    isALevelCrossed()
    while *A level is crossed*
        Storage of the current time $\hat{t_c}$ for the corresponding crossed level L_{iL} into t_c
        FPT $\leftarrow t_c - \hat{t_c}$
        Update iL^{th} row of maps of raw moments
        Update histograms
        isAnotherLevelCrossed()
    end
end
Transformation of raw moments into centred moments

Algorithm 1: FPT_map()

`isALevelCrossed()`

Input: X_i, X_{i-1}, L, *slope_iL*, iL, $N_{\mathbf{map}}$
Output: iL, *slope_iL*, *crossing*, *crossing_diff_slope*

```
crossing ← FALSE
crossing_diff_slope ← FALSE
if X_i > X_{i-1}
    if X_i ≥ L_1 and X_{i-1} ≤ L_{N_map}
        if slope_iL is positive
            if iL − 1 > 0 and X_{i-1} ≤ L_{iL-1}
                iL ← iL − 1
                slope_iL is positive again
                crossing← TRUE
            end
        else
            if iL > 0 and X_{i-1} ≤ L_{iL}
                iL ← iL − 1
                slope_iL is positive now
                crossing ← TRUE
                crossing_diff_slope ← TRUE
            end
        end
    end
else if X_i < X_{i-1}
    if X_i ≤ L_{N_map} and X_{i-1} ≥ L_1
        if slope_iL is negative
            if iL + 1 ≤ N_map and X_{i-1} ≥ L_{iL+1}
                iL ← iL + 1
                slope_iL is negative again
                crossing ← TRUE
            end
        else
            if iL ≤ N_map and X_{i-1} ≥ L_{iL}
                iL ← iL − 1
                slope_iL is negative now
                crossing ← TRUE
                crossing_diff_slope ← TRUE
            end
        end
    end
else
    if X_{i-1} = L_{iL}
        slope_iL is horizontal
        crossing ← TRUE
    end
end
```

Algorithm 2: isALevelCrossed()

`isAnotherLevelCrossed()`

Input: X_{i-1}, L, *slope_iL*, *prev_slope_iL*, iL, N_{map}
Output: iL, *crossing*

```
crossing ← FALSE
if slope_iL is positive
    if prev_slope_iL is positive
        if iL − 1 > 0 and X_{i−1} ≤ L_{iL−1}
            iL ← iL − 1
            crossing ← TRUE
        end
    else
        if iL > 0 and X_{i−1} ≤ L_{iL}
            crossing ← TRUE
        end
    end
else if slope_iL is negative
    if prev_slope_iL is negative
        if iL + 1 ≤ N_{map} and X_{i−1} ≥ L_{iL+1}
            iL ← iL + 1
            crossing ← TRUE
        end
    else
        if iL ≤ N_{map} and X_{i−1} ≥ L_{iL}
            crossing ← TRUE
        end
    end
end
```

Algorithm 3: isAnotherLevelCrossed()

2.1.2 Other specific features

In order to optimise the algorithm and its performances, several specific features have been used.

The first one is taking advantage of the vectorization capabilities offered by MATLAB by using the vector L_{met}. This vector is useful to reduce the computational time by avoiding redundant loops. Moreover, the vectorization of MATLAB has also been used in the computation of the FPT histograms. Indeed by determining all cells of the 3D matrix that need to be updated, the increment of these cells is performed directly without any explicit loop.

A second feature of the proposed algorithm concerns the windowing of signals with missing data. If a part of a signal has been corrupted or is missing, which is unfortunately not rare with SHM data, the user can discard that part. Indeed, since the algorithm also returns the occurrences of the first passage time, by sending one fraction of the signal at a time to the algorithm, the user can get the matrices with the data that is already processed for the centred moments calculation. A simple averaging of these matrices is possible and allows to concatenate information coming from several fragments of a corrupted signal with missing pieces.

The last feature concerns the handling of signal with low digitalisation or rounded values. Indeed, in case of low digitalisation, there are two major issues: (i) identical consecutive values resulting in a slope equal to zero and (ii) data values that correspond exactly to a level L_{iL}. While in a signal with significant digitalisation, these two cases are marginal, they occur much more frequently in case of low digitalisation. In order to limit the bias, the first issue is easily solved by taking into account the special case of the null slope in the functions `isALevelCrossed()` and `isAnotherLevelCrossed()` while the second issue required more attention. In the original version of the proposed algorithm if a data point was equal to a level L_{iL} this point was taken into account twice. To face this issue it has been decided that the FPT calculation is skipped if $L_{iL} = X_i$ except for the point $X(n)$, which is the first point encountered by the algorithm. This removes the double counting.

2.2 Efficiency of the proposed algorithm

In this section, the efficiency of the algorithm is discussed on two examples.

2.2.1 Example 1: Experimental data

As a first comparison, the data utilised in [88] has been re-used. The data come from an experimental setup of a tower crane whose results were measured in the wind tunnel of the University of Liège. The measured signals consist in the rotational position of a tower crane free to rotate in a turbulent flow. The number of points is equal to 3.6 millions with a time step $\Delta t = 0.001$ s.

To assess the efficiency of the proposed algorithm, the algorithm from [88] and the proposed algorithm processed the same data. **The algorithm featured in [88] took 2600 seconds to complete its calculations whereas, the proposed algorithm only required 6 seconds, resulting in a calculation time 400 times shorter.**

These good results indicate that the new algorithm is indeed a good candidate for processing larger amounts of data.

2.2.2 Example 2: Synthetic data

As a second comparison, a parametric study is conducted to demonstrate the effectiveness of the proposed algorithm in addressing various aspects of a problem. In this case three types of signals with very different spectra have been used: an Ornstein-Uhlenbeck (O-U) process, a Geometric Brownian Motion (GBM) and the displacement response of a single oscillator (1-DOF) with mechanical properties as per [110] (m =28.138 to, k =22495 kN/m, ξ =4%) and subjected to narrowband white noise excitation in the range [4; 5] Hz.

The first two processes are well-known theoretical stochastic processes. They have been generated numerically by using an Euler scheme and the definition of the Wiener process [96]. The third sample has been obtained by solving the motion equation of the single degree-of-freedom oscillator using the Newmark scheme under a loading history sampled from a narrow banded white noise around the first bending mode (4.5 Hz) of the corresponding specimen. Figure 2.2 shows two samples of each of these processes. A close-up view in the range $t \in [1000; 1020]$s offers a better picture of the processes at stake. Also, while the geometric Brownian motion is a transient process, the other two considered processes are Gaussian, as indicated by the histograms of the sampled time series.

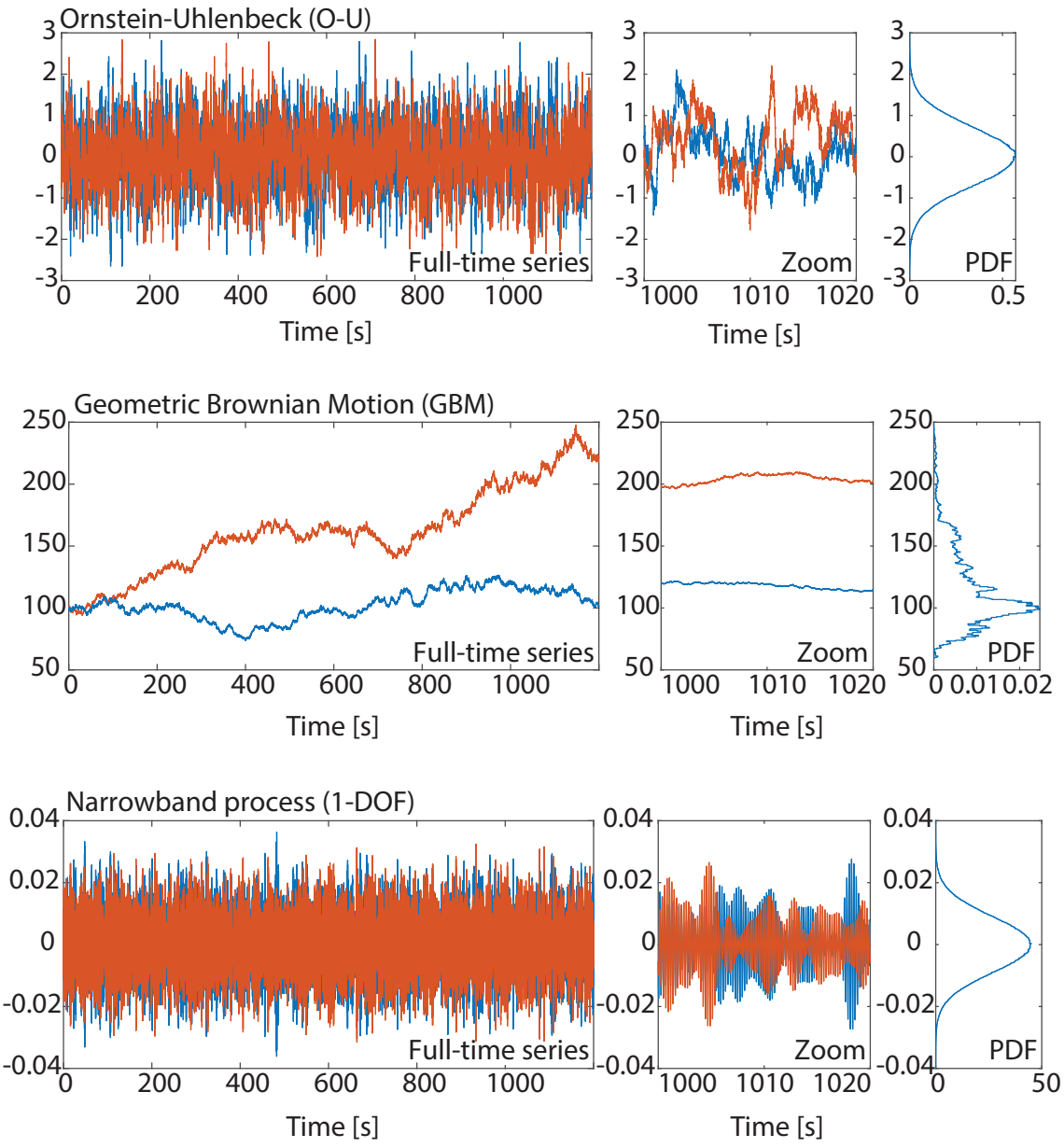

FIGURE 2.2: Generated samples of the three considered stochastic processes: the Ornstein-Uhlenbeck process, the Geometric Brownian Motion and a narrowband process. Two samples are shown for each process. The PDF on the right shows the distribution of sample values in the signal.

A reference case is obtained by computing the FPT map of samples of these three random processes. They are sampled at 500 Hz, for a duration of 10 s (i.e. contain 5000 data points) and the FPT map is established for $N_{\text{map}} \times N_{\text{map}} = 400$ values. For the three processes (O-U, GBM and 1-DOF), the mean execution times, averaged over 150 repetitions, are

O-U	GBM	1-DOF
0.0175 s	0.0105 s	0.0144 s

Unlike more traditional processing techniques, such as the Fourier transform, the computational burden associated with the establishment of an FPT map depends on the specific nature of the signal. In particular, the computational time associated with the geometric Brownian motion is significantly shorter than for the other two processes. As detailed in the following, this is a consequence of the drift associated with a geometric Brownian motion.

A parametric study has been carried out in order to determine the influence on the runtime (to compute the whole FPT map) of three major parameters that have been identified as having a possible influence on the quality of the resulting FPT map:

1. the total length of the signal;
2. the sampling frequency of the signal;
3. the number of level discretisation N_{map}.

The results of this analysis are reported in Figure 2.3 in terms of a wall-clock time, i.e. the elapsed time as displayed on a chronometer. This measure has been chosen over CPU-time as the latter is dependent on the number of processing cores utilised. The wall-clock time is represented for each studied parameter.

Moreover, for enhanced analysis of the influence of the different parameters on the total execution time, two distinct times, namely t_{cal} and t_{level}, have been utilised. The time t_{cal} is the time required to calculate FPTs and store them into matrices while t_{level} is the time needed to detect if one level is crossed. Together, t_{cal} and t_{level} constitute the total execution time. The order of magnitude of the MATLAB time accuracy is roughly 0.1s. The number of repetitions is therefore chosen as 150 in order to better discriminate between the different cases. Based on the number of measurements and the time accuracy of MATLAB, a threshold value equal to $0.1/\sqrt{150} = 8.10^{-3}$s has been estimated. Below this value, the estimation of the wall-clock time is inaccurate and the corresponding zone is coloured in light gray because the calculated time may be affected by other CPU tasks, for example. These performance tests have been carried out on a computer with the following specifications: CPU: Intel(R) Core(TM) i7-10510U CPU 2.30GHz, RAM: 16Go 2667MHz.

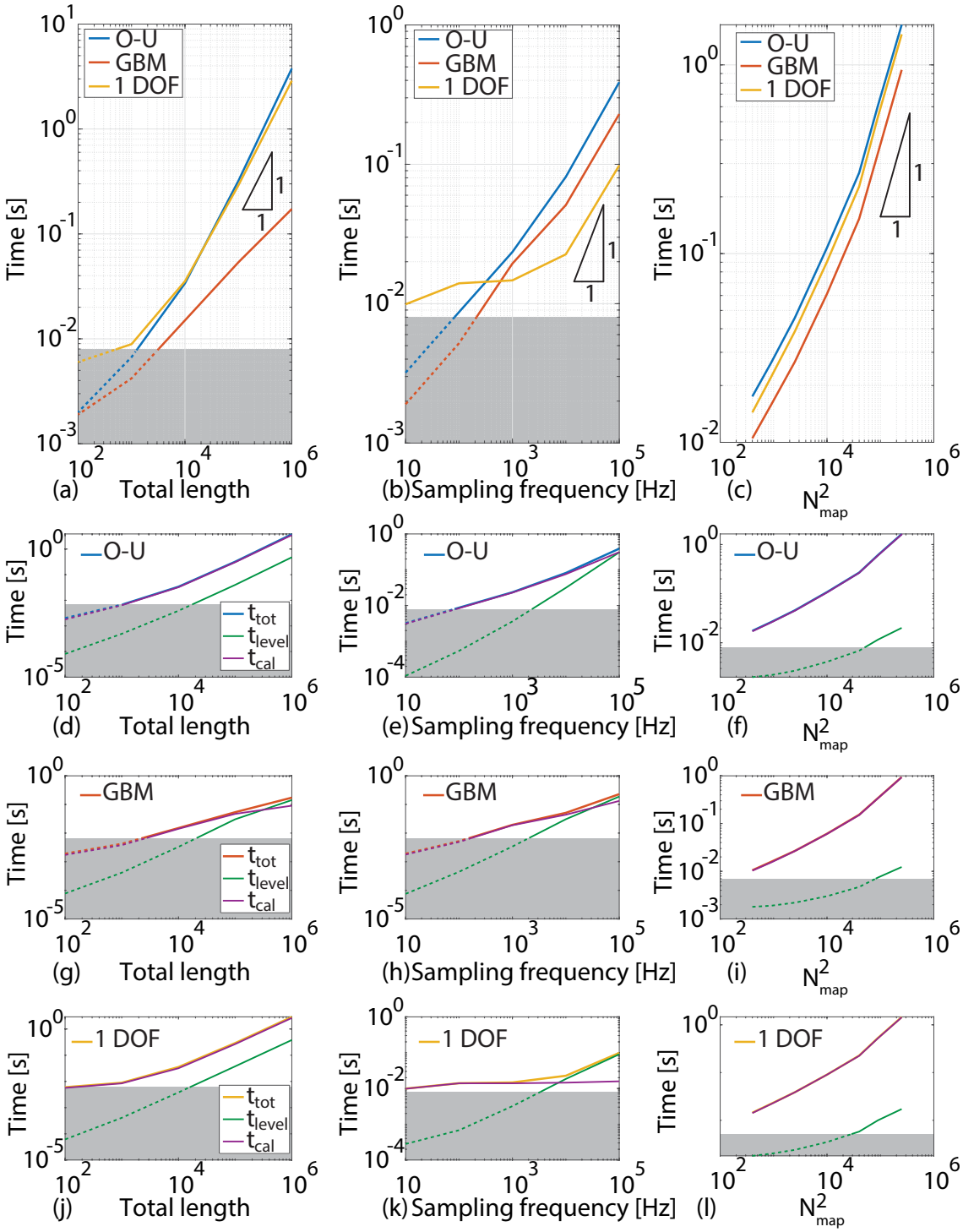

FIGURE 2.3: Execution time of the algorithm based on the influences (a,d,g,j) of the total length, (b,e,h,k) of the frequency and (c,f,i,l) of the parameter N_{map} for (d,e,f) the Ornstein-Uhlenbeck process, (g,h,i) the Geometric Brownian Motion and (j,k,l) a narrowband process.

In Figure 2.3(a), the influence of the signal length is shown. The sampling frequency is set at $f_s = 500$ Hz, and the parametric analysis concentrates on the number of data points in the signal. The total duration is $T = 0.2$ s for $n = 10^2$ and $T = 2000$ s for $n = 10^6$ points in the signal. In the worst case, the wall-clock time grows proportionally to the number of points. The geometric Brownian motion is the most advantageous case due to the peculiar occurrence of crossing times of this random process. In Figures 2.3(d), 2.3(g) and 2.3(j), t_{cal} and t_{level} are represented for each process. For the O-U and the narrowband 1-DOF processes, t_{cal} always exceeds t_{level} by at least one order of magnitude. This is not the case for the GBM process for which t_{level} is getting closer to t_{cal} and even becomes larger as the signal size increases. This deviation from the other two processes can be explained by the global exponential behavior of the GBM process. Eventually, this process stops passing through the lower levels after a certain time because the GBM is not stationary. Therefore, for the same number of points, fewer FPTs are calculated for the GBM process than for the other two processes. Consequently, as the signal size increases, the algorithm spends proportionally more time checking if a level is crossed than computing FPTs.

Figure 2.3(b) illustrates the influence of the sampling frequency. A total duration of $T = 10$ s is maintained and the sampling frequency is adjusted so that using $n = 10^2$ data points corresponds to a sampling frequency $f_s = 10$ Hz and using $n = 10^6$ data points corresponds to a sampling frequency $f_s = 100000$ Hz. In Figures 2.3(e) and 2.3(h), it can be observed that t_{level} is increasing faster than t_{cal}. Indeed, doubling the sampling frequency f_s does not necessarily double the number of calculated FPTs; in practice, this number usually decreases. However, the number of data points doubles, which results in a larger increment of t_{cal} compared to t_{level}. In Figure 2.3(k), the behaviour of t_{cal} is different. At a sampling frequency $f_s \approx 100$ Hz, t_{cal} is constant, which can be attributed to the numerical scheme. When the time step is small enough, i.e. the sampling frequency f_s is sufficiently high compared to the range of the band-limited white noise used as an input, the Newmark scheme under the same loading history will compute identical response signals, corresponding to the same number of calculated FPTs. Finally, it can be concluded that t_{cal} becomes dominant over t_{level} for each signal in this section beyond a sufficiently high sampling frequency f_s.

In Figure 2.3(c), the influence of N_{map} is shown. The proposed algorithm shows a uniform behaviour across all processes: the wall-clock time mainly depends on the number of calculated FPTs, i.e. is proportional to N_{map}^2. This trend is also observable in Figures 2.3(f), 2.3(i) and 2.3(l) where t_{cal} is at least one order of magnitude higher than t_{level}. For the same signal duration and sampling frequency, the O-U process exhibits more threshold crossings, thereby contributing to its longer runtime when compared to the 1-DOF and GBM processes.

Moreover, this algorithm is memory-efficient. Only the last encountered time for each level X_f is required to compute FPTs, reducing the memory usage of the algorithm.

2.3 Verification

In this section, the algorithm's results are compared with theoretical values to verify the accuracy of the algorithm. Among the 3 processes considered so far, the Ornstein-Uhlenbeck process has been chosen since it possesses available analytical solutions and resembles the typical signals that could be measured in an SHM program. The mathematical formulas for computing the PDF and the centred statistical moments of the O-U process have been summarised in Appendix A based on [111]. Their mathematical expressions of these formulas are complicated and based on integrals, such as the imaginary error function. Therefore, the analytical expression of the narrowband 1-DOF process is intractable. The stochastic differential equation of the O-U process is

$$\mathrm{d}X_t = \beta(\alpha - X_t)\mathrm{d}t + \sigma \mathrm{d}W_t \tag{2.3}$$

whose parameters are $\alpha = 0$, $\sigma = 1$, and $\beta = 1$ rad/s. Equation 2.3 is solved numerically with an Euler-Maruyama scheme [112]. By using Monte Carlo simulations, samples of this O-U process are generated and the maps of average FPT and standard deviation of FPT are computed. Histograms of the first passage time are also computed for some selected combinations of (X_0, X_f).

Equation 2.3 has been integrated with three different time steps, corresponding to sampling frequencies 500 Hz, 5000 Hz and 50000 Hz. This allows appreciating the impact of this simulation parameter on the accuracy of FPT maps. Moreover, a large number of simulations has been used and the results of each run have been merged in order to have at least 10^6 FPTs for each combination of (X_0, X_f). This large number allows to narrow down the confidence intervals on the FPT statistics. In Figure 2.4(a), the average FPT map is represented. The numerical results accurately match the theoretical results summarised in Appendix A, especially for $f_s = 5000$ Hz and $f_s = 50000$ Hz. As expected, greater sampling frequencies improve accuracy. Figures 2.4(b,c,d) show absolute errors at sampling frequencies of 500 Hz, 5000 Hz and 50000 Hz. Table 2.1 displays the highest relative errors for the average FPT at various ratios $\dfrac{f_s}{f_{O-U}}$, where $f_{O-U} = \dfrac{\beta}{2\pi}$ Hz is the characteristic frequency of the O-U process. These values are located near the main diagonal of the map where X_0 and X_f are close to each other. They correspond to very short passage times and are affected by the discretisation.

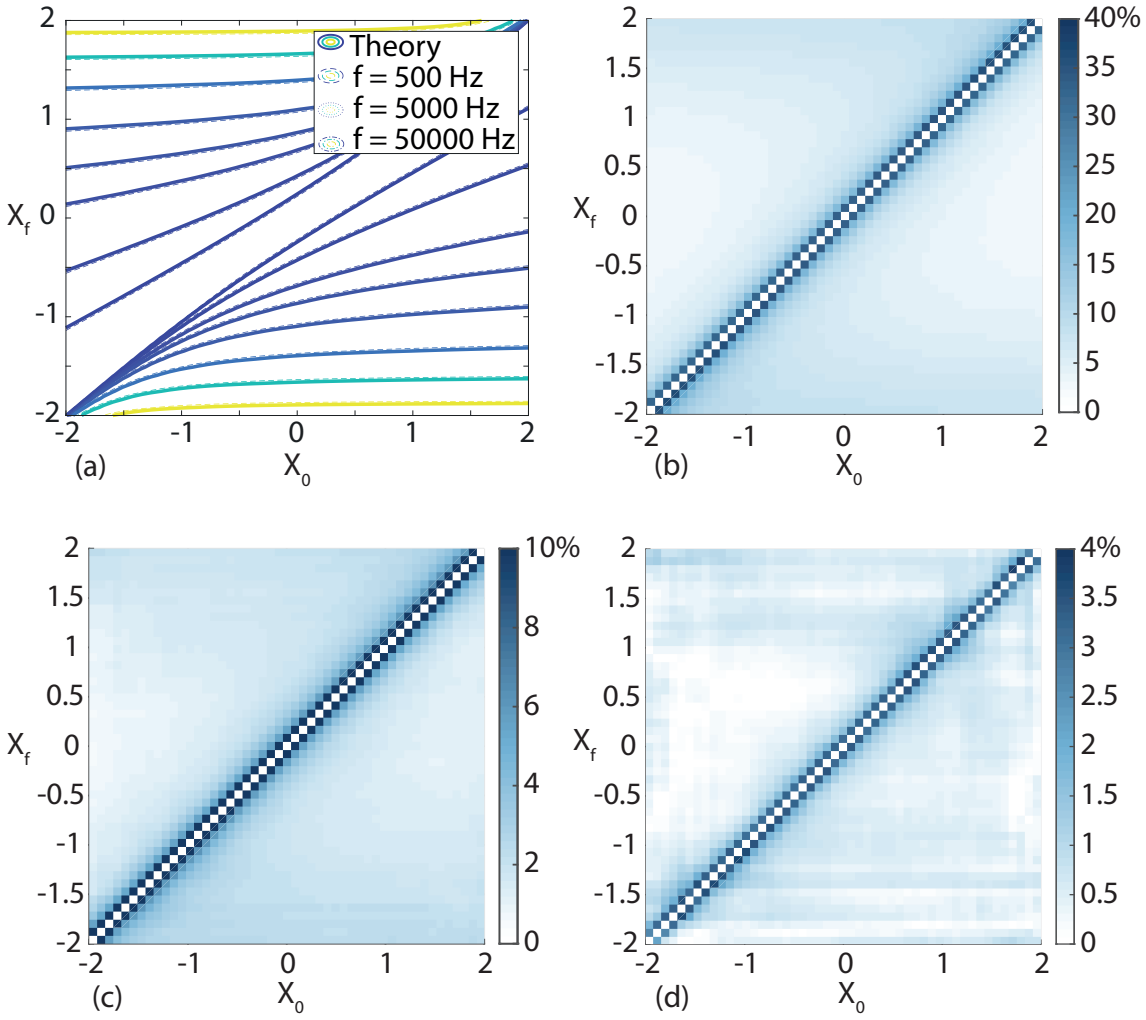

FIGURE 2.4: (a) Average FPT map, (b,c,d) Error map [in %] of the average FPT for a frequency of (b) 500 Hz, (c) 5000 Hz and (d) 50000 Hz.

TABLE 2.1: Maximum errors for the average and the STD of FPT for different ratios $\frac{f_s}{f_{O-U}}$.

Ratio $\frac{f_s}{f_{O-U}}$	≈ 3000	≈ 30000	≈ 300000
Maximum error on average of FPT	36%	11%	4%
Maximum error on STD of FPT	19%	6%	3%

In Figure 2.5(a), the STD of FPT is shown for various combinations of (X_0, X_f). Again, the contour lines overlap significantly, similar to the average FPT map. In Figures 2.5(b,c,d), relative errors are plotted for frequencies of 500 Hz, 5000 Hz and 50000 Hz. The maximum values are listed in Table 2.1. It can be seen that the maximum relative errors on the map of the STD of FPT are lower than the maximum errors of the average FPT map for the same frequency. The largest error is always located near the main diagonal. The error reduces to below 1% when considering combinations of (X_0, X_f) that satisfy the constraint $|X_0 - X_f| \gtrsim 0.2$.

The algorithm can precisely compute the FPT centred moments. However, the quality of values situated around the main diagonal of the map is impacted by the ratio $\frac{f_s}{f_{O-U}}$. This limitation is more attributable to the simulation process rather than to the algorithm itself. Indeed, it has been shown that when this ratio is equal to 30000 or 300000, the error is significantly reduced. Therefore, the sampling frequency f_s should be chosen in accordance with the characteristic frequency of the O-U process f_{O-U}.

Besides the average FPT maps and STD of FPT maps, histograms of the FPT are also illustrated for 9 combinations of (X_0, X_f) located at different places of the FPT map, in order to get a better understanding of the distribution of the FPT for a given set (X_0, X_f). These empirical PDFs are shown in Figure 2.6 together with the analytical solution, given as a reference. The location of the combination (X_0, X_f) is indicated by a red square on the pictogram.

In Figures 2.6(c,e,g), corresponding to combinations located close to the main diagonal of the map, the order of magnitude of the average FPT is the same as the time step or even below. There, FPTs are overestimated due to the large time step, resulting in a higher mean value. This explains the large relative errors computed in that area. By increasing the sampling frequency, the time step is reduced and for 50000 Hz, the shape of the PDF is well represented.

In Figures 2.6(a,b,d,f,h,i), corresponding to combinations (X_0, X_f) lying out of the main diagonal of the map, two observations can be made:

1. The shape of the PDF matches the theoretical one. However, it can be observed that the PDF is slightly overestimated for 500 Hz and 5000 Hz for higher FPT values. This is a well-know issue [113, 114] that directly comes from the small sampling frequency of the numerical signal simulation. By using a smaller time step (= a higher sampling frequency), the probability of obtaining extreme FPT values is reduced. Hence, it follows that the results obtained using a sampling frequency of 500 Hz and 5000 Hz slightly overestimate the probability of large FPT values.

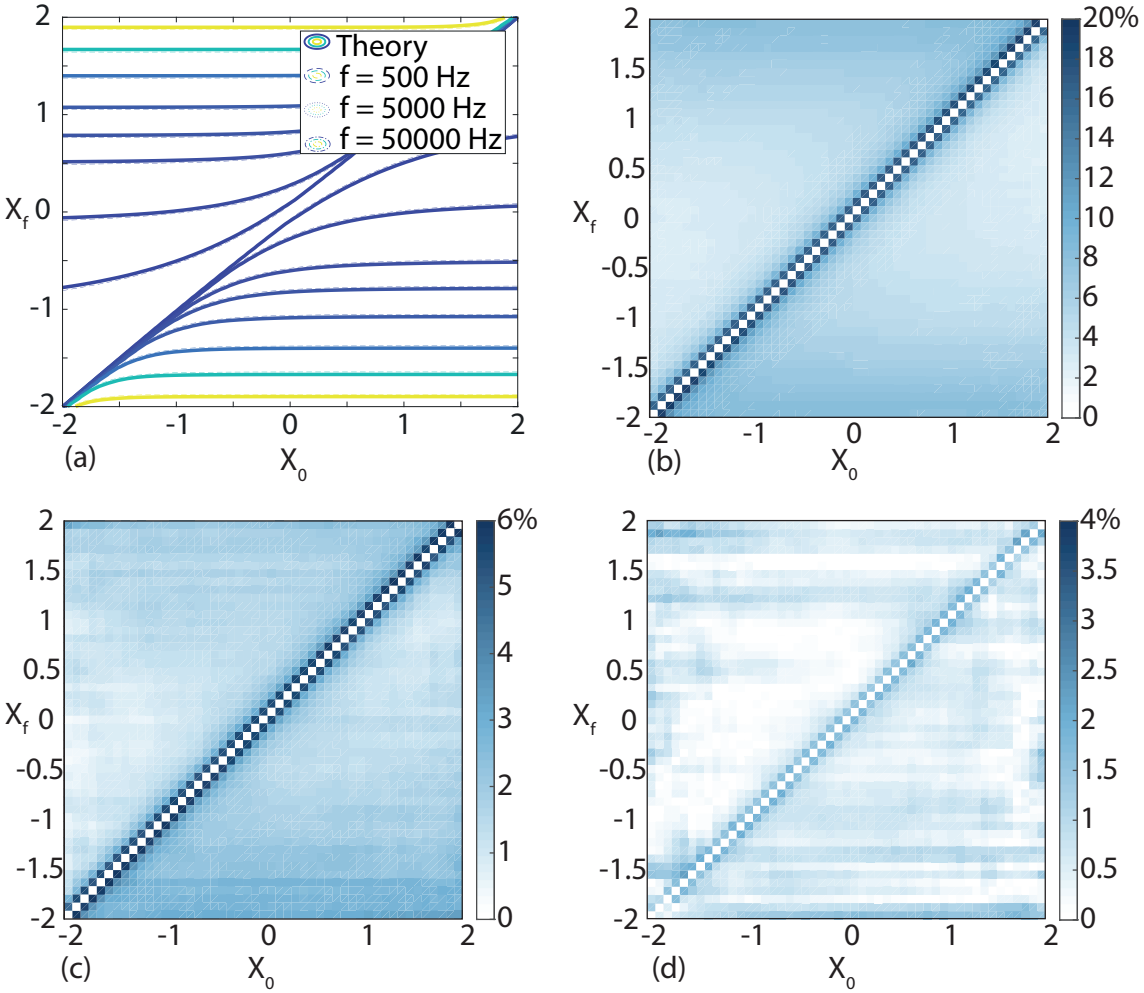

FIGURE 2.5: (a) STD of FPT map, (b,c,d) Error map [in %] of the STD of FPT for a frequency of (b) 500 Hz, (c) 5000 Hz and (d) 50000 Hz.

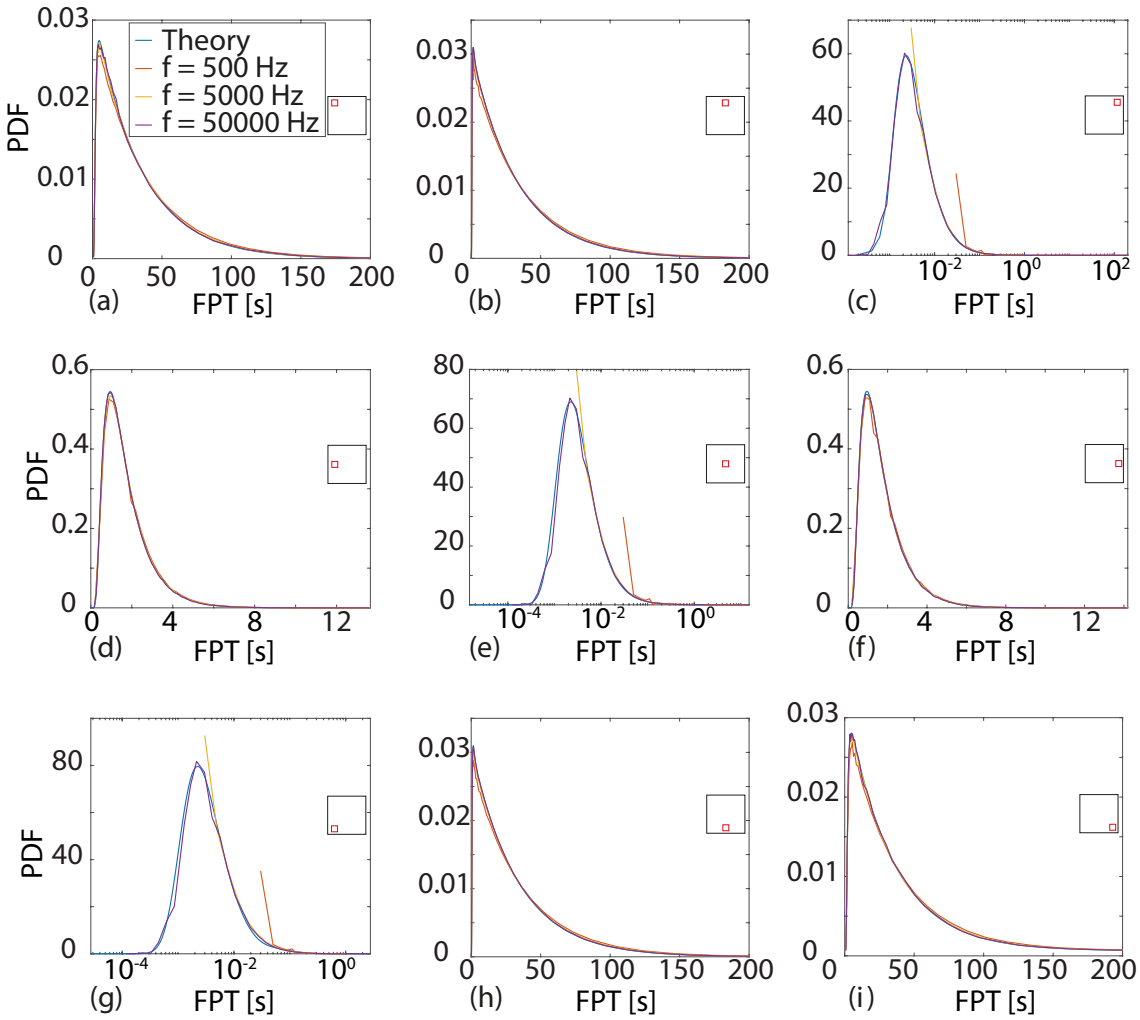

FIGURE 2.6: PDFs of FPT for various values of (X_0, X_f): (a) $(-1.84, 1.84)$, (b) $(0.04, 1.84)$, (c) $(1.76, 1.84)$, (d) $(-1.84, 0.04)$, (e) $(-0.04, 0.04)$, (f) $(1.84, -0.04)$, (g) $(-1.84, -1.76)$, (h) $(-0.04, -1.84)$, (i) $(1.84, -1.84)$. Comparison of the theoretical solution Eq. A.1, and results obtained with the proposed algorithm applied to sampled values of the O-U process (500, 5000 or 50000 Hz).

2. The O-U process is symmetrical and therefore, the PDFs of FPT for (X_0, X_f) and $(-X_0, -X_f)$ are identical. As a result, the maps and PDFs enjoy a central symmetry about $(X_0, X_f) = (0, 0)$. The proposed algorithm can adequately model this symmetrical behaviour.

2.4 Illustration of the computation of FPT maps for experimental data

This section presents the application of the proposed algorithm to compute FPT maps of a narrowband measured signal from an experimental setup. The experimental setup is described in Chapter 4. It will be first demonstrated that any time signal, employed as an input of the proposed algorithm, derived from an experiment, can also be computed to yield FPT maps. The narrowband signal used here is not much different from the synthetic one, generated in the previous section. Nevertheless, this example is used to discuss the possible use of the slowly varying envelope of the narrowband process, and its FPT maps.

In this instance, the measured signal is the velocity. It has been normalised by its interquartile range, the difference between the 75th and the 25th percentiles. Moreover, the median has been subtracted. Figure 2.7 illustrates the resulting signal, its PDF, which reflects the statistical symmetry, and the PSD of the resulting signal, whose frequency content is located in the frequency range $[35, 43]$Hz. The sampling frequency f_s of the signal is equal to 2048 Hz. In the same figure, the envelope, constructed using the Hilbert transform, of the normalised velocity is also represented. This envelope will be discussed further in this section.

Figures 2.8(a) and (b) depict the Average FPT map and STD of FPT map, respectively, for the normalised velocity. As observed in the previous section, the symmetry of the FPT maps is well represented, even if the maps are derived from experimental data this time.

To further elaborate, in Figure 2.9, the histograms of FPT are shown.

The shape of the histogram (h) is explained based on Figure 2.10. In this case, the combination (X_0, X_f) is equal to $(-0.04, -1.59)$. Over a long time period, multiple intersections (black dots) are computed between the signal and the level X_0 without crossing the level X_f at all. Once the level X_f is crossed for the first time, the First Passage Time is computed. The computed FPTs correspond to the right peak of the histogram, called cluster. At a specific point in time, various intersections (green dots) occur between the level X_f and the signal. Two distinct behaviours are observed. On the one hand, when the slope of the signal is negative at the intersection between the level X_0 and the signal (blue dots), the FPTs are the smallest. The computed FPTs are approximately equal to a quarter of the natural period T_1, where $T_1 \approx \frac{1}{39} \approx 0.025$ seconds. On the other hand,

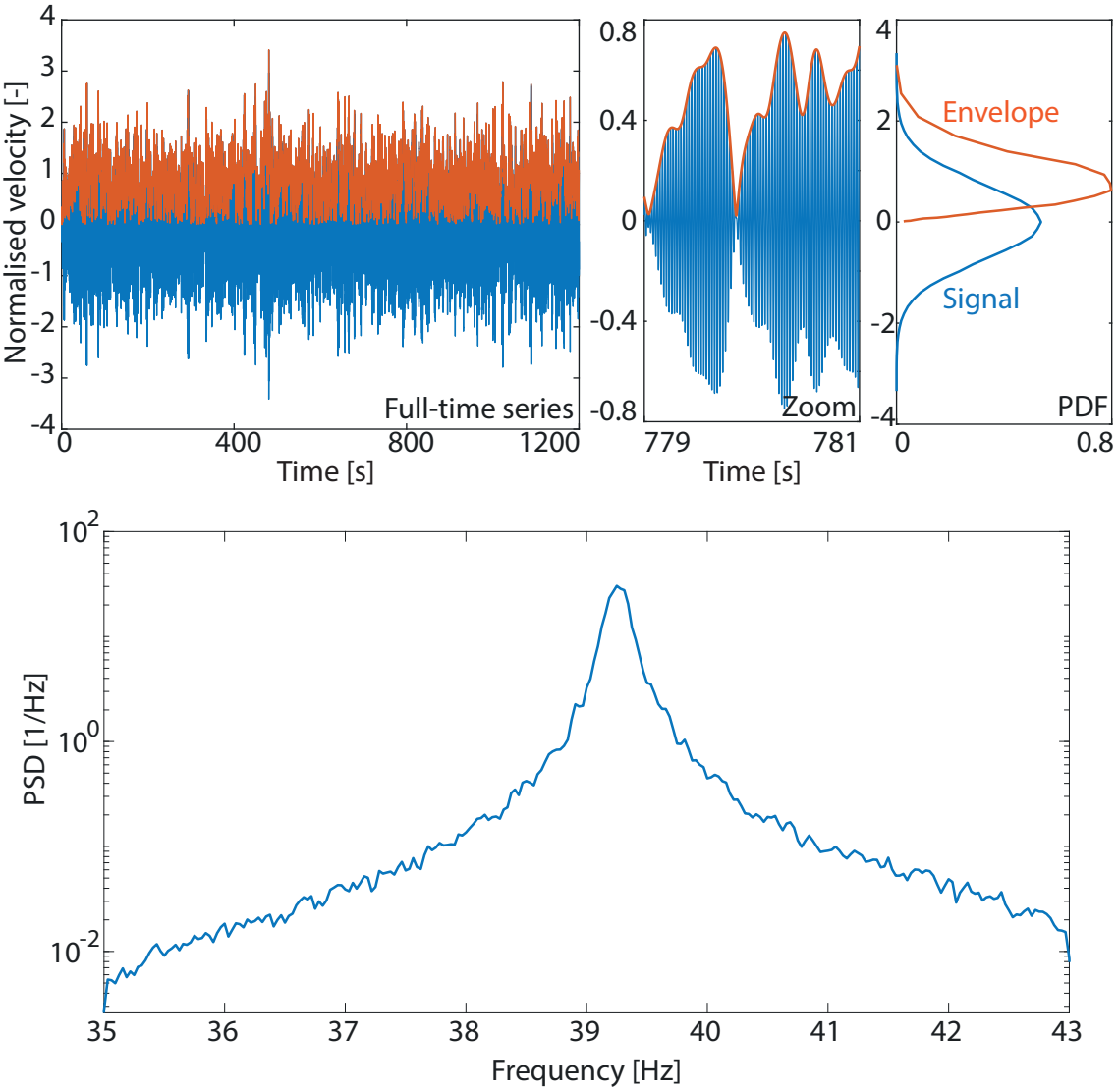

FIGURE 2.7: Measured signal (blue), its upper envelope (orange) obtained with the Hilbert transform, their respective PDFs, and the PSD of the measured signal.

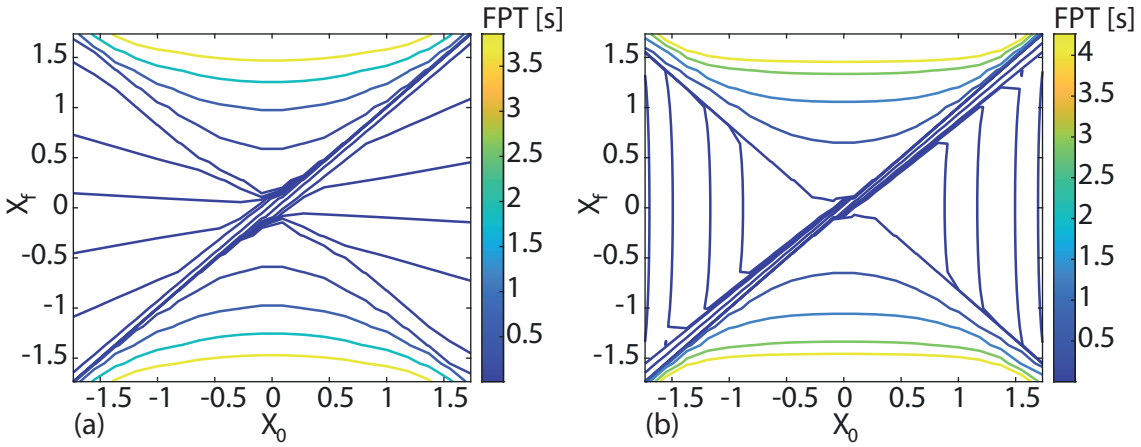

FIGURE 2.8: FPT maps of the normalised velocity: (a) Average FPT map and (b) STD of FPT map.

if the slope of the signal is positive at the intersection between the level X_0 and the signal (yellow dots), then three-quarters of the natural period T_1 are required to cross for the first time the level X_f. These computed FPTs correspond to the middle peak of the histogram.

In Figure 2.9, based on FPT histograms (d) and (f), a bimodality in the FPT can be observed. If the signal is increasing, the first time to hit a higher level is lower than if the signal is decreasing. The opposite is also true for a lower level. This is the reason why the FPT histogram is a mixture of two distributions, as represented in Figure 2.9(d), (f), and (g). This explanation is also valid for the other histograms even if the peaks of the PDF of FPT are less symmetric.

The shapes of the FPT histograms obtained in this experiment differ significantly from those observed in the previous section for the O-U process.

It can also be observed that the FPTs are generally smaller or equal to the natural period T_1 in all subfigures.

The statistical symmetry between (a) and (i), (d) and (f), and (c) and (g) can be observed. However, a slight difference can be noticed between (a) and (i) by comparing the highest peak in the histograms. Indeed, the data measured from the experiment has a finite length.

As explained, by considering the fast dynamics of the system, FPTs are generally smaller than the natural period T_1. Thefore, a slight change in the natural frequency can significantly impact the shape of the FPT histograms. This is why the envelope of the measured signal has been taken into account. This envelope can be computed with the Hilbert transform. Only the upper envelope is shown in Figure 2.7. It can also be observed that the envelope is statistically asymmetrical based on its PDF.

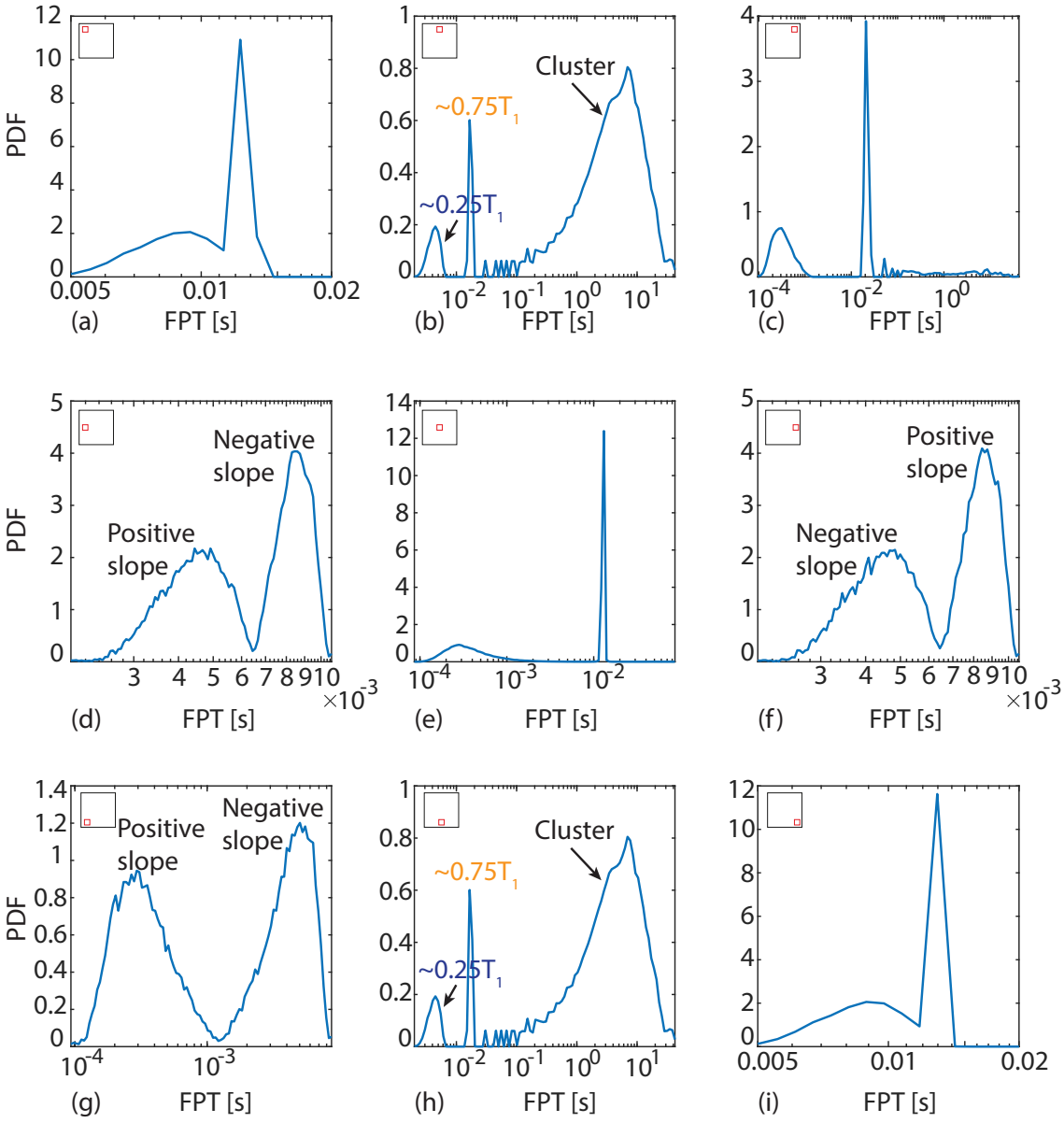

FIGURE 2.9: Histograms of FPT for the normalised velocity for various values of (X_0, X_f): (a) $(-1.59, 1.59)$, (b) $(0.04, 1.59)$, (c) $(1.52, 1.59)$, (d) $(-1.59, 0.04)$, (e) $(-0.04, 0.04)$, (f) $(1.59, -0.04)$, (g) $(-1.59, -1.52)$, (h) $(-0.04, -1.59)$, (i) $(1.59, -1.59)$.

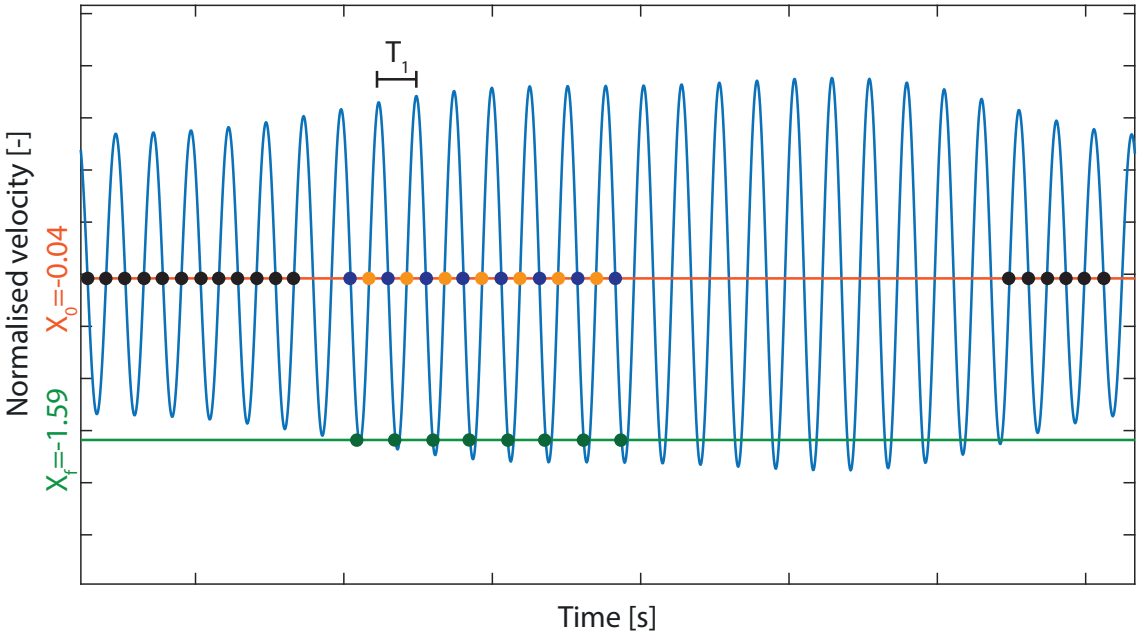

FIGURE 2.10: Zoom on the measured signal. Computation of FPTs for (X_0, X_f): (h) $(-0.04, -1.59)$.

In Figure 2.11, the Average FPT map and the STD of FPT map of this envelope are shown. The maps are asymmetrical. They start from $X_0 > 0$ since the upper envelope is positive. The upper part of the map, above the main diagonal, contains higher values of the FPT centred statistical moments than in the lower part (see yellow contour line). This indicates that, for the envelope of this experimental signal, once a higher level X_0 has been reached, it requires, on average, less time to cross a lower level X_f than in the opposite case if $X_0 < X_f$.

The histograms of FPT computed for the envelope of the normalised velocity are shown in Figure 2.12. The histograms of FPT are not statistically similar two by two, anymore. Indeed, for example, the histogram of FPT (a) does not correspond to the histogram of FPT (i).

Since the envelope evolves on a slow timescale, the FPTs, computed when the envelope of the signal is used as input, are considerably larger than those shown in Figure 2.9. Furthermore, and as a consequence, the distributions of FPT are now much smoother.

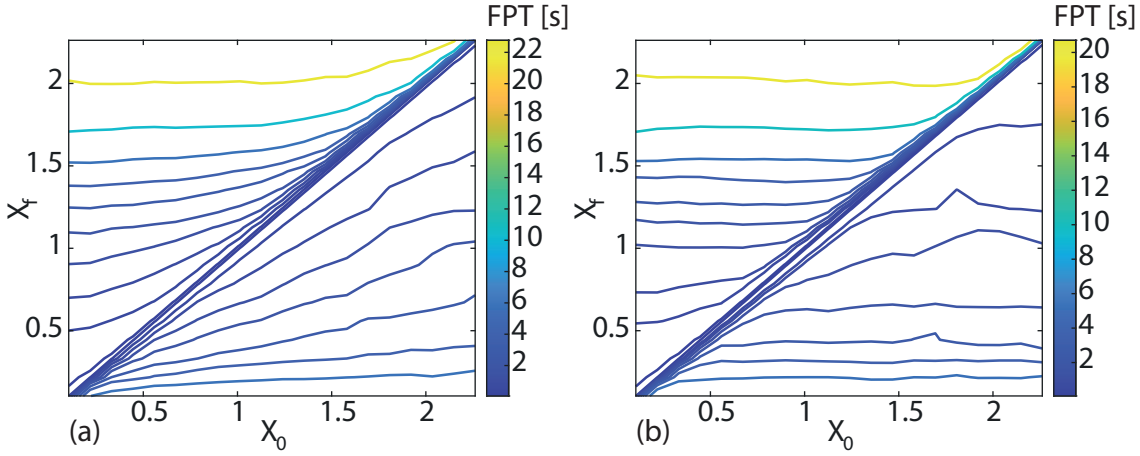

FIGURE 2.11: FPT maps of the envelope of the normalised velocity: (a) Average FPT map and (b) STD of FPT map.

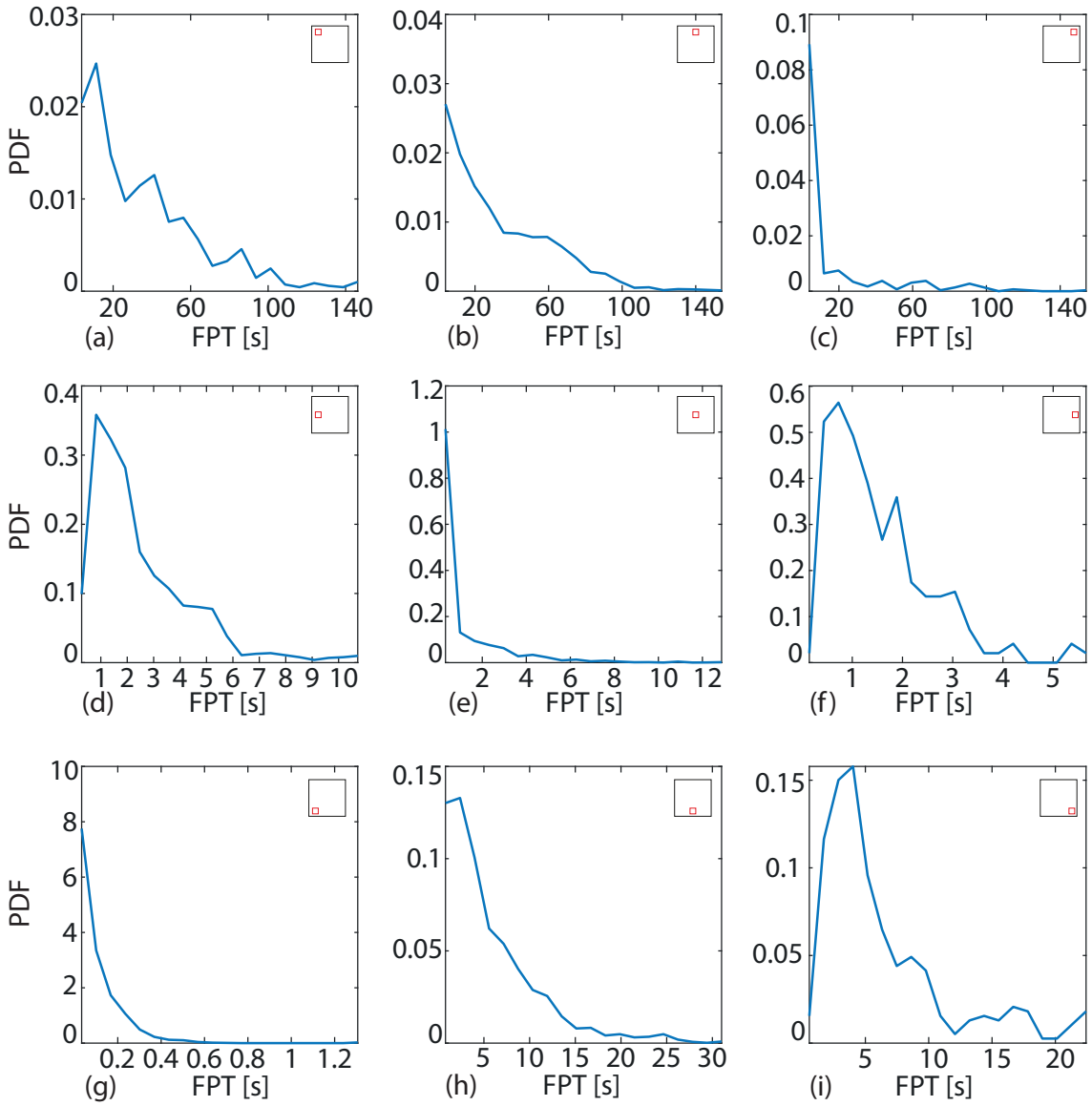

FIGURE 2.12: Histograms of FPT for the envelope of the normalised velocity for various values of (X_0, X_f): (a) $(0.19, 2.17)$, (b) $(1.20, 2.17)$, (c) $(2.13, 2.17)$, (d) $(0.19, 1.20)$, (e) $(1.16, 1.20)$, (f) $(2.17, 1.16)$, (g) $(0.19, 0.24)$, (h) $(1.16, 0.19)$, (i) $(2.17, 0.19)$.

2.5 Conclusion

A novel and optimised algorithm has been presented in this chapter as a signal processing tool for discrete-time signals. The objective of this algorithm is to compute centred statistical moments and histograms of FPTs in an efficient manner for different sets of (X_0, X_f).

The efficiency of the proposed algorithm has been evaluated by comparison to a direct method. The proposed algorithm is 400 times faster. The fast computation of this algorithm is attributed to interesting features such as the backward signal analysis and the MATLAB vectorization.

Additionally, a parametric study was conducted, varying three major parameters for three different stochastic processes: the Ornstein-Uhlenbeck process, the geometric Brownian motion and a narrowband process. The objective was the assess the efficiency of the algorithm by computing FPT maps and histograms for very different stochastic processes to understand the impact of these parameters on the algorithm execution time. This has revealed the ability to deal with stationary and non-stationary processes, and to deal with processes of various frequency contents.

The accuracy of the results has also been studied through the Ornstein-Uhlenbeck process for which analytical expressions of the PDF and moments of the FPT exist. A good agreement was observed between analytical and numerical results.

Finally, experimental data have been utilised as input for the algorithm. The FPT maps and histograms have been computed, illustrating that the proposed algorithm is capable of computing FPTs for recorded signals, a task that will be extensively called in the SHM method proposed in the following chapters. In addition, it has been highlighted that, for narrowband processes, the rapid oscillations, from experimental data, can mainly impact the FPT histograms shape. However, when the envelope of the experimental data, obtained with the Hilbert transform, is processed with the proposed algorithm, FPT with naturally longer passage times are obtained. The processing of this envelope will, in fact, serve as a basic ingredient for the SHM methodology proposed in Chapter 3.

Chapter 3

A Novel Method for damage detection and localisation

In this chapter, a novel methodology based on First Passage Times is proposed for the damage detection and localisation. This methodology relies on 3 different steps:

1. An experimental protocol to collect and pre-process data,
2. The FPT algorithm described in Chapter 2,
3. The comparison of FPT maps to detect changes.

After having been described, the sensitivity of the methodology is assessed by using numerical simulations. In the last step, four different scenarios are studied. In the first scenario, a damage is added to the numerical model and the sensitivity to damage detection is estimated. Then, to test the method's robustness against other factors, its ability to detect damage is analysed by providing other presumed unmeasured disturbances on top of the numerical damage. Three other scenarios take into account the wind loading as an unmeasured force, an additive noise that can pollute the measured signal, and the influence of sampling frequency.

3.1 Overview of the proposed methodology

3.1.1 Damage detection

The proposed methodology for damage detection consists of several steps. First, vibrations are measured under a known loading, at least known from its statistical properties, e.g. Power Spectral Density function (PSD). The known loading is a band-limited white noise whose PSD is constant in the frequency range $[f_{\min}; f_{\max}]$.

The eigenfrequency of a structure may change over time due to the occurrence of a damage or environmental effects. The selected frequency range is chosen to ensure that this eigenfrequency is always located within this frequency range.

Then, the vibration data, materialised as acceleration, velocity or displacement measured at various places, is pre-processed. Numerical filters are used and the slow envelope is extracted based on the Hilbert transform.

Then, the pre-processed data is used as an input in the FPT algorithm described in Chapter 2.

Finally, the FPT maps are computed in the healthy and current states.

FPT maps of statistical moments of FPT, like the mean and the STD, have been used to perform damage detection but their sensitivity was not sufficient to detect slight structural changes, related to early damage detection. Hence, by comparing FPT histograms, it appeared that the distribution of FPT can be considered as a good candidate for early damage detection and this step of the methodology only relies on FPT histograms and not its statistical moments anymore. In this case, the FPT histograms are compared two-by-two, in the healthy and current states.

Diverse methods exist for this comparison and are presented in Section 3.3 as well as a novel method. If discrepancies between the FPT histograms are highlighted, therefore, the structure in its current state is significantly different from the healthy state, and the current state is identified as a damaged state.

3.1.2 Damage localisation

The proposed methodology for damage localisation relies on the same experimental protocol, FPT algorithm and FPT histograms comparison described in Section 3.1.

Since the method treats one signal at a time, the notion of spatial distribution of information is inexistent.

By comparing the FPT histograms from the experimental setup and those from the numerical model, the damage localisation can be performed. This requires the construction of a numerical model, which must then be updated. In the traditional way, the model updating finishes when a good match is reached between its eigenfrequencies and mode shapes and the identified experimental natural frequencies and mode shapes in the healthy state [115]. However, it is now also possible, based on FPT maps, to update the numerical model until a good match between FPT maps is encountered. The updated model is called a digital twin model.

Secondly, to locate the damage, the digital twin model is used. By modifying its mass and stiffness matrices, its response is also affected. Therefore, FPT histograms are different in each configuration. The stiffness and mass matrices are modified until the FPT maps from the digital twin model correspond to those obtained from the experiment, resulting in a good identification of the

type of damage and damage localisation. Therefore, in contrast with the damage identification, the damage localisation relies on the similarity of FPT histograms.

3.2 Pre-processing: Numerical filters and slow envelope

Before using the measured data as an input of the proposed FPT algorithm, it is pre-processed via numerical filters before computing the envelope obtained with the Hilbert transform. The sole objective of these numerical filters is to improve the test repeatability.

The first filter is a bandpass filter applied in the range $[f_{\min}, f_{\max}]$, corresponding to the frequency range of the band-limited loading. This filter consists in filtering the signal between the minimum and maximum frequencies of the PSD of the force signal, which is a band-limited white noise, as shown in Figure 3.1(a). It discards the frequency content outside of the targeted frequency range, isolating a single eigenmode at a time.

The second filter aims to compensate for the slight possible discrepancy between the actual PSD of the loading (presented earlier) and the targeted PSD. Indeed in an open-loop testing, it is possible that the PSD of the loading differs from one test to another. To compensate for this undesired effect, a frequency content adjustment can be applied to the signal.

Assuming that the system is linear time-invariant for each state and remains the same, the following equations, in frequency domain, can be derived

$$\begin{cases} HX_{\text{ref}} = F_{\text{ref}} \\ HX_{\text{curr}} = F_{\text{curr}} \end{cases}$$

where H is the transfer function in the current state, X is the structure response and F is the external loading, and indices ref and curr correspond to the reference and current states.

In the proposed methodology, the loading is a band-limited white noise and the loading remains the same for each state. To detect a damage, the objective is to compare the FPT maps from X_{ref} and X_{curr} and determine if there exists a discrepancy. Therefore, it is mandatory that the loading is identical between each state, meaning that the PSDs of the loading from one state to another remains also identical. If the frequency content of F_{curr} differs from F_{ref}, therefore, X_{ref} and X_{curr} are different. Even if the structure stays the same, and the discrepancy detected on the FPT maps could solely come from this difference.

Hence, the following correction is used

$$\widetilde{X}_{\text{ref}} = \frac{F_{\text{ref}}}{F_{\text{curr}}} X_{\text{curr}}.$$

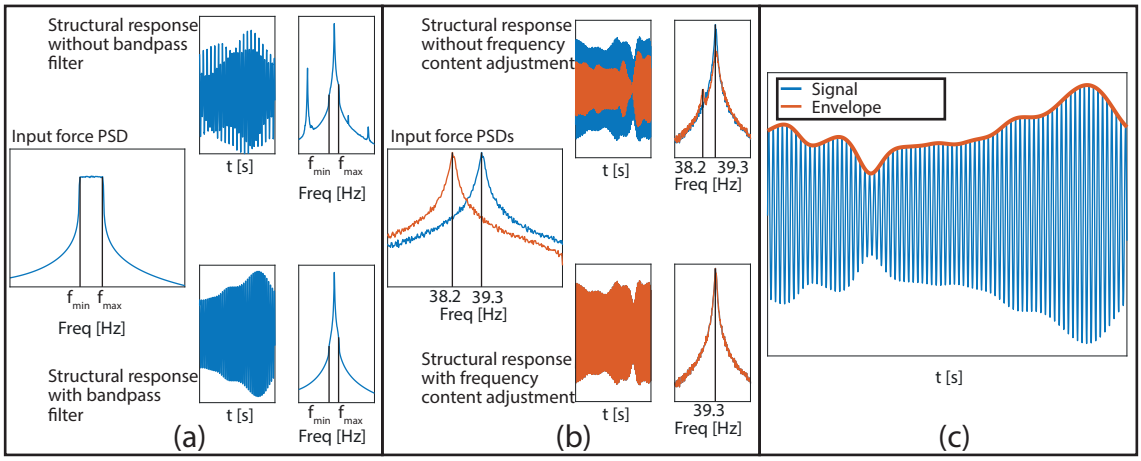

FIGURE 3.1: Transformations applied to the input signals: (a) bandpass filter in the range of $[f_{min}, f_{max}]$ of the input force, (b) frequency content ajustment aiming at compensating variations between two input force PSDs, and (c) the signal envelope obtained with the Hilbert transform.

It provided the response that could be measured in the current state if the forcing had been F_{ref} instead of the (slightly different) forcing F_{curr}.

In Figure 3.1(b), two loadings with slightly different PSD functions are shown for the same 1-DOF structure. The blue curve of the input force is chosen as the reference case F_{ref} while the orange curve is shifted to the left, resulting in a modification of the frequency content of the input force F_{curr}. The natural frequency of the system is approximately 39.3 Hz. Without the frequency content adjustment filter, a small peak can be observed around 38.2 Hz, where the peak of the PSD of the force F_{curr} is located. This peak has a strong influence on the response of the structure, and, therefore, on the proposed methodology. By applying the frequency content adjustment filter, the two PSD functions of the structure response, X_{ref} and X_{curr}, are almost perfectly matched.

The final step consists in taking the slow envelope of the measured signal by utilising the Hilbert transform. The proposed methodology heavily relies on the FPT histograms shape. As mentioned in Chapter 2, by computing FPT histograms based on the fast dynamics of the signal, the order of magnitude of FPTs is similar to the natural period. Therefore, if a shift occurs in the natural period, the FPT histograms shape changes completely, jeopardising the damage detection. The FPTs computed with the slow envelope of the signal are larger than the natural period, resulting in smoother and more stable FPT histograms shapes. Moreover, many other fields also use the Hilbert transform for signal processing [116] and a procedure based on the Hilbert transform has even already been used for detecting low damage level [117]. Figure 3.1(c) shows the signal envelope obtained with the Hilbert transform.

3.3 Comparison of cumulated histograms (ECDF)

3.3.1 Existing methods

The proposed method hinges on the two-by-two comparison of histograms of FPT. In the literature, it is more common to compare cumulated histograms, also called, Empirical CDFs (ECDFs). This comparison is repeated for every couple (X_0, X_f) of the map.

The rationale behind this comparison is that, if two structures are identical, the ECDFs of FPT are identical while if the ECDFs of FPT differ, then, the two structures are different. How different they need to be to detect changes depends on the sensitivity of the method to undesired and unmeasured perturbation. This will be discussed in Section 3.4.

By now, it is important to be able to quantify the differences between two cumulated histograms. In the literature, several 2-sample tests can be used to compute values called *distances*. These distances reflect the difference between two FPT histograms. If the distance is equal to zero, the FPT histograms are exactly the same, meaning that the two studied dynamical systems are also similar. Conversely, if the distance is large, the 2 structures are different. Below is a non-exhaustive list of 2-sample tests used and compared for the damage detection and localisation. In Figure 3.2, The specificities of each test are shown graphically. All `Matlab` 2-sample test functions come from the same package [118].

Kolmogorov-Smirnov (KS) test

The Kolmogorov-Smirnov distance is the largest difference between two ECDFs, as shown in Figure 3.2(a). The Kolmogorov-Smirnov test is probably the simplest method to implement [119].

Kuiper (K) test

The Kuiper test computes two differences instead of one, as opposed to the KS test. As shown in Figure 3.2(b), these two differences are simply the largest upper $\left(\mathrm{D}^{+}\right)$ and lower $\left(\mathrm{D}^{-}\right)$ differences between two ECDFs. The Kuiper distance is then the sum of these two differences [120].

Cramer-Von Mises (CVM) test

The Cramer-Von Mises distance is the sum of all the squared differences between two ECDFs [121], as shown in Figure 3.2(c).

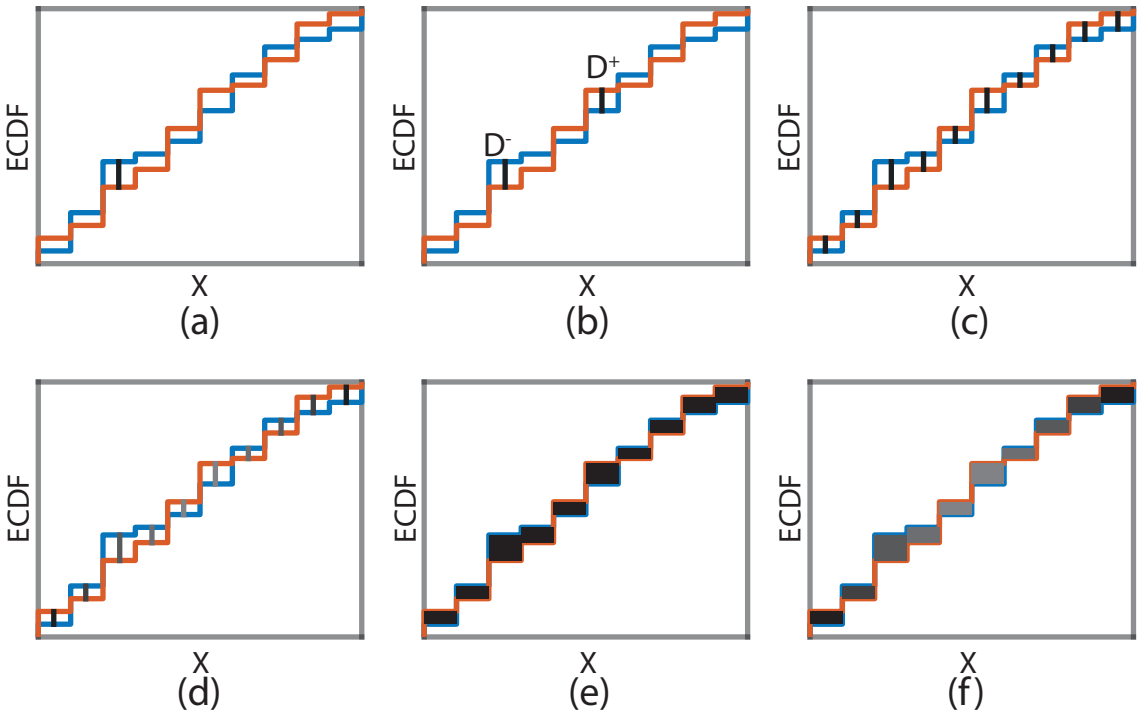

FIGURE 3.2: 2-sample tests for comparing ECDFs: (a) Kolmogorov-Smirnov test, (b) Kuiper test, (c) Cramer-Von Mises test, (d) Anderson-Darling test, (e) Wasserstein and (f) Wasserstein-Anderson-Darling.

Anderson-Darling (AD) test

The Anderson-Darling test is also based on the sum of the square of all differences between two ECDFs, but this time each difference is weighted [122]. The Anderson-Darling test focuses more on the tails of the distribution as shown in Figure 3.2(d). If the colour is lighter, it means that the weight is smaller and therefore, a difference in these areas has less impact on the Anderson-Darling distance.

Wasserstein (W) test

Instead of focusing on the algebraic difference of two cumulative histograms, the Wasserstein test is based on the area between two ECDFs, as shown in Figure 3.2(e). This test is often associated with the optimal transport. Therefore, this test distance can be seen as the amount of "material" that needs to be moved in order to obtain the second empirical histogram [123].

Wasserstein-Anderson-Darling (WAD) test

The Wasserstein-Anderson-Darling test is the most sophisticated test as it combines the idea of the Wasserstein test and the weights of the Anderson-Darling test. This test still computes the area between two ECDFs, but this time, some parts of that area are weighted by focusing on the tails [124]. If the colour is lighter, it means that the weight is smaller and therefore, this part of the area has less influence on the Wasserstein-Anderson-Darling distance as shown in Figure 3.2(f).

Existing methods are based on the concept of distance. If the distance is small, the ECDFs are similar.

3.3.2 Another method inspired by hypothesis testing

In addition to these 2-sample tests, another test is proposed. It differs from the other 2-sample tests as it does not rely on distances or areas measured from two histograms. Instead, it relies on the sample distribution of FPT histograms. It consists in dividing the signal into N shorter signals of equal length to approximate the sampling distribution of the FPT histograms. A typical choice is N = 8. Then, N maps of FPT histograms are obtained. The objective of this test is to compare the sample distribution of FPT histograms at different percentiles in the healthy state, represented by the blue curves in Figure 3.3(a), and in the current state, shown by the orange curve.

For a given percentile p, it is assumed that the mean value of the ECDFs of FPT in the healthy state, $\bar{x} = \frac{1}{N}\sum_1^N x_i$ with $i = 1, ..., N$, is equal to the mean value of the ECDFs of FPT in the current state $\bar{y}$. This is a null hypothesis H_0 and in the current proposition, this hypothesis is statistically tested. Without loss of generality and for application purposes, it has been decided to restrict the percentile values to the range 0.1 to 0.9 with a step of 0.05, as shown in Figure 3.3(a). This choice is motivated by the fact that the sensitivity to small changes in the tails of the ECDFs can have a large impact on the comparison of the sample distribution of ECDFs of FPT. Furthermore, it is assumed that the distribution of these means follows a normal distribution $\bar{X} \rightarrow \mathcal{N}\left(\bar{x}, \frac{\sigma_x}{\sqrt{N}}\right)$, where σ_x is the standard deviation of all the x_i. Therefore, the distribution of the difference of the means also follows a normal distribution $Z = \bar{X} - \bar{Y} \rightarrow \mathcal{N}(m_z, \sigma_z)$, where $m_z = 0$ (null hypothesis H_0) and $\sigma_z = \frac{\sqrt{\sigma_x^2+\sigma_y^2}}{\sqrt{N}}$. Hence, it is possible to compute the α-values for this test as

$$\alpha = \text{prob}\left(Z > |z|\right) = 2\left(1 - \Phi\left(\frac{|z|-m_z}{\sigma_z}\right)\right),$$

where $z = \bar{x} - \bar{y}$ and Φ is the CDF of the standard normal distribution. The computation of the α-value for a given $|z|$ is illustrated in Figure 3.3(b). Based on this definition, $\alpha \in [0; 1]$.

The proposed statistical test is based on α-values. If the α-value is close to 1, the ECDFs are statistically similar at the given percentile p.

For each percentile p, an α-value is calculated. From the experience developed over the course of this thesis, considering percentiles from 0.1 to 0.9 with a step of 0.05 provides a relevant comparison of the ECDFs. The final step consists in averaging all computed α-values (17 in total) to get only one value translating the similarity of the two compared ECDFs.

If the average of α-values is close to 1, the ECDFs are similar.

Furthermore, if all FPTs are identical, as it is the case on the main diagonal $X_0 = X_f$, the α-value is not finite as the standard deviation of the sample distribution of the ECDFs of FPT is equal to zero. However, this does not impact the comparison of the FPT histograms as, on the main diagonal of the map, all FPTs are always equal to 0 in any healthy or damaged state.

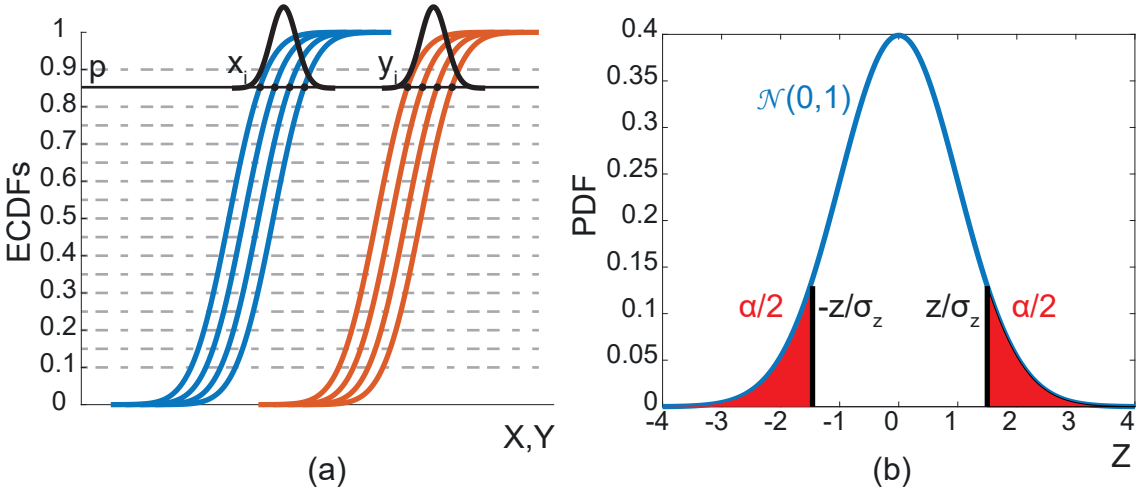

FIGURE 3.3: Illustration of the proposed statistical testing: (a) computation of the x_i and y_i for a given percentile p and (b) computation of the α-value for a given $|z|$.

3.4 Sensitivity of the methodology

A numerical model has been created and virtually damaged to quantify the sensitivity of the proposed methodology with respect to undesired perturbations. The numerical model is shown in Figure 3.4(a). It models a 50-m bridge and consists of beam elements. The size of the cross section has been chosen to represent a standard bridge deck, whose width is 18 meters. The numerical model is made of 10 elements. The material chosen for this bridge section is steel only, whose Young Modulus E = 205000 MPa and density is equal to 7850 kg/m^3. The inertia of the section is equal to 0.04 m^4 and its area is equal to 0.2 m^2.

The input force applied to the structure is located at midspan (node 6) and the acceleration of the structure is measured at node 4. The damage is detected based on this sole acceleration. To simulate a damage in the numerical model, a rotational spring has been added at node 8. Three different damaged cases are considered. The rotational spring stiffness is decreased from "infinity" (10^{15} [Nm/rad]) in the healthy state, meaning that the connection between the seventh and eighth elements is perfectly built-in, to $5 \cdot 10^9$ [Nm/rad] in the third damaged case. By adding this rotational spring to the numerical model, it results in a decrease of the eigenfrequencies as shown in Figure 3.4(b). The first bending mode has been chosen for the damage detection. The eigenfrequencies of the first bending mode in each case can be found in Table 3.1 as well as the relative change and the rotational spring stiffness. The relative change of the frequencies is computed as follow $\frac{f_{\text{healthy}} - f_{\text{damaged}}}{f_{\text{healthy}}}$.

Moreover, the simulation time has been fixed to 4 hours. This duration is set to obtain reproducible results for each 2-sample test as well as the proposed statistical test.

Based on 4 different scenarios, the sensitivity of the proposed methodology is assessed. In the first scenario, the damage detection sensitivity is determined, which represents the corner stage of the suggested methodology. Then, three other scenarios are based on the wind loading as an unmeasured force, which is added to the external loading, an additive measurement noise that can directly pollute the measured signal, and the influence of the sampling frequency.

3.4.1 Test repeatability in ideal conditions

To study the sensitivity of the proposed methodology under damage only, the damage detection is assessed considering three different input forces for the reference case as well as for each damaged case. For each given combination (X_0, X_f), α-values and distances can be computed by comparing the ECDFs of FPT of each case with those of the first reference case. The remaining two reference cases are

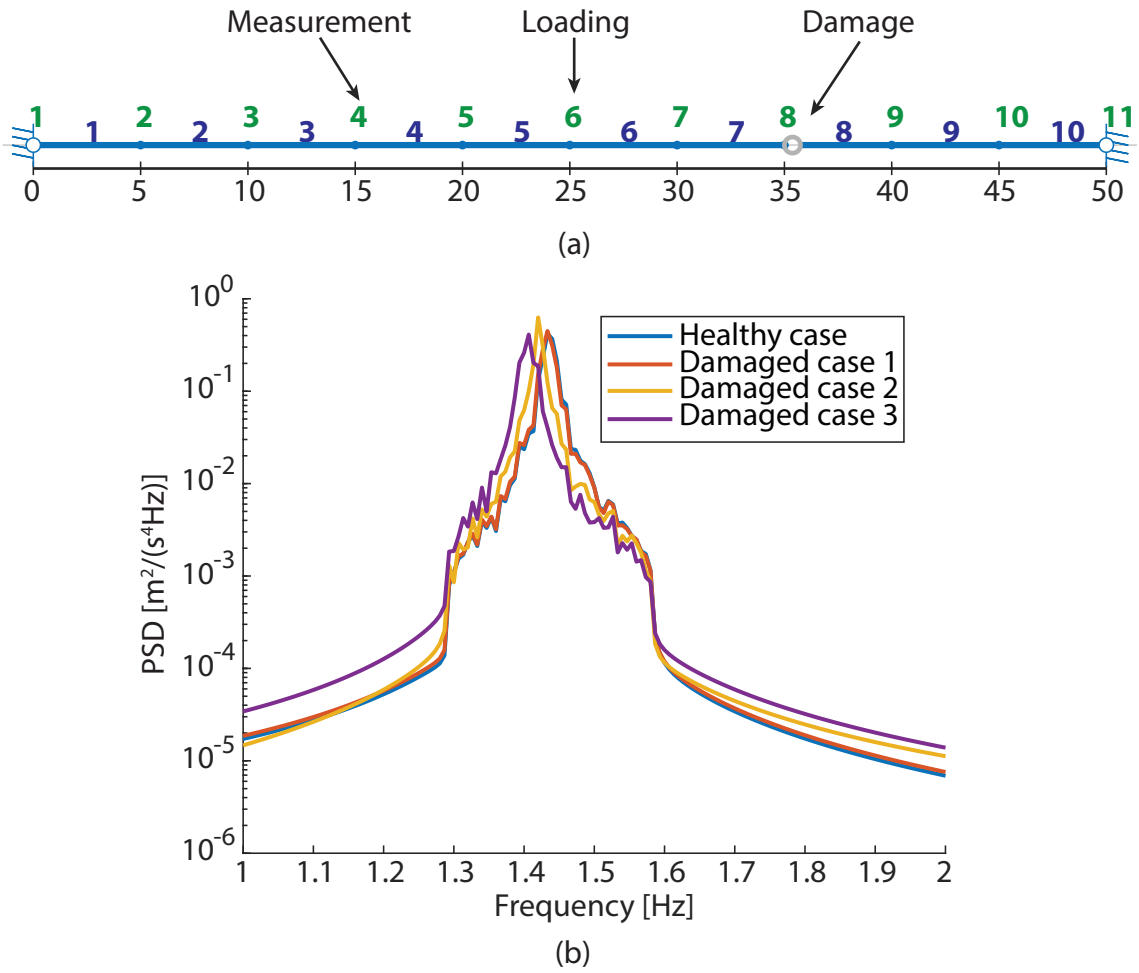

FIGURE 3.4: (a) Numerical model and (b) PSDs of the first bending mode for the reference case and each damaged case.

TABLE 3.1: Stiffness of the rotational spring, eigenfrequencies of the first bending mode in each case and their relative change with the healthy state.

	Rotational spring stiffness [Nm/rad]	First bending mode frequency [Hz]	Relative change [%]
Healthy case	∞	1.4360	0
Damaged case 1	10^{11}	1.4344	0.11
Damaged case 2	10^{10}	1.4205	1.08
Damaged case 3	$5 \cdot 10^{9}$	1.4055	2.12

used to evaluate the sensitivity of the methodology to differentiate between very small damage, in damaged case 1, and variations resulting from test repeatability.

In order to provide a visual representation of the damage detection, the ECDFs of α-values and distances over the entire map are shown in Figure 3.5. If the two compared cases are similar, therefore, α-values and distances are on average close to 1 and 0 respectively. This results in ECDFs of α-values that are close to the lower right corner and ECDFs of distances that are close to the y-axis. The reference case 1 compared to itself represents the scenario where all α-values and distances are equal to 1 and 0, respectively.

Moreover, it can be observed that each scenario is distinct from the others, resulting in a proper damage identification or at least a ranking of the various damage levels. The ECDFs are moving from the right to the left for the proposed statistical test in Figure 3.5(a) and from left to the right for the 2-sample tests in Figures 3.5(b-g) when going from the reference case to the damaged cases. In the damaged case 1, the ECDFs are close to those of the reference case. Indeed, the modal parameters of the numerical model in the damaged case 1 do not differ significantly from those in the reference case. Indeed, the relative change on eigenfrequencies for the first bending mode varies by 0.1% only. Then, the ECDFs are moving further away from the reference case in the damaged case 2 and even further in the damaged case 3, showing that the damage applied to the structure increases. Finally, the same conclusions can be drawn for each 2-sample test and the proposed statistical test, showing a redundancy in the obtained results and making the proposed methodology more robust.

3.4.2 Influence of additive loading (wind load)

To go further in the sensitivity assessment of the proposed methodology, unmeasured wind loads are applied to the structure in addition to the input force. These wind loads are applied to the whole bridge deck and are then transformed into nodal forces.

In this example, two different wind speeds have been chosen: 5 and 10 m/s. These wind speeds correspond to the average wind speed U_∞. To generate the wind fluctuating part, the PSD of Von Karman has been chosen and is given by

$$S_u(\omega) = \frac{L \cdot \sigma_u^2}{\pi U_\infty \left(1 + 70.7\left(\frac{\omega}{2\pi} \cdot \frac{L}{U_\infty}\right)^2\right)^{5/6}}$$

where $L = 30$m is the scale of the turbulence scale and σ_u is the standard deviation of the turbulent wind and is equal to 1 and 2 m/s when U_∞ is equal to 5 and 10 m/s respectively.

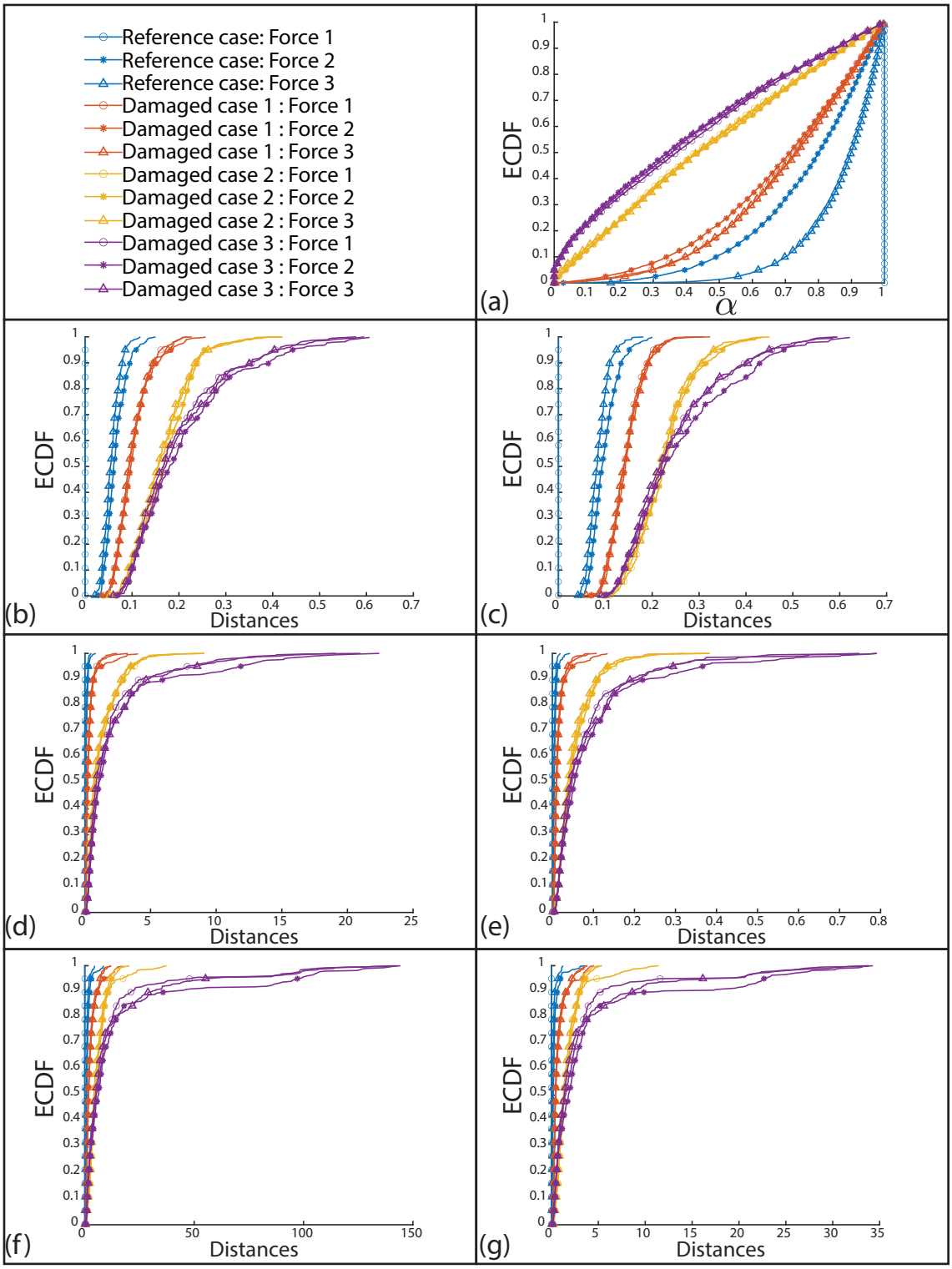

FIGURE 3.5: Sensitivity of the proposed methodology - damage detection: (a) the proposed statistical test and 2-sample tests (b) KS, (c) K, (d) CVM, (e) AD, (f) W and (g) WAD.

Moreover, the wind loads are spatially correlated. The coherence PSD is the following [125]

$$\Gamma_u(\omega) = e^{-\frac{C\cdot\omega\cdot\Delta x}{4\pi U_\infty}}$$

where $C = 11.5$ is the coefficient of coherence and $\Delta x = 5$m is distance between two nodes.

The lift coefficient C_L, used to compute wind loads, is equal to 0.9 [126]. More information about the generation of spatially correlated signals and wind loads can be found in [127] and in chapter 9 of [128].

Again, for a better visualisation, the ECDFs of the α-values as well as the distances are shown in Figure 3.6.

- A clear distinction can be made for each scenario, meaning that the damage detection is slightly disturbed by these wind loads and is feasible.
- For each wind speed, each damaged case is well separated from the others.
- When the wind speed is approaching 10m/s, the reference case is close to the damaged case 1 without or with the smallest wind load (5 m/s).

3.4.3 Influence of additive measurement noise

The next scenario takes into account the noise that affects the measured signal. This noise is generated as a band-limited white noise. The frequency range chosen for the noise is [0.5;5]Hz. Different Noise Levels (NL) have been selected, going from 5% to 100%. NL is defined as

$$\mathrm{NL} = \frac{\sigma_{\text{signal+noise}} - \sigma_{\text{signal}}}{\sigma_{\text{signal}}} = \sqrt{1 + (\mathrm{N/S})^2} - 1$$

where σ is the standard deviation and N/S is noise over signal ratio.

When the level is NL = 100%, it means that the standard deviation of the noisy signal is twice greater than the reference signal without noise. The effect of the added noise can be directly seen in the PSDs as shown in Figure 3.7. By increasing the noise level, the frequency ranges that are mainly subjected to changes are the ones close to $f_{\min} = 1.29$ Hz and $f_{\max} = 1.58$ Hz. Thanks to the filtering, every modification outside the frequency range $[f_{\min}; f_{\max}]$ is discarded.

In Figure 3.8, it can be seen that the noise greatly affects the damage detection. It is important to mention that a level of noise greater than 10% already represents a high noise level. However, for the completeness of this sensitivity study, it has been decided to use higher noise levels. The only results displayed are the ECDFs of α-values from the proposed statistical test. For the other 2-sample tests, the same conclusions can be drawn. Except for Figure 3.8(a), the

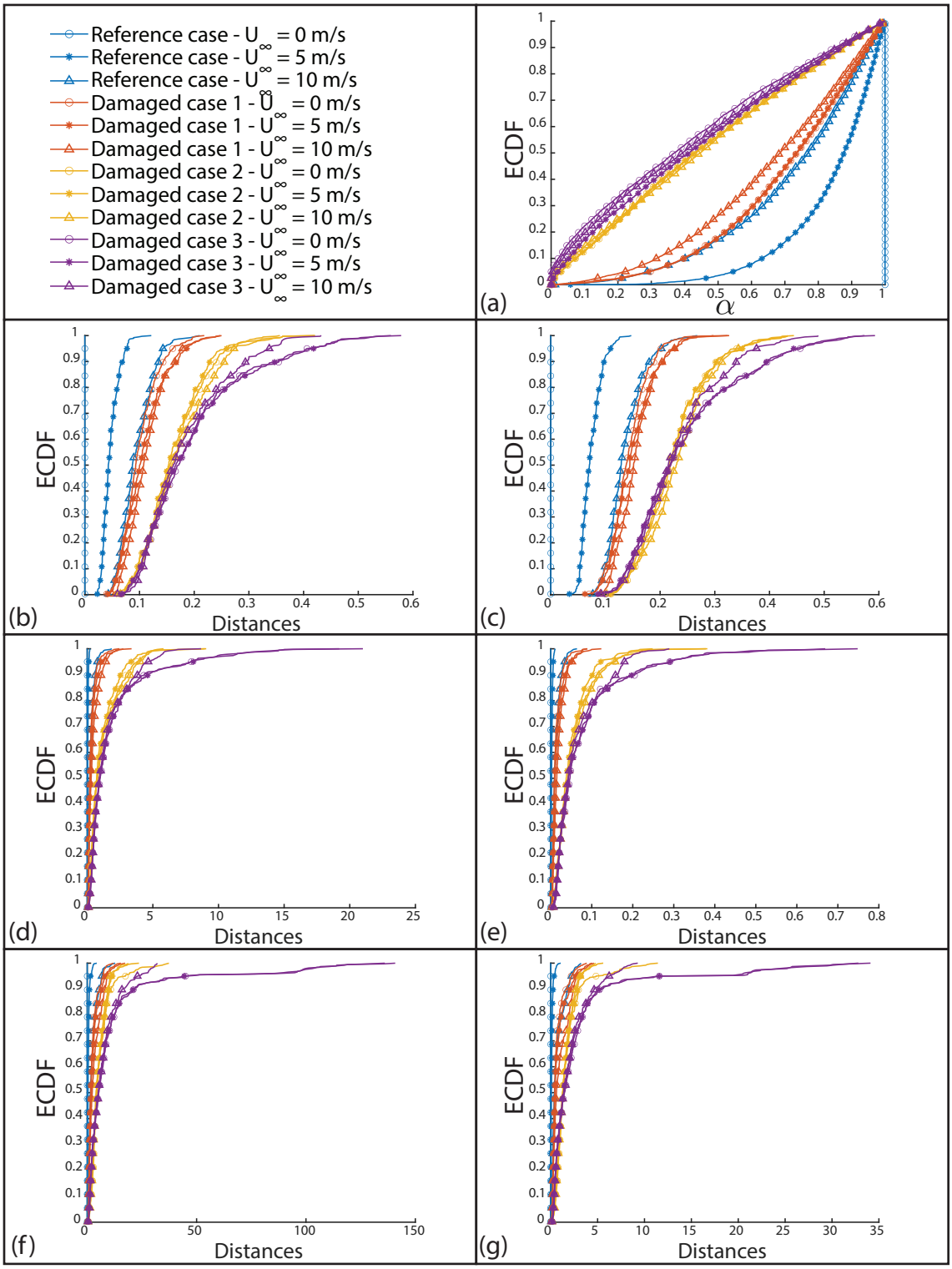

FIGURE 3.6: Sensitivity of the proposed methodology - damage detection under wind load: (a) the proposed statistical test and 2-sample tests (b) KS, (c) K, (d) CVM, (e) AD, (f) W and (g) WAD.

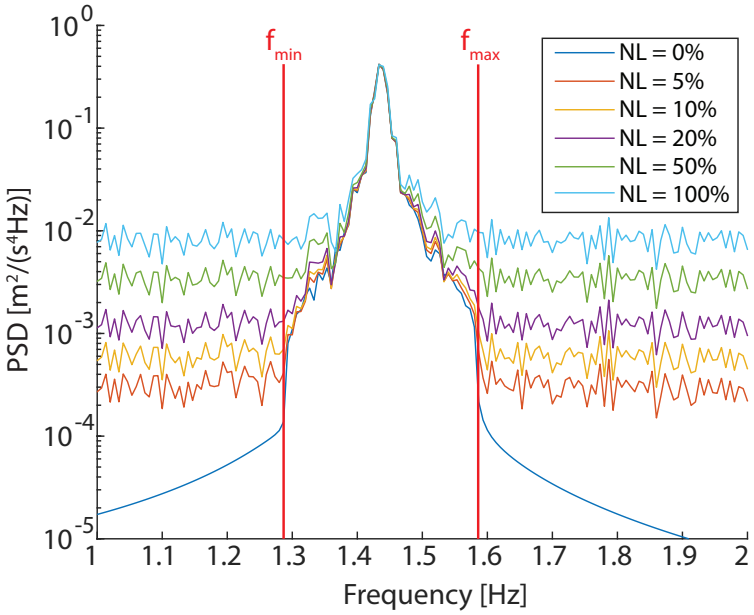

FIGURE 3.7: PSDs of the measured acceleration of the structure under the input force and added noise.

ECDFs of the signal without noise are shown in grey to improve the comparison with ECDFs of the signals with noise. In Figure 3.8(b), it can be seen that a noise level of 5% for the reference already exceeds the threshold of the damaged case 1 without noise. This is expected since the two cases are really similar to each other. However, a noise level higher than 10% for the reference case is required to surpass the threshold imposed by the damaged cases 2 and 3. In Figure 3.8(c), it can be observed that for the same noise level, the ECDFs of the α-values in the reference case are always slightly lower than the ECDFs of the α-values in the damaged case 1. This shows that the damage detection is still performing well for the same noise level and is able to make distinction between two systems with close modal properties. In Figure 3.8(d), it can be seen that when the noise level is important, superior or equal to 50%, the ECDFs of the α-values for each case almost coincide. In this scenario, the damage detection fails and is not able to make the distinction between a small damage, as in damaged case 1, and a higher damage, like in damaged cases 2 and 3.

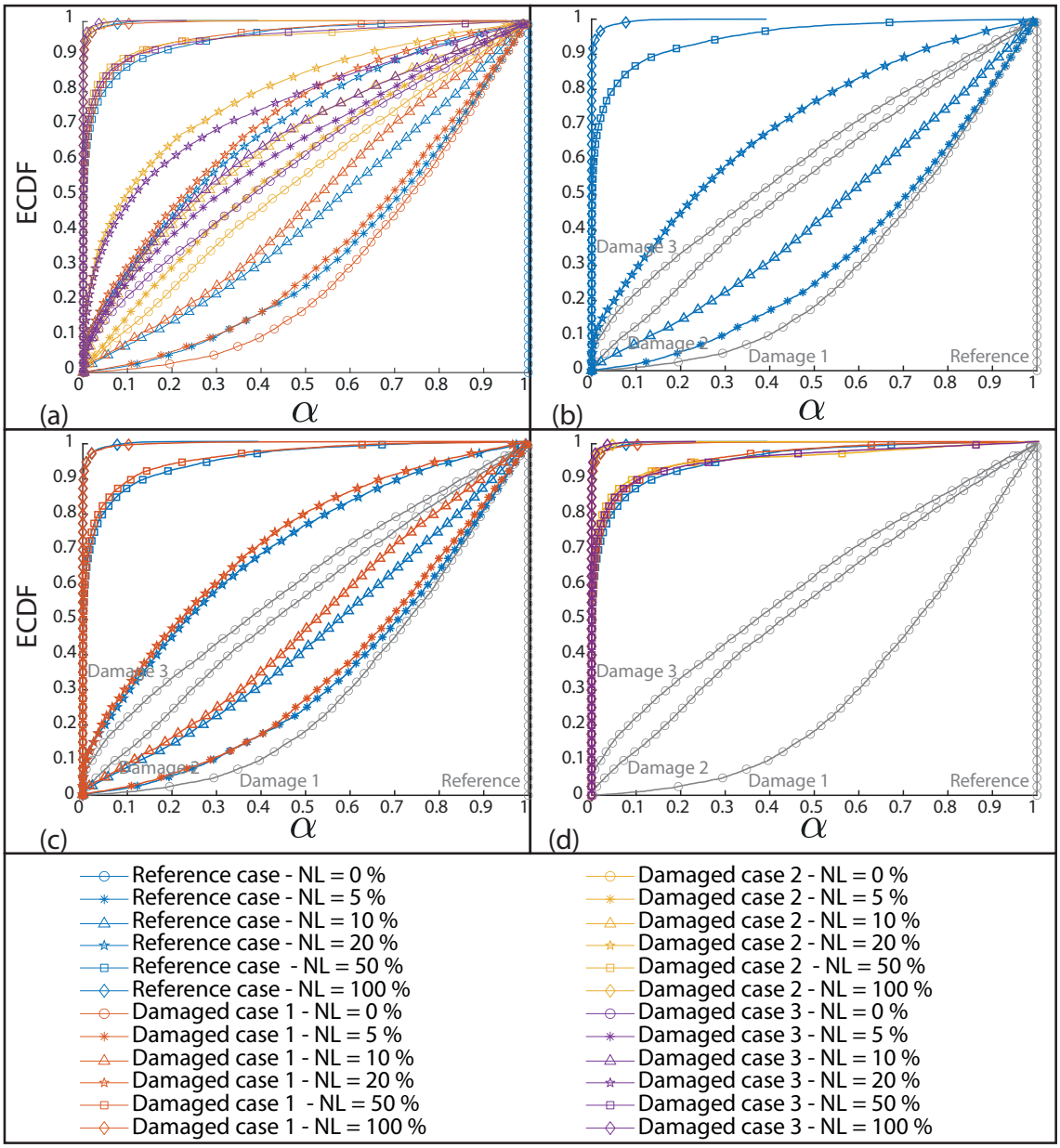

FIGURE 3.8: Sensitivity of the proposed methodology - damage detection under different noise levels: (a) influence of the noise in each state, (b) influence of the noise in the reference case, (c) influence of the noise in the reference case and damaged case 1, and (d) influence of the noise at noise levels 50% and 100%.

3.4.4 Influence of sampling frequency

The final scenario accounts for the sampling frequency. Before introducing the structural acceleration into the FPT algorithm, the input signal is resampled. The reference sampling frequency has been fixed at 50 Hz. The other sampling frequencies tested are 10, 20 and 100 Hz. In Figure 3.9, it can be observed that each case is well distinct from the others, meaning that the damage detection methodology is marginally affected by the sampling frequency. However, it can be noticed that a sampling frequency of 10 Hz or even 20 Hz may be too small for a eigenfrequency of 1.43 Hz. This is why, in the reference case, the 10 Hz sampling frequency is the furthest from the 50 Hz sampling frequency, taken as the reference sampling frequency.

In general cases, 20 points per period are sufficient. As the eigenfrequency of the first bending mode is equal to 1.46 Hz, a sampling frequency of 30 Hz is considered sufficient. However, if the sampling frequency is below this threshold, the signal is badly discretised. This phenomenon is called aliasing. Conversely, if the sampling frequency is excessively high, such as 100 Hz, it becomes ineffective as the signal has already been adequately discretised.

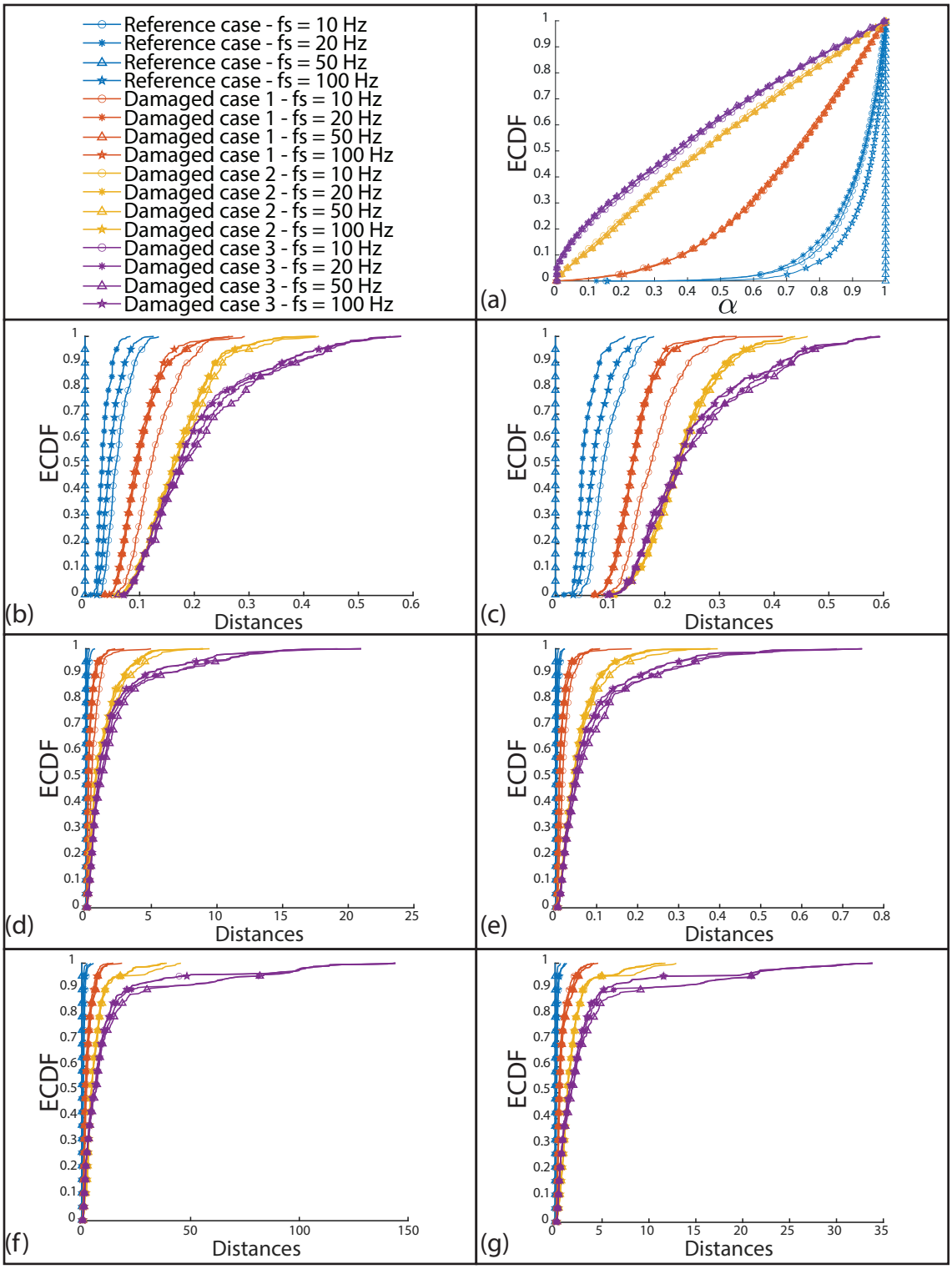

FIGURE 3.9: Sensitivity of the proposed methodology - damage detection under different sampling frequencies: (a) the proposed statistical test and 2-sample tests (b) KS, (c) K, (d) CVM, (e) AD, (f) W and (g) WAD.

3.5 Conclusion

In this chapter, the proposed methodology for damage detection and localisation has been described. This methodology hinges on two main parts. The first one relies on the pre-processing of the input signal. Indeed, this pre-processing is intended to be as general as possible and reduces some negative aspects of using the raw input signal that could undermine the damage detection. The pre-processing relies on two filters, a band-pass filter between $[f_{\min}, f_{\max}]$ and a frequency content adjustment filter, before computing the envelope of the filtered input signal by using the Hilbert transform. The second part of the proposed methodology is based on 2-sample tests coming from the literature and a proposed statistical test. For each combination (X_0, X_f) of the map, an ECDF of FPT can be computed. In two different states (healthy/reference, and current), these two ECDFs can be compared for each combination (X_0, X_f). Therefore, distances or α-values are obtained. It has been decided either to use the average of these distances and α-values as an indicator for damage detection or to plot the ECDFs of these distances and α-values for a more detailed graphical representation. At the end of this chapter, the sensitivity of the proposed methodology has been assessed through four different scenarios. Globally, the methodology has shown a great robustness for damage detection in the four studied scenarios.

Chapter 4

Small-scale laboratory test

The algorithm developed in Chapter 2 and the proposed method for damage detection and localisation described in Chapter 3 are applied to a small-scale lab test under supervised conditions. The experimental setup is described. Then, a digital twin model of the experimental setup is created and updated. The expected performance of damage detection is assessed, first, by using a simple numerical model. Second, the proposed damage detection method is applied to detect changes in the experimental setup, which are incurred by slightly modifying the mass distribution of the tested specimen. Finally, the updated digital twin model is used to locate the "damage" by comparing its map of FPT histograms with the one computed from the experimental results.

4.1 Experimental setup

A small-scale experiment [97] has been carried out at the *LTAS-Vibrations et Identification des Structures* (LTAS-VIS) laboratory unit of the Department of Aerospace and Mechanical Engineering at the University of Liège. The experimental setup is illustrated in Figure 4.1(a) to (d) and consists of a steel strip clamped at both ends and pre-stressed with a mass suspended at the lower extremity. An electrodynamic vibration shaker (TV 50009) is mounted on the structure as shown in Figure 4.1(a). It applies horizontal force close to the strip end. The material properties and the geometry of the steel strip are given in Tables 4.1 and 4.2.

Table 4.1: Geometrical properties of the steel strip.

Parameter	Value	Units
Length	498	mm
Width	25	mm
Thickness	0.4	mm
Pre-stress mass	1.816	kg

TABLE 4.2: Material properties of the steel strip.

Parameter	Value	Units
Density	7767	kg/m^3
Young modulus	206	GPa
Poisson ratio	0.33	[-]

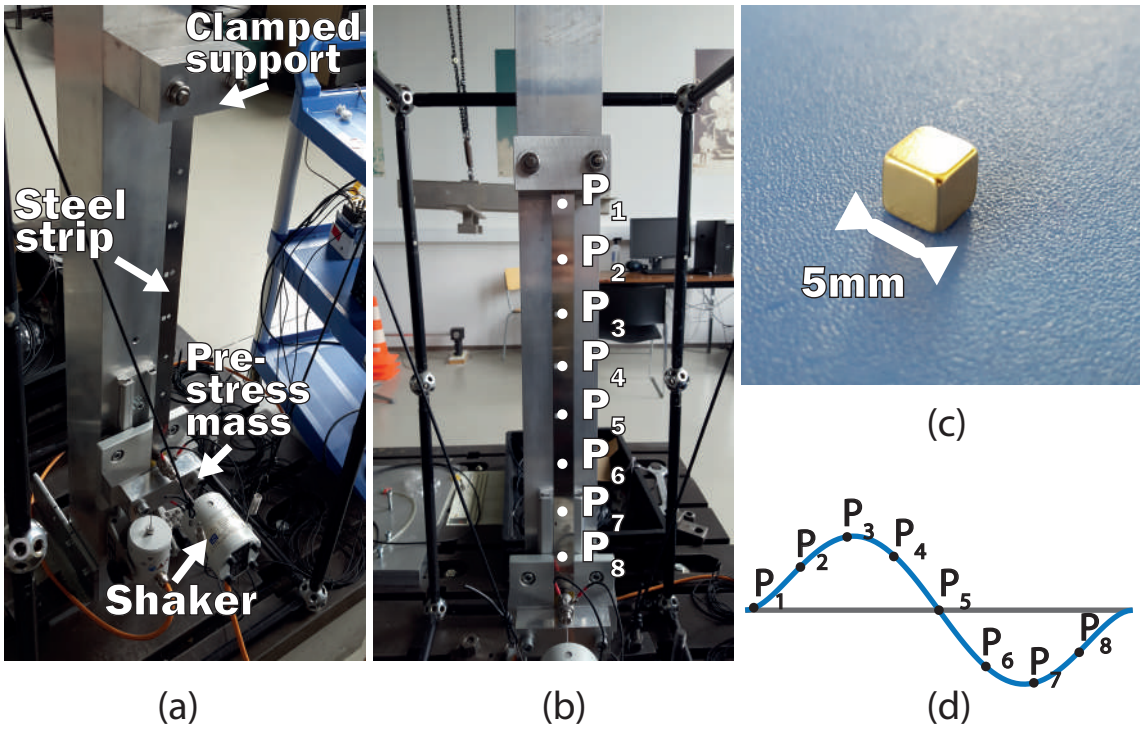

FIGURE 4.1: Experimental setup: (a) side view, (b) front view, (c) magnet used as a structural modification applied to the steel strip, and (d) second bending mode.

The response velocity of the structure is measured at several points along the strip thanks to a Polytec MSA-400 OFV-552 laser transducer as shown in Figure 4.1(b). Points P_1 to P_8 refer to the eight positions where vibrations have been measured.

To simulate damage to the structure, a small magnet was placed at three different locations: P_1, P_2 and P_3. The addition of the magnet slightly changes the mass distribution of the steel strip. The side length of the cubic magnet, represented in Figure 4.1(c), is 5mm and its weight is 0.95g. Its ID article is W-05-N50-G from Supermagnete [129].

The structure without the magnet corresponds to the reference case while the three considered damaged cases correspond to configurations where the magnet is placed on the structure.

4.1.1 Modal analysis of the reference structure

A modal analysis was performed in order to obtain reference values for the natural frequencies and the mode shapes of the steel strip. To do so, a broadband white noise was injected through the horizontal shaker at low amplitude (to avoid non-linearity effects). A frequency range of [3; 200]Hz was used in order to capture the first six bending modes [108]. The experiment was repeated eight times, by moving the laser position, from P_1 to P_8, to capture the same number of structural responses. The SSI-COV algorithm was then used to obtain the natural frequencies and damping ratios. Since measurements at each point were not taken simultaneously, another approach was necessary for the mode shapes. They were obtained by computing the standard deviation of the structural responses filtered around each peak of the PSD of the velocity. This was feasible because each peak was well distant from the others, see Figure 4.2 where the PSD of the velocity at point P_3 is shown. Therefore, the amplitude of the mode shapes can be directly linked with the standard deviation at each point P_i and the sign of the correlation coefficient with an arbitrarily chosen reference point. The natural frequencies and damping ratios are given in Table 4.3 and the first 6 bending modes are represented in Figure 4.3.

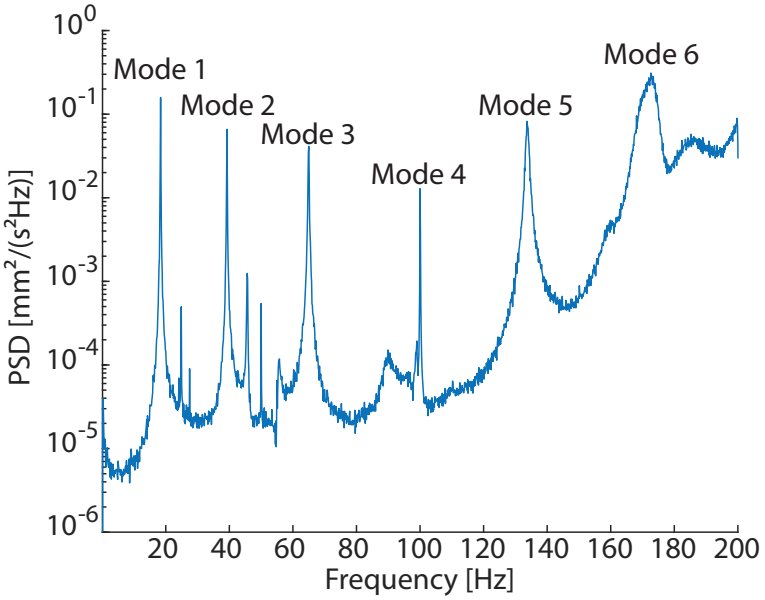

FIGURE 4.2: PSD of the velocity at Point P_3 recorded under broadband excitation.

TABLE 4.3: Identified natural frequencies and damping ratios of the first 6 bending modes (reference state).

	Natural frequency [Hz]	Damping ratio [%]
1st bending mode	18.26	0.13
2nd bending mode	39.25	0.39
3rd bending mode	64.74	0.18
4th bending mode	97.43	0.90
5th bending mode	133.74	0.36
6th bending mode	173.83	0.90

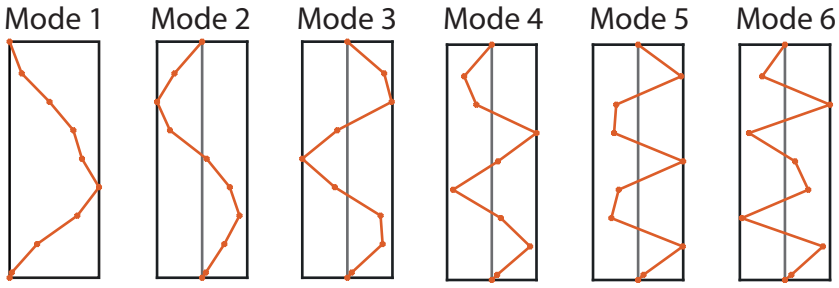

FIGURE 4.3: First six identified bending modes.

4.1.2 Modal analysis of the damaged structure

The second bending mode is selected to assess the new method for damage detection and localisation. Before this assessment, another modal identification of the damaged state is performed while focusing on this mode. A band-limited white noise is generated in the frequency range [35; 43]Hz, see Figure 4.4, and the generated time series is injected through the shaker. For each damaged scenario, the test is repeated three times. For each test, the same signal is used as an input and the velocity of the strip is measured at point P_3. The PSDs of the velocity in a reference scenario and in the damaged scenarios are shown in Figure 4.5. As the magnet moves from P_1 to P_3, the natural frequency of the structure decreases, as expected. In fact, when the magnet is located in P_1, the modal mass in the 2^{nd} bending mode is slightly modified, resulting in a small modification of the natural frequency. However, when the magnet is located at P_3, it is close to the anti-node of the second bending mode, see Figure 4.1(d), which causes a higher increase of the modal mass compared to the other two damaged scenarios. The natural frequencies of the second bending mode for all of the scenarios are listed in Table 4.4, together with the relative frequency difference compared to the reference case, which read as follows

$$\Delta = \frac{f_{\text{damaged case}} - f_{\text{reference case}}}{f_{\text{reference case}}}.$$

These values vary from 0.15% for the damaged case P_1 up to 2.7% when the magnet is located at P_3. Typical modal-based methods, detecting damages based on changes of frequencies, would typically trigger for changes Δ of 1 to 5%. Above the damage is obvious, below, it might not be detected due to additional disturbances. The values shown in Table 4.4 indicate that the considered damaged states correspond to configurations where modal-based methods face difficulties (magnet in P_1/P_2) or start to detect with confidence (magnet in P_3). This sets expectations for the proposed method.

TABLE 4.4: Natural frequency of the second bending mode for each scenario and the relative frequency difference between each damaged scenario and the reference scenario.

Case	Natural frequency [Hz]	Relative difference Δ [%]
Reference	39.25	0
Damage at P_1	39.31	-0.15
Damage at P_2	38.78	1.2
Damage at P_3	38.19	2.7

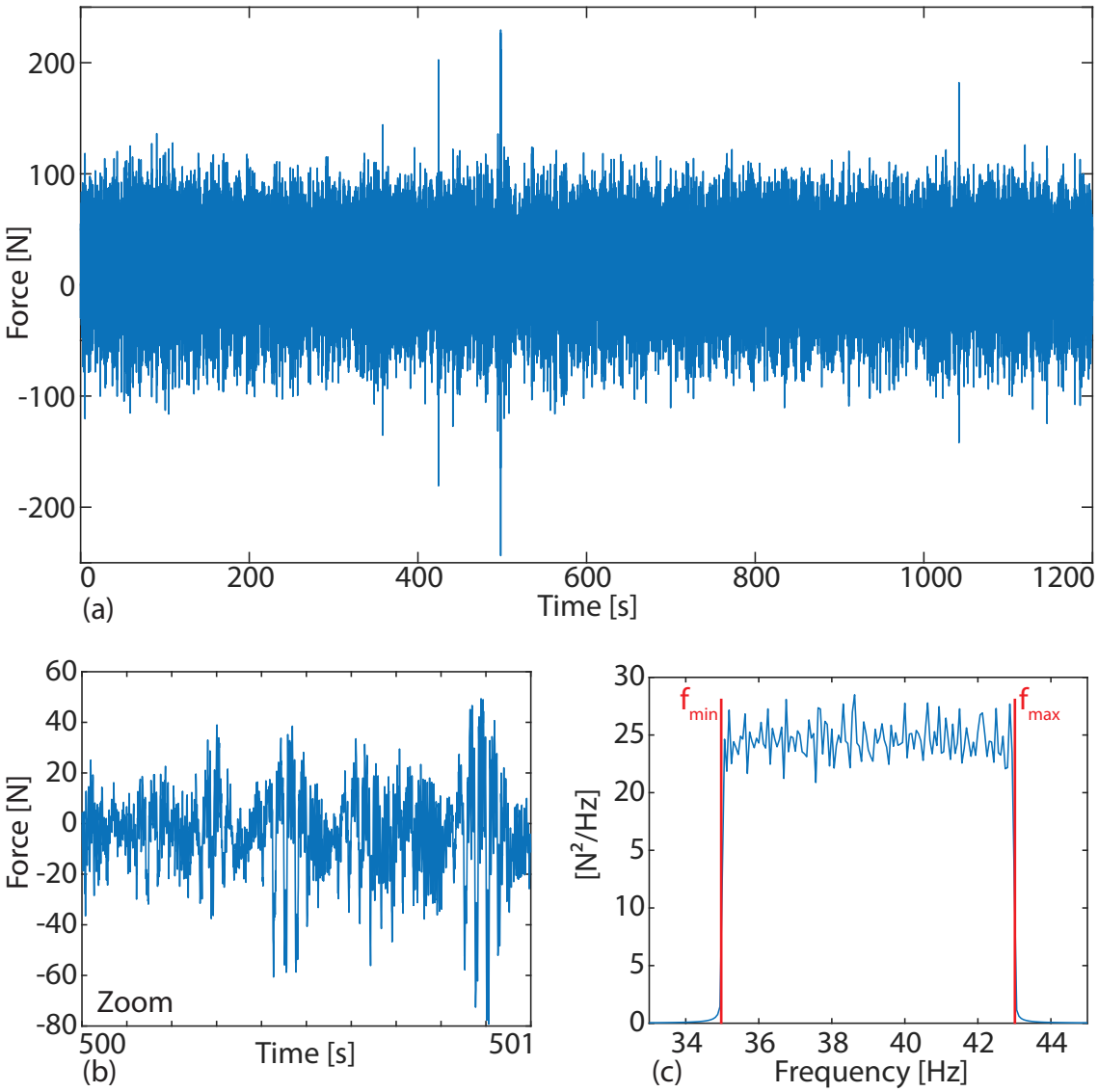

FIGURE 4.4: (a) Time signal of the input force, (b) zoom and (c) its PSD.

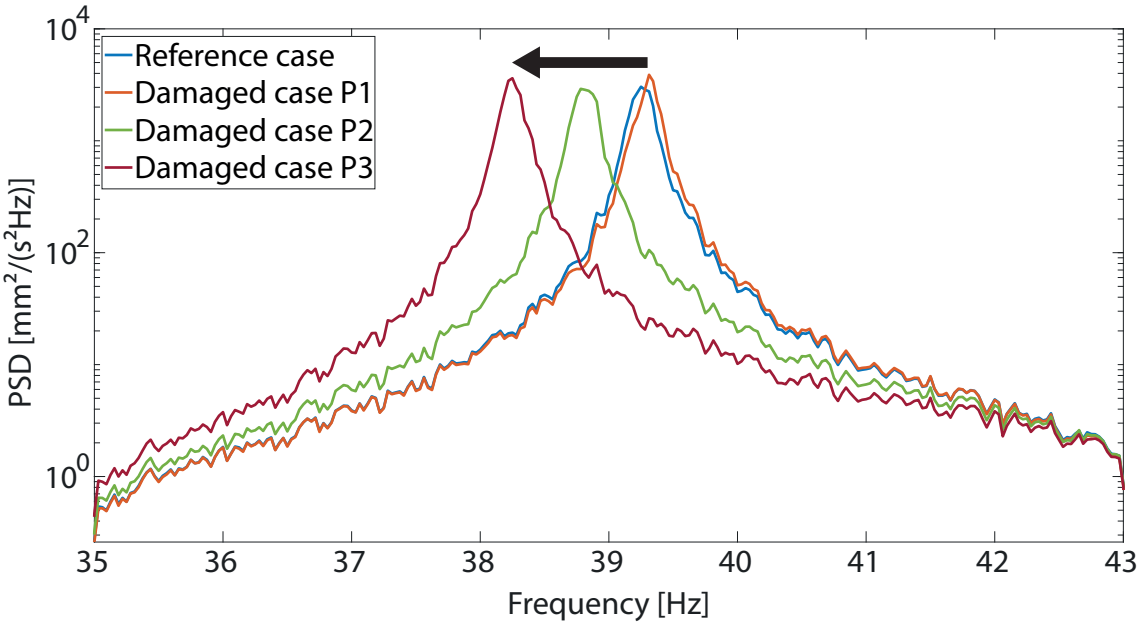

FIGURE 4.5: Comparison of the PSDs of the velocity at Point P_3 for the reference case and the damaged cases.

4.2 Digital Twin model

A digital twin model of the experimental setup is also developed. It is used to perform the damage localisation. The model is sketched in Figure 4.6 and consists of 80 beam elements. The stiffness and mass matrices of the elements are constructed according to standard finite element approaches (see Appendix B). The mass of the shaker head is also included in the mass matrix. The damping matrix is obtained by combining the mass and stiffness matrices according to the Rayleigh model, with $\alpha = 1.53$ [1/s] and $\beta = 6.29 \cdot 10^{-6}$ [s]. The eigenfrequencies obtained with this numerical model are given in Table 4.5. It can be seen that the discrepancies between the eigenfrequencies are large for the fifth and sixth bending modes. The relative difference has been computed as

$$\delta_f = \frac{f_{\text{numerical}} - f_{\text{experimental}}}{f_{\text{experimental}}}.$$

Figure 4.6(c) shows the Modal Assurance Criterion[1] (MAC) between the identified modes and the modes of the current numerical model. It can be seen that the MAC values for the fifth and sixth bending modes are also much lower than 1, which means that the current numerical model is not able to reproduce these two

[1]The MAC is a good indicator of the fit of a numerical model. If the MAC is close 1, it means that the two compared modes are close to each other while, if the MAC tends to 0, the two modes are significantly different

TABLE 4.5: Comparison between the eigenfrequencies of the experimental setup and the eigenfrequencies of the initial numerical model.

Bending mode	Experimental eigenfrequencies [Hz]	Numerical eigenfrequencies [Hz]	Difference δ_f [%]
1^{st} mode	18.35	18.88	2.86
2^{nd} mode	39.25	40.21	2.45
3^{rd} mode	64.74	66.29	2.39
4^{th} mode	97.30	96.39	−0.94
5^{th} mode	133.73	122.84	−8.14
6^{th} mode	171.93	150.75	−12.32

modes. Moreover, some values outside the main diagonal are close to 1, showing that a similarity exists between the fifth experimental and sixth numerical bending modes.

In order to improve this first numerical model, some minor changes were made, yielding an updated numerical model. A small rotation at the supports was allowed by adding a rotational spring and the mechanical model of the shaker itself has been included. A schematic of the updated numerical model is shown in Figure 4.6(b). The main parameters that were then adjusted are the rotational stiffness of the supports and the prestress mass value. By using a standard least square method, the frequency differences were minimised until a residual of less than 1% was obtained for each eigenfrequency. The resulting values of each parameter are listed in Appendix B. In Table 4.6, the updated eigenfrequencies are shown as well as the updated MAC in Figure 4.6(d). The shapes of the first six bending modes are plotted in Figure 4.6(e). The good agreement between the experimental and numerical eigenmodes demonstrates the quality of the finite element model updating procedure. Nevertheless, the first experimental bending mode is not well identified. This is because the relative amplitude of the first bending mode near the supports is much smaller compared to higher bending modes. Therefore, if a slight perturbation occurs in the force injected through the shaker, it significantly influences the first bending mode, leading to a worse identification for this bending mode than for the others. This also explains why the 2^{nd} mode was used to assess the proposed SHM method.

In addition to comparing the numerical model and the experimental setup by using MAC values and eigenfrequencies, it is now also possible to compare them by using FPT maps. These results echo the results presented in Section 2.4. For this comparison, the normalised velocity is used. This normalisation is obtained by dividing the velocity by its interquartile range and by subtracting its mean value. Then, the envelope is constructed with the Hilbert transform and the FPT is computed on the basis of these signals.

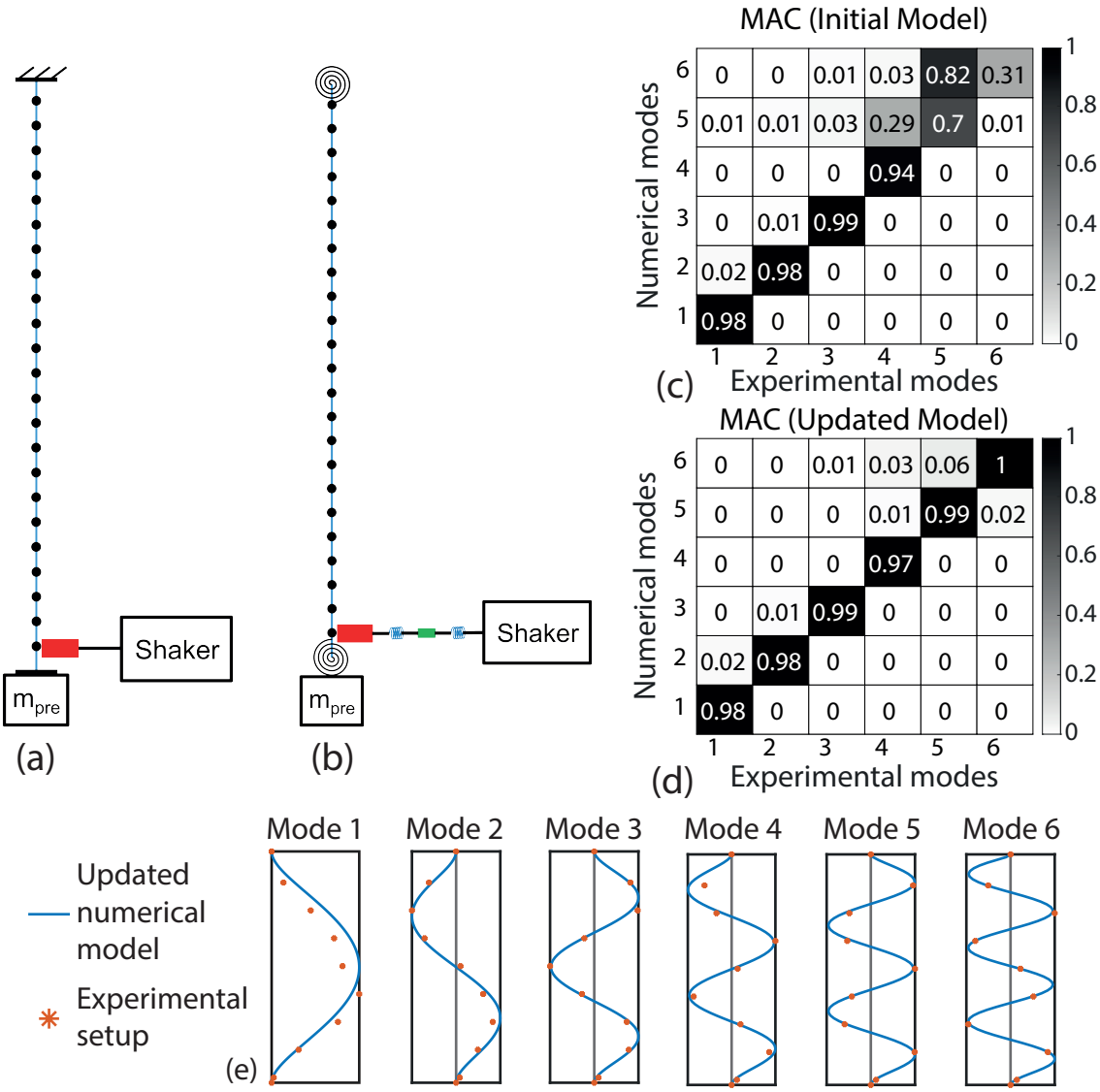

FIGURE 4.6: (a) Initial numerical model, (b) updated numerical model, (c) MAC for the initial numerical model, (d) MAC for the updated numerical model and (e) eigenmodes of the first six bending modes for the updated model (blue curves) and the experimental setup (orange stars).

TABLE 4.6: Comparison between the eigenfrequencies of the experimental setup and the eigenfrequencies of the updated numerical model.

Bending mode	Experimental eigenfrequencies [Hz]	Numerical eigenfrequencies [Hz]	Difference δ_f [%]
1^{st} mode	18.35	18.26	−0.52
2^{nd} mode	39.25	39.16	−0.24
3^{rd} mode	64.74	65.25	0.79
4^{th} mode	97.30	97.17	−0.13
5^{th} mode	133.73	134.21	0.35
6^{th} mode	171.93	171.72	−0.12

In Figures 4.7(a) and (b), the Average FPT map and the STD of FPT map are respectively depicted in both the numerical and experimental settings. The curves with the same colour represent identical FPT statistical values. It can be seen that the results are similar, especially in the lower half of the maps, under the main diagonal. However, the average as well as the STD of the FPTs are underestimated in the numerical model for large X_f levels, located in the upper left half of the maps. Indeed, the yellow curve of the experimental setup is at lower X_f levels than the curve of the numerical model.

In Figure 4.8, some FPT histograms are shown. As expected, based on the aformentioned discussion about the maps of statistical moments of FPT, a good agreement is observed between the histograms. The observation concerning the underevaluation of the FPTs in the upper half of the map is highlighted in Figures 4.8(a) and (b). Indeed, the curve of the numerical model is at higher X_f levels than the curve of the experimental setup when X_0 is small while it is the opposite for larger X_0 levels, resulting in an underestimation of the averages and STDs of FPT. Therefore, FPT histograms are more sensitive to detect changes than the average of FPT map and the STD of FPT map, which do not sufficiently discriminate.

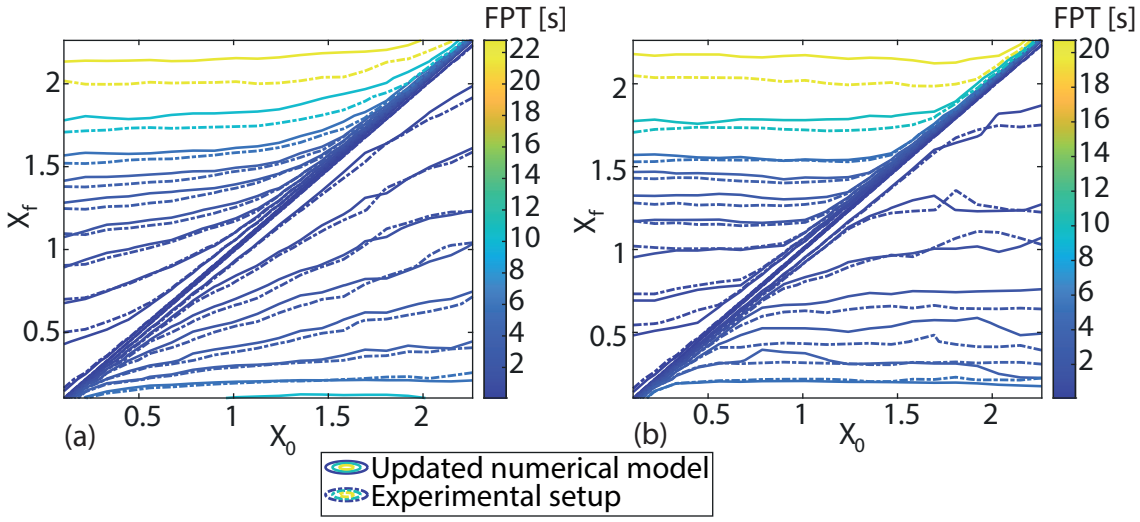

FIGURE 4.7: Comparison of FPT maps of the envelope of the normalised velocity for the experimental setup and the updated numerical model: (a) Average FPT map and (b) STD of FPT map.

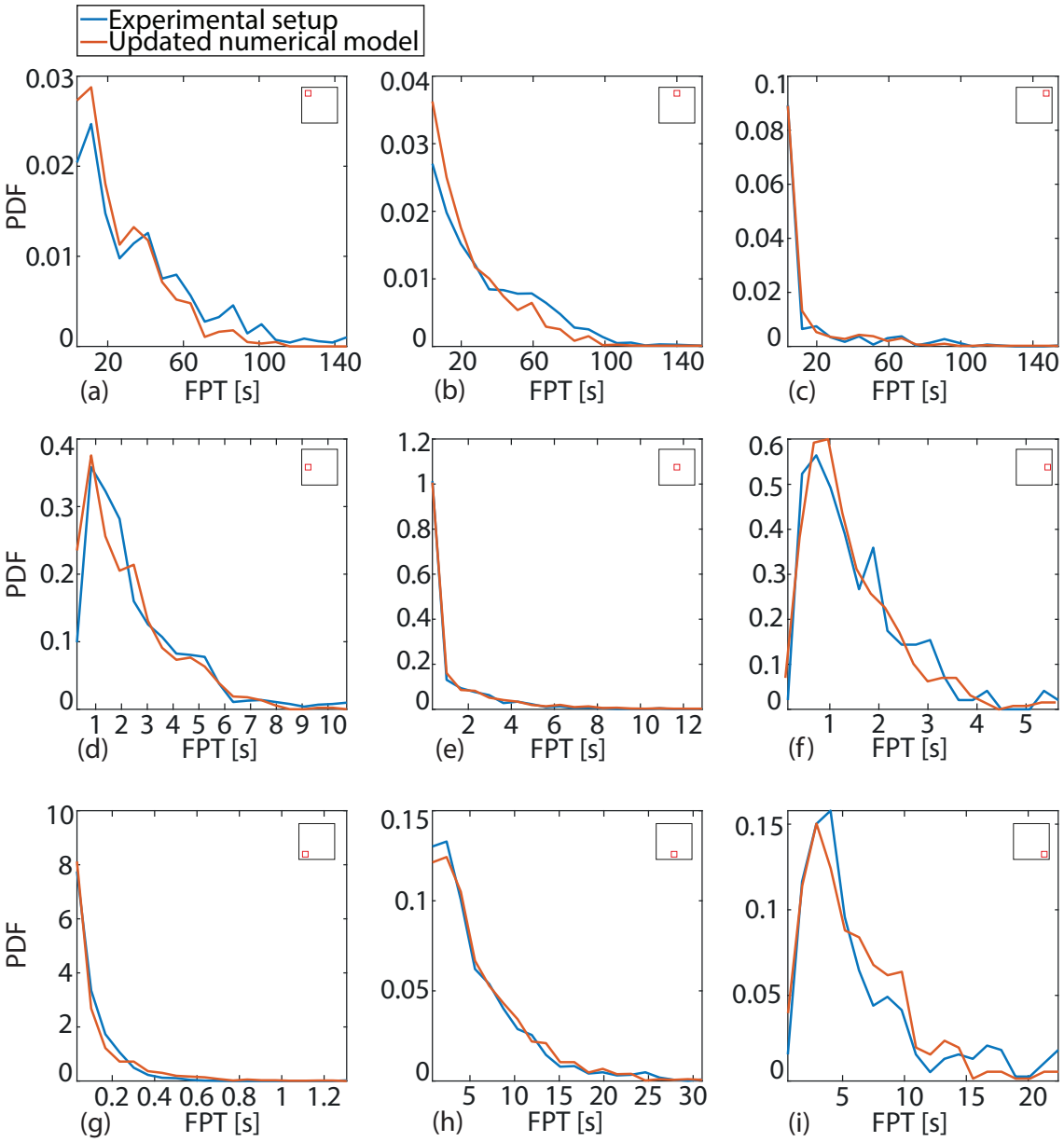

FIGURE 4.8: Comparison of histograms of FPT for the envelope of the normalised velocity of the experimental setup and the updated numerical model both in the reference state for various values of (X_0, X_f): (a) $(0.19, 2.17)$, (b) $(1.20, 2.17)$, (c) $(2.13, 2.17)$, (d) $(0.19, 1.20)$, (e) $(1.16, 1.20)$, (f) $(2.17, 1.16)$, (g) $(0.19, 0.24)$, (h) $(1.16, 0.19)$, (i) $(2.17, 0.19)$.

4.3 Illustration of Damage detection

In this section, the proposed method is applied to detecting damage by means of numerical experiments in a single degree-of-freedom system. The objective of using a simple numerical model is to determine the efficiency of the damage detection methodology proposed in Chapter 3 when the mass or the stiffness vary. Then, the methodology is applied to the experimental setup described earlier in this Chapter.

4.3.1 With a simple numerical model

FPT histograms have demonstrated the ability to detect slight changes in the structural response. For each structural response, a FPT map can be computed. Therefore, if a structural parameter changes, then the structural response is also affected, resulting in a modification of the FPT map. The objective is to demonstrate that the computed FPT map is unique for a given set of structural parameters.

To achieve this, a set of three parameters (μ, κ, λ) has been selected. The equation of motion of a single degree-of-freedom (DOF) system is given by the following relationship:

$$\mu m\ddot{x}(t) + c\dot{x}(t) + \kappa k x(t) = \lambda F(t).$$

The λ parameter modifies the amplitude of the external loading, which impacts damage detection, while the parameters μ and κ influence the mass and stiffness of the structure respectively.

A simple numerical model, whose properties are similar as those of the 2^{nd} bending mode of the experimental setup, has been employed as a single DOF system. This choice is motivated by the study of a numerical case that is similar to the experimental setup in order to assess the effectiveness of the proposed methodology. This sandbox example is used to discuss the well-posedness of the problem. The values chosen for the eigenfrequency, modal mass, modal stiffness and damping ratio ξ can be found in Table 4.7. The modal mass of the steel strip could not be identified using the output-only identification method. It is therefore arbitrarily chosen to be equal to $m = 1$ kg.

A reference set of parameters $(\mu, \kappa, \lambda) = (\mu_d, \kappa_d, \lambda_d) = (0.95, 0.9311, 1)$ has been arbitrarily selected. By modifying the set of parameters (μ, κ, λ) in a range, the FPT histograms obtained with the set of parameters (μ, κ, λ) are expected to be different. They are compared with those computed for the reference set of parameters $(\mu_d, \kappa_d, \lambda_d)$.

To illustrate this, four different sets of parameters are first selected: one set (a) close to the reference set of parameters $(\mu_d, \kappa_d, \lambda_d)$ and three sets (b,c,d) for which

TABLE 4.7: The eigenfrequency, the modal mass, the modal stiffness and the damping ratio ξ of the 1-dof system.

Parameters	Values	Units
Natural frequency	39.31	Hz
Modal mass m	1	kg
Modal stiffness k	61025	N/m
Damping ratio	0.0039	[-]

TABLE 4.8: Sets of parameters (μ, κ, λ) to illustrate their influence on the map of α-values.

Case	(μ, κ, λ)	Comment
Reference	$(0.95, 0.9311, 1.00)$	Reference set of parameters
(a)	$(0.95, 0.93, 1.00)$	Small change for κ
(b)	$(0.98, 0.93, 1.00)$	Change for μ
(c)	$(0.95, 0.90, 1.00)$	Change for κ
(d)	$(0.95, 0.93, 0.90)$	Change for λ

one parameter at a time is significantly different. Table 4.8 shows these different sets of parameters. For each selected set of parameters, FPT histograms are computed and compared to those obtained with the reference set of parameters $(\mu_d, \kappa_d, \lambda_d)$. Therefore, the proposed statistical test is used to compare these histograms and for each combination (X_0, X_f), an α-value is obtained.

Figure 4.9 shows the α-values for the four selected sets of parameters (μ, κ, λ) compared with the reference set of parameters $(\mu_d, \kappa_d, \lambda_d)$. In Figure 4.9(a), the choice of $(\mu, \kappa, \lambda) = (0.95, 0.93, 1.00)$ is the closest to $(\mu_d, \kappa_d, \lambda_d) = (0.95, 0.9311, 1)$. This results in higher α-values being obtained for the majority of (X_0, X_f) combinations compared to those obtained when the values of the parameters (μ, κ, λ) are more different from the reference parameters $(\mu_d, \kappa_d, \lambda_d)$, as illustrated in Figures 4.9(b), (c) and (d). Consequently, the average of α-values over the entire map provides an indicator, represented as a scalar value, for each set of parameters (μ, κ, λ). This indicator is a good canditate to highlight the differences between the FPT histograms from the reference set of parameters $(\mu_d, \kappa_d, \lambda_d)$ and those from varying sets of parameters (μ, κ, λ) in a given range. The same conclusions can be drawn for the distances computed with the existing 2-sample tests except that, for the set of parameters (a), the distances are on average significantly smaller than those for the sets of parameters (b,c,d).

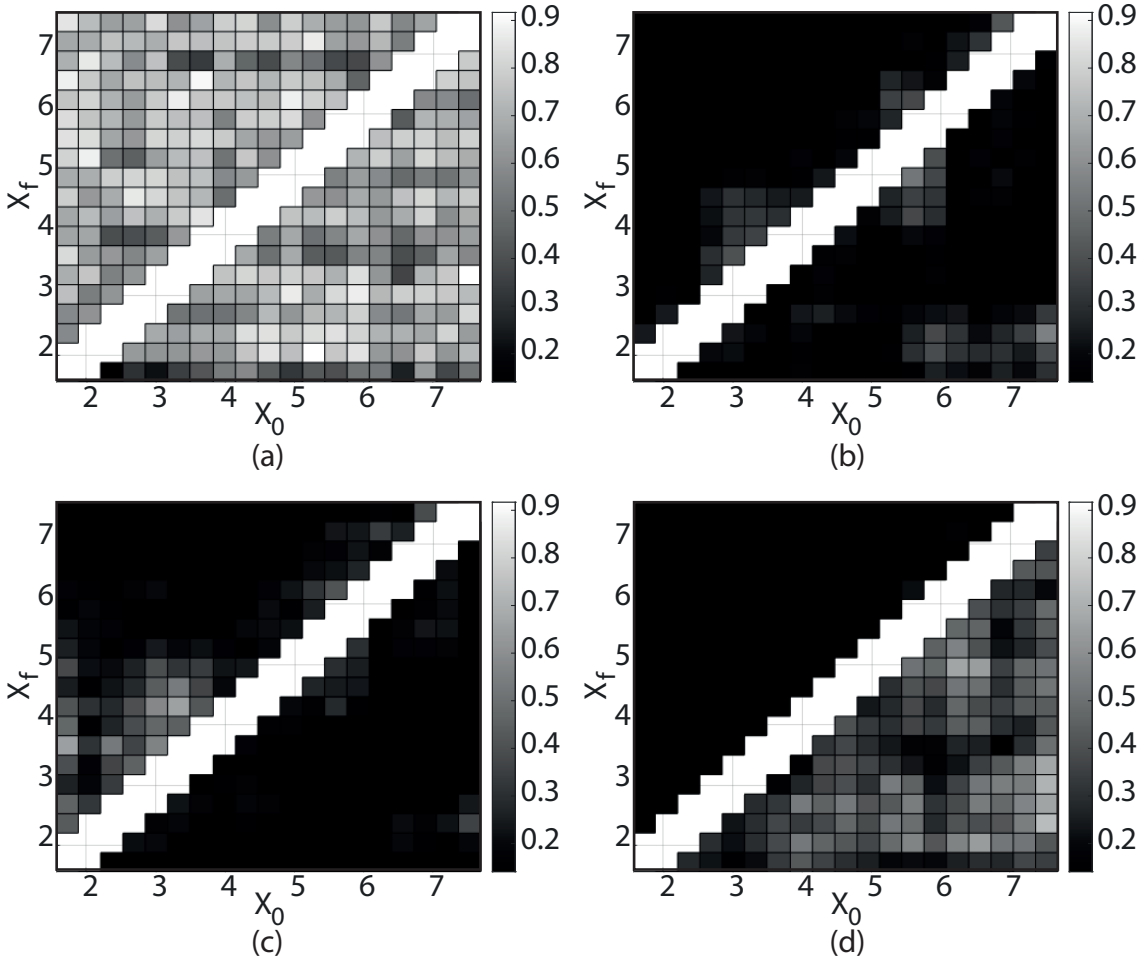

FIGURE 4.9: Illustration of the influence of the parameters (μ, κ, λ) on damage identification by means of α-values when (μ, κ, λ) is equal to (a) $(0.95, 0.93, 1.00)$, (b) $(0.98, 0.93, 1.00)$, (c) $(0.95, 0.90, 1.00)$, and (d) $(0.95, 0.93, 0.90)$ with the reference $(\mu_d, \kappa_d, \lambda_d)$ being set to $(0.95, 0.9311, 1.00)$.

Next, only the influence of the parameters μ and κ is studied, while $\lambda = 1$.

In Figure 4.10, for $\lambda = 1$, the proposed indicator, relying on the average of α-values or distances over the entire map, is shown for the proposed statistical test and for each 2-sample test. Some distances of the 2-sample tests have been shown with a log scale for better visualisation. Each test provides a favorable value of the indicator when (μ, κ) is close to (μ_d, κ_d). The red square corresponds to the optimal value of the indicator, corresponding to the greatest average of the α-values or the smallest average of the distances, while the black dot corresponds to the reference set of parameters (μ_d, κ_d). The tests performing well are the proposed method (based on α-values), the Cramer-Von Mises and the Wasserstein tests (based on distances).

Furthermore, in each subfigure, a preferred line can be seen along the main diagonal. This line corresponds to the following condition

$$\frac{\kappa}{\mu} \approx 1$$

for which the natural frequency is conserved. In this case, the natural frequency is equal to 39.31 Hz. This shows that the frequency has a leading influence on the indicator. If the frequency slightly changes, the indicator drops significantly: this translates that there is a high sensitivity with respect to the eigenfrequency, resulting in an ill-conditioned problem.

The same process can be repeated but for different values of λ. This shows the influence of the force amplitude over the sensitivity of the proposed methodology.

In Figure 4.11, it can be observed that the optimal parameters (μ, κ) are shifted along the main diagonal as λ changes. Indeed, if $\lambda < 1$, the location of the maximum average of α-values is located in the bottom left corner while if $\lambda > 1$, it is located in the upper right corner. Therefore, the optimal set of parameters (μ, κ) changes with λ. By increasing the applied load, the structural response increases proportionally. Therefore, the map is shifted by a factor λ in the (X_0, X_f) plane. To obtain a map which is similar to the original one, it is necessary to change the stiffness in the same ratio, which will shift back the FPT map in the (X_0, X_f) plane. Moreover, the ratio $\frac{\kappa}{\mu}$ must remain close to 1. This explains why the optimal point travels along the diagonal.

Nevertheless, this phenomenon of increasing or decreasing signal amplitude occurs mainly in numerical models. If the amplitude of the eigenmode is not well captured, it can lead to an increase or a decrease in the structural response even if the input force applied to the system is the same. Therefore, in order to avoid this problem, a special attention should be given to the response amplitude of the numerical model.

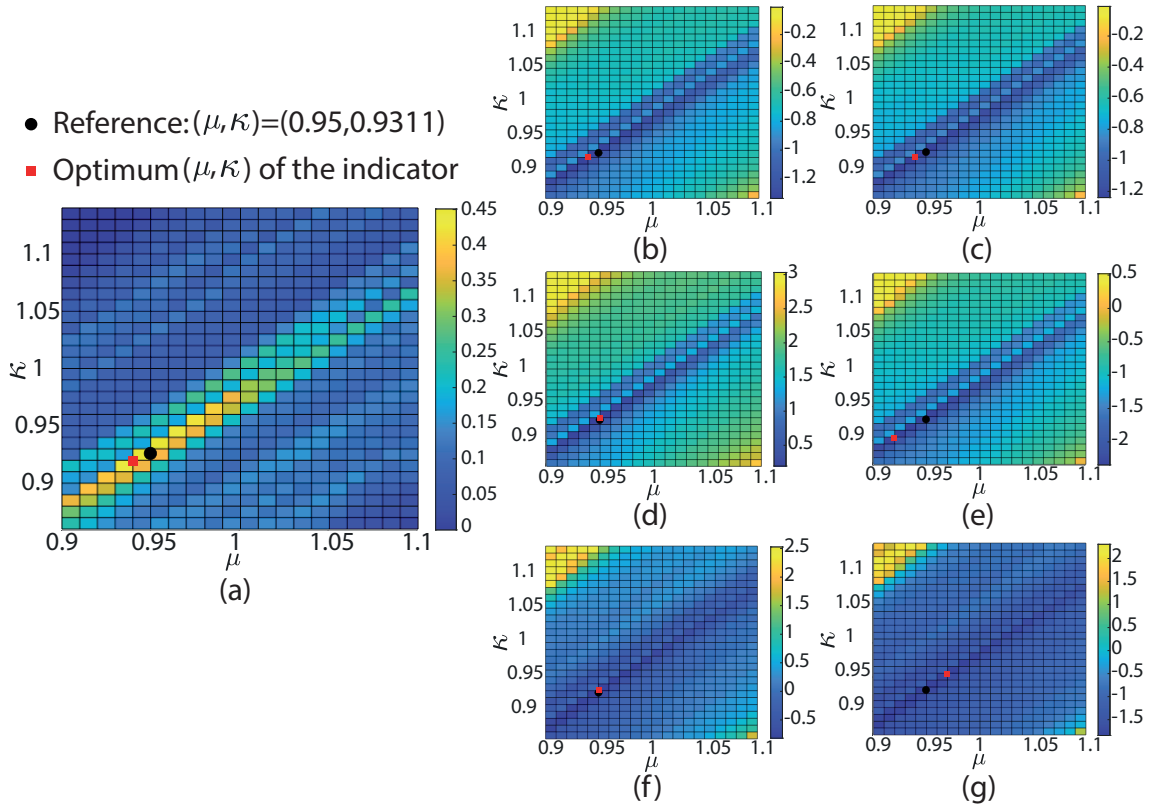

FIGURE 4.10: Influence of (μ, κ) on the average of α-values and distances. $\lambda = 1$, for (a) the proposed statistical test, (b) the KS test, (c) the K test, (d) the CVM test, (e) the AD test, the (f) W test, and (g) the WAD test.

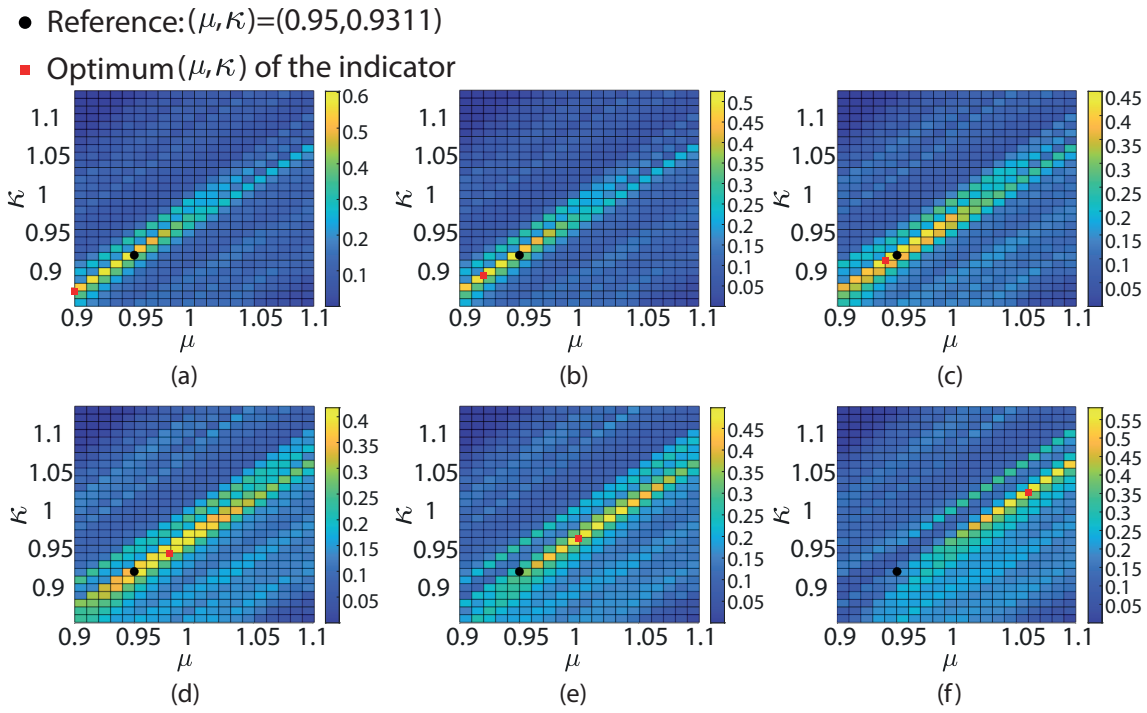

FIGURE 4.11: Influence of (μ, κ) on the average of α-values. (a) $\lambda = 0.95$, (b) 0.98, (c) 1.00, (d) 1.02, (e) 1.05, and (f) 1.10.

Thanks to this numerical example, the sensitivity of FPT maps has been demonstrated by using the average of α-values and distances. In the following, the distribution of α-values and distances is considered as it provides better information over the entire map. Moreover, the similar results, obtained by comparing 2 full maps of FPT distribution for each 2-sample test and the proposed statistical test, contribute to fact that FPT histograms are able to capture and detect slight changes in the structural response due to a small variation of the structural parameters. As it has been demonstrated, modifications to the force amplitude can significantly impact the proposed method. Therefore, it is important to keep a similar force amplitude to improve the robustness of the proposed methodology.

4.3.2 With the experimental setup

It has already been shown that the proposed method is able to identify occurrence of "damage" [102]. In this section, four different cases are considered: the reference case and three damaged cases, when the magnet is placed at points P_1 (damaged case 1), P_2 (damaged case 2), and P_3 (damaged case 3). For each case, the test has been repeated 3 times. The velocities of the steel strip were only measured at point P_3. The signals have been processed according to the methodology described in Chapter 3. For each combination (X_0, X_f) of the map, it is possible to obtain either an α-value or a distance by comparing all cases with the reference case 1.

Instead of using the averages of the α-values or the distances, the ECDFs, which correspond to the distribution of these values are used as they offer better discrimination capabilities. They are plotted in Figure 4.12. These plots serve as a visual representation of the damage detection. As a reminder, when α-values are close to 1, ECDFs are very similar while for the distances, they must be close to 0.

It can be observed in Figure 4.12(a) that each scenario can be well distinguished. Moreover, as the damage increases from P_1 to P_3, a shape change in the ECDFs of α-values is observed, varying from a curve close to the lower right corner to a curve close to the upper left corner. This shape change is caused by the decrease of α-values when the damage increases, resulting in greater differences observed in the FPTs for each combination (X_0, X_f).

In Figures 4.12(b), (c), (d), (e), (f) and (g), the conclusions are similar for the 2-sample tests. Each scenario is well identified and separated from the other ones. This results in a shift in the ECDFs of the distances from left to right. However, there is an intersection for the W and WAD test between the reference test 2 and the damaged case P_1. This kind of intersection shows a lack of sensitivity with the test. Interestingly, the shapes of the ECDFs of the distances are different from those in Section 3.4. This is because the ECDFs are now data-driven and the dynamics of the system in the lab does not follow those of the perfect numerical models, as used in Section 3.4.

Nonetheless, in this case, all ECDFs of α-values or distances exhibit acceptable results for damage detection. Hence, with the proposed method, it is possible to represent easily if a damage occurred on the structure. Figure 4.13 represents the "rule-of-the-diagonal". This rule is straightforward. Based on the ECDF of α-values, if the ECDF is located in the bottom right corner, under the main diagonal, no damage has occurred. Otherwise, if the ECDF is spotted in the upper left corner, above the main diagonal, then, damage is detected.

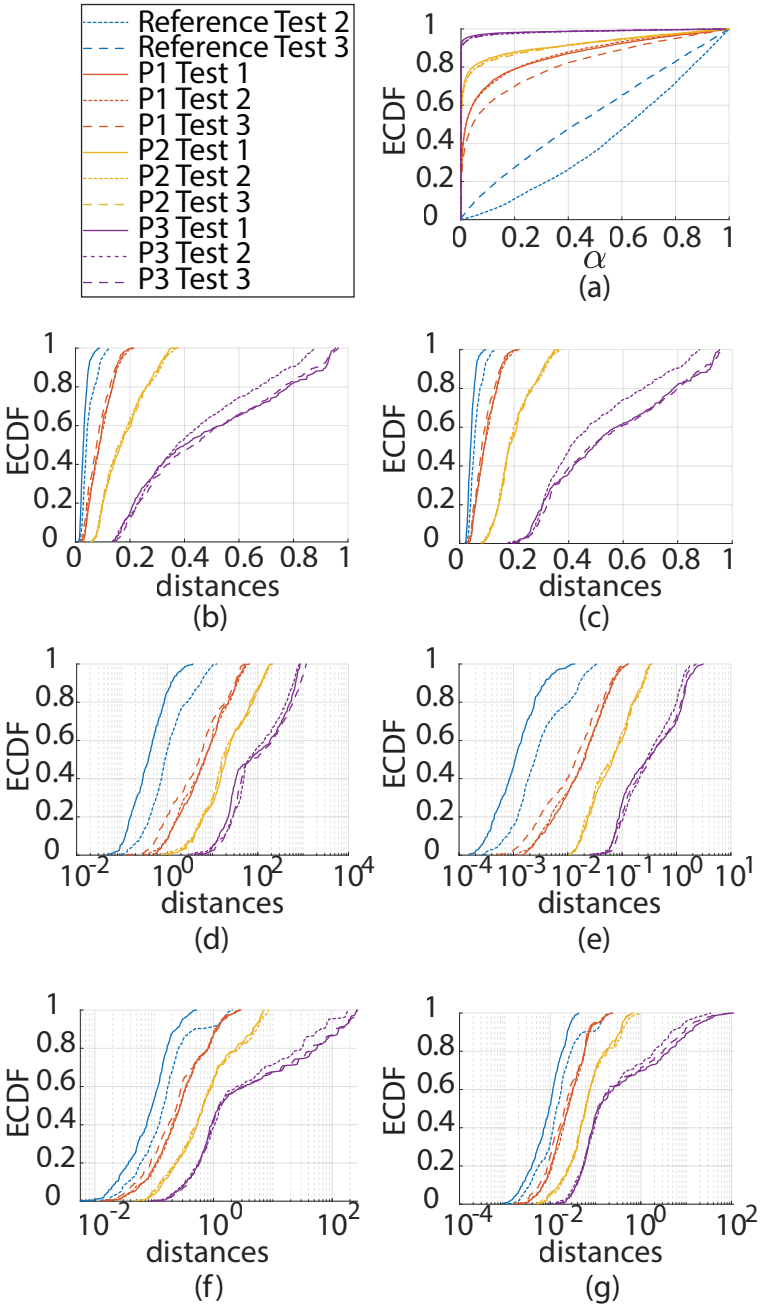

FIGURE 4.12: ECDFs of the indicators for each test compared to the reference case test 1: (a) the proposed statistical test, (b) the KS test, (c) the K test, (d) the CVM test, (e) the AD test, (f) the W test, and (g) the WAD test.

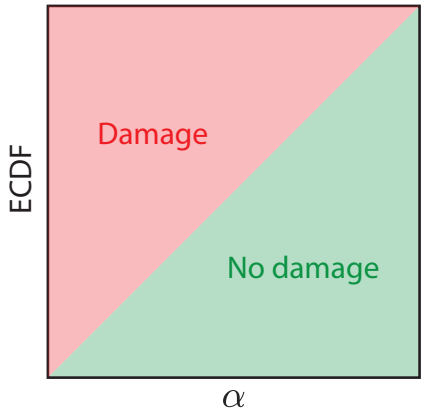

FIGURE 4.13: The "rule-of-the-diagonal".

With the "rule-of-the-diagonal", damage detection becomes straightforward with the proposed methodology.

For a more compact and quantified view of these results, in Table 4.9, the average of α-values from Figure 4.12(a) are gathered in the second column while the other columns are used for the averages of distances from Figures 4.12(b), (c), (d), (e), (f) and (g). A clear distinction can be made by comparing the different cases. The α-values decrease as the damage increases while they remain equivalent when considering the same case. For the distances, the conclusions are similar except that they increase as the damage increases.

By comparing Table 4.9 with Table 4.4, containing the relative differences on natural frequencies, it becomes evident that the methods based on FPT maps are more sensitive to detect damage at early stage. Indeed, with the proposed methods, damage can be detected even if the relative difference is as small as 0.15%.

TABLE 4.9: Comparison of α-values and distances obtained with each method averaged over the entire FPT map.

	Proposed test	KS test	K test	CVM test	AD test	W test	WAD test
Reference case test 2	0.59	0.03	0.04	0.56	0.00	0.01	0.11
Reference case test 3	0.45	0.05	0.06	1.85	0.01	0.03	0.27
Damaged case P1 test 1	0.13	0.09	0.10	12.11	0.03	0.04	0.46
Damaged case P1 test 2	0.13	0.09	0.10	12.52	0.03	0.04	0.46
Damaged case P1test3	0.18	0.08	0.09	10.09	0.02	0.03	0.42
Damaged case P2 test 1	0.08	0.18	0.20	39.89	0.10	0.11	1.47
Damaged case P2 test 2	0.08	0.18	0.20	40.91	0.10	0.13	1.60
Damaged case P2 test 3	0.08	0.18	0.20	41.13	0.10	0.12	1.50
Damaged case P3 test 1	0.01	0.48	0.54	231.35	0.63	4.03	34.21
Damaged case P3 test 2	0.02	0.44	0.47	202.14	0.50	1.82	19.17
Damaged case P3 test 3	0.01	0.49	0.54	283.97	0.59	3.24	33.63

4.4 Illustration of Damage localisation

The proposed method is also able to localise changes, by comparing experimental data with virtual modifications of the digital twin model [103].

To perform damage localisation, the updated numerical model described in Section 4.2 is used. The magnet, which is an additional mass to an element of the mass matrix of the numerical model, is placed along each node of the model. If the mechanical properties of the numerical model are close to the experimental setup, i.e. the magnet position for the numerical model corresponds exactly to the magnet position for the experimental setup, then the ECDFs of the FPT for the numerical model and the experimental setup are also similar. The considered damage localisation indicator is the average of α-values or distances over the entire map. So to localise the damage, one can simulate the FPT maps of the velocity at point P_3 in all variants of the model where the magnet is attached at a different node[2]. Then, for each variant, the average of the α-values (or distances) is computed and this proxy is used to conclude as per the plausibility of this location for the damage.

However, due to the location of the shaker close to the lower support, it has been found that the amplitude of the second bending mode was overestimated for all damaged cases at the loading point. This is due to a modification of the mode shape near the supports, which comes from the existence of a boundary layer in this thin flexible strip [130]. Therefore, the mode shapes of the specimen actually change when magnets are added. While these changes have minor importance in the middle of the span, they significantly affect the mode shape at the shaker position (inside the boundary layer). Consequently, it is important to account for the change of loading conditions. Beside, the small dissipation of energy at the supports, which is related to the small allowed rotation, is also tributary of this boundary layer behaviour. Unfortunately, the extensive modal analysis was not repeated for the damage configurations. Therefore, both the damping of the numerical model and the amplitude of its response were multiplied by coefficients that were adjusted to the data to compensate for this effect. The values of these coefficients can be found in Table 4.10.

In Figure 4.14, the indicators (averages of the α-values or distances) are plotted for each damaged case and each test. The y-axis is the adimensional abscissa along the steel strip, which is simply the coordinate divided by the total length of the strip.

A first observation is related to the symmetry of the indicators around $y = 0.5$, which is the half-length of the strip. In fact, with the numerical model, we are only able to capture the amplitude variations of the selected bending mode. Since

[2]In this case, the magnet mass is known but not its location on the strip.

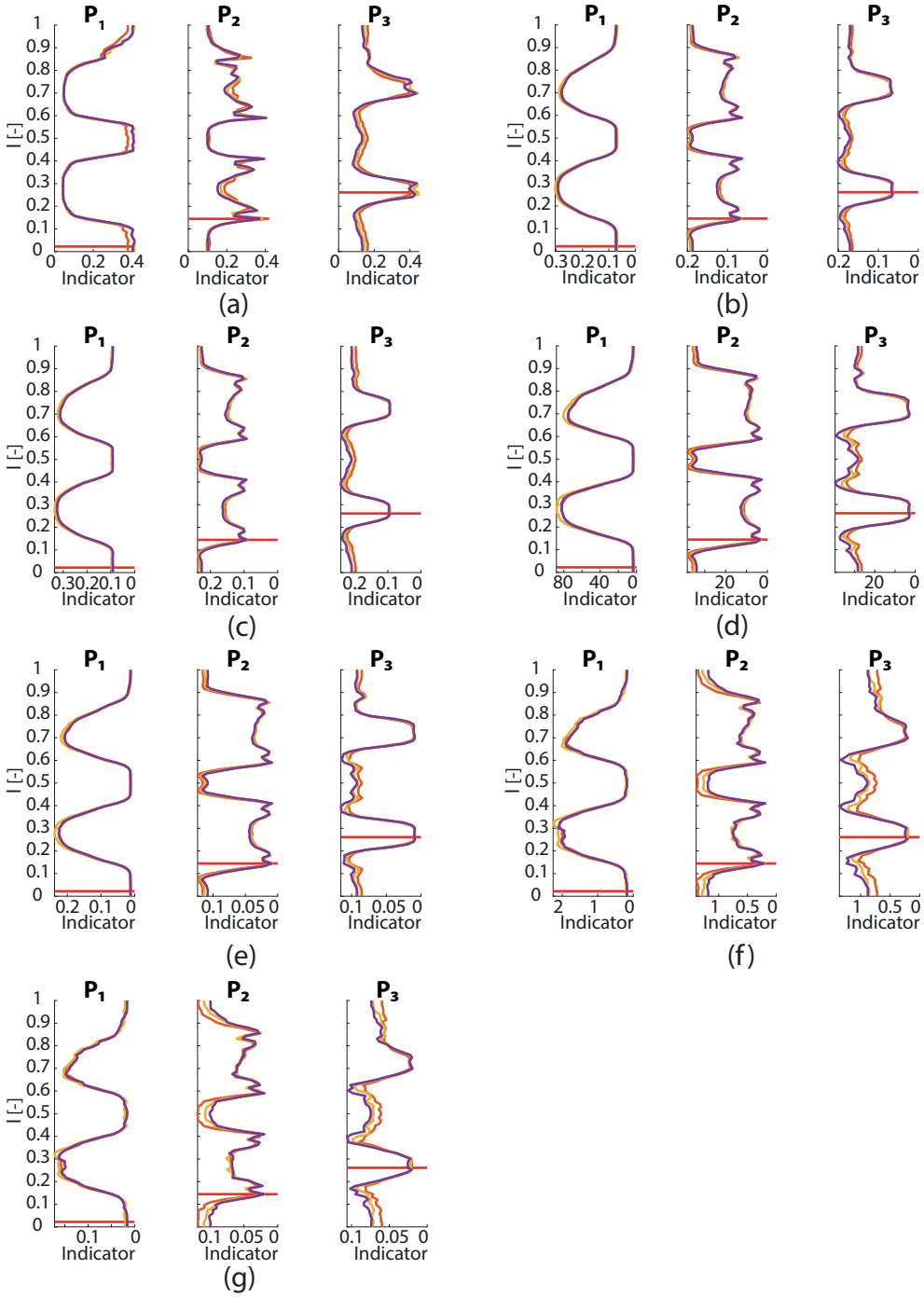

FIGURE 4.14: Indicators for the damage localisation when damage is localised at points P_1, P_2, P_3: (a) the proposed statistical test, and the (b) KS, (c) K, (d) CVM, (e) AD, (f) W, and (g) WAD tests. The red line indicates the actual position of the magnet.

TABLE 4.10: Coefficients for the damping and the amplitude of the numerical model response for each damaged case.

Damaged case	Damping coefficient	Amplitude coefficient
P_1	4.5	1
P_2	2.5	0.64
P_3	3	0.55

the second bending mode is symmetrical around midspan, in absolute value, the computed results should also be symmetrical around midspan.

The second observation corresponds to the indicator curves being different for each damaged case. Indeed, each reference and damaged scenario was repeated three times. It is evident that for all indicators, the obtained results are similar, meaning that each test of each scenario has the same conclusion. The only slight discrepancy, appearing between each test, is located where the indicator is small, especially for damaged cases P_2 and P_3.

The third observation that can be made is that all the indicators tend to be at their maximum where the magnet is located (red line), which confirms the suitability of the methodology proposed in this thesis. Moreover, the sizes of the regions where the indicators are maximum vary according to the damaged case. It can be seen that when the magnet is located at point P_3, the sizes of the two regions are quite small. These two regions are located, as expected, where the magnet is getting close to the antinode of the second bending mode. When the magnet is located at P_1, three regions emerge: two near the supports and one at midspan. Indeed, in the damaged case P_1, the virtual damage is so small that the method is able to find that the magnet is located where the modal amplitude is small. The modification of the structure response amplitude is slightly affected when the magnet is near the supports or at midspan because the amplitude of the second bending mode at midspan is null. When the magnet is at P_2, two large regions surrounded by two peaks can be seen. However, these regions are smaller for the proposed method, meaning that it can detect the damaged case P_2 more easily compared to the methods based on distances. In addition, these peaks are narrow, meaning that they represent a good starting point for investigations, for instance visually to confirm occurrence of damage. Indeed, the probability of encountering the damage at the peak locations is the highest even if the indicator between these peaks tends to be closer to the maximum value of the peaks, except for the proposed method, compared to the damaged cases P_1 and P_3.

It is also important to have a look at where the indicator values are small compared to the maximum values. Indeed, even if the damage cannot be restricted to narrow areas, the fact of discarding regions of the studied structure matters as it reduces the time needed for investigations and improves the quality of the

investigation in the necessary regions. If we have a better look at the indicators graphs for P_2 and P_3, it is clear that the damage has a very low probability of being close to the supports.

Finally, in order to improve the results, especially when the magnet is at point P_2, other modes could be used. This allows to combine the information coming from various modes and restricts the search zone to overlapping areas where the damage has a high probability of being found. Moreover, instead of focusing only on bending modes, torsional modes could also be taken into account if a 3-dimensional model of the studied structure is created. In addition, each indicator has shown a great capability of localising the damage, which offers greater confidence in the proposed methodology thanks to the complementarity of the results.

4.5 Conclusion

In this chapter, the proposed methodology, described in Chapter 3, has been applied to detect and localise damage in a simple structure. The experimental setup parameters were introduced and a numerical model was then created and updated based on these parameters. Damage detection was assessed by processing the velocity signals from the experiment. The proposed statistical test was used and compared to well-known 2-sample tests for each damaged case generated by adding a magnet at three different places on the structure. The results obtained for each test were similar. This indicates that damage detection was feasible, even when the relative difference on natural frequencies was as small as 0.15%, and a difference between the reference case and each damaged case was observed, resulting in an increase of distances and a decrease of α-values. Besides, in this Chapter, the "rule-of-the-diagonal" has been proposed and used. With this rule, damage detection becomes straightforward with the proposed methodology. If the ECDF of α-values is located above the main diagonal, damage is detected.

In addition, a digital twin model was used to perform damage localisation. The magnet has been virtually placed at each node of the digital twin model. The chosen indicator was the average of distances or α-values and it yielded good results. Indeed, for each damaged case, the indicator's maximum value was found near the magnet's exact location. Furthermore, the indicator demonstrated that certain regions on the steel strip have a low probability of damage, where the minimum value was computed. This can help to highlight areas where investigations should take place to visually confirm the damage.

Chapter 5

Large-scale outdoor test

This chapter is dedicated to the early detection of a small damage in a large-scale outdoor specimen, based on the proposed methodology. In a series of tests, deliberate damage is progressively created in a prestressed concrete beam by cutting tendons one-by-one. This bridge concrete beam is also submitted to uncontrolled environmental effects, like temperature variations and humidity. Firstly, the experimental setup is described. Secondly, the modal identification of the beam in the reference state is performed and the vertical mode shapes are identified. Then, the damaged scenarios are illustrated and the proposed method is used to identify occurrence of damage based on measured accelerations under repeatable broadband excitation with a shaker. The results obtained in some selected scenarios are compared for the proposed statistical test and 2-sample tests. Moreover, a comparison with the results after temperature compensation is also discussed. The last section focuses on the influence of a train that passes near the experimental setup, which adds significant noise to the measured accelerations.

5.1 Experimental setup

5.1.1 Overview of the experimental campaign

The experimental setup is made of a prestressed concrete beam extracted from the dismantled bridge of Mersch (Luxembourg). This bridge was put into operation in 1957. Due to safety issues, it was demolished in 2016. One bridge beam has been brought to the University campus Belval in Esch-Sur-Alzette in Luxembourg. The University of Luxembourg has already studied this specimen in previous research programs [110, 131, 132], as a continuous effort to build knowledge about SHM [133]. Our involvement in this project has been made possible thanks to a cross university research project supported by the FNR (Luxembourg) and FNRS (Belgium).

Figure 5.1 shows a satellite view of the experimental setup. The laboratory is also represented. Moreover, a railway is located near the experimental setup. Its influence on the damage identification is discussed at the end of this chapter.

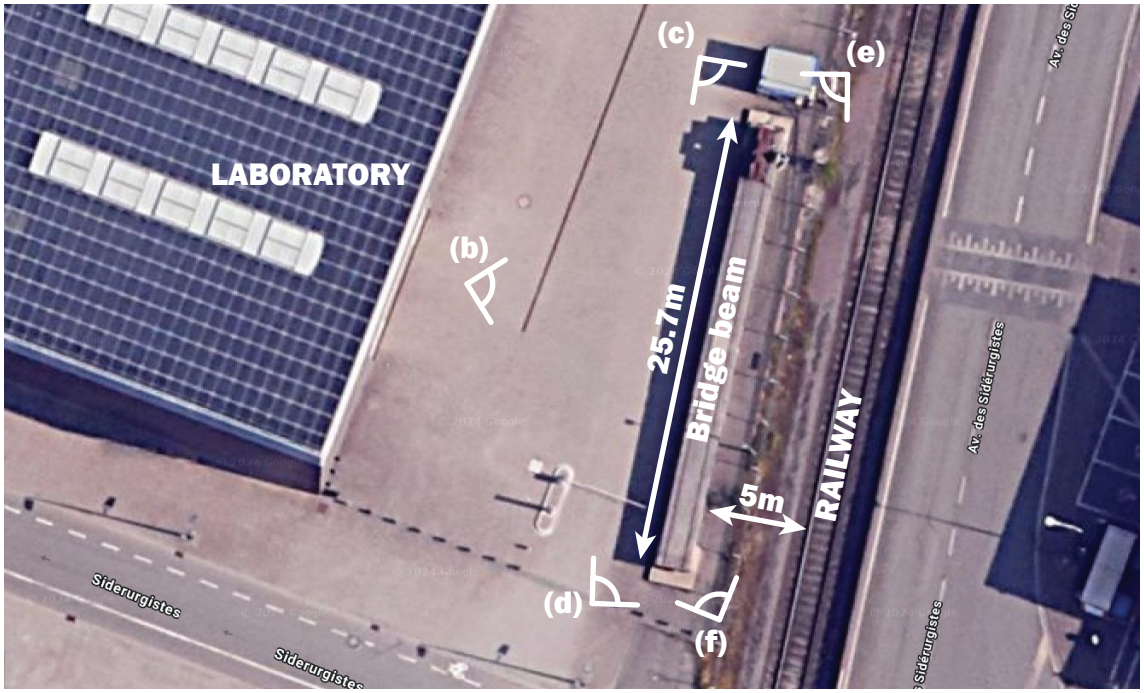

FIGURE 5.1: Satellite view (Google maps) of the experimental setup.

Different views of the beam, (b-f) from Figure 5.1, are shown in Figure 5.2. The convention *from the lab to the rails* and *from the rails to the lab*, borrows from [131], is adopted in this chapter, respectively meaning that the rails or the laboratory are behind the beam.

The experimental setup also comprises of a trolley and a shaker, which are described further in the thesis. The setup is depicted in Figure 5.3(a). Deliberate damage is progressively added by cutting tendons one-by-one, see Figure 5.3(b) and (c) for the damage region and the tendons. Figure 5.3(d) shows the portable circular saw used to cut the tendons.

Each tendon cut corresponds to a Damaged Scenario (DS). A total of four damaged scenarios have been considered. They are labelled DS1, DS2, DS3 , and DS4.

During each damaged scenario, vibration tests have been repeated 4 or 5 times. These tests consist of using the shaker to make the beam vibrate in a frequency range around one or several modes. These tests are described in Section 5.3. It has been decided to repeat the tests multiple times and over several days in order to cover various environmental conditions and for damage propagation. Indeed, once a tendon has been cut, damage may not be fully developed in the entire beam and taking into account this delay is crucial.

The total test campaign is represented on a timeline, in Figure 5.4. The total duration of the campaign was 11 months. The reference scenario was measured

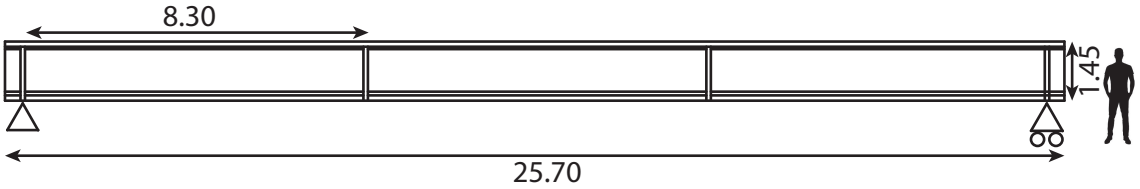

(a)

(b)

(c)

(d)

(e)

(f)

FIGURE 5.2: Pictures of the beam.

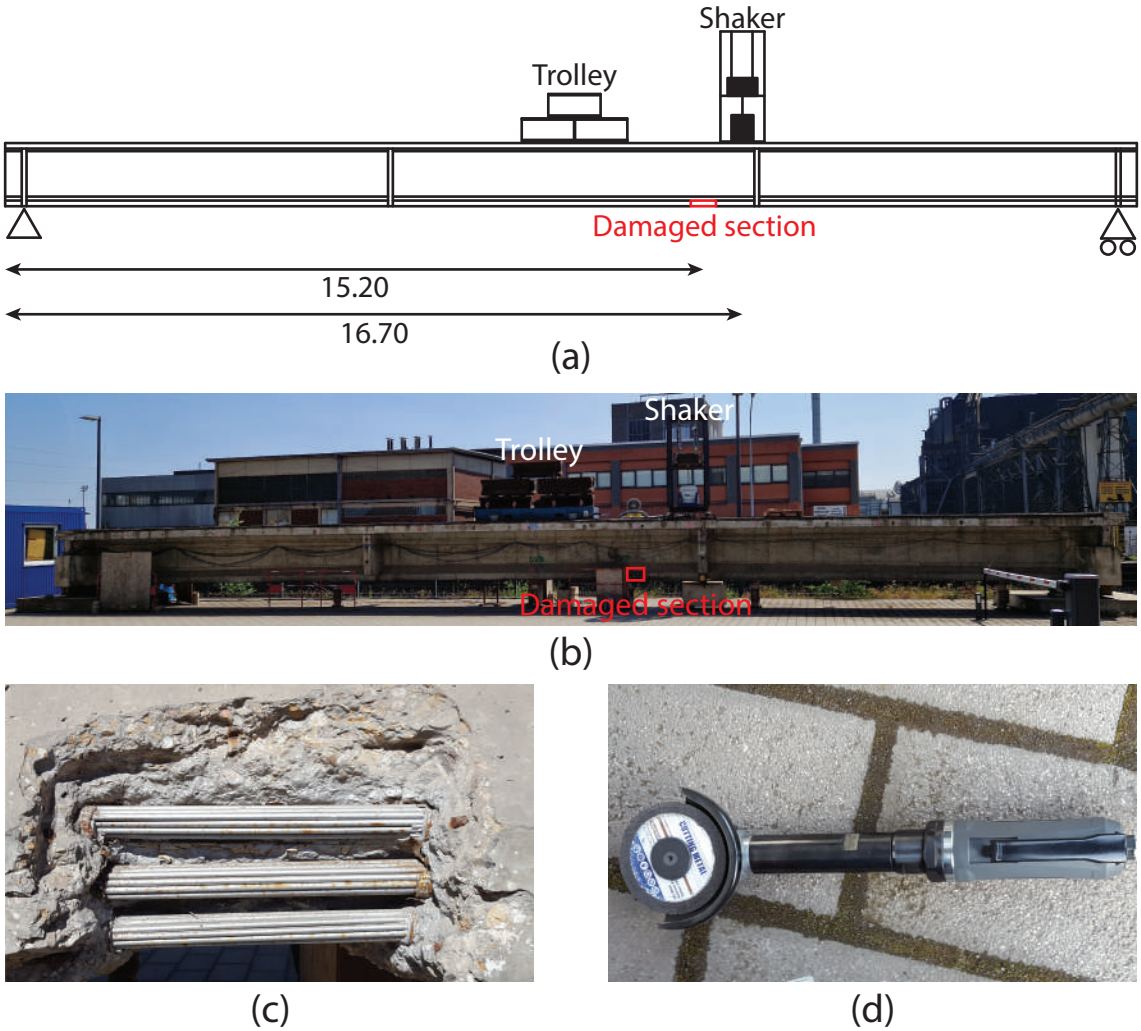

FIGURE 5.3: (a) Representation of the beam with the shaker, the trolley and the damaged section, (b) picture of the experimental setup during the tests, (c) tendons and damaged section and (d) the portable circular saw.

FIGURE 5.4: Timeline of the experimental campaign.

on July 21st 2022. Then, the first tendon was cut 2 months later in September 13th. The waiting time between two test days is usually around 1 to 2 weeks. On November 8th, the second tendon was cut. After DS2-2, a break of 2 months occurred. The accelerometers are sensitive to humidity and during these two months, the negative temperatures can have a significant impact on the measurements. Indeed, the humidity inside the cracks on the beam surface may be frozen and expelled during vibration tests. To avoid this phenomenon, it was decided to wait until temperatures came back above 0 Celcius degrees. Therefore, on February 2nd, tests recommenced with DS2-3 and DS2-4. On February 24th, the third tendon was cut. Due to bad weather conditions, DS3-2 was postponed until March 16th. The fourth tendon was cut on May 16th. The last test day was on June 16th for DS4-3 and DS4-4.

5.1.2 Prestressed concrete bridge beam

The total bridge beam length is 25.7 m. The width and the height are 1.90 m and 1.45 m respectively, see Figure 5.2. The total weight of the beam is around 34 t. The beam is supported by a fixed bearing and a movable bearing. Each bearing is made, from bottom to top, of a thick steel plate, a circular rod, a H-beam 200 and a thick steel plate [131]. The circular rod of the fixed bearing was welded to the lower steel plate to prevent it from rolling.

The cross section of the beam is varying linearly from the edges to its center. In Figure 5.5, two beam sections are shown. In Figure 5.5(a), the section of the beam near the edge is represented while in Figure 5.5(b), the section of the beam at midspan is shown. It can be observed that the section becomes thinner towards the center, reducing the web area of the beam at midspan.

The prestressing of the beam was done by using 8 tendons. A tendon is made of 12 round bars of 7 mm. During the construction phase, these tendons were prestressed and grounted to the beam by using mortar. The role of this mortar is to allow a good force transfer between the tendons and the concrete beam and to protect the tendons from corrosion.

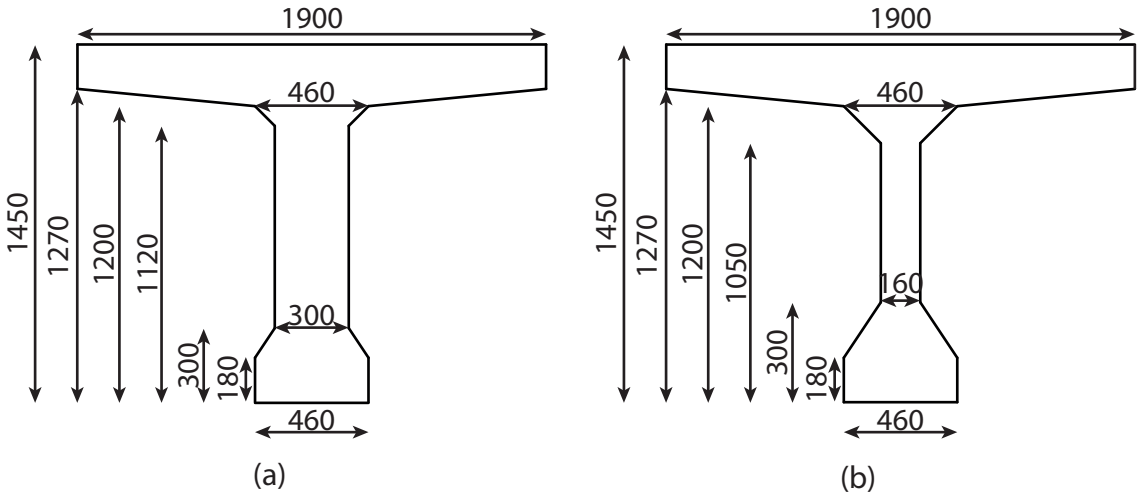

FIGURE 5.5: Cross section of the beam (a) near the edge and (b) at midspan. Units: mm.

Above the beam, a thin layer of asphalt is still present. The thickness of this asphalt layer is around 7.5 cm on the whole beam.

A more comprehensive description of the beam is given in [131] from which relevant information was extracted here.

5.1.3 Trolley and shaker

The shaker, used during the dynamic tests, was designed by the University of Luxembourg. It is made of an eletrodynamic shaker TIRAvib (TV50350/LS120), a mass of 500 kg, four springs and a steel frame (1.0 m x 1.2 m x 2.5 m). The total weight of the shaker is around 1.2 t. Additional information about the shaker system can be found in [134, 135]. In Figure 5.6, the shaker is shown. The eletrodynamic shaker moves the mass, attached to the steel frame by 4 springs. This shaker is used for modal identification and damage detection.

On the bridge beam, a trolley, which acts as dead load, was added to the experimental setup as it can be seen in Figure 5.7. This trolley carries 9 HEB1000 beams. The total weight of the trolley is approximately 8.8 t and its length is equal to 3 m. The trolley is also equipped with wheels in order to move on the top of the beam from one side to the other. When the shaker is on the beam, it obstructs the passage and prevents the trolley to move accross the entire beam.

FIGURE 5.6: Picture of shaker on the beam.

FIGURE 5.7: Pictures of the trolley.

5.1.4 Accelerometers and temperature sensors

Accelerometers were installed on the beam before each test. As they are sensitive to humidity, they were always dismounted after the tests. Machined grub screws were glued into the concrete beam to facilitate this task and conserve the exact accelerometers location.

A total of 23 PCB PIEZOTRONICS model 393B04 accelerometers were used: accelerometers number 1 to 20 are positioned vertically while accelerometers from 21 to 23 are placed horizontally, see Figure 5.8. The accelerometer number 10, which was fixed to the bottom face of the top flange of the beam, was vertically located under the shaker, which was on the top flange, while the accelerometer number 20 was put under the bottom flange of the beam, close to the damaged section. A sketch, representing the accelerometer locations, is depicted in Figure 5.8. The accelerometer locations are the same for the modal identification and the damage detection.

Temperatures were measured using seven PT100 sensors. Four sensors (T1 - T4) were placed inside a 100-millimeter hole, which was then closed with glue, to measure the temperatures of the concrete beam as well as another sensor T5, which was mounted inside the top of the beam to measure the temperature of the asphalt. Two other sensors were used to measure the ambient air temperature. They were placed on top of the container next to the beam and protected from direct sunlight by using a bright cover right above them. The temperature sensor locations are shown in Figure 5.9.

In addition to accelerometers and temperature sensors, displacement transducers and laser-based measurement system were also present on the experimental setup. Further information can be found in Chapter 3 in [131]. This equipment is not used in this thesis as it provides static measurements. These measurements will be used in a forthcoming PhD thesis that was developed at the University of Luxembourg in parallel with this work [136].

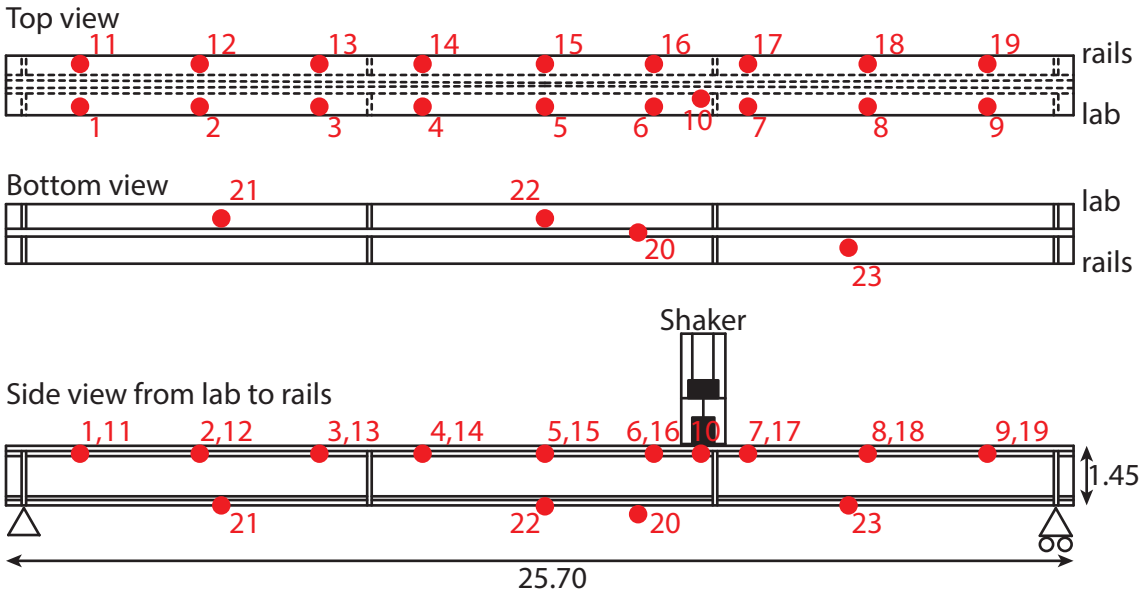

FIGURE 5.8: Accelerometers location on the bridge beam.

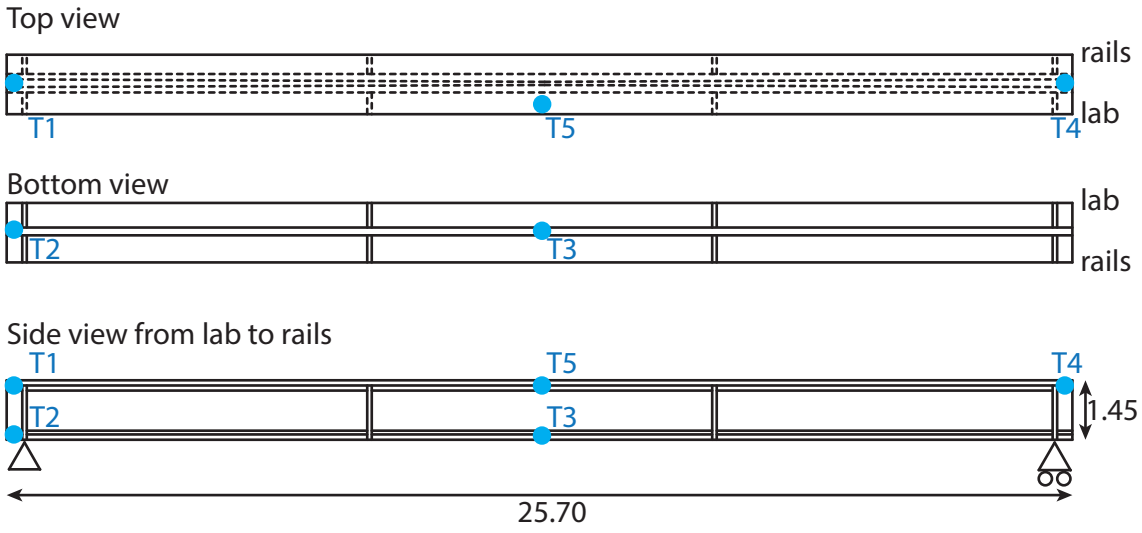

FIGURE 5.9: Temperature sensor locations inside the bridge beam.

5.2 Modal identification in the reference state

The modal identification of the beam in the reference state, when the trolley is at midspan and with the shaker on the beam, see Figure 5.3(a), has been performed. A band-limited white noise, whose frequency content is located between 2 and 25 Hz and whose RMS is equal to 137 N, has been used to measure the accelerations of the beam. Then, the SSI-COV algorithm, with a selected time window equal to 3 seconds for the covariance matrix, was used to identify a total of 4 mode shapes with vertical components in this frequency range: the first 2 bending and torsion modes. These modes are shown in Figure 5.10. For a better representation of the vertical modes, only the accelerometers [1-9, 11-19] have been used. Table 5.1 shows the natural frequencies and damping ratios of the 4 vertical modes.

In Figure 5.11, the trace of the PSD matrix of all accelerometers is shown. Five distinct peaks can be observed. The first bending and torsion modes and the second bending and torsion modes correspond respectively to peaks number 1, 2, 4 and 5. The peak number 3 has been identified as the 1st horizontal mode but it is not illustrated due to the lack of horizontal accelerometers. The natural frequencies of the 4 vertical modes are reported in Table 5.1. On the stabilisation diagram, a model order of n = 30 has been selected. For this model order, all vertical modes were stabilised in frequency and in damping.

TABLE 5.1: Identified natural frequencies and damping ratios of 4 bending and torsional modes in the frequency range [2; 25] Hz, in the reference state.

	Natural frequency [Hz]	Damping ratio [-]
First bending mode	3.93	0.0418
First torsion mode	6.99	0.0251
Second bending mode	17.72	0.0278
Second torsion mode	20.05	0.0224

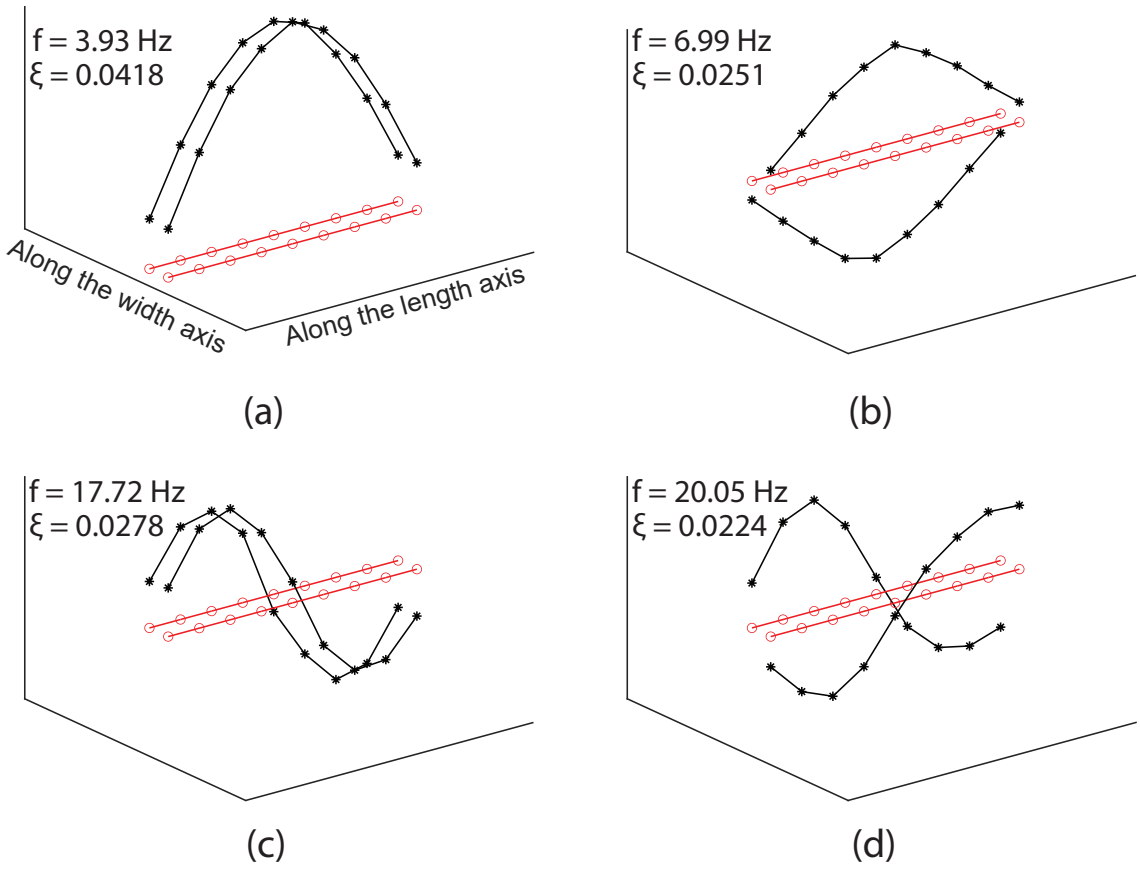

FIGURE 5.10: (a) First bending mode and (b) torsion mode, (c) second bending mode and (d) torsion mode.

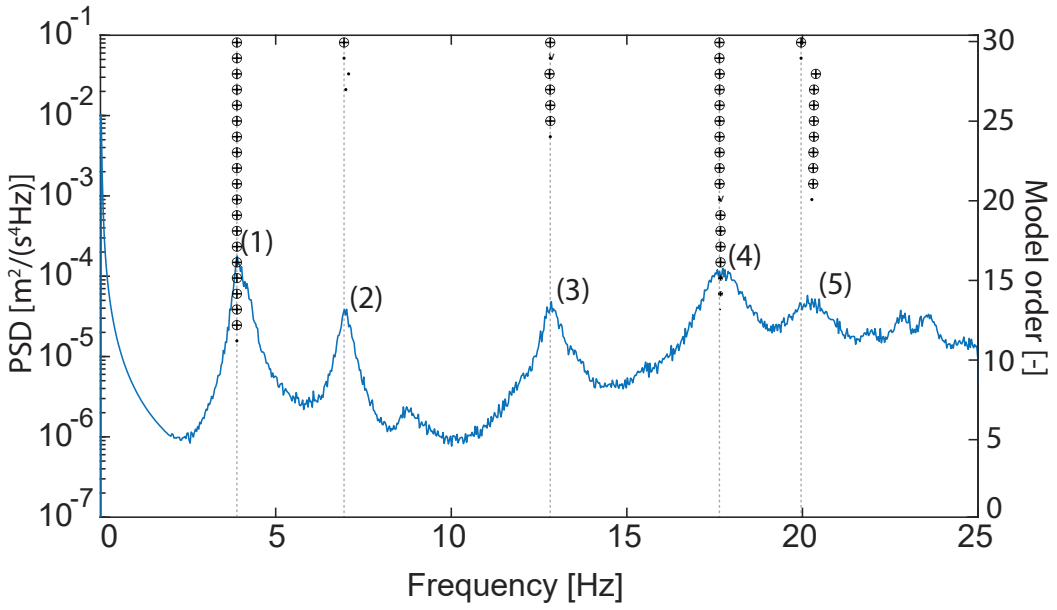

FIGURE 5.11: Trace of the PSD matrix of all accelerometers (vertical and horizontal) and stabilisation diagram.

5.3 Damaged scenarios

To apply damage to the structure, it was decided to cut tendons at one section of the beam, see Figure 5.3.

Four different damaged scenarios were considered. In each damaged scenario, a new tendon was cut except for DS4, for which half a tendon was cut as shown in Figure 5.12. In Figure 5.13, it can be observed that the concrete was still partially surrounding the back of the tendon number 4. Therefore, it was not possible to fully cut this tendon.

Figure 5.14 shows pictures of the tendons cut process. Before each tendon cut, strain gauges were installed on 3 bars of the tendon to quantify the prestressing force that was in the tendons before cutting [136].

The objective of this experiment is to detect small damage for which no surface change of the structure can be observed. This is why it was decided to cut tendons until first cracks appeared and propagated along the beam surface. This happened in DS3 on both side of the beam as shown in Figure 5.15(a-c). In DS4, the crack elongated and widened even more. It was clear that, at this stage, a damage occurred on the beam by performing a visual inspection only. Hence, DS4 was the last damaged scenario of this experimental campaign.

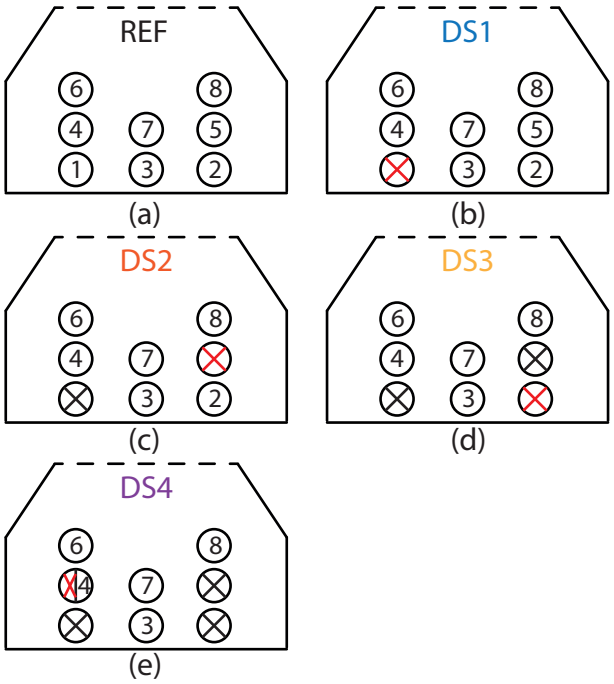

FIGURE 5.12: Damaged scenarios: (a) reference state, damaged states (b) 1, (c) 2, (d) 3, and (e) 4.

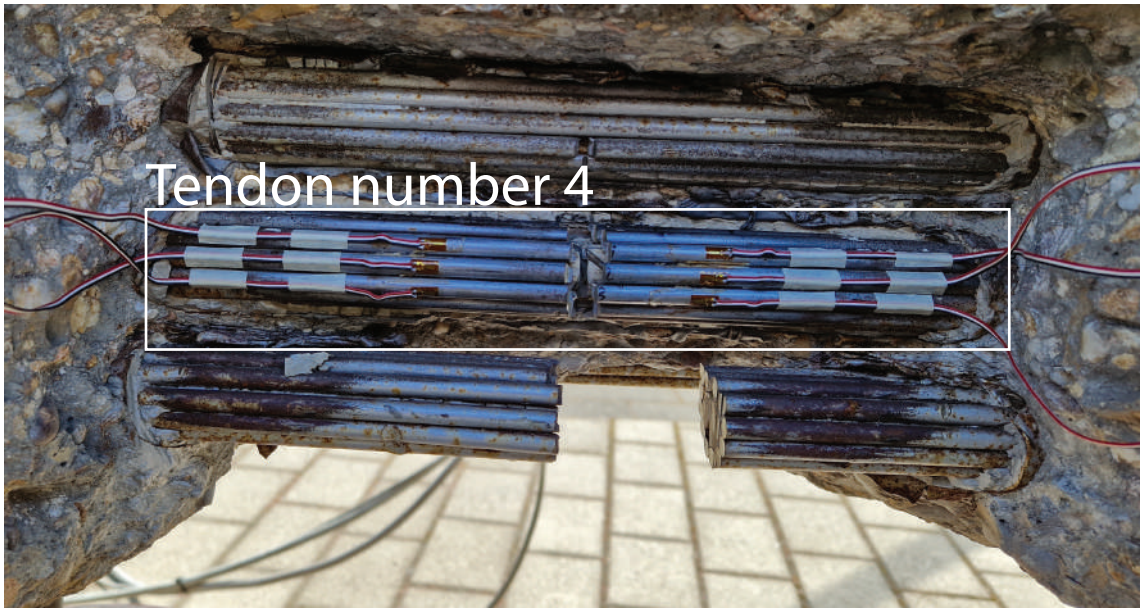

FIGURE 5.13: Damaged scenario 4 with tendon number 4 half cut.

In Table 5.2, the test dates are reported as well as the dates on which the tendons were cut and the weather during the tests. In each damaged scenario, the tests were repeated 4 times on 3 different dates. The first crack was expected to appear between DS3 and DS4. Therefore, two additional tests were added right before cutting the third and fourth tendons, corresponding to DS2-5 and DS3-5.

A test scenario, which is made of 3 different tests, is repeated 4 or 5 times for each damaged scenario. For each test, the accelerations of the beam are measured by injecting a band-limited white noise by the shaker in the beam . The frequency range of the PSDs of these band-limited white noises was selected carefully to isolate one or various modes.

- Test A: Frequency range = $[3.6; 4.6]$ Hz. The first bending mode is the only mode inside this frequency range.
- Test B: Frequency range = $[3.6; 7.5]$ Hz. In this frequency range, the first bending and torsion modes are located.
- Test C: Frequency range = $[2; 25]$ Hz. Various modes are inside this frequency range whose the first and second bending and torsion modes.

The PSD of each band-limited white noise is shown in Figure 5.16. The Root Mean Squares (RMSs) of each noise, from Test A to Test C, are equal to 172.97, 164.41, and 136.83 N respectively.

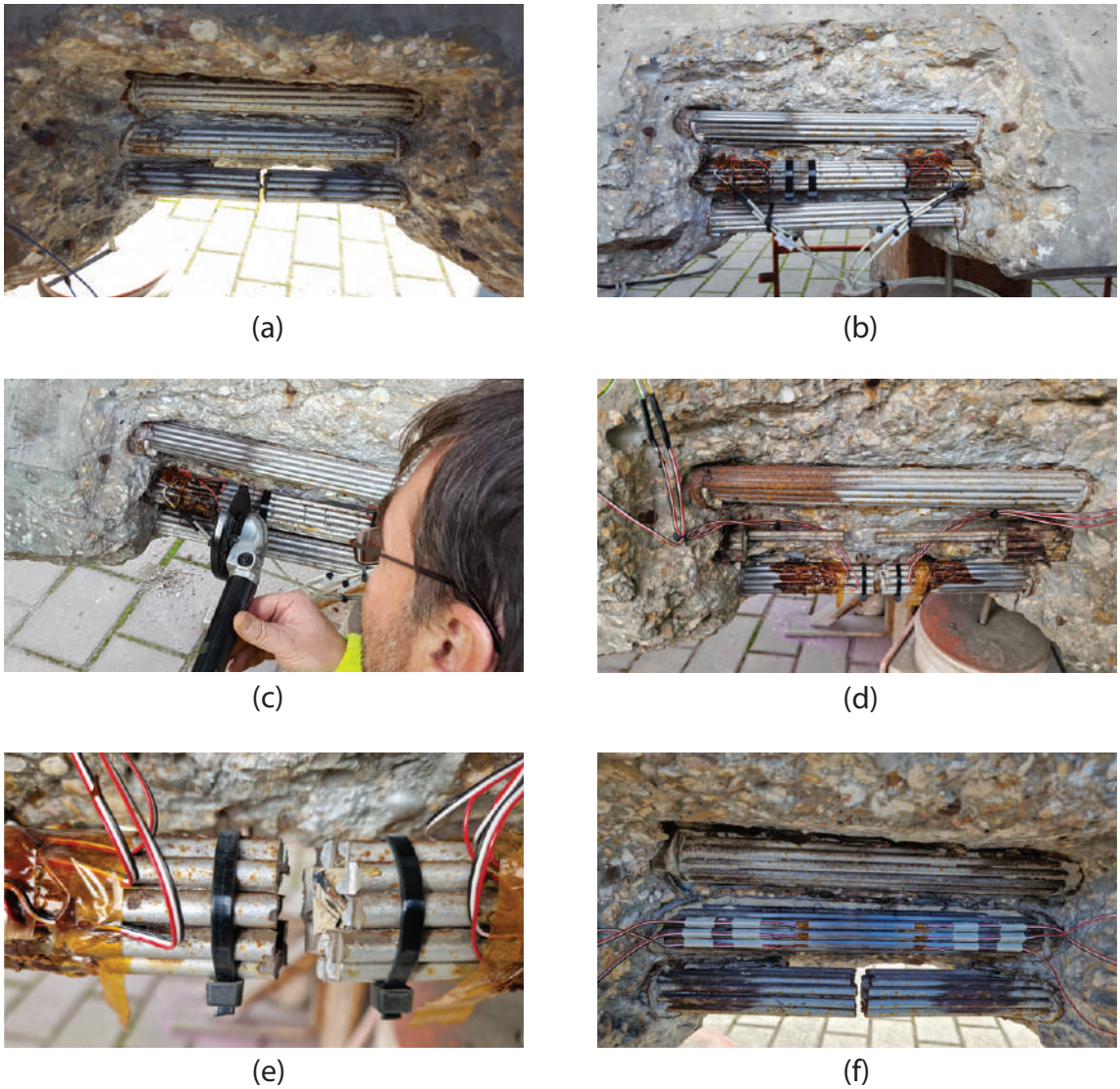

FIGURE 5.14: (a) Tendon number 1 is cut in DS1, (b) strain gauges on tendon number 5 in DS2, (c) tendon number 5 is being cut in DS2, (d) tendon number 2 is cut in DS3, (e) zoom on tendon number 2 in DS3, and (f) strain gauges on tendon number 4 in DS4.

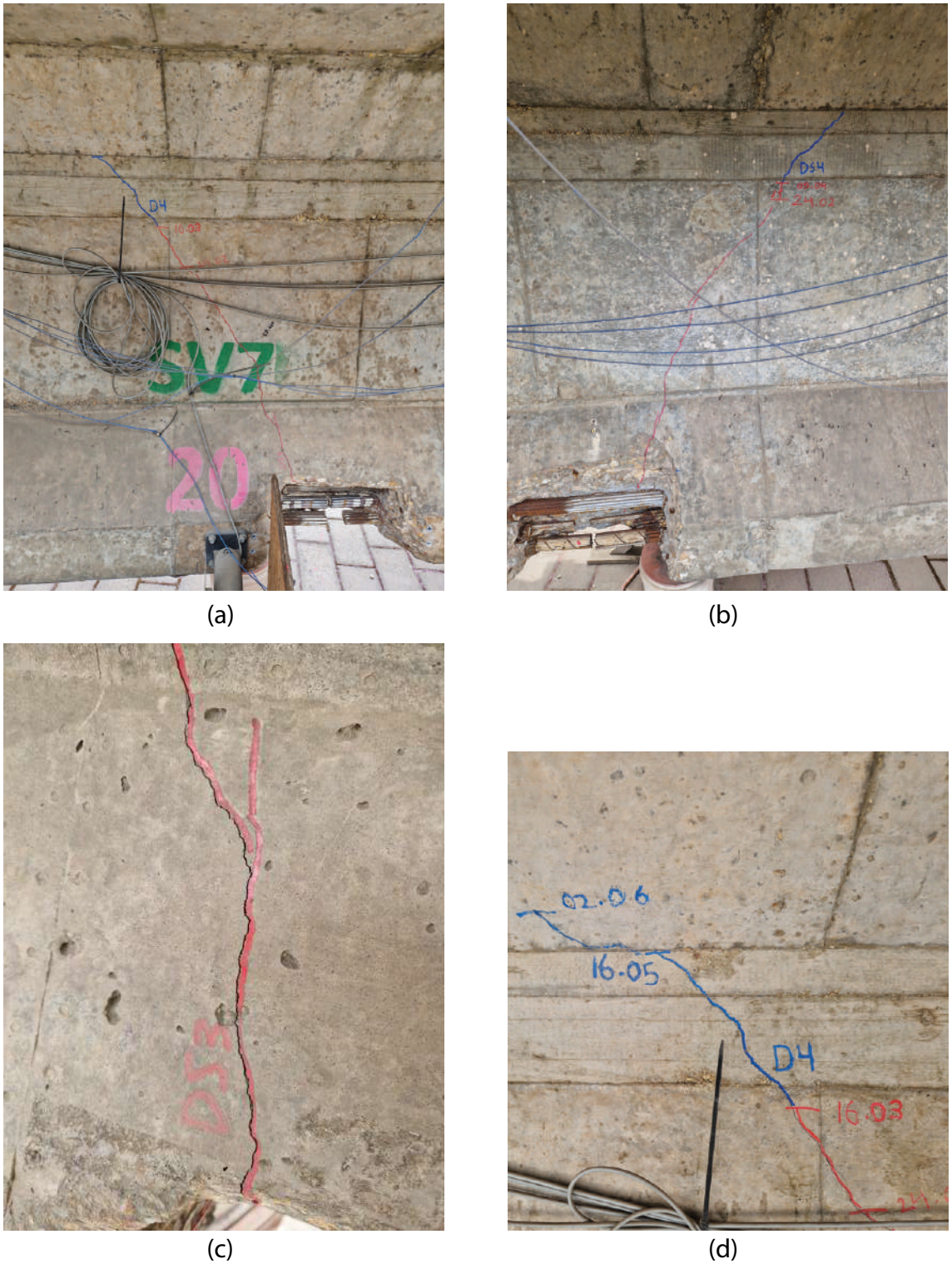

FIGURE 5.15: Cracks on the beam (a) from lab to rails and (b) from rails to lab, zoom on the crack that appeared (c) in DS3, and (d) in DS4.

TABLE 5.2: Overview of the tests and tendons cut.

Dates	Tests	Weather
21/07/2022	Reference: Healthy state	Cloudy
13/09/2022	Cut of the first tendon	/
30/09/2022	DS1-1	Sunny
06/10/2022	DS1-2	Sunny
19/10/2022	DS1-3 and DS1-4	Foggy
08/11/2022	Cut of the second tendon	/
18/11/2022	DS2-1	Cloudy and light rain
01/12/2022	DS2-2	Cloudy
02/02/2023	DS2-3 and DS2-4	Cloudy
24/02/2023	DS2-5 Cut of the third tendon DS3-1	Cloudy / Cloudy and partially sunny
16/03/2023	DS3-2	Sunny
05/04/2023	DS3-3 and DS3-4	Sunny
16/05/2023	DS3-5 Cut of the fourth tendon DS4-1	Partially sunny / Sunny
02/06/2023	DS4-2	Sunny
16/06/2023	DS4-3 and DS4-4	Sunny

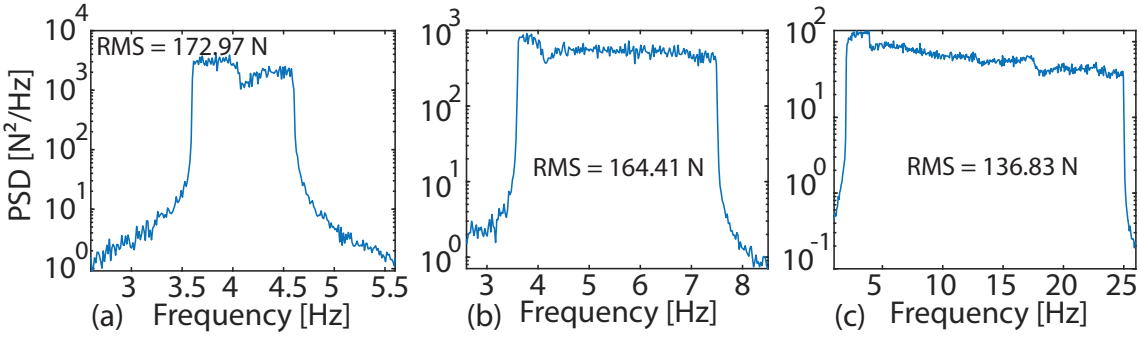

FIGURE 5.16: PSDs of the band-limited white noise for (a) Test A, (b) Test B, and (c) Test C.

Out of the 23 accelerometers placed on the structure, only 6 have been selected for damage detection. They correspond to the accelerometers with the highest RMS value. The highest RMS value means that the signal intensity is the highest and by assuming that the noise level remains the same for all accelerometers, therefore, selecting the accelerometers with the highest RMS value results in analysing the data with the lowest noise to signal ratio. Based on this criterion, accelerometers 4-5-6 and 14-15-16 were selected. These accelerometers are the closest to midspan of the beam, see Figure 5.8.

5.4 Damage Identification

In this section, the proposed method is illustrated to identify damage occurrence. Test A and Test B have been taken into account for some selected scenarios. The results are also compared with and without temperature compensation. Then, nonlinear behaviour is discussed in the light of the force amplitude. Finally, due to the proximity of the railway close to the experimental setup, the influence of train passage is assessed.

5.4.1 Without temperature compensation

Test A: First bending mode

Damage detection is illustrated with selected scenarios: DS1-3, DS1-4, DS2-2, DS3-4, and DS4-2.

In Figure 5.17, the acceleration of the accelerometer 5 and its PDF in the reference scenario are represented. It exhibits the typical features of a narrowband Gaussian process.

Figure 5.18 shows the PSDs of the acceleration for the first bending mode and for accelerometer number 5. This accelerometer was selected because its RMS value is the highest. Moreover, the shape of the PSDs of the acceleration for the same scenario is similar for all accelerometers.

It can be observed that the PSDs of the acceleration for the damaged scenarios are shifted compared with the the PSD of the acceleration for the reference scenario. This shift hints a change of the frequency content of the beam. This change of frequency content can be possibly linked with a potential damage that occurred on the beam.

Using a peak picking method, the natural frequency of the first bending mode for each selected scenario is reported in Table 5.3. The relative change on natural frequencies Δ is given as

$$\Delta = \frac{f_{\text{damaged}} - f_{\text{reference}}}{f_{\text{reference}}}.$$

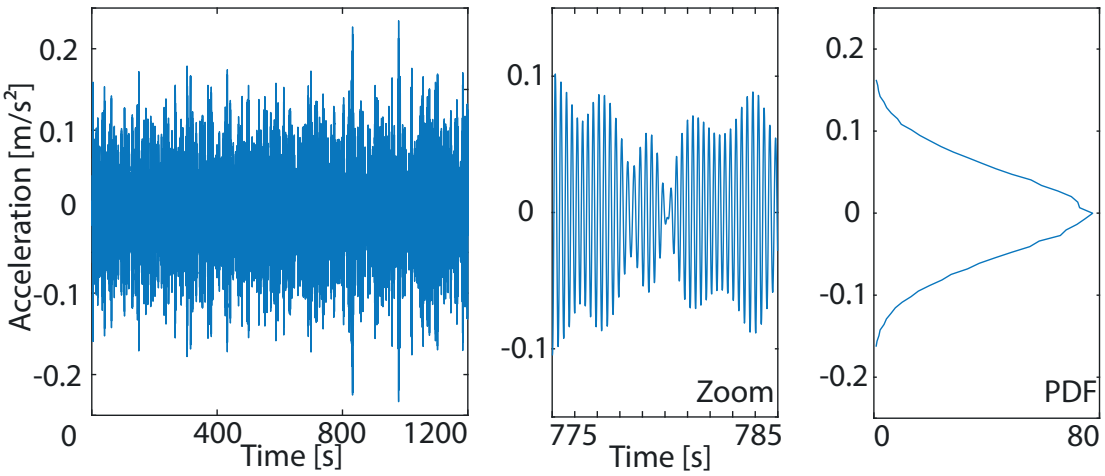

FIGURE 5.17: Acceleration from accelerometer 5 in the reference scenario, zoom on a small time window, and PDF of the acceleration.

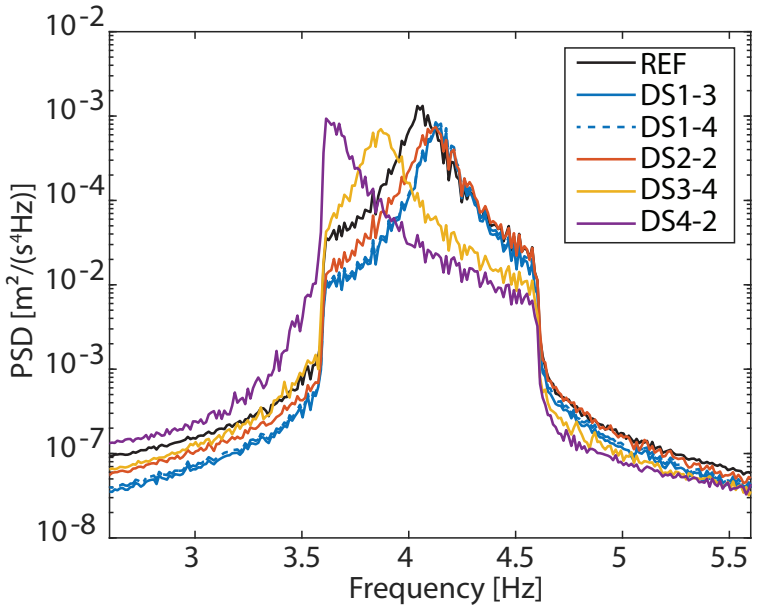

FIGURE 5.18: PSDs of the acceleration of accelerometer 5 for the reference state, DS1-3, DS1-4, DS2-2, DS3-4, and DS4-2 for Test A.

TABLE 5.3: Natural frequency of the first bending mode for the reference state, DS1-3, DS1-4, DS2-2, DS3-4, and DS4-2.

States	Frequency	Δ[%]
REF	4.08	0
DS1-3	4.14	1.47
DS1-4	4.14	1.47
DS2-2	4.12	0.98
DS3-4	3.87	-5.15
DS4-2	(< 3.6)	/

The natural frequency computed with the peak picking method for DS4-2 may be even lower. Indeed, in Figure 5.18, the peak of the PSD of the acceleration for this damaged scenario hits $f_{\min} = 3.6\,\text{Hz}$. It results in an estimation of the natural frequency as the maximum value of the peak could have been located below 3.6 Hz.

In addition, it can be observed that the PSDs of the acceleration for DS1-3 and DS1-4 are very similar. Indeed, as reported in Table 5.2, during these tests, the weather was foggy with nearly no temperature variation observed during the day as well as no temperature gradient on the beam.

Another observation that can be made is that the relative change on natural frequencies Δ is smaller for DS2-2 than for DS1-3 and DS1-4, which was expected to be the opposite as the damage has increased between DS1 and DS2.

Therefore, it results that relying on the natural frequencies for damage detection is not satisfactory in this case. Use of temperature compensation is discussed later.

Before and without any temperature compensation, the proposed method, described in Chapter 3 is applied to the same selected damaged scenarios. The accelerations provided by accelerometers 4-5-6 and 14-15-16 are pre-processed and then sent to the FPT algorithm.

The ECDFs of FPT for each combination of (X_0, X_f) between the healthy state and each damaged state are then compared. Some ECDFs of FPT for the reference state and DS2-2 are shown in Figure 5.19. They correspond to various combinations (X_0, X_f) of the FPT maps, localised with the red square in the pictograms. The ECDFs of FPT between these two states do not coincide except in the bottom left corner. Moreover, a tendency is represented: when $X_0 < X_f$, above the main diagonal of the map (a,b,d), the ECDFs of FPT for DS2-2 are on the right of those for the reference state, resulting in greater FPTs on average for DS2-2. This means that, in damaged state DS2-2, when X_0 is crossed, it takes more time to reach a higher level X_f on average.

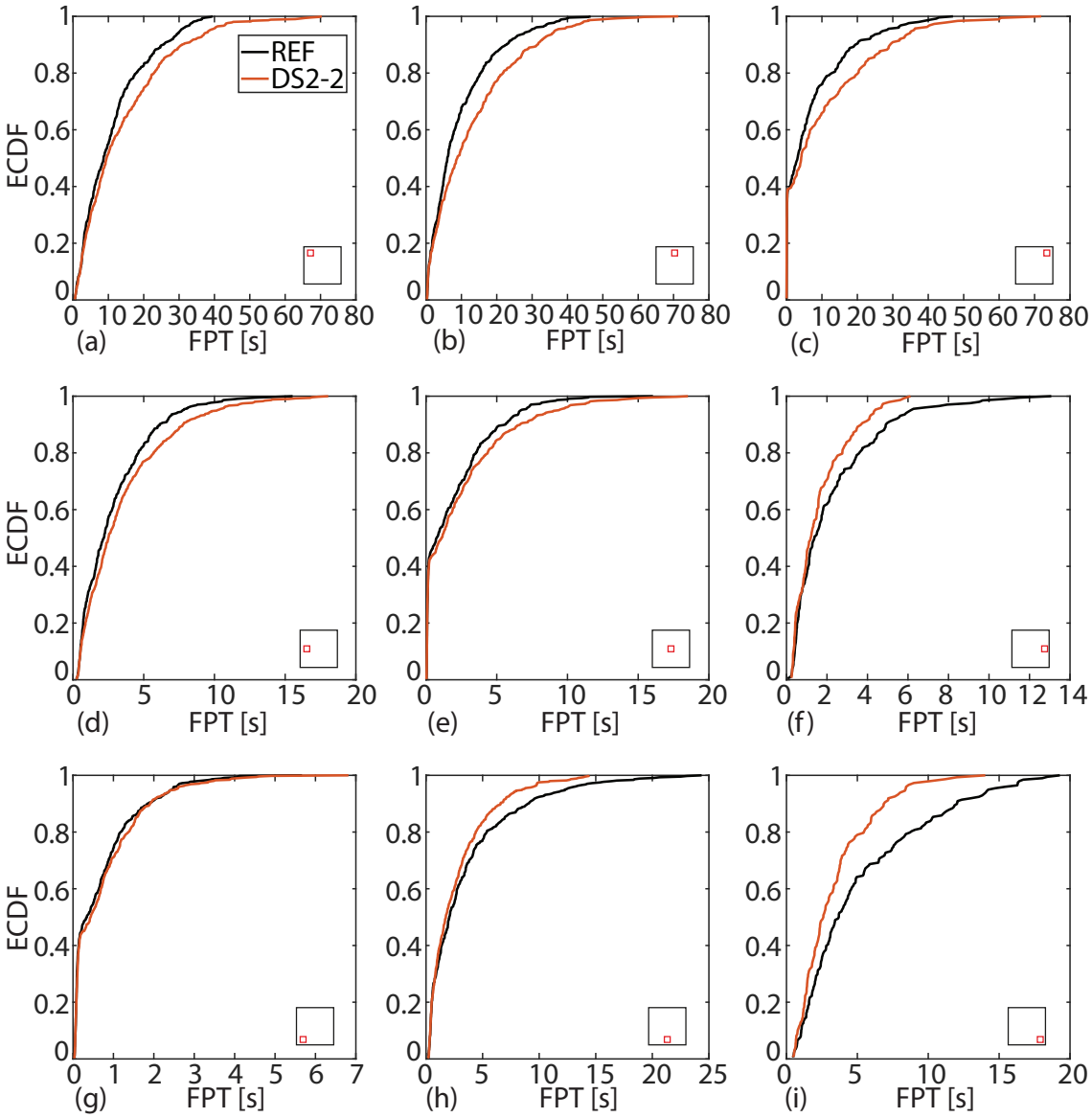

FIGURE 5.19: ECDFs of FPT for the envelope of the acceleration of accelerometer 5 for various values of (X_0, X_f): (a) $(0.0034, 0.0107)$, (b) $(0.0068, 0.0107)$, (c) $(0.0102, 0.0107)$, (d) $(0.0034, 0.0073)$, (e) $(0.0068, 0.0073)$, (f) $(0.0107, 0.0073)$, (g) $(0.0034, 0.0039)$, (h) $(0.0068, 0.0039)$, (i) $(0.0107, 0.0039)$.

This tendency is inverted when $X_0 > X_f$, under the main diagonal of the map (f,h,i). The FPTs are smaller on average for DS2-2.

These discrepancies between the ECDFs of FPT are essential for damage detection, as already mentioned. Each selected damaged state is compared with the reference state in the following for the proposed statistical test as well as for the KS and WAD tests. The ECDFs of α-values and distances for these 3 tests are shown in Figures 5.20, 5.21 and 5.22 respectively.

The averages of α-values and distances are reported for each accelerometer in each damaged state in Tables 5.4, 5.5 and 5.6 for the proposed test and for the KS and WAD tests respectively. The KS and WAD tests have been selected because they are the simpliest, for the KS test, and the most sophisticated, for the WAD test, of the 2-sample tests. Moreover, they show the same tendency as the other 2-sample tests. Therefore, the AD, CVM, K and W tests are shown in Appendix C to avoid redundancy.

The first observation concerns DS1-3 and DS1-4. In these damaged scenarios, the ECDFs of α-values and distances coincide almost perfectly for each test. Indeed, as reported in Table 5.2, the weather was foggy, limiting the effects of temperatures on the results. Therefore, this shows that, under the same environmental conditions, the tests between identical scenarios, in this case DS1, are repeatable.

Secondly, the ECDFs of α-values and distances distinctively highlight damage but also rank damaged scenarios in the right order, except for accelerometers 15 and 16 for DS3-4 and DS4-2. Therefore, the damage detection is always successful but the order of damaged scenarios depends on the choice of accelerometers. In addition, the observed differences revealed by the method based on FPTs are capable of a better discrimination than a method based on relative changes of natural frequencies obtained for each accelerometer.

Finally, in Figures 5.21 and 5.22, it can be observed that ECDFs of distances intersect each other. The intersection points are highlighted with a pictogram. These intersections show that the KS and WAD tests lack sensitivity for damage detection in this case. The proposed statistical method, based on the sampling distribution of ECDFs of FPTs, is more consistent. Moreover, based on the "rule-of-the-diagonal" proposed in Chapter 4, regarding the position of the ECDF with the diagonal, it is seen that each selected scenario is identified as a damaged scenario because the ECDFs of α-values are located in the upper half area, above the main diagonal of the map.

Another easy way to assess damage detection with the proposed statistical test is based on the average of α-values. Indeed, if this average is greater than 0.5, meaning that the ECDF of α-values is in the lower half region of the map, then no damage is identified. However, in Table 5.4, each reported average of α-values is lower than 0.5, resulting in ECDFs of α-values that are in the upper

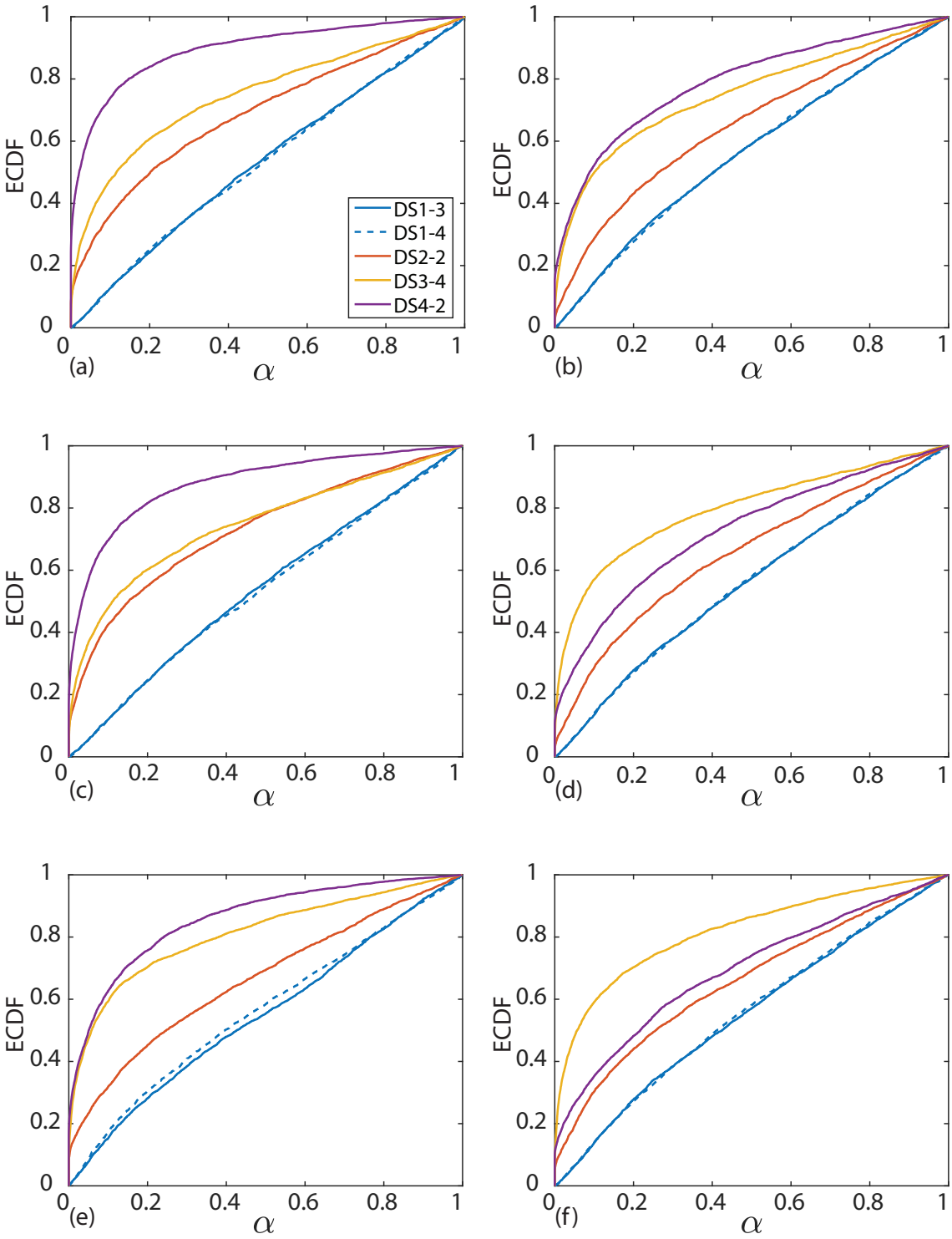

FIGURE 5.20: ECDFs of α-values for accelerometers (a) 4, (b) 14, (c) 5, (d) 15, (e) 6, and (f) 16 for Test A in DS1-3, DS1-4, DS2-2, DS3-4, and DS4-2 compared to the reference scenario. Test A.

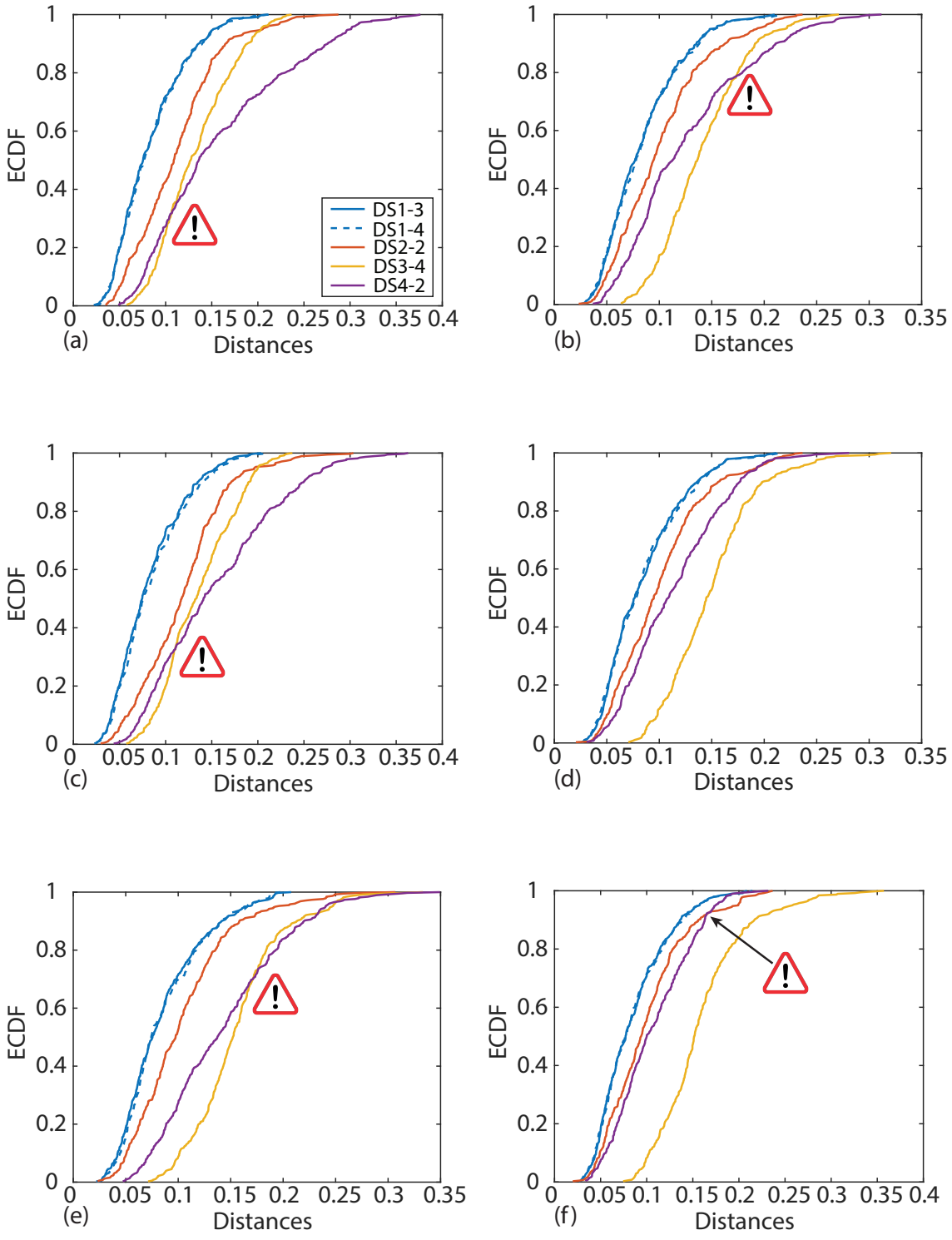

FIGURE 5.21: ECDFs of the KS distances for accelerometers (a) 4, (b) 14, (c) 5, (d) 15, (e) 6, and (f) 16 for Test A in DS1-3, DS1-4, DS2-2, DS3-4, and DS4-2 compared to the reference scenario.

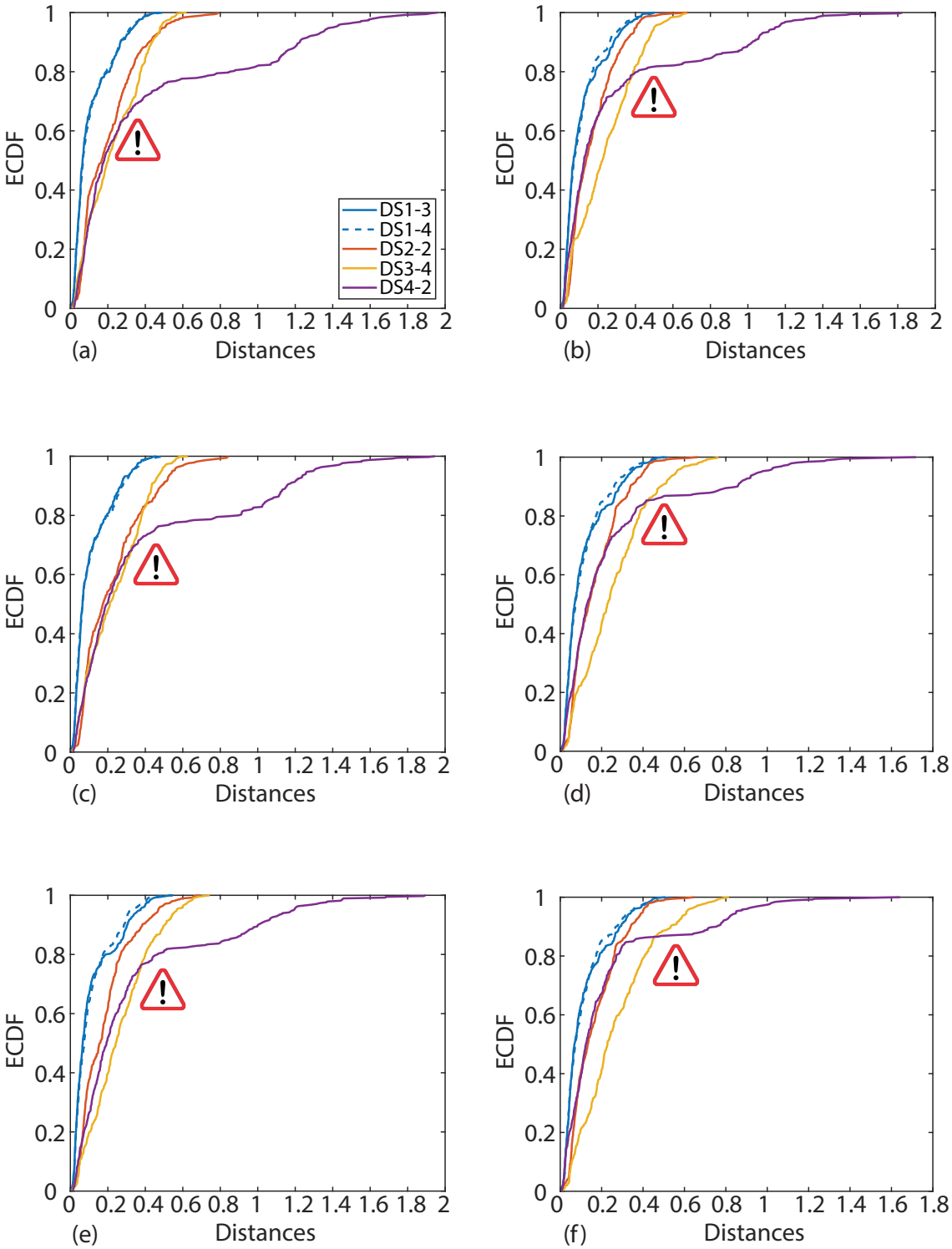

FIGURE 5.22: ECDFs of the WAD distances for accelerometers (a) 4, (b) 14, (c) 5, (d) 15, (e) 6, and (f) 16 for Test A in DS1-3, DS1-4, DS2-2, DS3-4, and DS4-2 compared to the reference scenario.

half of the map. Hence, each selected scenario is correctly identified as damaged scenario with the proposed statistical test, even DS1-3 and DS1-4 with very limited damage.

For the rest of this section, to avoid redundancy, only the ECDFs of α-values are shown. The ECDFs of the distances of the 6 other 2-sample tests are reported in Appendix C.

TABLE 5.4: Average of α-values for accelerometers 4, 5, 6, 14, 15 and 16 in DS1-3, DS1-4, DS2-2, DS3-4, and DS4-2.

	Accelerometers					
	4	5	6	14	15	16
DS1-3	0.47	0.46	0.45	0.44	0.45	0.45
DS1-4	0.47	0.47	0.44	0.44	0.45	0.44
DS2-2	0.31	0.27	0.34	0.35	0.35	0.34
DS3-4	0.25	0.25	0.19	0.25	0.20	0.18
DS4-2	0.10	0.12	0.14	0.21	0.27	0.31

TABLE 5.5: Average of KS distances for accelerometers 4, 5, 6, 14, 15 and 16 in DS1-3, DS1-4, DS2-2, DS3-4, and DS4-2.

	Accelerometers					
	4	5	6	14	15	16
DS1-3	0.08	0.08	0.08	0.08	0.08	0.08
DS1-4	0.08	0.09	0.09	0.08	0.08	0.08
DS2-2	0.11	0.12	0.10	0.10	0.10	0.10
DS3-4	0.13	0.14	0.16	0.14	0.15	0.16
DS4-2	0.16	0.15	0.14	0.13	0.11	0.11

TABLE 5.6: Average of WAD distances for accelerometers 4, 5, 6, 14, 15 and 16 in DS1-3, DS1-4, DS2-2, DS3-4, and DS4-2.

	Accelerometers					
	4	5	6	14	15	16
DS1-3	0.11	0.11	0.11	0.11	0.11	0.11
DS1-4	0.11	0.11	0.11	0.11	0.11	0.11
DS2-2	0.20	0.23	0.18	0.17	0.17	0.17
DS3-4	0.23	0.23	0.26	0.24	0.25	0.27
DS4-2	0.41	0.39	0.34	0.30	0.25	0.23

Test B: First bending and torsional modes

The selected damaged scenarios for illustrations under Test B are DS1-2, DS2-5, DS3-3 and DS4-4.

In Figure 5.23, the PSDs of the acceleration of the first bending and torsion modes are shown for the accelerometer 5.

By using the peak picking method, the natural frequencies of these two modes are reported in Table 5.7 as well as the relative change on natural frequencies Δ. Once again, it can be observed that the PSD of the acceleration in DS4-4 is affected by the minimum frequency $f_{\min} = 3.6$ Hz of the frequency range used in the Test B. Therefore, the natural frequency obtained for this damaged scenario may be lower than $f_{\min}$.

It appears that DS3-3 is the closest to the reference state because its relative change on natural frequencies Δ, for both first bending and torsion modes, is the smallest (in absolute value). A modal-based method relying on natural frequencies would erroneously conclude that DS3 is less damaged than DS2. This reinforces the fact that using only the natural frequencies is not sufficiently robust to perform damage detection.

In Figure 5.24, the ECDFs of α-values for the proposed test are shown and their average is reported in Table 5.8. The results are computed by taking into account the first bending and torsion modes together.

First, damage detection in DS1-2 for the Test B failed. Indeed, in Figure 5.24, it can be observed that all ECDFs of α-values for all accelerometers are located in the lower half of the map so that application of the "rule-of-the-diagonal" would conclude that DS1 is not damaged. This is also visible by looking at the DS1-2 row of Table 5.8: all averages of α-values are higher or really close to 0.5. However, for the other 3 damaged scenarios, a damage can be observed.

Second, for accelerometers 4-5-6, damaged scenarios are very nicely ordered. Nevertheless, DS2-5 and DS3-3 cross each other for accelerometers 15 and 16. Due to the crossing, it results in almost the same average of α-values for accelerometers 15 and 16 in DS2-5 and DS3-3, see Table 5.8.

Therefore, Test B is less conclusive than Test A. This could be related to the use of the Hilbert transform. Indeed, in Test B, the first bending and torsional modes are considered. Consequently, the proposed method works better for isolated modes, one-by-one.

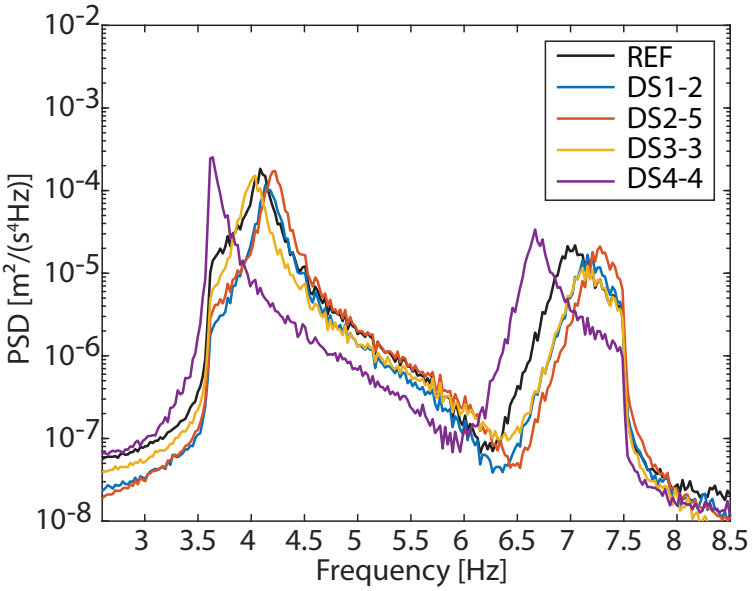

FIGURE 5.23: PSDs of the acceleration of accelerometer 5 for the reference state, DS1-2, DS2-5, DS3-3, and DS4-4 for Test B.

TABLE 5.7: Natural frequency of the first bending and torsion modes for the reference state, DS1-2, DS2-5, DS3-3, and DS4-4.

	1st bending mode		1st torsion mode	
States	Frequency	Δ[%]	Frequency	Δ[%]
REF	4.06	0	6.99	0
DS1-2	4.16	2.46	7.14	2.15
DS2-5	4.20	3.45	7.25	3.72
DS3-3	4.00	−1.48	7.10	1.57
DS4-4	(< 3.6)	/	6.66	−4.72

TABLE 5.8: Average of α-values for accelerometers 4, 5, 6, 14, 15 and 16 in DS1-2, DS2-5, DS3-3, and DS4-4.

	Accelerometers					
	4	5	6	14	15	16
DS1-2	0.63	0.66	0.65	0.52	0.49	0.49
DS2-5	0.34	0.36	0.43	0.31	0.28	0.30
DS3-3	0.20	0.16	0.23	0.21	0.27	0.30
DS4-4	0.12	0.13	0.13	0.21	0.18	0.19

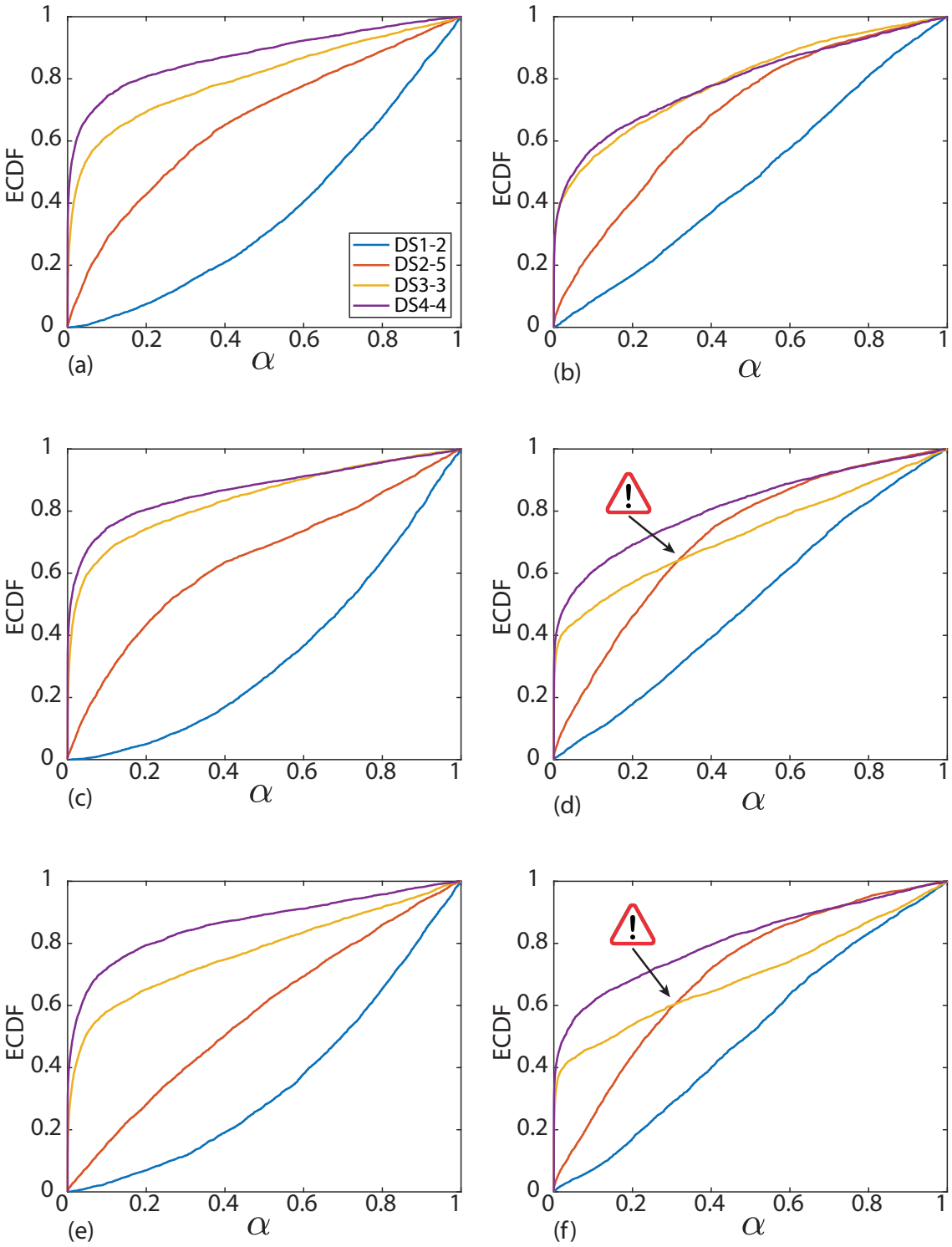

FIGURE 5.24: ECDFs of α-values for accelerometers (a) 4, (b) 14, (c) 5, (d) 15, (e) 6, and (f) 16 for Test B in DS1-2, DS2-5, DS3-3, and DS4-4 compared to the reference scenario.

Test A in another configuration

For Test A, another combination of damaged scenarios can be considered. This new combination consists of DS1-2, DS3-3 and DS3-4. In this case, the temperature influence is shown.

The PSDs of the acceleration from the accelerometer 5 in these selected damaged states are shown in Figure 5.25 and the natural frequencies, obtained by using the peak picking method, are reported in Table 5.9. In this particular case, the natural frequencies show the expected tendency with the damage. Indeed, the relative change on natural frequencies Δ is smaller for DS1-2 than for DS3-3 and DS3-4. However, a large difference can be observed between the relative change Δ for DS3-3 and DS3-4. It should have been expected that the natural frequencies would remain the same for DS3-3 and DS3-4 as they correspond to the same damaged state and were performed on the same day. Indeed, even if these tests were done during the same day, for DS3-3 it was in the early morning while for DS3-4 in the early afternoon. During this day, the sun was shining and large temperature discrepancies could be observed between the face exposed to the sun (Temperature sensor T4) and the face always in the shadow (Temperature sensor T2). For DS3-3, the temperature difference between these two faces is equal to 10 Celsius degrees while for DS3-4, this difference reached 15 Celsius degrees.

In Figure 5.26, the ECDFs of α-values for the proposed statistical test are displayed. The average of α-values is reported in Table 5.10. It can be observed that the ECDFs of α-values are all located in the upper half of the map, resulting in a successful damage detection for each accelerometer in all selected damaged scenarios.

However, for accelerometers 4 and 5, the ECDFs of α-values in DS1-2 are above those in DS3-3, which means that in this case, damage is not ordered correctly.

Finally, as already mentioned with the natural frequencies for DS3-3 and DS3-4, the ECDFs of α-values for each accelerometer are well distinct. This echoes with the remark mentioning the large temperature difference measured on the faces of the beam always exposed to the sun and in the shadow.

Consequently, based on the "rule-of-the-diagonal", the proposed method is still able to detect damages but the temperature creates some inconsistencies.

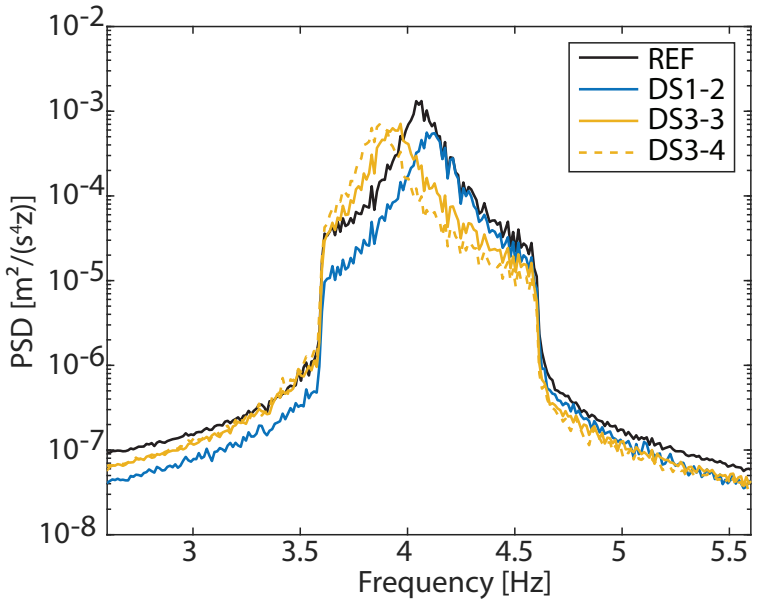

FIGURE 5.25: PSDs of the acceleration of accelerometer 5 for the reference state, DS1-2, DS3-3, and DS3-4 for Test A.

TABLE 5.9: Natural frequency of the first bending mode for the reference state, DS1-2, DS3-3, and DS3-4.

States	Frequency	Δ[%]
REF	4.08	0
DS1-2	4.12	0.98
DS3-3	3.92	−3.92
DS3-4	3.87	−5.15

TABLE 5.10: Average of α-values for accelerometers 4, 5, 6, 14, 15 and 16 in DS1-2, DS3-3, and DS3-4.

	Accelerometers					
	4	5	6	14	15	16
DS1-2	0.35	0.33	0.36	0.43	0.42	0.42
DS3-3	0.38	0.39	0.33	0.37	0.33	0.31
DS3-4	0.25	0.25	0.19	0.25	0.20	0.18

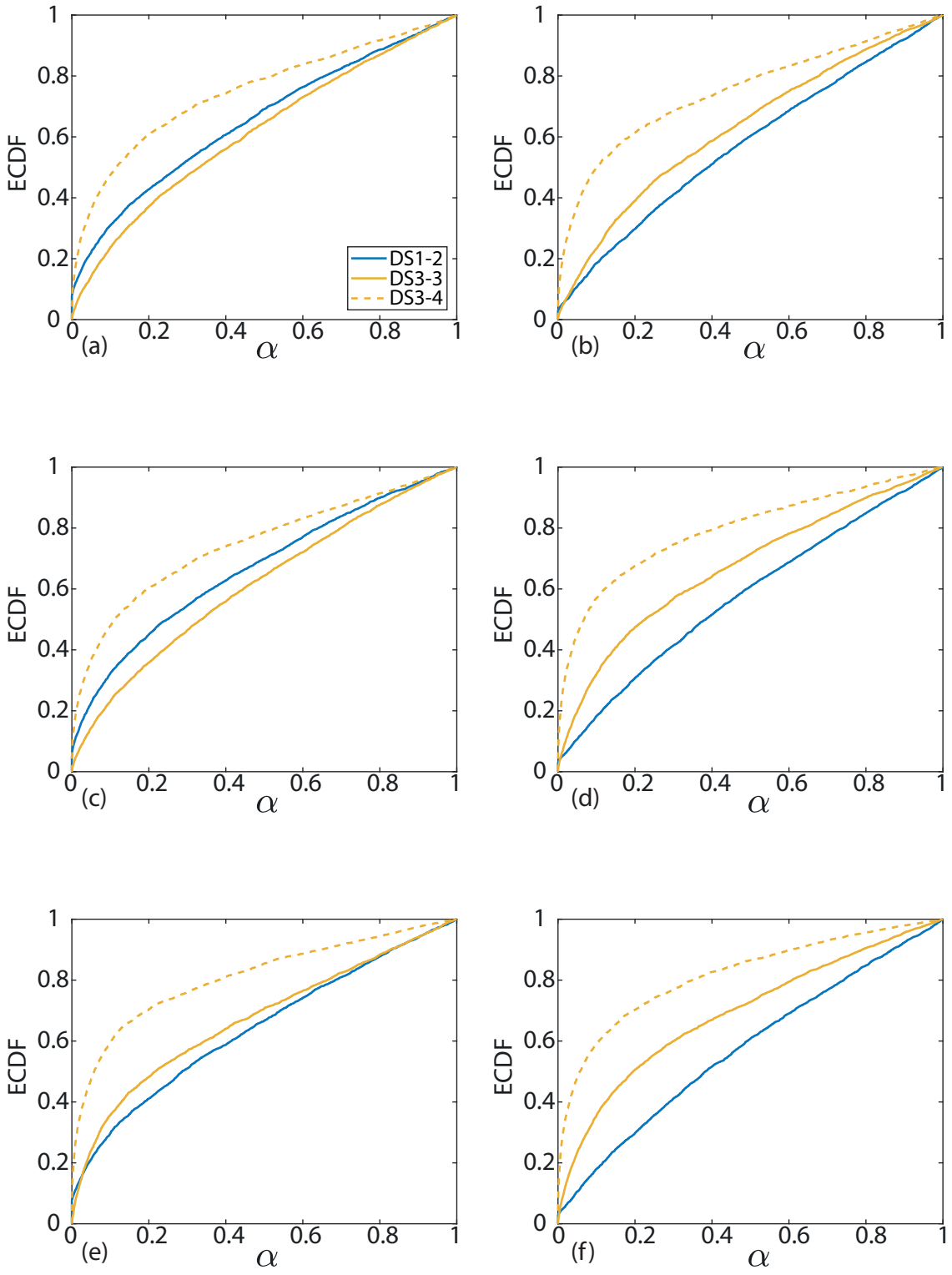

FIGURE 5.26: ECDFs of α-values for accelerometers (a) 4, (b) 14, (c) 5, (d) 15, (e) 6, and (f) 16 for Test A in DS1-2, DS3-3, and DS3-4 compared to the reference scenario.

5.4.2 With temperature compensation

As shown earlier, the temperature, and especially the temperature gradient, plays in important role on natural frequencies and FPTs. These temperature effects are impactful on the damage detection in SHM and new techniques have to be developed to tackle this challenge [137, 138]. Moreover, some previous experiments were performed on the beam under investigation and showed the effects of temperature on static and quasi-static measurements [139]. The impact of temperature is of the same order magnitude as damages.

Therefore, temperature compensation can significantly improve the results, which are, in this case, the ranking of damaged states, from DS1 to DS4. Indeed, damage detection, based on the "rule-of-the-diagonal, is already working.

The University of Luxembourg developed a method to compensate temperature effects [138]. Thanks to the collaboration between the Univeristy of Liège and the University of Luxembourg for this project, temperature compensation has been applied to the FPT-approach. This method hinges on the linear fitting of the natural frequencies identified under different temperatures. More advanced details and results about temperature compensation will be presented in the twin PhD thesis being currently developed at the University of Luxembourg [136].

The same method is used in this section to correct natural frequencies based on measured temperatures during the tests. Based on the recommendations from the University of Luxembourg, the reference temperature sensor selected for temperature compensation is the sensor T5, which measures the temperature of the asphalt layer. Indeed, it has been shown that the asphalt layer, bonded to the beam, whose stiffness greatly varies with temperature, influences the stiffness of the whole structure [140].

In Figure 5.27, the linear fitting is shown. Compared to the original fitting, the optimal slope is imposed to be the same for each damaged scenario. This decision is motivated by the fact that, at early damage stage, the behaviour of a structure remains similar. Moreover, the fitting curves are ranked in order from top to bottom. Indeed, with the increase of damage from DS1 to DS4, the stiffness of the beam diminishes, which results in a decrease of natural frequencies. Finally, the optimal slope of the linear fitting in each damaged state is negative. This is related to material properties. When the asphalt layer and the concrete heat up, their stiffness decreases and, therefore, the natural frequency is also reduced.

Once the fitting has been done, a corrected frequency is calculated based on the raw frequency and the slope of the fitting curves. The corrected frequency is given by

$$f_{\text{corr}} = m\,(T_{\text{ref}} - T_{\text{meas}}) + f_{\text{raw}} \tag{5.1}$$

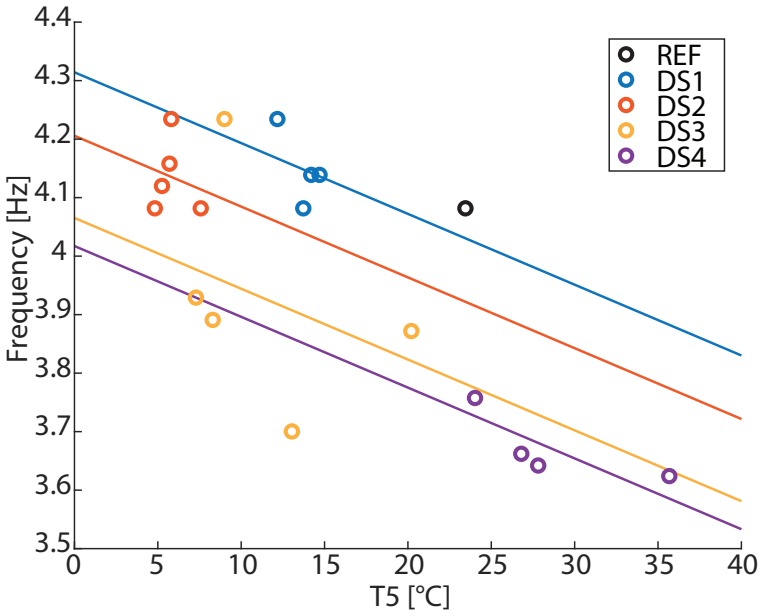

FIGURE 5.27: Temperatures of sensor T5 versus frequencies of the first bending mode: linear fitting for each damaged state by imposing the same slope.

where m is the slope from the fitting, T_{ref} is the average over the entire test of the measured temperature T5 of the asphalt layer and is equal to 23.4 °C, T_{meas} corresponds to the average of the measured temperature during the test and f_{raw} is the measured frequency.

In Table 5.11, the raw and corrected frequencies are reported for DS1-2, DS3-3 and DS3-4. It can be observed that all corrected frequencies are smaller than the raw frequencies.

As mentioned earlier, the temperature effect impacts the results for these damaged states. Therefore, it has been decided to perform temperature compensation to see if it improves the results for the FPT method.

To apply temperature compensation to the FPTs, the ratio between the raw and corrected natural frequencies is used. By multiplying the FPTs by this ratio, a strech or a contraction of the time axis is performed. If the corrected frequency is smaller than the raw frequency, as it is the case here, the ratio is greater than 1. Therefore, the FPT values are increased, resulting in a stretching of the time axis.

In Figure 5.28, the ECDFs of α-values are depicted with (plain lines) and without (dashed lines) temperature compensation.

Invoking the "rule-of-the-diagonal", the damage detection is still correctly performed. Indeed, all ECDFs of α-values are located inside the upper half of the map.

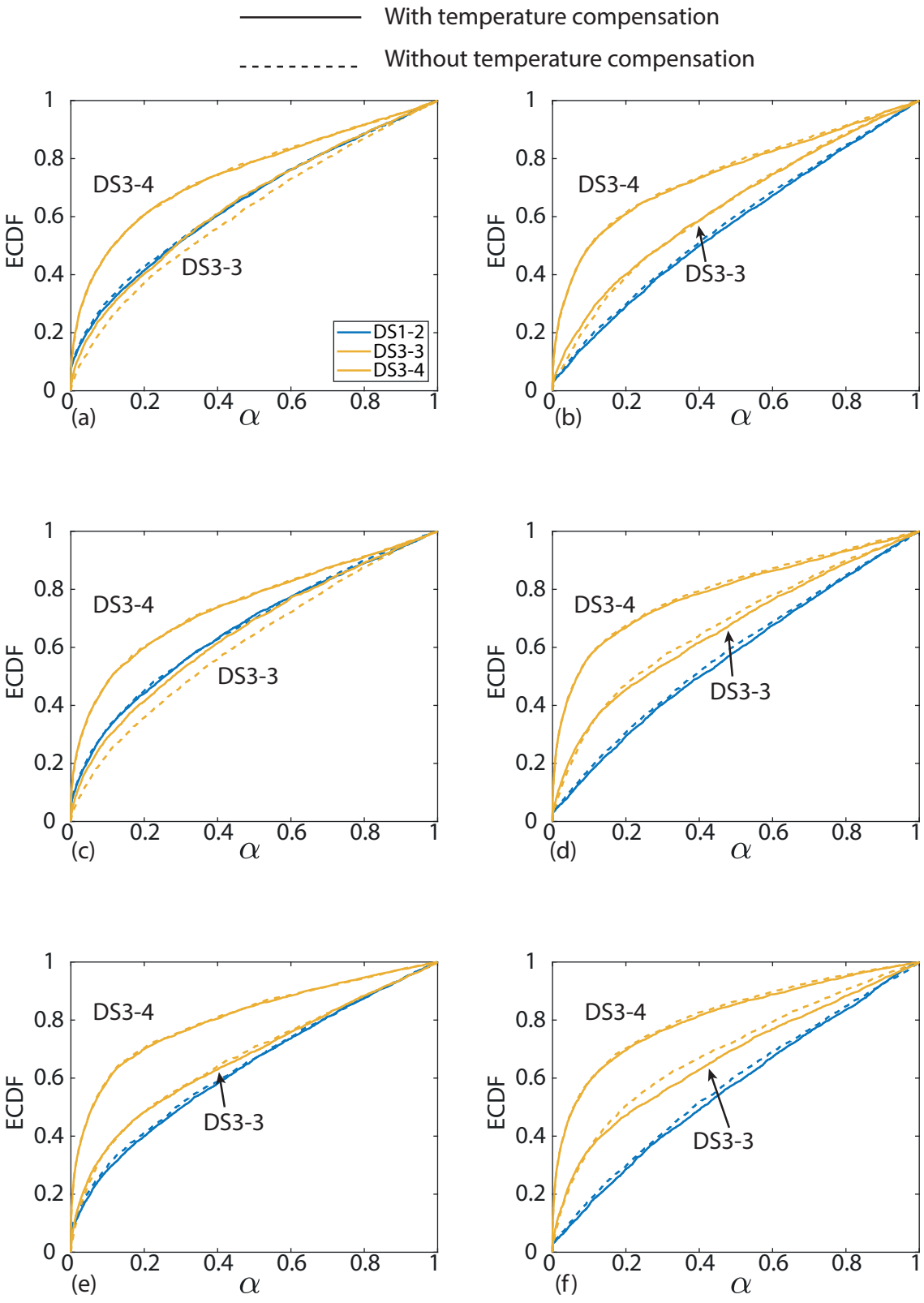

FIGURE 5.28: ECDFs of α-values for accelerometers (a) 4, (b) 14, (c) 5, (d) 15, (e) 6, and (f) 16 for Test A in DS1-2, DS3-3, and DS3-4 compared to the reference scenario with (plain lines) and without (dashed lines) temperature compensation.

TABLE 5.11: Raw and corrected natural frequencies of the first bending mode for DS1-2, DS3-3 and DS3-4.

	f_{raw} [Hz]	f_{corr} [Hz]	$\frac{f_{\text{raw}}}{f_{\text{corr}}}$ [-]
DS1-2	4.12	3.96	1.03
DS3-3	3.92	3.73	1.05
DS3-4	3.87	3.83	1.01

TABLE 5.12: Average of α-values for accelerometers 4, 5, 6, 14, 15 and 16 in DS1-2, DS3-3, and DS3-4 with temperature compensation.

	Accelerometers					
	4	5	6	14	15	16
DS1-2	0.35	0.34	0.37	0.43	0.43	0.44
DS3-3	0.35	0.35	0.33	0.37	0.34	0.33
DS3-4	0.25	0.25	0.19	0.25	0.21	0.19

Furthermore, it can be observed that for DS3-4, the results are similar. Indeed, the asphalt layer temperatures in DS3-4 and in the reference state are close to each other, resulting in ratios $\frac{f_{\text{raw}}}{f_{\text{corr}}}$ close to 1.

For DS1-2 and DS3-3, the results are slightly improved, especially for accelerometers 4 and 5, the ECDFs of α-values are closer. For these two damaged states, this results in really close averages of α-values for these two accelerometers, see Table 5.12.

However, even with temperature compensation, the results between DS3-3 and DS3-4 are only slightly improved. A distinct discrepancy is still observable between these two tests while they were performed on the same day. Some hypotheses can be formulated as the humidity in the beam that varies during the day, especially sunny day, or the temperature gradient that makes temperature compensation more difficult. To reduce environmental effects on the measurements, two solutions can be proposed:

1. Perform the test during cloudy days [139]

2. Perform a longer test campaign only dedicated to study the temperature effects on natural frequencies of the structure. Having a larger amount of frequencies versus temperatures data allows the use of more sophisticated methods such as Principal Component Analysis [137] or artificial intelligence algorithms that can find patterns in the collected data [141], which, in turn, results in more reliable temperature compensations.

5.4.3 Influence of loading amplitude at shaker

The results obtained from Test C are similar to those shown for Test A and Test B. However, the amplitude of the force varies with the considered test, see Figure 5.16. Dealing with concrete structures means that cracks already exist in the structure. The beam structure studied in this Chapter has aged for almost 50 years, submitted to environmental conditions as well as chemical agents from the bridge usage and, finally, moved from site to the laboratory. Therefore, the number of cracks is higher than freshly cast concrete structures.

The softening, associated with a wider opening of these existing cracks [142] is observable by increasing the force amplitude. Indeed, the apparent stiffness of the structure decreases, resulting in a decrease of natural frequencies. The discrepancy observed between natural frequencies from small or large force amplitudes can reach 2 to 3% [143, 142].

In Figure 5.29, the PSDs of the acceleration of the first bending mode during DS2-2 is depicted for each test. The force amplitude decreases from Test A to Test C, which were performed within an hour, resulting in a decrease of natural frequencies as mentioned already. As seen in Figure 5.16, the frequency content in the neighbourhood of the natural frequency drops by one order of magnitude from Test A to Test B, and then again by one order of magnitude from Test B to Test C.

Therefore, for the proposed method in Chapter 3, which hinges on the frequency content adjustment, it is mandatory that the force amplitude remains constant for each test. Indeed, this frequency content adjustment relies on the hypothesis that the structural response is linear in each state considered separately.

Hence, to improve the robustness of the entire process, it is important to work with controlled excitation if possible relying on a closed loop control system for the shaker.

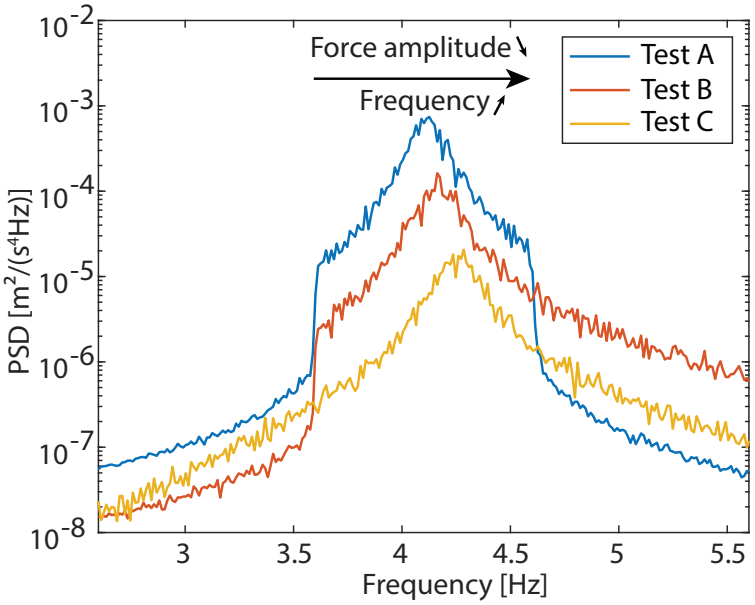

FIGURE 5.29: PSDs of the acceleration of accelerometer 5 for DS2-2. Softening in the concrete beam due to different shaker amplitudes for the natural frequency of the first bending mode.

5.4.4 Sensitivity of the results due to passage of trains

As shown in Figure 5.1, railways were close to the experimental setup. Therefore, it may happen that during a test, a train passes. Due to the proximity with the experimental setup, the influence of the train is directly visible by comparing Figures 5.30(a) and (b). These figures represent the acceleration of the beam during DS1-3 for the accelerometer 5 and for Test A. For an even clearer representation of the influence of the train on the signal, the wavelet of the acceleration is performed in Figure 5.30(c). It can be seen that the train mainly impacts the frequency range [13; 22]Hz.

Therefore, by considering the first bending mode whose natural frequency is located around 4 Hz and filtering around this frequency, the influence of the train can be completely discarded. In Figure 5.31, the ECDFs of α-values of the proposed statistical test are shown. It can be seen that the ECDFs with and without the influence of the train are close to each other for all accelerometers. Therefore, it can be concluded that the train effect on the damage detection was neutralised thanks to the bandpass filter.

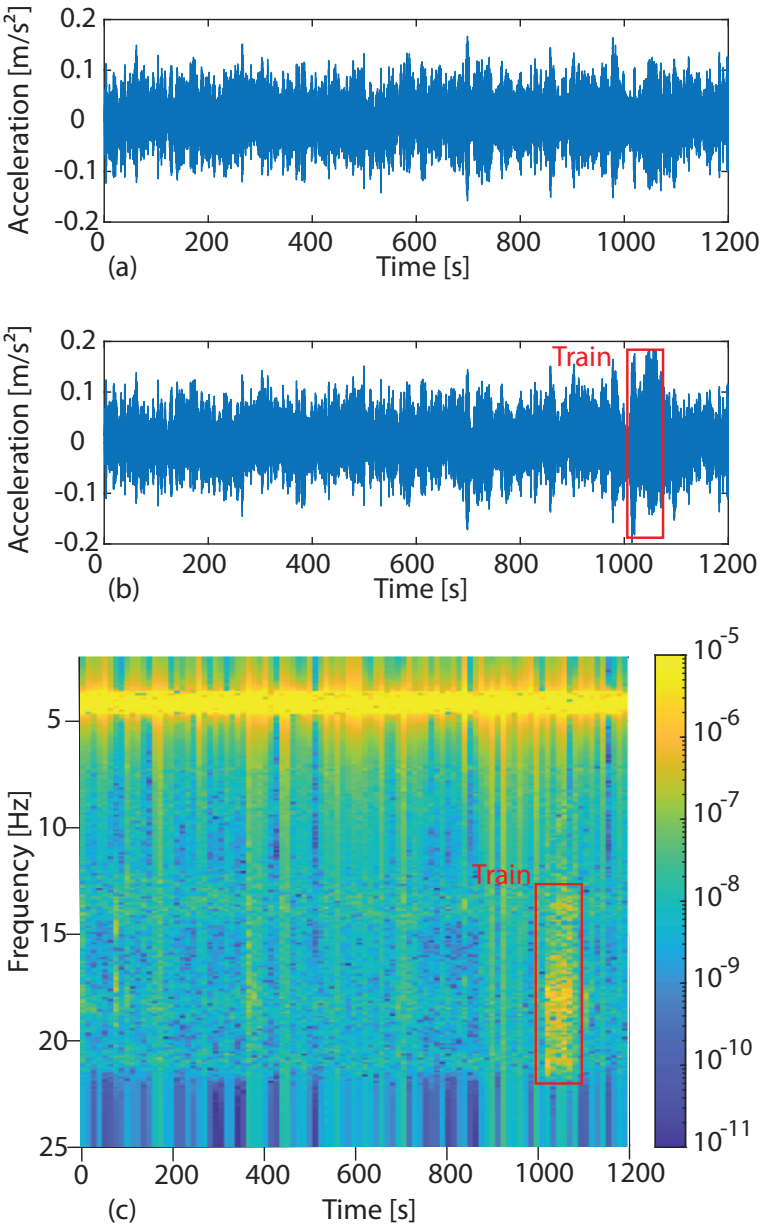

FIGURE 5.30: Influence of the train on the time signal: (a) no train, (b) train, and (c) wavelet of the time signal with train during DS1-3 for the accelerometer 5 and for Test A.

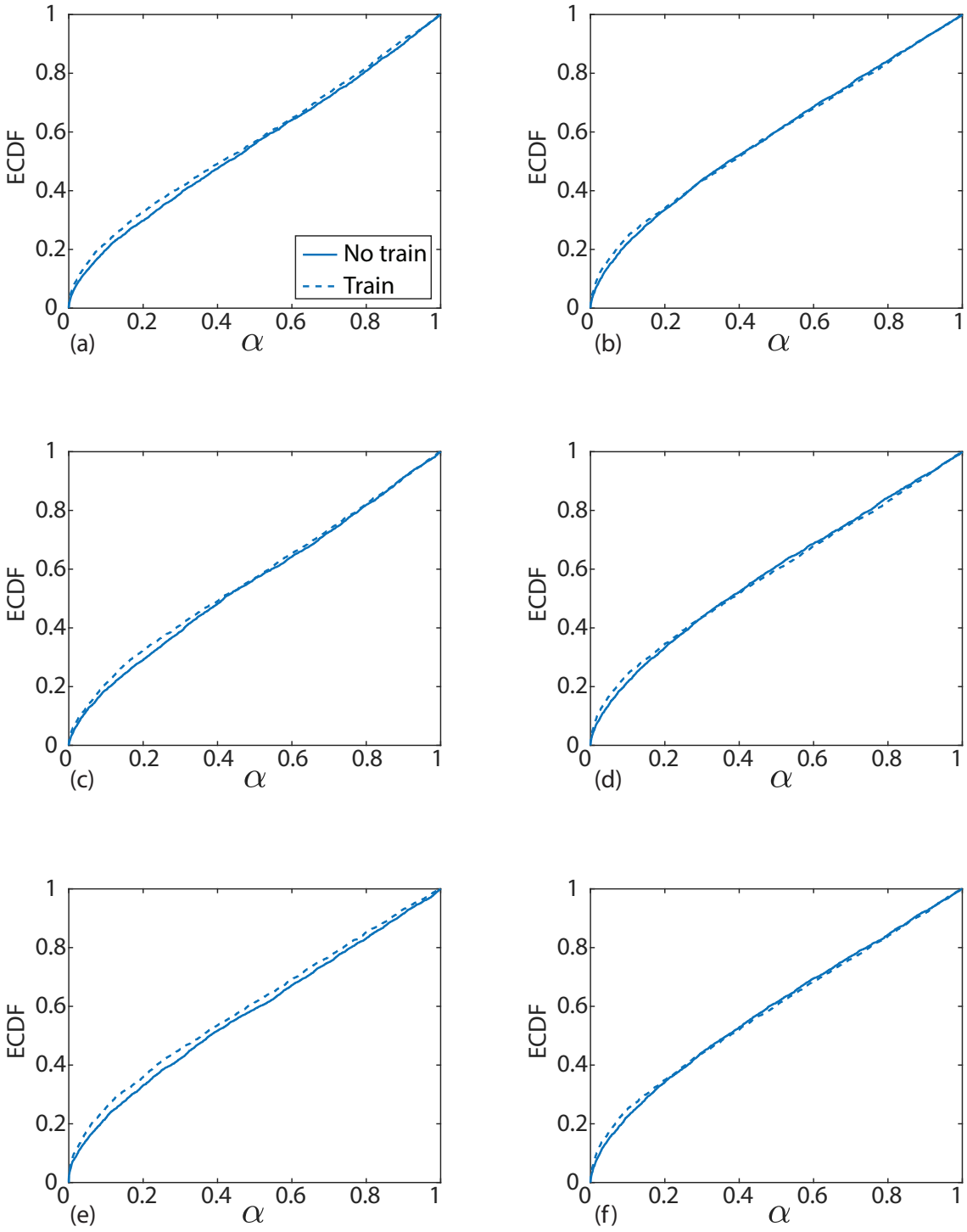

FIGURE 5.31: ECDFs of α-values for accelerometers (a) 4, (b) 14, (c) 5, (d) 15, (e) 6, and (f) 16 for Test A in DS1-3 compared to the reference scenario with and without passage of train.

5.5 Conclusion

In this last Chapter, damage detection, based on the proposed method, was performed on a concrete beam from a demolished prestressed concrete bridge. Five different scenarios were considered: 1 reference state and 4 damaged states.

It has been shown that a strategy based on natural frequencies only struggles with damage detection. However, with the ECDFs of both α-values from the proposed statistical test and distances from the 2-sample tests provided sufficient discrepancies between each damaged scenario, even in the early damage stages (DS1 and DS2), before the occurrence of cracks.

The proposed statistical test performed better than the 2-sample tests and has been chosen as the best test for damage detection. In addition, as proposed in Chapter 4, the "rule-of-the-diagonal" was successful in a straightforward observation of damage. Once again, its efficacy has been demonstrated to perform damage detection, which adds even more weight to the use of the proposed statistical test.

Moreover, with the proposed method, damaged scenarios could generally be ordered correctly from DS1 to DS4. This means that, in addition to damage detection, by comparing the ECDFs of α-values or distances for each damaged scenario, the proposed method can evaluate the damage level qualitatively.

The influence of temperature effects has also been studied. It has been seen that the proposed method can still detect a damage but the order of damaged scenarios can be inverted. To reduce the temperature influence, temperature compensation has been performed. Nevertheless, the results only slightly improved with temperature compensation.

The non-linear behaviour of the beam, has also been highlighted. In this case, the apparent stiffness of the beam is influenced by the amplitude of the force injected by the shaker in the structure. Therefore, keeping the same force amplitude is mandatory for the proposed method because it relies notably on the frequency content adjustment. Using a closed loop control system for the shaker could prevent this issue and improve the robustness of the entire process.

Finally, additive unmeasured noise might not corrupt at all the proposed methodology, especially when the frequency content of the additional source of excitation lies outside the range of natural frequencies. This has been demonstrated by processing data with and without passing trains.

Chapter 6

Conclusion

This thesis presents a new methodology based on First Passage Times for the Structural Health Monitoring in civil engineering. This method has been applied to two experimental setups, demonstrating its efficacy in damage detection at early stage.

Firstly, a novel algorithm has been developed to efficiently compute First Passage Times from both synthetic and experimental signals. Indeed, First Passage Times are the keystone of the proposed method for damage detection. The necessity to process data efficiently enables the measurement of longer time series. In addition, large structures are frequently equipped with multiple sensors. Therefore, the quantity of data to be processed is considerable and the proposed algorithm is also suitable for this type of application. Indeed, it has been demonstrated that the proposed algorithm is 400 times faster than the direct approach used until recently. Furthermore, the algorithm has also been validated by comparing the computed and theoretical First Passage Times statistical moments and distributions for the Ornstein-Uhlenbeck process. A very good agreement has been observed between the analytical and numerical results.

Secondly, a novel methodology for Structural Health Monitoring has been developed. This methodology is based on two main steps: the pre-processing of measured data and the comparison of First Passage Time histograms between the healthy and current states of a structure. The aformentioned methodology hinges on 3 different steps: a bandpass filter, a frequency content adjustment filter and the envelope of the measured signal obtained with the Hilbert transform. This helps to enhance the robustness of the proposed methodology by minimising some of the negative aspects associated with utilising the raw input signal, which could potentially compromise damage detection. The latter is made of 2-sample tests, coming from the literature, and a new proposed statistical test that are employed to compare First Passage Time histograms in the healthy and current states. The First Passage Time histograms demonstrate superior capability to detect slight changes compared to the centred statistical moments of First Passage Time maps,

rendering them the optimal choice for the proposed Structural Health Monitoring method. If discrepancies between First Passage Time histograms are highlighted, it can be concluded that the structure is significantly different from its healthy state, and that the current state is therefore identified as damaged state. Finally, the sensitivity of the proposed methodology has been assessed, showing a high degree of robustness for damage detection in the presence of unmeasured forces or additive measurement noise.

Thirdly, the proposed methodology is applied to two experimental setups: a small-scale laboratory test and a large-scale outdoor test. The former has been employed to perform damage detection and localisation. It has been demonstrated that the proposed method, based on First Passage Times, is capable of detecting changes between the healthy and current states, while the relative difference on natural frequencies is as small as 0.15%. This illustrates the sensitivity of the method to identify damage at early stage.

Moreover, the "rule-of-the-diagonal" has been introduced and used for straightforward damage detection. If the Empirical Cumulative Density Function of α-values is above the main diagonal, then damage is detected. In order to localise the damage, a digital twin model has been employed. For each combination of the twin model parameters, a unique map of First Passage Time histograms is generated. The aformentioned parameters are then modified until a good match is observed between the maps from the experimental setup and those from the digital twin model, indicating that the model parameters correspond to those of the experimental setup. It has been demonstrated that this methodology is able to highlight regions on a structure where damage is most likely to have occurred, even at early stage.

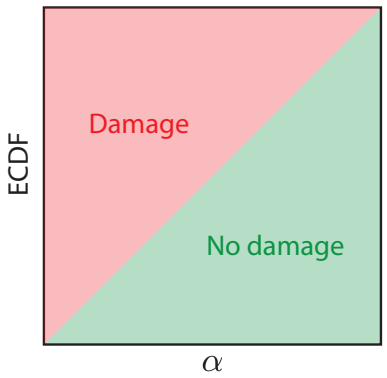

The rule-of-the-diagonal

In the context of the large-scale outdoor test submitted to environmental effects, it has been shown that a strategy based on natural frequencies only is unable to effectively detect damage. Nevertheless, the First Passage Time histograms were able to identify discrepancies between the healthy and damaged states, even in the presence of early-stage damage that did not exhibit visible cracks. In addition, the damaged states could also be ordered correctly from low to high damage. The proposed statistical test demonstrated higher performances than the 2-sample tests from the literature, rendering it the optimal method for damage detection. Furthermore, the application of the "rule-of-the-diagonal" was once again successful. Finally, the efficacy of the proposed method in detecting damage was evaluated in the presence of temperature effects and unmeasured noise. In both cases, the method was able to successfully identify damage.

Therefore, the proposed method based on First Passage Times has demonstrated good performances in the detection of damage at early stage.

Future Perspectives

On large structures, many sensors are typically deployed at the same location. This is the case for continuous monitoring. Therefore, by comparing two signals at different locations, a spatial dependency could be highlighted for damage localisation, thereby negating the necessity for numerical models. An extension to the First Passage Time algorithm could be implemented in order to accept two different signals as input, instead of accepting one single signal currently. The generated maps, based on two input signals, could be called cross-First Passage Time maps. One signal is employed for the levels X_0, while the other is used for the levels X_f. This approach could also be extended to the computation of two measured signals at different moments in time, in the healthy and current states.

The quantity of information provided by the maps of First Passage Time histograms is considerable, as they can be regarded as 3-D matrices. Consequently, artificial intelligence can play a major role in the analysis of this type of data, especially in the field of pattern recognition. Indeed, it has been demonstrated that First Passage Time histograms are sufficiently sensitive to detect damage at early stage. However, this could make them susceptible to detecting changes from any source other than damage. The shape of the histograms of First Passage Times or histograms of First Passage Times at specific combinations (X_0, X_f) may conceal certain patterns that are characteristic of damage or other sources, such as environmental conditions. Once trained, pattern recognition could be employed to discard the undesired effects from the histograms of First Passage Times, thereby enhancing the ability to detect damage and localise it at early stage.

It has been demonstrated that the method based on First Passage Times outperforms those based on natural frequencies only. Therefore, the proposed method could be employed in parallel with static methods, such as those based on the stiffness matrix, to improve damage detection.

Bibliography

[1] C. R. Farrar and K. Worden, "An introduction to structural health monitoring," *Philosophical Transactions of the Royal Society A: Mathematical, Physical and Engineering Sciences*, vol. 365, no. 1851, pp. 303–315, 2007.

[2] K. Worden and J. M. Dulieu-Barton, "An overview of intelligent fault detection in systems and structures," *Structural Health Monitoring*, vol. 3, no. 1, pp. 85–98, 2004.

[3] G. Egidi, L. Salvati, and S. Vinci, "The long way to tipperary: City size and worldwide urban population trends, 1950–2030," *Sustainable Cities and Society*, vol. 60, p. 102148, 2020.

[4] M. C. Brown, J. P. Gomez, M. L. Hammer, J. M. Hooks, *et al.*, "Long-term bridge performance high priority bridge performance issues.," tech. rep., United States. Federal Highway Administration. Office of Infrastructure, 2014.

[5] Z. Deng, M. Huang, N. Wan, and J. Zhang, "The current development of structural health monitoring for bridges: A review," *Buildings*, vol. 13, no. 6, p. 1360, 2023.

[6] F. Lo Iacono, G. Navarra, and M. Oliva, "Structural monitoring of "himera" viaduct by low-cost mems sensors: characterization and preliminary results," *Meccanica*, vol. 52, pp. 3221–3236, 2017.

[7] A. Sivasuriyan, D. S. Vijayan, W. Górski, Ł. Wodzyński, M. D. Vaverková, and E. Koda, "Practical implementation of structural health monitoring in multi-story buildings," *Buildings*, vol. 11, no. 6, p. 263, 2021.

[8] A. Sivasuriyan, D. S. Vijayan, R. Munusami, and P. Devarajan, "Health assessment of dams under various environmental conditions using structural health monitoring techniques: a state-of-art review," *Environmental Science and Pollution Research*, pp. 1–12, 2021.

[9] M. El Mountassir, S. Yaacoubi, and F. Dahmene, "Reducing false alarms in guided waves structural health monitoring of pipelines: Review synthesis and debate," *International Journal of Pressure Vessels and Piping*, vol. 188, p. 104210, 2020.

[10] H. Pezeshki, H. Adeli, D. Pavlou, and S. C. Siriwardane, "State of the art in structural health monitoring of offshore and marine structures," in *Proceedings of the Institution of Civil Engineers-Maritime Engineering*, vol. 176, pp. 89–108, Thomas Telford Ltd, 2023.

[11] N. Hlaing, P. G. Morato, J. S. Nielsen, P. Amirafshari, A. Kolios, and P. Rigo, "Inspection and maintenance planning for offshore wind structural components: integrating fatigue failure criteria with bayesian networks and markov decision processes," *Structure and Infrastructure Engineering*, vol. 18, no. 7, pp. 983–1001, 2022.

[12] A. Orgnoni, R. Pinho, M. Moratti, N. Scattarreggia, G. M. Calvi, *et al.*, "Critical review and modelling of the construction sequence and loading history of the collapsed morandi bridge," *Int. J. Bridge Eng*, vol. 10, no. 3, pp. 37–62, 2022.

[13] V. Cusati, S. Corcione, and V. Memmolo, "Impact of structural health monitoring on aircraft operating costs by multidisciplinary analysis," *Sensors*, vol. 21, no. 20, p. 6938, 2021.

[14] J. S. Nielsen, D. Tcherniak, and M. D. Ulriksen, "A case study on risk-based maintenance of wind turbine blades with structural health monitoring," *Structure and Infrastructure Engineering*, vol. 17, no. 3, pp. 302–318, 2021.

[15] P. G. Morato, K. G. Papakonstantinou, C. P. Andriotis, J. S. Nielsen, and P. Rigo, "Optimal inspection and maintenance planning for deteriorating structural components through dynamic bayesian networks and markov decision processes," *Structural Safety*, vol. 94, p. 102140, 2022.

[16] N. R. Kapoor, A. Kumar, H. C. Arora, and A. Kumar, "Structural health monitoring of existing building structures for creating green smart cities using deep learning," in *Recurrent Neural Networks*, pp. 203–232, CRC Press, 2022.

[17] S. Hassani and U. Dackermann, "A systematic review of advanced sensor technologies for non-destructive testing and structural health monitoring," *Sensors*, vol. 23, no. 4, p. 2204, 2023.

[18] A. Sofi, J. J. Regita, B. Rane, and H. H. Lau, "Structural health monitoring using wireless smart sensor network–an overview," *Mechanical Systems and Signal Processing*, vol. 163, p. 108113, 2022.

[19] H. Momeni and A. Ebrahimkhanlou, "High-dimensional data analytics in structural health monitoring and non-destructive evaluation: A review paper," *Smart Materials and Structures*, vol. 31, no. 4, p. 043001, 2022.

[20] K. Eltouny, M. Gomaa, and X. Liang, "Unsupervised learning methods for data-driven vibration-based structural health monitoring: a review," *Sensors*, vol. 23, no. 6, p. 3290, 2023.

[21] R.-T. Wu and M. R. Jahanshahi, "Data fusion approaches for structural health monitoring and system identification: Past, present, and future," *Structural Health Monitoring*, vol. 19, no. 2, pp. 552–586, 2020.

[22] D. J. Inman, C. R. Farrar, V. Lopes, V. Steffen, Lopes, and Steffen, "Damage prognosis for aerospace, civil and mechanical systems preface," 2005.

[23] R. Gorgin, Y. Luo, and Z. Wu, "Environmental and operational conditions effects on lamb wave based structural health monitoring systems: A review," *Ultrasonics*, vol. 105, p. 106114, 2020.

[24] M. Govindasamy, G. Kamalakannan, C. Kesavan, and G. K. Meenashisundaram, "Damage detection in glass/epoxy laminated composite plates using modal curvature for structural health monitoring applications," *Journal of Composites Science*, vol. 4, no. 4, p. 185, 2020.

[25] S. Schommer, V. H. Nguyen, S. Maas, and A. Zürbes, "Model updating for structural health monitoring using static and dynamic measurements," *Procedia engineering*, vol. 199, pp. 2146–2153, 2017.

[26] S. W. Doebling, C. R. Farrar, M. B. Prime, and D. W. Shevitz, "Damage identification and health monitoring of structural and mechanical systems from changes in their vibration characteristics: a literature review," 1996.

[27] O. Avci, O. Abdeljaber, S. Kiranyaz, M. Hussein, M. Gabbouj, and D. J. Inman, "A review of vibration-based damage detection in civil structures: From traditional methods to machine learning and deep learning applications," *Mechanical systems and signal processing*, vol. 147, p. 107077, 2021.

[28] D. García and D. Tcherniak, "An experimental study on the data-driven structural health monitoring of large wind turbine blades using a single accelerometer and actuator," *Mechanical Systems and Signal Processing*, vol. 127, pp. 102–119, 2019.

[29] H. Choi, S. Choi, and H. Cha, "Structural health monitoring system based on strain gauge enabled wireless sensor nodes," in *2008 5th International Conference on Networked Sensing Systems*, pp. 211–214, IEEE, 2008.

[30] C. Rodrigues, C. Felix, and J. Figueiras, "Fiber-optic-based displacement transducer to measure bridge deflections," *Structural health monitoring*, vol. 10, no. 2, pp. 147–156, 2011.

[31] R. S. Concepcion, F. R. G. Cruz, F. A. A. Uy, J. M. E. Baltazar, J. N. Carpio, and K. G. Tolentino, "Triaxial mems digital accelerometer and temperature sensor calibration techniques for structural health monitoring of reinforced concrete bridge laboratory test platform," in *2017IEEE 9th International Conference on Humanoid, Nanotechnology, Information Technology, Communication and Control, Environment and Management (HNICEM)*, pp. 1–6, IEEE, 2017.

[32] D. Goyal and B. Pabla, "The vibration monitoring methods and signal processing techniques for structural health monitoring: a review," *Archives of Computational Methods in Engineering*, vol. 23, pp. 585–594, 2016.

[33] R. Zaurin and F. Necati Catbas, "Structural health monitoring using video stream, influence lines, and statistical analysis," *Structural Health Monitoring*, vol. 10, no. 3, pp. 309–332, 2011.

[34] H. Sohn, C. R. Farrar, N. F. Hunter, and K. Worden, "Structural health monitoring using statistical pattern recognition techniques," *J. Dyn. Sys., Meas., Control*, vol. 123, no. 4, pp. 706–711, 2001.

[35] C. R. Farrar and K. Worden, *Structural health monitoring: a machine learning perspective*. John Wiley & Sons, 2012.

[36] A. C. Neves, J. Leander, I. González, and R. Karoumi, "An approach to decision-making analysis for implementation of structural health monitoring in bridges," *Structural Control and Health Monitoring*, vol. 26, no. 6, p. e2352, 2019.

[37] N. Makhoul, "Bayesian decision-making process including structural health monitoring data quality for bridge management," *KSCE Journal of Civil Engineering*, pp. 1–18, 2024.

[38] A. Behnia, H. K. Chai, and T. Shiotani, "Advanced structural health monitoring of concrete structures with the aid of acoustic emission," *Construction and Building Materials*, vol. 65, pp. 282–302, 2014.

[39] Z. Kral, W. Horn, J. Steck, *et al.*, "Crack propagation analysis using acoustic emission sensors for structural health monitoring systems," *The Scientific World Journal*, vol. 2013, 2013.

[40] M. Geuzaine, F. Foti, and V. Denoël, "Minimal requirements for the vibration-based identification of the axial force, the bending stiffness and the flexural boundary conditions in cables," *Journal of Sound and Vibration*, vol. 511, p. 116326, 2021.

[41] M. Geuzaine, F. Foti, E. Verstraelen, P. Toussaint, and V. Denoël, "Development of a general monitoring program for bridge stays and hangers in wallonia," in *2nd International Symposium on the Dynamics and Aerodynamics of Cables*, 2021.

[42] L. Sun, Z. Shang, Y. Xia, S. Bhowmick, and S. Nagarajaiah, "Review of bridge structural health monitoring aided by big data and artificial intelligence: From condition assessment to damage detection," *Journal of Structural Engineering*, vol. 146, no. 5, p. 04020073, 2020.

[43] Z. Liu and N. Mrad, "Validation of strain gauges for structural health monitoring with bayesian belief networks," *IEEE Sensors Journal*, vol. 13, no. 1, pp. 400–407, 2012.

[44] H. Jo, J.-W. Park, B. Spencer, H.-J. Jung, *et al.*, "Develoment of high-sensitivity wireless strain sensor for structural health monitoring," *Smart Struct. Syst*, vol. 11, no. 5, pp. 477–496, 2013.

[45] T. Hasiotis, E. Badogiannis, and N. G. Tsouvalis, "Application of ultrasonic c-scan techniques for tracing defects in laminated composite materials," *Strojniški vestnik-Journal of Mechanical Engineering*, vol. 57, no. 3, pp. 192–203, 2011.

[46] M. H. B. Afzal, S. Kabir, and O. Sidek, "An in-depth review: Structural health monitoring using fiber optic sensor," *IETE Technical Review*, vol. 29, no. 2, pp. 105–113, 2012.

[47] D. Sasi, S. Philip, R. David, and J. Swathi, "A review on structural health monitoring of railroad track structures using fiber optic sensors," *Materials Today: Proceedings*, vol. 33, pp. 3787–3793, 2020.

[48] W. Dong, Y. Huang, B. Lehane, and G. Ma, "Xgboost algorithm-based prediction of concrete electrical resistivity for structural health monitoring," *Automation in Construction*, vol. 114, p. 103155, 2020.

[49] D. Heinz, B. Halek, J. Krešák, P. Peterka, G. Fedorko, and V. Molnár, "Methodology of measurement of steel ropes by infrared technology," *Engineering Failure Analysis*, vol. 133, p. 105978, 2022.

[50] C. Xing, P. Wang, and W. Dong, "Research on the bridge monitoring method of ground-based radar," *Arabian Journal of Geosciences*, vol. 13, no. 23, p. 1267, 2020.

[51] M. A. Machado, K.-N. Antin, L. S. Rosado, P. Vilaça, and T. G. Santos, "High-speed inspection of delamination defects in unidirectional cfrp

by non-contact eddy current testing," *Composites Part B: Engineering*, vol. 224, p. 109167, 2021.

[52] Y. Zhang, Q. Wang, and S. Huang, "Structure health monitoring of concrete structures using magnetic flux leakage," 2022.

[53] A. Van der Wielen, L. Courard, and F. Nguyen, "Nondestructive detection of delaminations in concrete bridge decks," in *Proceedings of the XIII Internarional Conference on Ground Penetrating Radar*, pp. 1–5, IEEE, 2010.

[54] A. N. Trandafir, G. T. Proestos, and B. I. Mihaylov, "Detailed crack-based assessment of a 4-m deep beam test specimen," *Structural Concrete*, vol. 24, no. 1, pp. 756–770, 2023.

[55] Y. Tan and L. Zhang, "Computational methodologies for optimal sensor placement in structural health monitoring: A review," *Structural Health Monitoring*, vol. 19, no. 4, pp. 1287–1308, 2020.

[56] I. Reichert, P. Olney, and T. Lahmer, "Combined approach for optimal sensor placement and experimental verification in the context of tower-like structures," *Journal of Civil Structural Health Monitoring*, vol. 11, pp. 223–234, 2021.

[57] Z.-q. Lu, Z.-y. Wu, H.-f. Yang, and Y. He, "Optimal sensor placement using improved sensitivity analysis method," in *2009 First International Conference on Information Science and Engineering*, pp. 619–622, IEEE, 2009.

[58] T. M. Cavalier, W. A. Conner, E. del Castillo, and S. I. Brown, "A heuristic algorithm for minimax sensor location in the plane," *European Journal of Operational Research*, vol. 183, no. 1, pp. 42–55, 2007.

[59] P. F. Giordano, S. Quqa, and M. P. Limongelli, "The value of monitoring a structural health monitoring system," *Structural safety*, vol. 100, p. 102280, 2023.

[60] A. Rytter, "Vibrational based inspection of civil engineering structures," 1993.

[61] P. Kumar, S. Batchu, S. R. Kota, *et al.*, "Real-time concrete damage detection using deep learning for high rise structures," *IEEE Access*, vol. 9, pp. 112312–112331, 2021.

[62] K. Ghoulem, T. Kormi, and N. Bel Hadj Ali, "Damage detection in non-linear civil structures using kernel principal component analysis," *Advances in Structural Engineering*, vol. 23, no. 11, pp. 2414–2430, 2020.

[63] S. Gres, M. D. Ulriksen, M. Döhler, R. J. Johansen, P. Andersen, L. Damkilde, and S. A. Nielsen, "Statistical methods for damage detection applied to civil structures," *Procedia engineering*, vol. 199, pp. 1919–1924, 2017.

[64] D. Zonta, D. Bernal, *et al.*, "Strain-based approaches to damage localization in civil structures," *Proc. of IMAC XXIV, St. Louis, MO., Paper*, vol. 197, 2006.

[65] M. D. Ulriksen, D. Tcherniak, L. M. Hansen, R. J. Johansen, L. Damkilde, and L. Frøyd, "In-situ damage localization for a wind turbine blade through outlier analysis of stochastic dynamic damage location vector-induced stress resultants," *Structural Health Monitoring*, vol. 16, no. 6, pp. 745–761, 2017.

[66] A. A. Cury, C. C. Borges, and F. S. Barbosa, "A two-step technique for damage assessment using numerical and experimental vibration data," *Structural Health Monitoring*, vol. 10, no. 4, pp. 417–428, 2011.

[67] R. D. Adams, P. Cawley, C. J. Pye, and B. J. Stone, "A vibration technique for non-destructively assessing the integrity of structures," *Journal of mechanical engineering science*, vol. 20, no. 2, pp. 93–100, 1978.

[68] C. Modena, D. Sonda, and D. Zonta, "Damage localization in reinforced concrete structures by using damping measurements," *Key engineering materials*, vol. 167, pp. 132–141, 1999.

[69] A. Pandey, M. Biswas, and M. Samman, "Damage detection from changes in curvature mode shapes," *Journal of sound and vibration*, vol. 145, no. 2, pp. 321–332, 1991.

[70] A. C. Dederichs and O. Øiseth, "A novel and near-automatic mode tracking algorithm for civil infrastructure," *Journal of Sound and Vibration*, vol. 573, p. 118217, 2024.

[71] D. Dyer and R. Stewart, "Detection of rolling element bearing damage by statistical vibration analysis," *Journal of Mechanical Design*, vol. 100, pp. 229–235, 1978.

[72] M. Jayawardhana, X. Zhu, R. Liyanapathirana, and U. Gunawardana, "Statistical damage sensitive feature for structural damage detection using ar model coefficients," *Advances in Structural Engineering*, vol. 18, no. 10, pp. 1551–1562, 2015.

[73] N. Cheraghi, G. Zou, and F. Taheri, "Piezoelectric-based degradation assessment of a pipe using fourier and wavelet analyses," *Computer-Aided Civil and Infrastructure Engineering*, vol. 20, no. 5, pp. 369–382, 2005.

[74] Q. Pu, Y. Hong, L. Chen, S. Yang, and X. Xu, "Model updating–based damage detection of a concrete beam utilizing experimental damped frequency response functions," *Advances in Structural Engineering*, vol. 22, no. 4, pp. 935–947, 2019.

[75] Y. Yang and S. Nagarajaiah, "Blind identification of damage in time-varying systems using independent component analysis with wavelet transform," *mechanical systems and signal processing*, vol. 47, no. 1-2, pp. 3–20, 2014.

[76] B. Chen, S.-l. Zhao, P.-y. Li, *et al.*, "Application of hilbert-huang transform in structural health monitoring: A state-of-the-art review," *Mathematical Problems in Engineering*, vol. 2014, 2014.

[77] X. Ye, T. Jin, and C. Yun, "A review on deep learning-based structural health monitoring of civil infrastructures," *Smart Struct. Syst*, vol. 24, no. 5, pp. 567–585, 2019.

[78] Y. Duan, Q. Chen, H. Zhang, C. B. Yun, S. Wu, and Q. Zhu, "Cnn-based damage identification method of tied-arch bridge using spatial-spectral information," *Smart Struct. Syst*, vol. 23, no. 5, pp. 507–520, 2019.

[79] A. Zhang, K. C. Wang, Y. Fei, Y. Liu, C. Chen, G. Yang, J. Q. Li, E. Yang, and S. Qiu, "Automated pixel-level pavement crack detection on 3d asphalt surfaces with a recurrent neural network," *Computer-Aided Civil and Infrastructure Engineering*, vol. 34, no. 3, pp. 213–229, 2019.

[80] C. Ray W. and P. Joseph, *Dynamics of structures*. Computer & Structures, 1995.

[81] A. Depouhon, E. Detournay, and V. Denoël, "Accuracy of one-step integration schemes for damped/forced linear structural dynamics," *International Journal for Numerical Methods in Engineering*, vol. 99, no. 5, pp. 333–353, 2014.

[82] O. C. Zienkiewicz, R. L. Taylor, and J. Z. Zhu, *The finite element method: its basis and fundamentals*. Elsevier, 2005.

[83] B. I. Mihaylov, E. C. Bentz, and M. P. Collins, "Two-parameter kinematic theory for shear behavior of deep beams.," *ACI Structural Journal*, vol. 110, no. 3, 2013.

[84] I. A. Kougioumtzoglou and P. D. Spanos, "Response and first-passage statistics of nonlinear oscillators via a numerical path integral approach," *Journal of Engineering Mechanics*, vol. 139, no. 9, pp. 1207–1217, 2013.

[85] H. Vanvinckenroye, "The first passage time as an analysis tool for the reliability of stochastic oscillators," 2018.

[86] S. K. Kim, "Mean first passage time for a random walker and its application to chemical kinetics," *The Journal of Chemical Physics*, vol. 28, no. 6, pp. 1057–1067, 1958.

[87] Z. Hu, L. Cheng, and B. Berne, "First passage time distribution in stochastic processes with moving and static absorbing boundaries with application to biological rupture experiments," *The Journal of chemical physics*, vol. 133, no. 3, p. 034105, 2010.

[88] H. Vanvinckenroye, T. Andrianne, and V. Denoël, "First passage time as an analysis tool in experimental wind engineering," *Journal of Wind Engineering and Industrial Aerodynamics*, vol. 177, pp. 366–375, 6 2018.

[89] Y. Qiao, W. Xu, J. Sun, and H. Zhang, "Reliability of electrostatically actuated mems resonators to random mass disturbance," *Mechanical Systems and Signal Processing*, vol. 121, pp. 711–724, 2019.

[90] P. Patie, *On some first passage time problems motivated by financial applications*. PhD thesis, Universität Zürich, 2004.

[91] P. C. Chu, "First passage time analysis for climate prediction," in *Stochastic Physics and Climate Modelling* (T. N. Palmer and P. Williams, eds.), ch. 6, pp. 157–190, Cambridge: Cambridge University Press, 2009.

[92] Z. Schuss, *Theory and applications of stochastic processes: an analytical approach*, vol. 170. Springer Science & Business Media, 2009.

[93] A. Preumont, *Random Vibration and Spectral Analysis/Vibrations aléatoires et analyse spectral*, vol. 33. Springer Science & Business Media, 2013.

[94] H. Langtangen, "A general numerical solution method for fokker-planck equations with applications to structural reliability," *Probabilistic engineering mechanics*, vol. 6, no. 1, pp. 33–48, 1991.

[95] T. Canor and V. Denoël, "Transient fokker–planck–kolmogorov equation solved with smoothed particle hydrodynamics method," *International journal for numerical methods in engineering*, vol. 94, no. 6, pp. 535–553, 2013.

[96] T. Primožič, "Estimating expected first passage times using multilevel monte carlo algorithm," 2011.

[97] E. Delhez, H. Vanvinckenroye, J.-C. Golinval, and V. Denoël, "Numerical and experimental study of first passage time of a steel strip subjected to forced and parametric excitations," in *Proceedings of the 28th International Conference on Noise and Vibration Engineering*, September 2018.

[98] E. Delhez, H. Vanvinckenroye, V. Denoël, and J.-C. Golinval, "Experimental and numerical study of the second order moment of the first passage time of a steel strip subjected to forced and parametric excitations," in *Special Topics in Structural Dynamics & Experimental Techniques, Volume 5* (N. Dervilis, ed.), (Cham), pp. 39–42, Springer International Publishing, 2020.

[99] H. Vanvinckenroye and V. Denoël, "Average first-passage time of a quasi-hamiltonian mathieu oscillator with parametric and forcing excitations," *Journal of Sound and Vibration*, vol. 406, pp. 328–345, 2017.

[100] H. Vanvinckenroye and V. Denoël, "Second-order moment of the first passage time of a quasi-hamiltonian oscillator with stochastic parametric and forcing excitations," *Journal of Sound and Vibration*, vol. 427, pp. 178–187, 2018.

[101] K. Theunissen and V. Denoël, "An efficient algorithm for the computation of the first passage time maps of a given signal," *Mechanical Systems and Signal Processing*, vol. 207, p. 110884, 2024.

[102] K. Theunissen, E. Verstraelen, J.-C. Golinval, and V. Denoël, "Influence of structural damages on first passage time maps," in *ISMA-USD Noise and Vibration Engineering Conference 2022*, 2022.

[103] K. Theunissen, E. Verstraelen, J. C. Golinval, and V. Denoël, "Localization of structural damage based on first passage times for a pre-stressed steel strip," in *Dynamics of Civil Structures, Volume 2* (H. Y. Noh, M. Whelan, and P. S. Harvey, eds.), (Cham), pp. 99–101, Springer Nature Switzerland, 2024.

[104] K. Theunissen and V. Denoël, "Fractional derivatives model of aeroelastic derivatives of bridge decks," in *Proceedings of the 8th European-African Conference on Wind Engineering*, 2022.

[105] H. A. Sturges, "The choice of a class interval," *Journal of the american statistical association*, vol. 21, no. 153, pp. 65–66, 1926.

[106] D. Freedman and P. Diaconis, "On the histogram as a density estimator: L 2 theory," *Zeitschrift für Wahrscheinlichkeitstheorie und verwandte Gebiete*, vol. 57, no. 4, pp. 453–476, 1981.

[107] S. Downing and D. Socie, "Simple rainflow counting algorithms," *International Journal of Fatigue*, vol. 4, no. 1, pp. 31–40, 1982.

[108] E. Delhez, "Experimental and numerical study of first passage time," 2018.

[109] MathWorks, "Vectorization." `https://www.mathworks.com/help/matlab/matlab_prog/vectorization.html`, Apr. 2022.

[110] T. Kebig, V.-A. Nguyen, M. Bender, M. Schäfer, and F. Maas, "Repeatability and precision of different static deflection measurements on a real bridge-part under outdoor conditions in view of damage detection," *Proceedings of the 10th International Conference on Structural Health Monitoring of Intelligent Infrastructure*, vol. SHMII 10, 2021.

[111] A. Lipton and V. Kaushansky, "On the first hitting time density of an ornstein-uhlenbeck process," *arXiv preprint arXiv:1810.02390*, 2018.

[112] P. E. Kloeden and E. Platen, *Numerical Solution of Stochastic Differential Equations*, vol. 23. Springer Berlin, Heidelberg, 1992.

[113] P. E. Kloeden and E. Platen, "Higher-order implicit strong numerical schemes for stochastic differential equations," *Journal of statistical physics*, vol. 66, no. 1, pp. 283–314, 1992.

[114] S. D. Brown, R. Ratcliff, and P. L. Smith, "Evaluating methods for approximating stochastic differential equations," *Journal of mathematical psychology*, vol. 50, no. 4, pp. 402–410, 2006.

[115] N. Maia and J. Silva, *Theoretical and Experimental Modal Analysis*. Engineering dynamics series, Research Studies Press, 1997.

[116] Y.-W. Liu, "Hilbert transform and applications," in *Fourier Transform Applications* (S. Salih, ed.), ch. 12, pp. 291–300, Croatia: InTech, 2012.

[117] F. Lo Iacono, G. Navarra, and A. Pirrotta, "A damage identification procedure based on hilbert transform: experimental validation," *Structural Control and Health Monitoring*, vol. 19, no. 1, pp. 146–160, 2012.

[118] A. Koorosh, "Ecdf-based distance measure algorithms." `https://github.com/koo-ec/ECDF-based-Distance-Measure/releases/tag/v1.1`, Apr. 2020.

[119] F. J. Massey Jr, "The kolmogorov-smirnov test for goodness of fit," *Journal of the American statistical Association*, vol. 46, no. 253, pp. 68–78, 1951.

[120] N. H. Kuiper, "Tests concerning random points on a circle," in *Nederl. Akad. Wetensch. Proc. Ser. A*, vol. 63, pp. 38–47, 1960.

[121] T. W. Anderson, "On the Distribution of the Two-Sample Cramer-von Mises Criterion," *The Annals of Mathematical Statistics*, vol. 33, no. 3, pp. 1148 – 1159, 1962.

[122] T. W. Anderson and D. A. Darling, "Asymptotic theory of certain "goodness of fit" criteria based on stochastic processes," *The annals of mathematical statistics*, pp. 193–212, 1952.

[123] P. J. Bickel and D. A. Freedman, "Some asymptotic theory for the bootstrap," *The annals of statistics*, vol. 9, no. 6, pp. 1196–1217, 1981.

[124] C. Dowd, "A new ecdf two-sample test statistic," *arXiv preprint arXiv:2007.01360*, 2020.

[125] V. Denoël, "Analyse de structures soumises au vent turbulent: de l'approche stochastique fréquentielle au transitoire non linéaire," 2002.

[126] "Eurocode en 1991–1–4."

[127] J. Heremans and V. Denoël, "Quality assessment of synthetic wind turbulence," in *Young Engineers Colloquium 2020*, 2020.

[128] V. Denoël, *Application des méthodes d'analyse stochastique à l'étude des effets du vent sur les structures du génie civil*. PhD thesis, ULiège - Université de Liège, 2005.

[129] Supermagnete, "Cube magnétique aimant cube 5 mm doré n50." `https://www.supermagnete.be/fre/aimants-cube-neodyme/cube-magnetique-5mm_W-05-N50-G`, May 2022.

[130] V. Denoël and E. Detournay, "Multiple scales solution for a beam with a small bending stiffness," *Journal of engineering mechanics*, vol. 136, no. 1, pp. 69–77, 2010.

[131] T. Kebig, *Reference measurements and simulations of static and dynamic characteristics of prestressed concrete bridges under outdoor conditions for structural health monitoring*. PhD thesis, Unilu - University of Luxembourg, Luxembourg, 2021.

[132] T. Kebig, N. Olbermann, M. Bender, A. Zürbes, and S. Maas, "Contactless measuring systems for structural health monitoring of bridges," in *Proceedings of the 1st Conference of the European Association on Quality Control of Bridges and Structures: EUROSTRUCT 2021 1*, pp. 269–276, Springer, 2022.

[133] V. H. Nguyen, S. Schommer, A. Zürbes, and S. Maas, "Structural health monitoring based on static measurements with temperature compensation," *Quality Specifications for Roadway Bridges, Standardization at a European Level*, 2016.

[134] D. Erdenebat, "Condition assessment of bridge structures by damage localisation based on the dad-method and close-range uav photogrammetry," 2020.

[135] J. Mahowald, *Evaluation of dynamic damage indicators on real-life civil engineering structures: Measurement uncertainty and environmental influences considered*. PhD thesis, Unilu - University of Luxembourg, Luxembourg, 2013.

[136] K. Dakhili, *Expected PhD thesis to come*. PhD thesis.

[137] V. H. Nguyen, J. Mahowald, J.-C. Golinval, and S. Maas, "Damage detection in civil engineering structure considering temperature effect," in *Dynamics of Civil Structures, Volume 4: Proceedings of the 32nd IMAC, A Conference and Exposition on Structural Dynamics, 2014*, pp. 187–196, Springer, 2014.

[138] V. H. Nguyen, S. Schommer, S. Maas, and A. Zürbes, "Static load testing with temperature compensation for structural health monitoring of bridges," *Engineering Structures*, vol. 127, pp. 700–718, 2016.

[139] K. Dakhili, T. Kebig, M. Schäfer, M. Maas, M. Bender, and A. Zürbes, "Temperature effect on static and quasi-static bridge measurements," in *Life-Cycle of Structures and Infrastructure Systems*, pp. 3174–3181, CRC Press, 2023.

[140] D. Waldmann, D. Erdenebat, F. Scherbaum, and S. Maas, "Investigation of temperature-dependent stiffness variation of a layer of asphalt and their possible effect on the deformation behaviour of concrete structures," in *6th International Conference on Experimental Vibration Analysis for Civil Engineering Structures, Duebendorf 2015*, 2015.

[141] M. Parziale, L. Lomazzi, M. Giglio, and F. Cadini, "Vibration-based structural health monitoring exploiting a combination of convolutional neural

networks and autoencoders for temperature effects neutralization," *Structural Control and Health Monitoring*, vol. 29, no. 11, p. e3076, 2022.

[142] S. Maas, S. Schommer, V. H. Nguyen, D. Waldmann, J. Mahowald, and A. Zürbes, "Some remarks on the influence of temperature-variations, non-linearities, repeatability and ageing on modal-analysis for structural health monitoring of real bridges," in *MATEC Web of Conferences*, vol. 24, EDP Sciences, 2015.

[143] M. Waltering, V. Bungard, D. Waldmann, A. Zürbes, S. Maas, and G. De Roeck, "Damage assessment of civil engineering structures by the observation of non-linear dynamic behaviour," in *Proceedings of the International Conference on Experimental Vibration Analysis for Civil Engineering Structures*, 2007.

[144] A. Nobile, L. Ricciardi, and L. Sacerdote, "Exponential trends of ornstein–uhlenbeck first-passage-time densities," *Journal of Applied Probability*, vol. 22, no. 2, pp. 360–369, 1985.

Appendix A

Ornstein-Uhlenbeck process

The Ornstein-Uhlenbeck process is defined as

$$\mathrm{d}X_t = \beta(\alpha - X_t)\mathrm{d}t + \sigma \mathrm{d}W_t \tag{A.1}$$

where α is a constant drift, $\beta > 0$, $\sigma > 0$ and W_t is a Wiener process.

The average FPT and STD of FPT values are given in [144]:

$$\text{average FPT}\left(X_f|X_0\right) = t_1\left(X_f|X_0\right) \tag{A.2}$$

$$\text{STD of FPT}\left(X_f|X_0\right) = \sqrt{t_2\left(X_f|X_0\right) - t_1^2\left(X_f|X_0\right)} \tag{A.3}$$

where

$$t_1\left(X_f|X_0\right) = \theta\left\{\sqrt{\pi}\left[\phi_1\left(\frac{X_f}{\sigma\sqrt{\theta}}\right) - \phi_1\left(\frac{X_0}{\sigma\sqrt{\theta}}\right)\right] + \psi_1\left(\frac{X_f}{\sigma\sqrt{\theta}}\right) - \psi_1\left(\frac{X_0}{\sigma\sqrt{\theta}}\right)\right\} \tag{A.4}$$

$$\begin{aligned} t_2\left(X_f|X_0\right) = {} & 2\theta t_1\left(X_f|X_0\right)\left[\sqrt{\pi}\phi_1\left(\frac{X_f}{\sigma\sqrt{\theta}}\right) + \psi_1\left(\frac{X_f}{\sigma\sqrt{\theta}}\right)\right] \\ & + 2\theta^2\left\{\sqrt{\pi}\ln\left(2\right)\left[\phi_1\left(\frac{X_f}{\sigma\sqrt{\theta}}\right) - \phi_1\left(\frac{X_0}{\sigma\sqrt{\theta}}\right)\right]\right. \\ & \left. -\sqrt{\pi}\left[\phi_2\left(\frac{X_f}{\sigma\sqrt{\theta}}\right) - \phi_2\left(\frac{X_0}{\sigma\sqrt{\theta}}\right)\right] - \psi_2\left(\frac{X_f}{\sigma\sqrt{\theta}}\right) + \psi_2\left(\frac{X_0}{\sigma\sqrt{\theta}}\right)\right\} \end{aligned} \tag{A.5}$$

$$\phi_1\left(z\right) = \mathrm{Erfi}\left(z\right) = \int_0^z \exp(t^2)\mathrm{d}t \tag{A.6}$$

$$\phi_2\left(z\right) = \sum_{n=0}^{\infty} \frac{z^{2n+3}}{\left(n+1\right)!\left(2n+3\right)} \sum_{k=0}^{n} \frac{1}{2k+1} \tag{A.7}$$

$$\psi_1(z) = \sum_{n=0}^{\infty} \frac{2^n}{(n+1)(2n+1)!!} z^{2n+2} \tag{A.8}$$

$$\psi_2(z) = \sum_{n=0}^{\infty} \frac{2^n z^{2n+4}}{(2n+3)!!(n+2)} \sum_{k=0}^{n} \frac{1}{k+1} \tag{A.9}$$

with $\theta = \frac{1}{\beta}$.

The theoretical values for the PDF of FPT are given in [111] by solving the backward problem. Firstly Equation (A.1) is rewritten as follows:

$$\mathrm{d}\bar{X}_{\bar{t}} = -\bar{X}_{\bar{t}}\mathrm{d}\bar{t} + \mathrm{d}W_{\bar{t}} \tag{A.10}$$

where $\bar{t} = \beta t$, $\bar{X} = \frac{\sqrt{\beta}}{\sigma}(X - \alpha)$, $\bar{X}_0 = \frac{\sqrt{\beta}}{\sigma}(X_0 - \alpha)$ and $\bar{X}_f = \frac{\sqrt{\beta}}{\sigma}(X_f - \alpha)$.

The backward equation for the cumulative hitting probability $G\left(\bar{t}, \bar{X}_0\right)$ reads

$$G_t\left(\bar{t}, \bar{X}_0\right) = -\bar{X}_0 G_{\bar{X}_0}\left(\bar{t}, \bar{X}_0\right) + \frac{1}{2} G_{\bar{X}_0\bar{X}_0}\left(\bar{t}, \bar{X}_0\right) \tag{A.11}$$

with $G\left(0, \bar{X}_0\right) = 0$ and $G\left(\bar{t}, \bar{X}_f\right) = 1$.

Finally, the first hitting density is given by $g\left(\bar{t}, \bar{X}_0\right) = G_t\left(\bar{t}, \bar{X}_0\right)$.

Appendix B

Numerical Model

Stiffness and mass matrices of the elements of the numerical model

In this Appendix, the stiffness, consistent-mass and consistent geometric-stiffness are written for a given element of length L [80]. Each beam element contains 2 nodes with two displacements allowed for each node: the transversal displacement v and the in-plane rotation θ. The parameters E and I are respectively the Young's modulus and the inertia of the element. The parameter $\bar{m}$ takes into account the uniformly distributed mass of the element and the parameter N is the constant prestressing force applied to the element.

Stiffness matrix

This matrix takes into account the stiffness of the elements at their nodes. For the special case of a uniform beam segment, the stiffness matrix can be expressed by

$$\begin{Bmatrix} f_{S1} \\ f_{S2} \\ f_{S3} \\ f_{S4} \end{Bmatrix} = \frac{2EI}{L^3} \begin{bmatrix} 6 & -6 & 3L & 3L \\ -6 & 6 & -3L & -3L \\ 3L & -3L & 2L^2 & L^2 \\ 3L & -3L & L^2 & 2L^2 \end{bmatrix} \begin{Bmatrix} v_1 \\ v_2 \\ \theta_1 \\ \theta_2 \end{Bmatrix}$$

Consistent-mass matrix

This matrix takes into account the mass distribution of the elements. In the special case of a beam with uniformly distributed mass the consistent-mass matrix can be written as

$$\begin{Bmatrix} f_{I1} \\ f_{I2} \\ f_{I3} \\ f_{I4} \end{Bmatrix} = \frac{\bar{m}L}{420} \begin{bmatrix} 156 & 54 & 22L & -13L \\ 54 & 156 & 13L & -22L \\ 22L & 13L & 4L^2 & -3L^2 \\ -13L & -22L & -3L^2 & 4L^2 \end{bmatrix} \begin{Bmatrix} \ddot{v}_1 \\ \ddot{v}_2 \\ \ddot{\theta}_1 \\ \ddot{\theta}_2 \end{Bmatrix}$$

Consistent geometric-stiffness matrix

This matrix takes into account the prestressing force within the elements due to the pre-stress mass. In the particular case where the axial force is constant along the length of the element, the consistent geometric-matrix is

$$\begin{Bmatrix} f_{G1} \\ f_{G2} \\ f_{G3} \\ f_{G4} \end{Bmatrix} = \frac{N}{30L} \begin{bmatrix} 36 & -36 & 3L & 3L \\ -36 & 36 & -3L & -3L \\ 3L & -3L & 4L^2 & -L^2 \\ 3L & -3L & -L^2 & 4L^2 \end{bmatrix} \begin{Bmatrix} v_1 \\ v_2 \\ \theta_1 \\ \theta_2 \end{Bmatrix}$$

Updated numerical model parameters

In addition to parameter values given in Tables 4.1 and 4.2, the parameter values used for the updated numerical model are listed in Table B.1.

TABLE B.1: Parameter values of the updated numerical model.

Parameter	Value	Units
Supports rotational stiffness	10000	[kg/s^2]
Prestress mass	1.707	[kg]
Shaker head mass	0.03	[kg]
Stinger stiffness	$4.617 \cdot 10^6$	[kg/s^2]
Shaker moving mass	0.015	[kg]
Shaker suspension stiffness	4000	[kg/s^2]
Shaker mass	1.7	[kg]

Appendix C

Empirical CDFs of distances from Chapter 5

C.1 Without temperature compensation

C.1.1 Test A: First bending mode

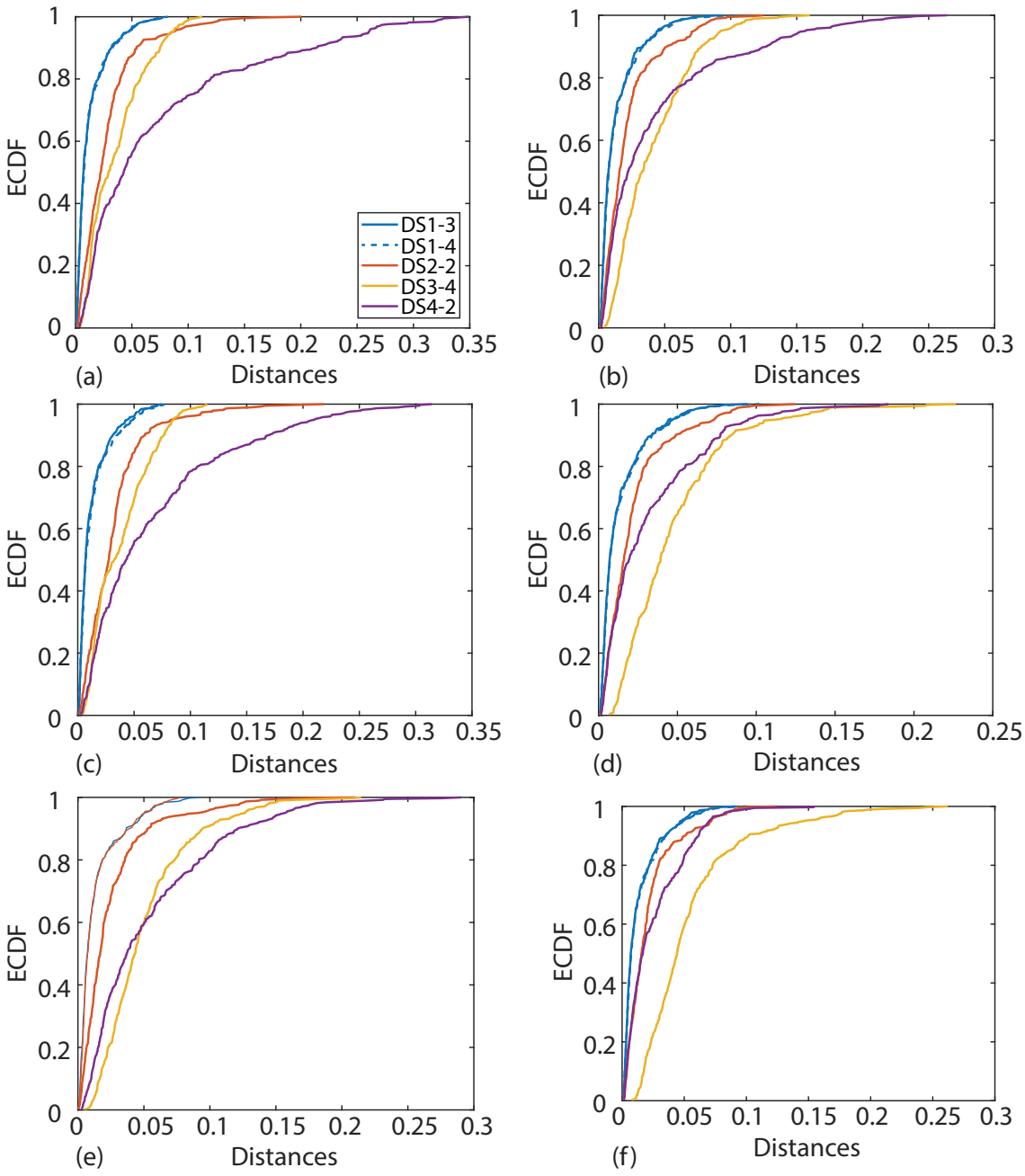

FIGURE C.1: ECDFs of the AD distances for accelerometers (a) 4, (b) 14, (c) 5, (d) 15, (e) 6, and (f) 16 for Test A in DS1-3, DS1-4, DS2-2, DS3-4, and DS4-2.

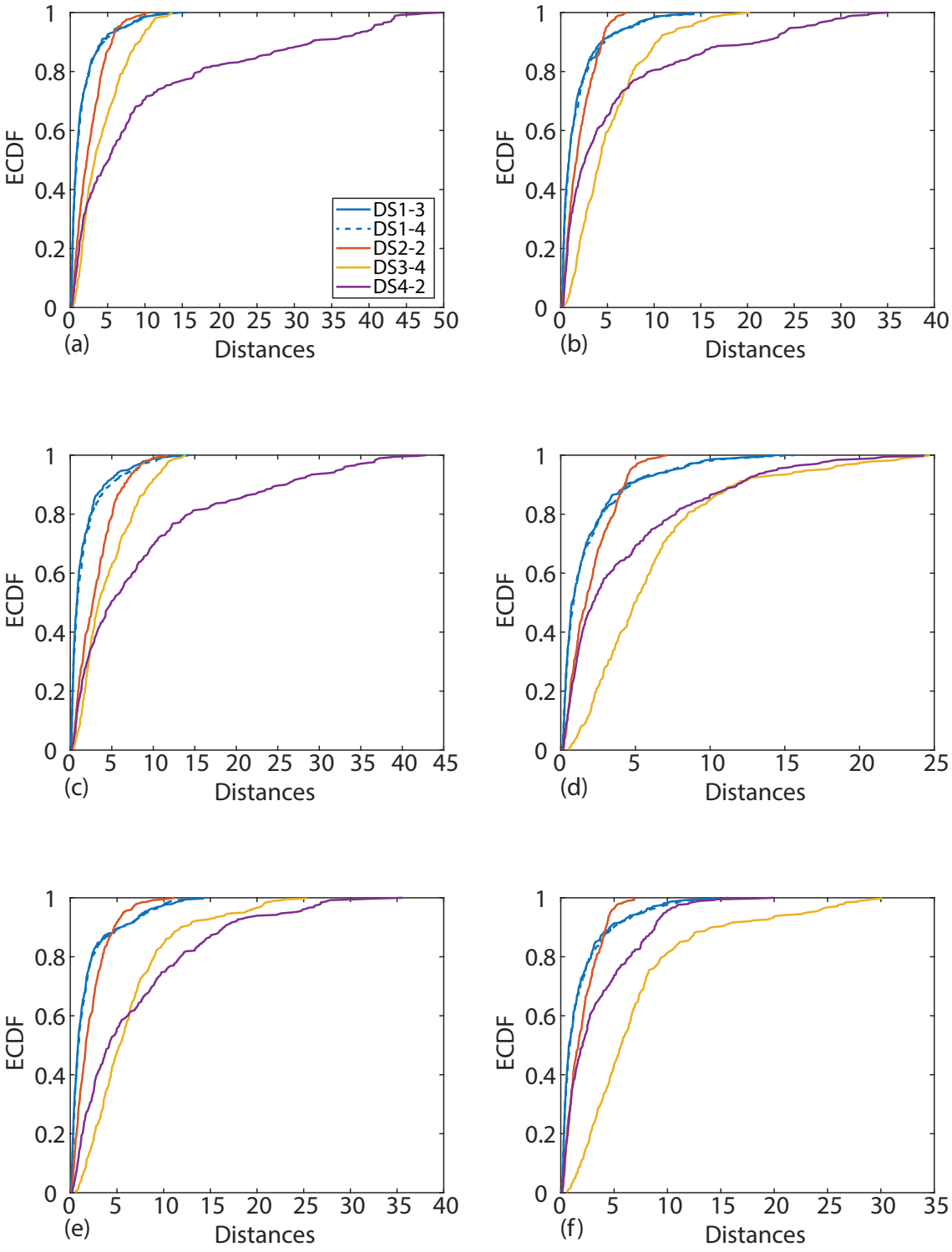

FIGURE C.2: ECDFs of the CVM distances for accelerometers (a) 4, (b) 14, (c) 5, (d) 15, (e) 6, and (f) 16 for Test A in DS1-3, DS1-4, DS2-2, DS3-4, and DS4-2.

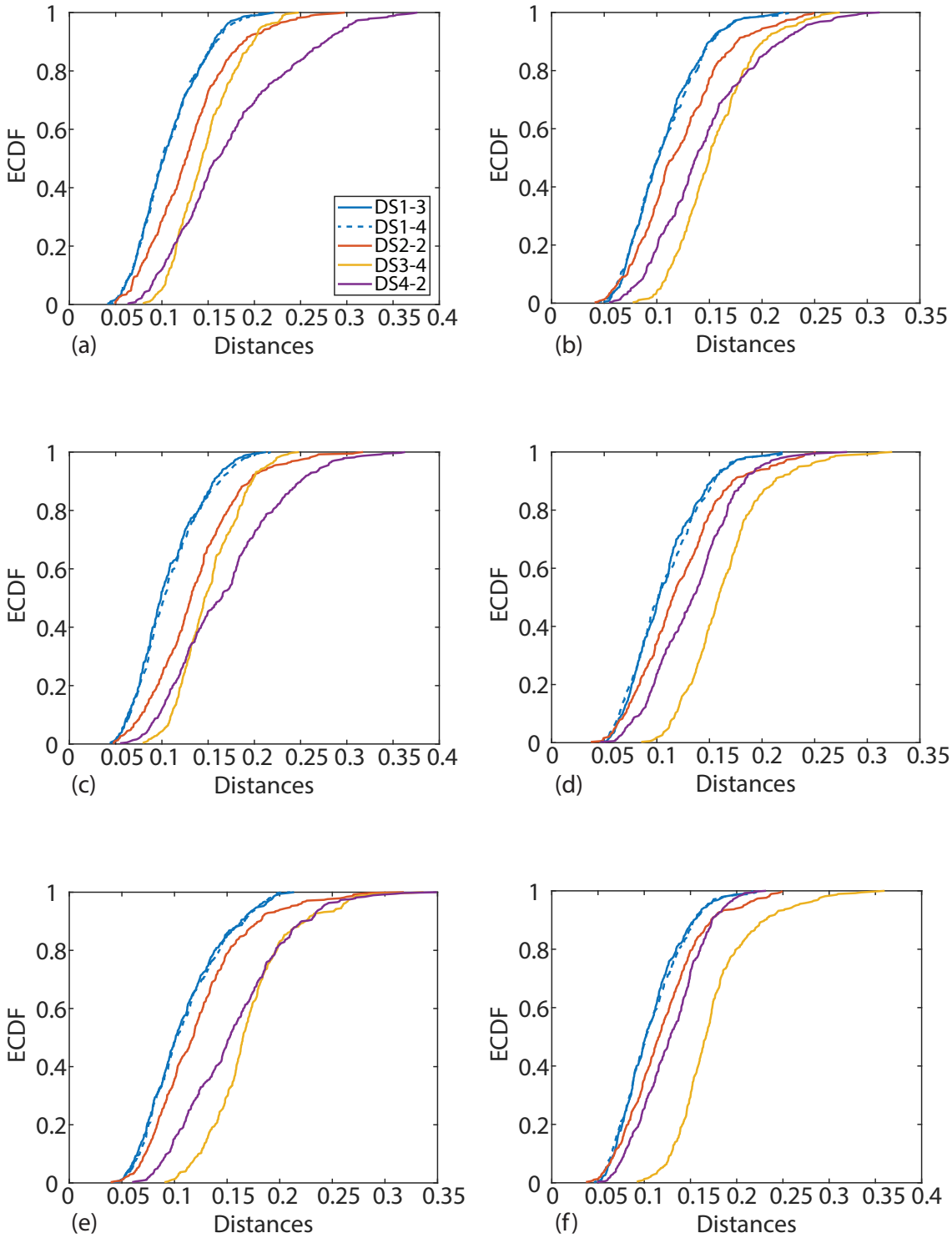

FIGURE C.3: ECDFs of the K distances for accelerometers (a) 4, (b) 14, (c) 5, (d) 15, (e) 6, and (f) 16 for Test A in DS1-3, DS1-4, DS2-2, DS3-4, and DS4-2.

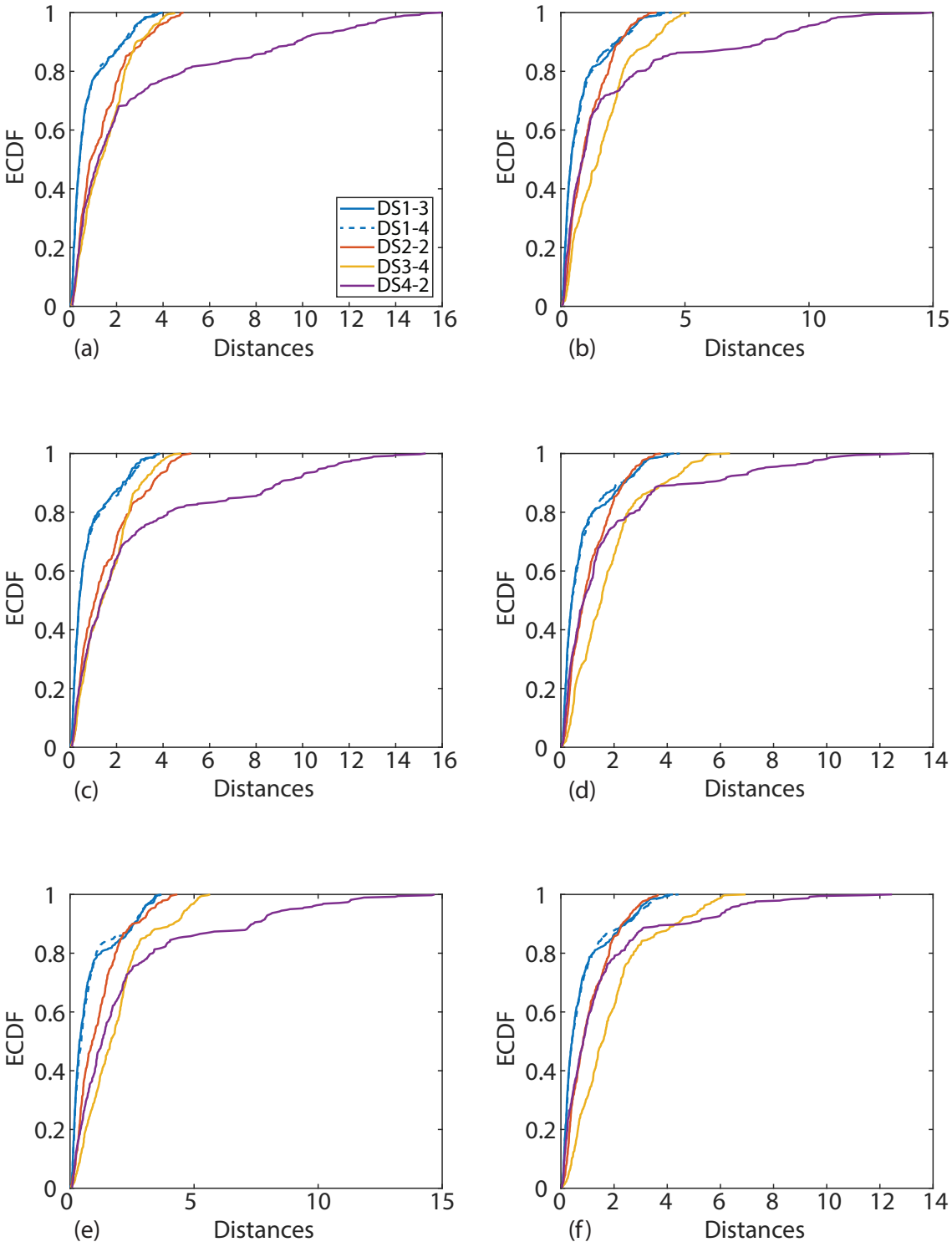

FIGURE C.4: ECDFs of the W distances for accelerometers (a) 4, (b) 14, (c) 5, (d) 15, (e) 6, and (f) 16 for Test A in DS1-3, DS1-4, DS2-2, DS3-4, and DS4-2.

C.1.2 Test B: First bending and torsional modes

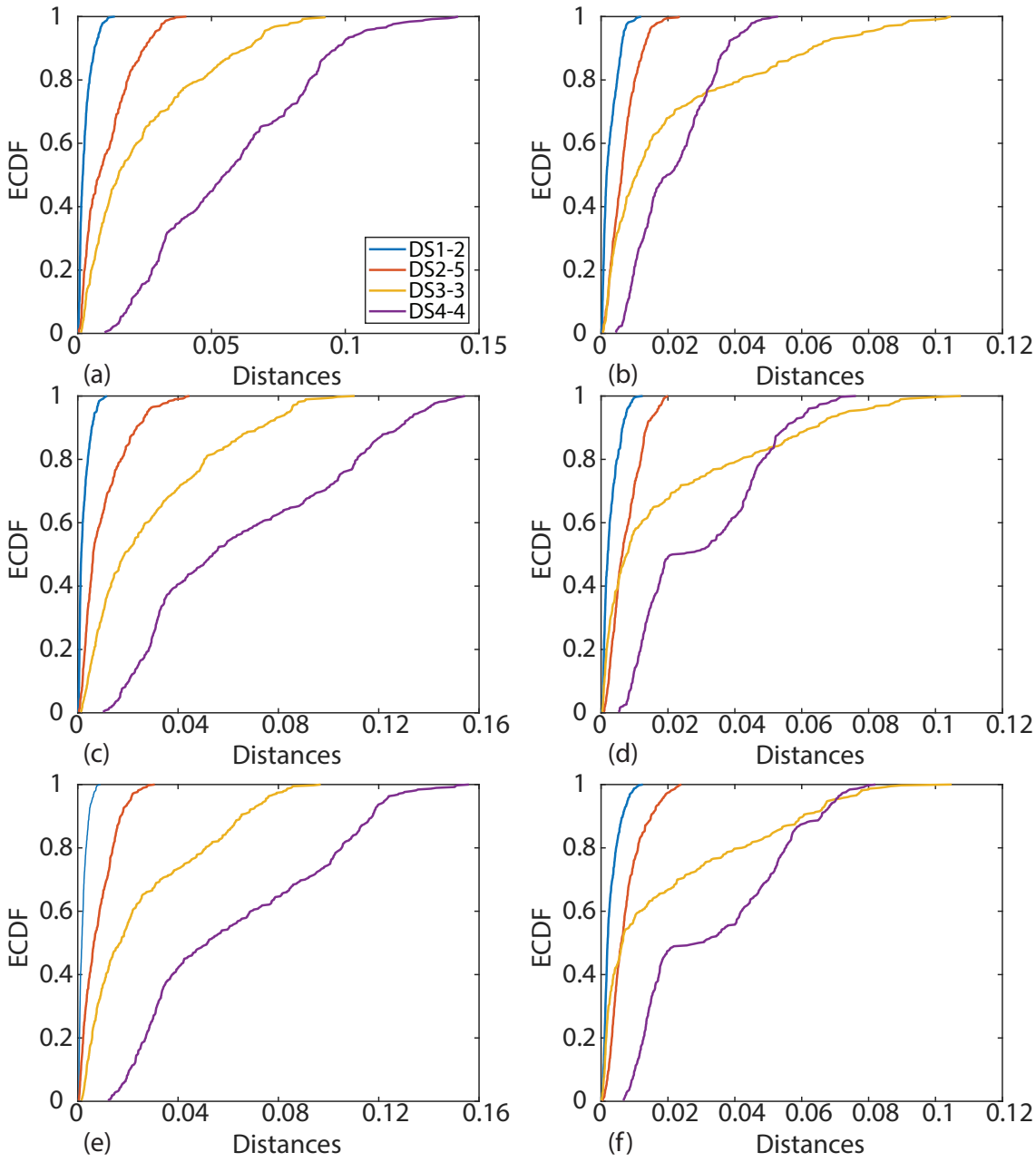

FIGURE C.5: ECDFs of the AD distances for accelerometers (a) 4, (b) 14, (c) 5, (d) 15, (e) 6, and (f) 16 for Test B in DS1-2, DS2-5, DS3-3, and DS4-4.

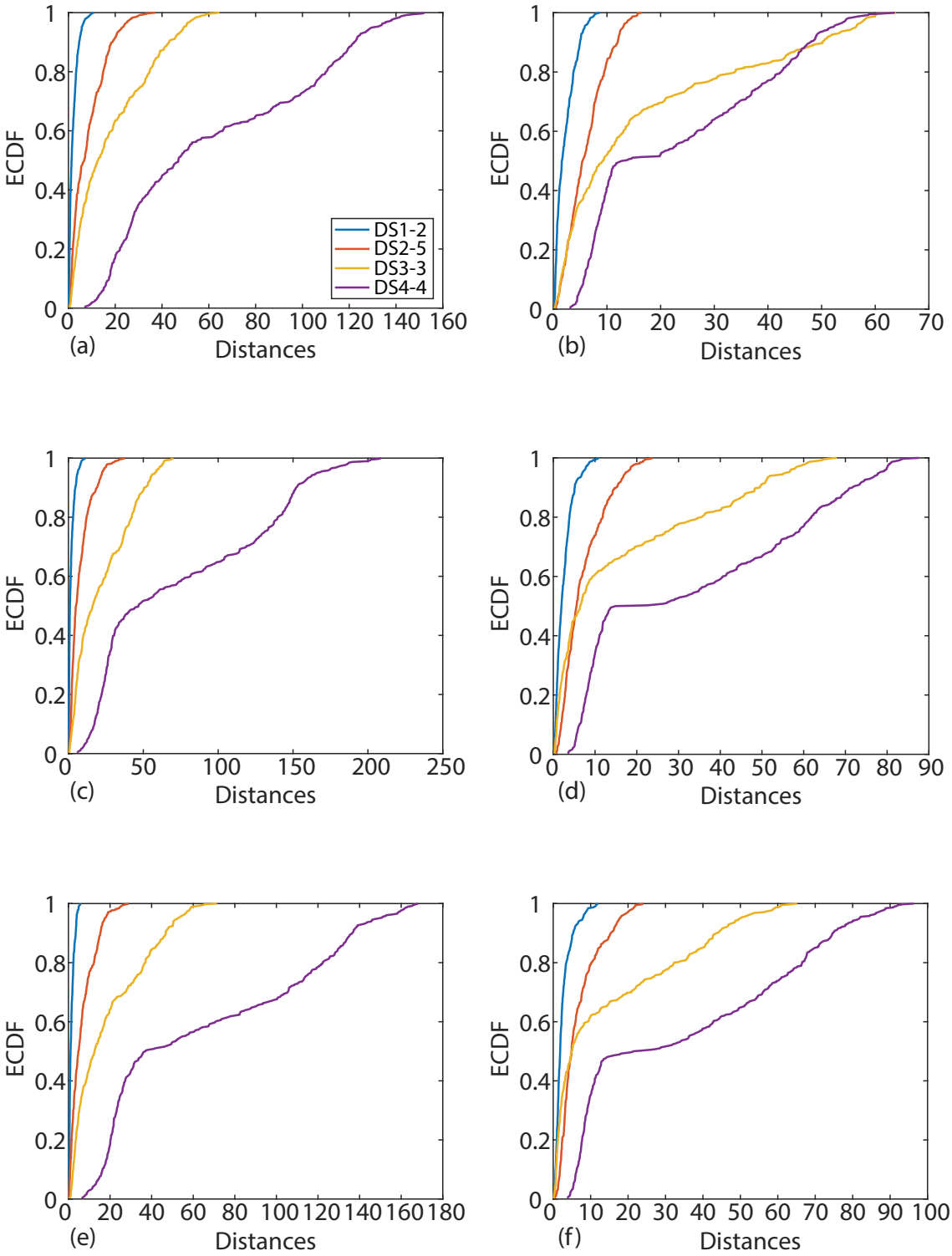

FIGURE C.6: ECDFs of the CVM distances for accelerometers (a) 4, (b) 14, (c) 5, (d) 15, (e) 6, and (f) 16 for Test B in DS1-2, DS2-5, DS3-3, and DS4-4.

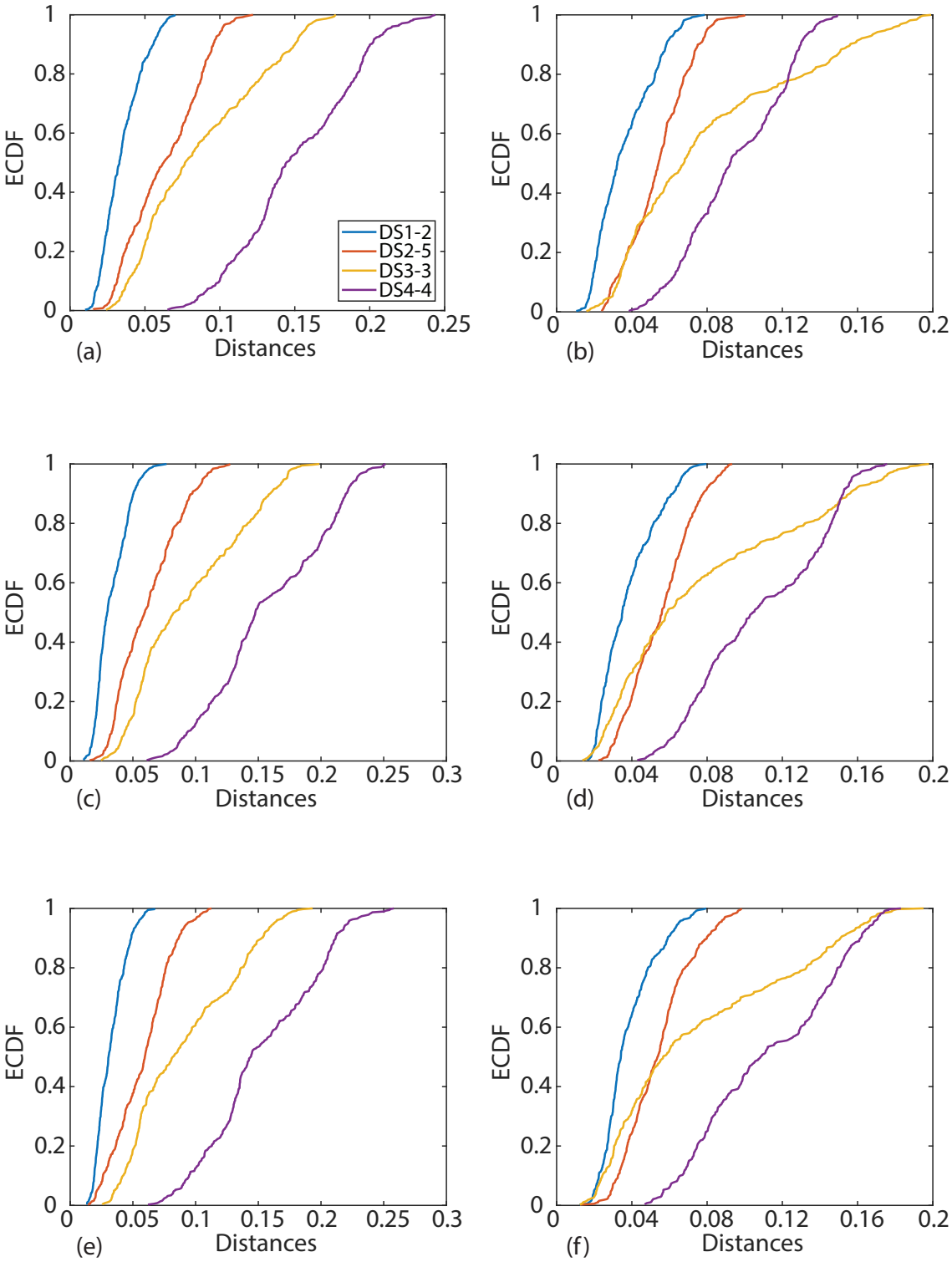

FIGURE C.7: ECDFs of the KS distances for accelerometers (a) 4, (b) 14, (c) 5, (d) 15, (e) 6, and (f) 16 for Test B in DS1-2, DS2-5, DS3-3, and DS4-4.

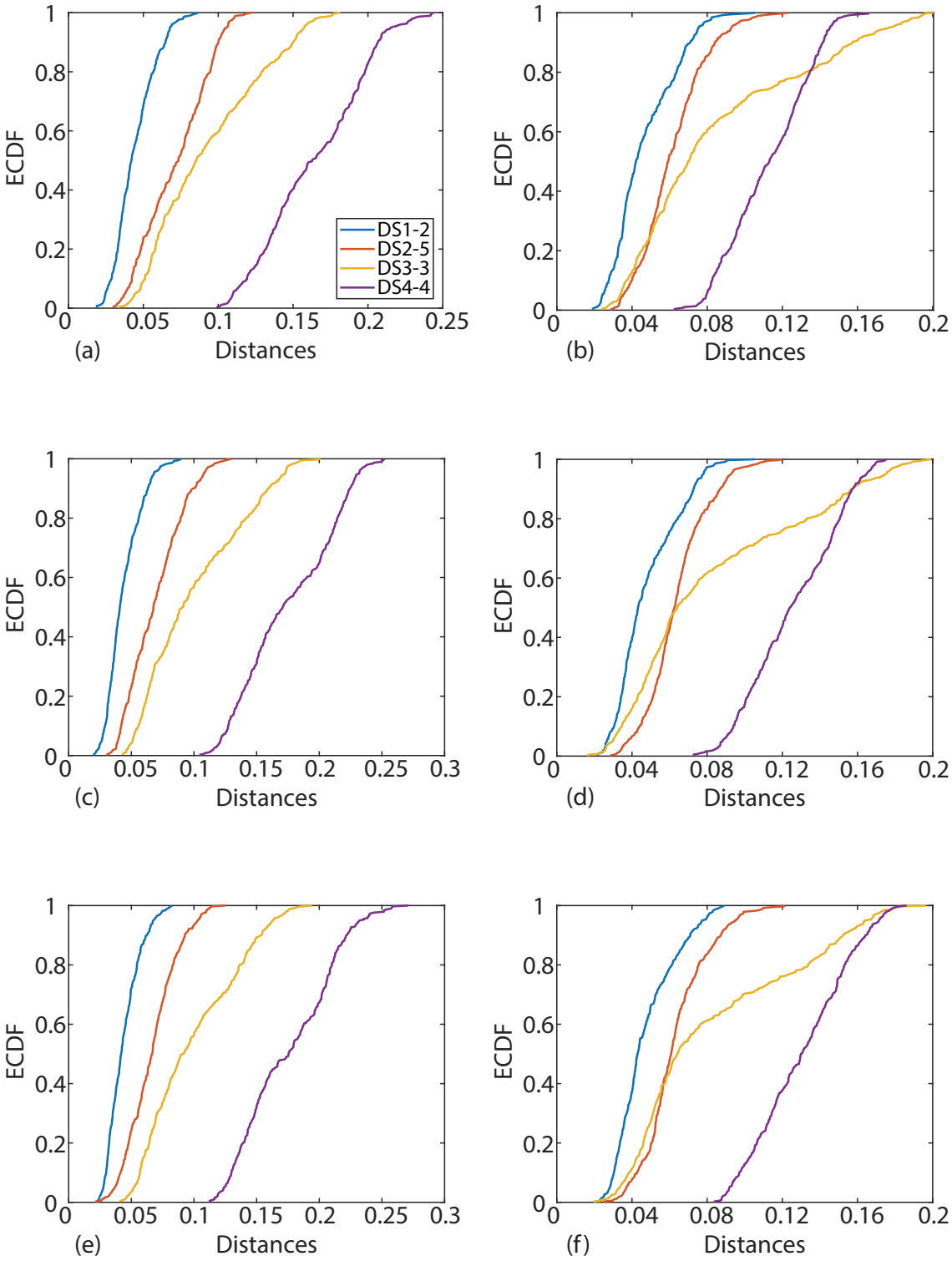

FIGURE C.8: ECDFs of the K distances for accelerometers (a) 4, (b) 14, (c) 5, (d) 15, (e) 6, and (f) 16 for Test B in DS1-2, DS2-5, DS3-3, and DS4-4.

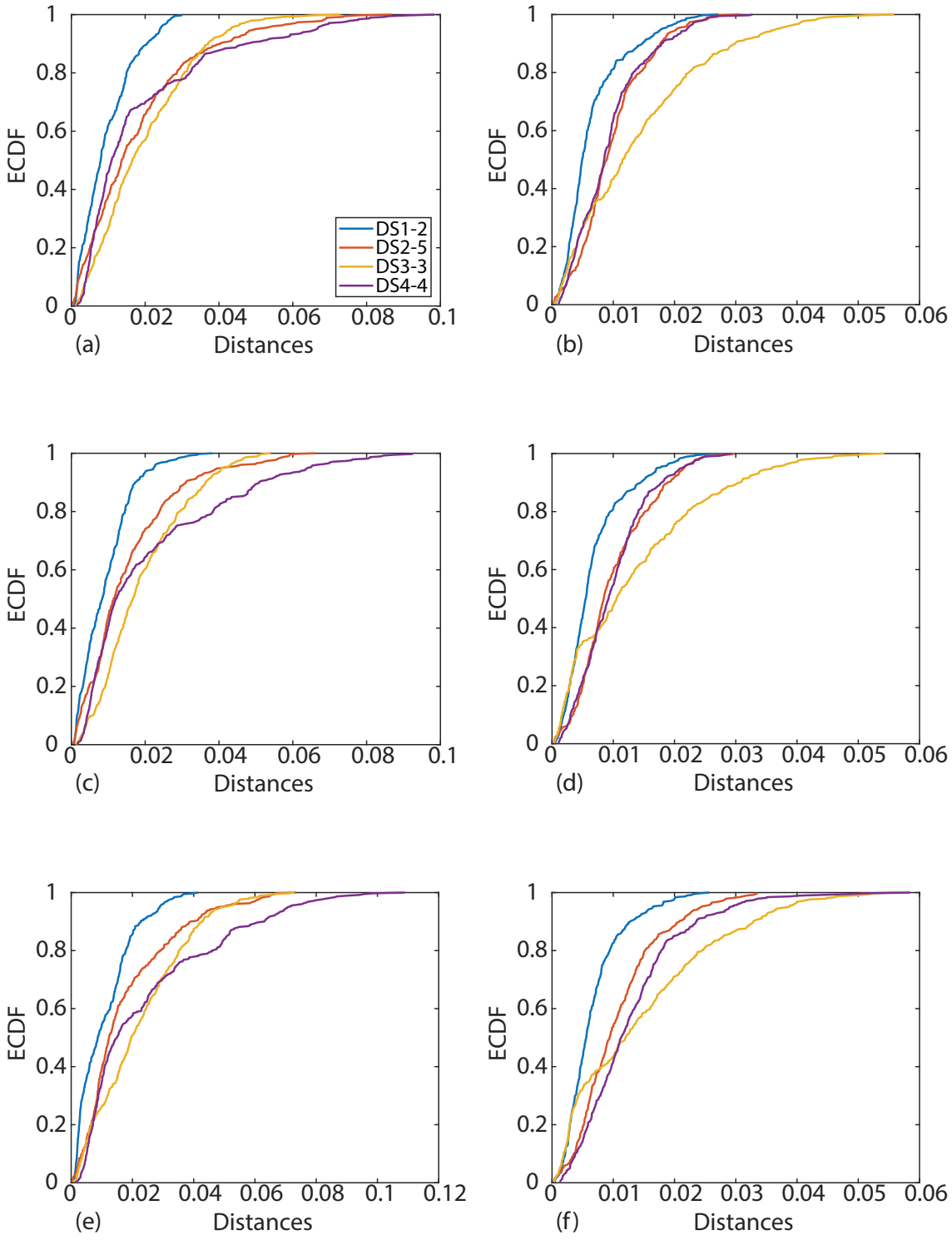

FIGURE C.9: ECDFs of the WAD distances for accelerometers (a) 4, (b) 14, (c) 5, (d) 15, (e) 6, and (f) 16 for Test B in DS1-2, DS2-5, DS3-3, and DS4-4.

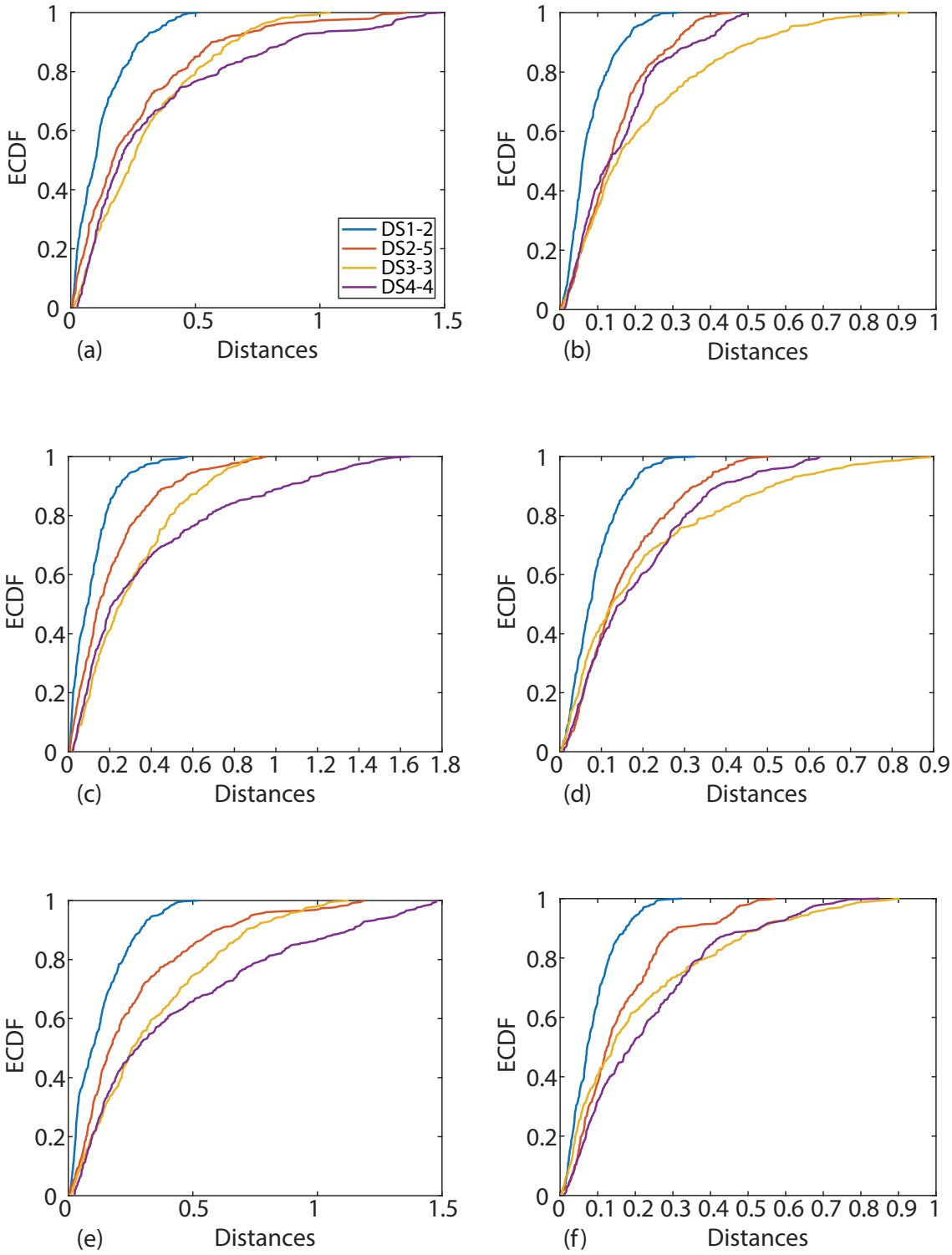

FIGURE C.10: ECDFs of the W distances for accelerometers (a) 4, (b) 14, (c) 5, (d) 15, (e) 6, and (f) 16 for Test B in DS1-2, DS2-5, DS3-3, and DS4-4.

C.1.3 Test A in another configuration: First bending mode

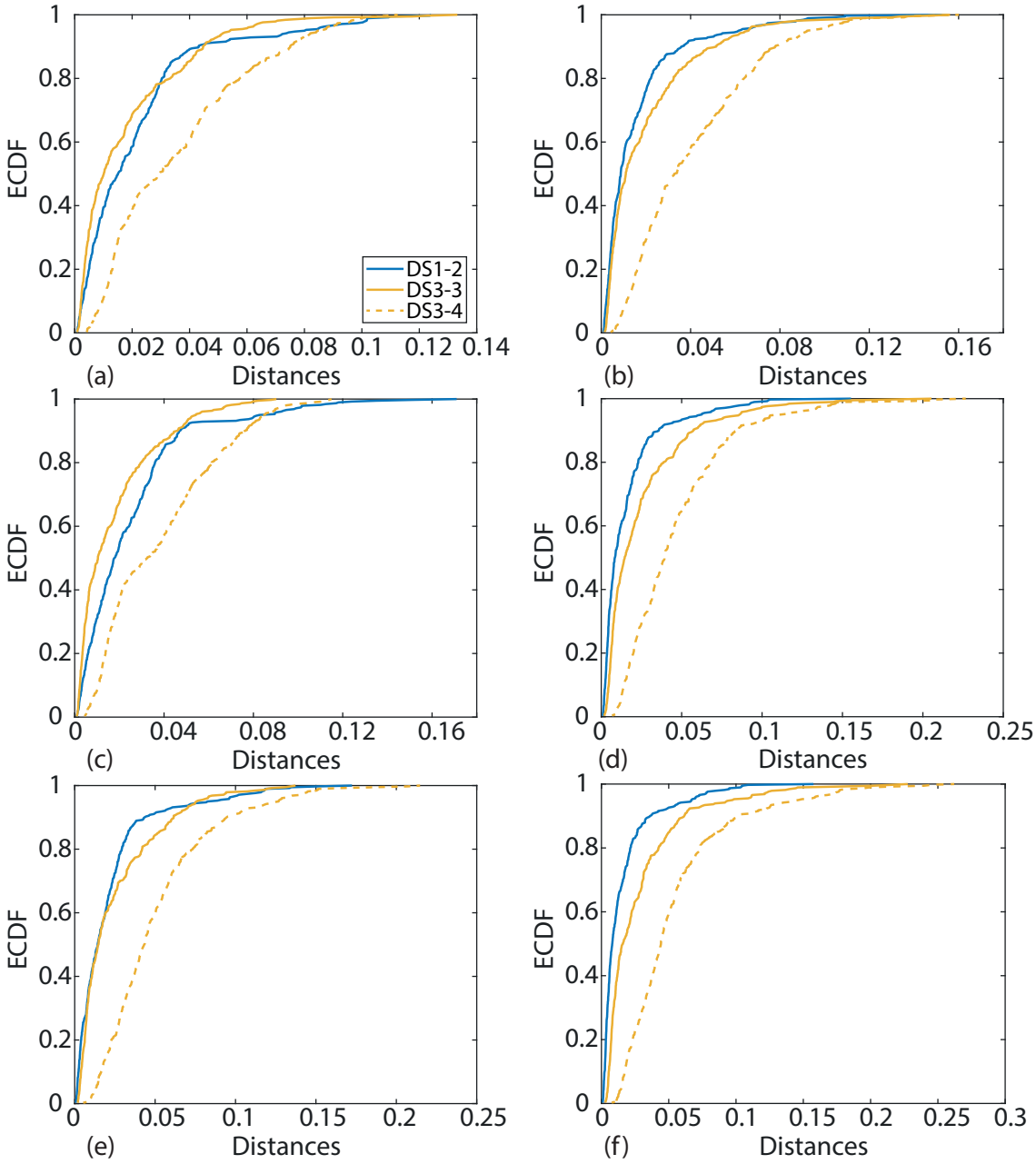

FIGURE C.11: ECDFs of the AD distances for accelerometers (a) 4, (b) 14, (c) 5, (d) 15, (e) 6, and (f) 16 for Test A in DS1-2, DS3-3, and DS3-4.

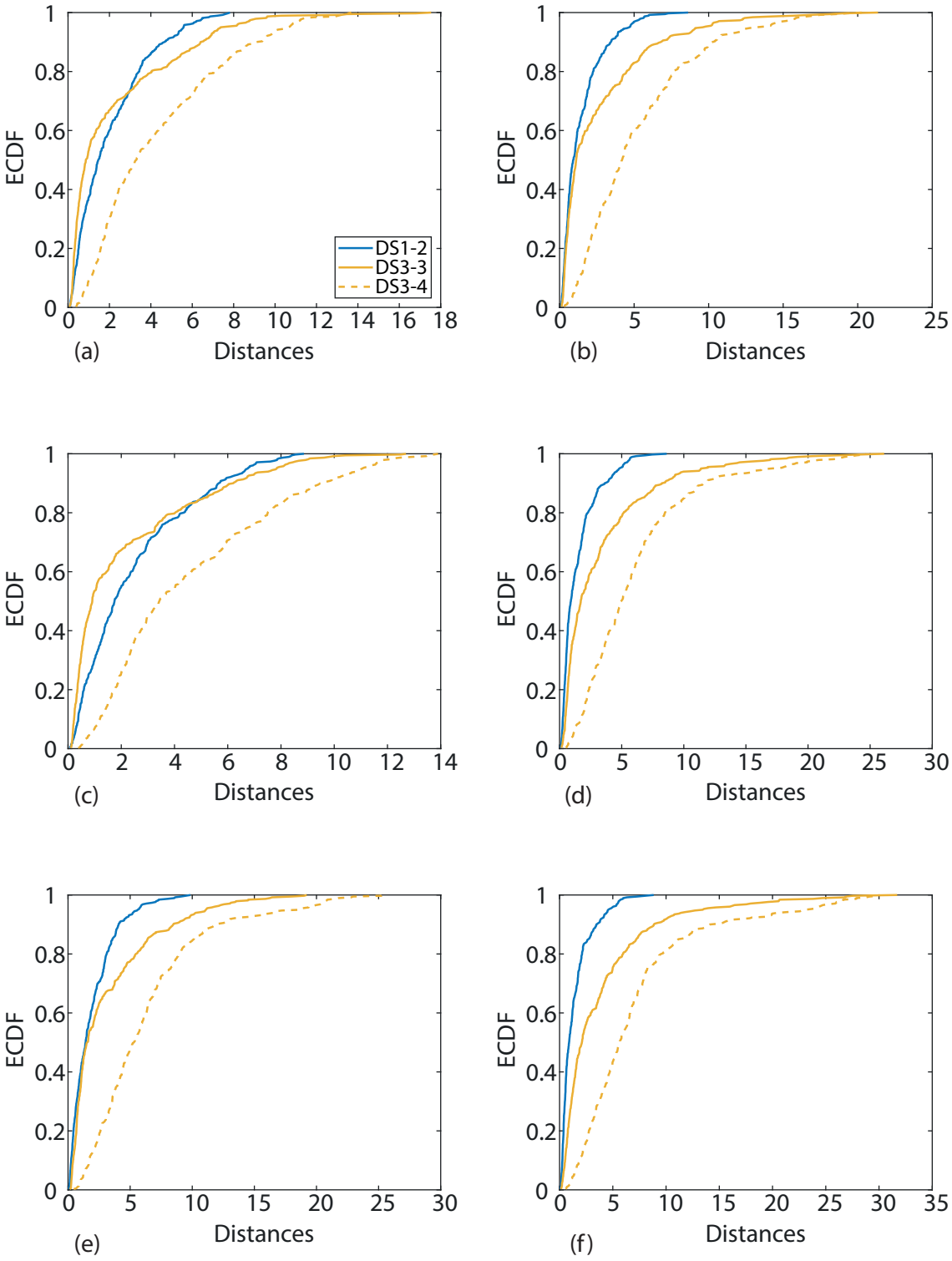

FIGURE C.12: ECDFs of the CVM distances for accelerometers (a) 4, (b) 14, (c) 5, (d) 15, (e) 6, and (f) 16 for Test A in DS1-2, DS3-3, and DS3-4.

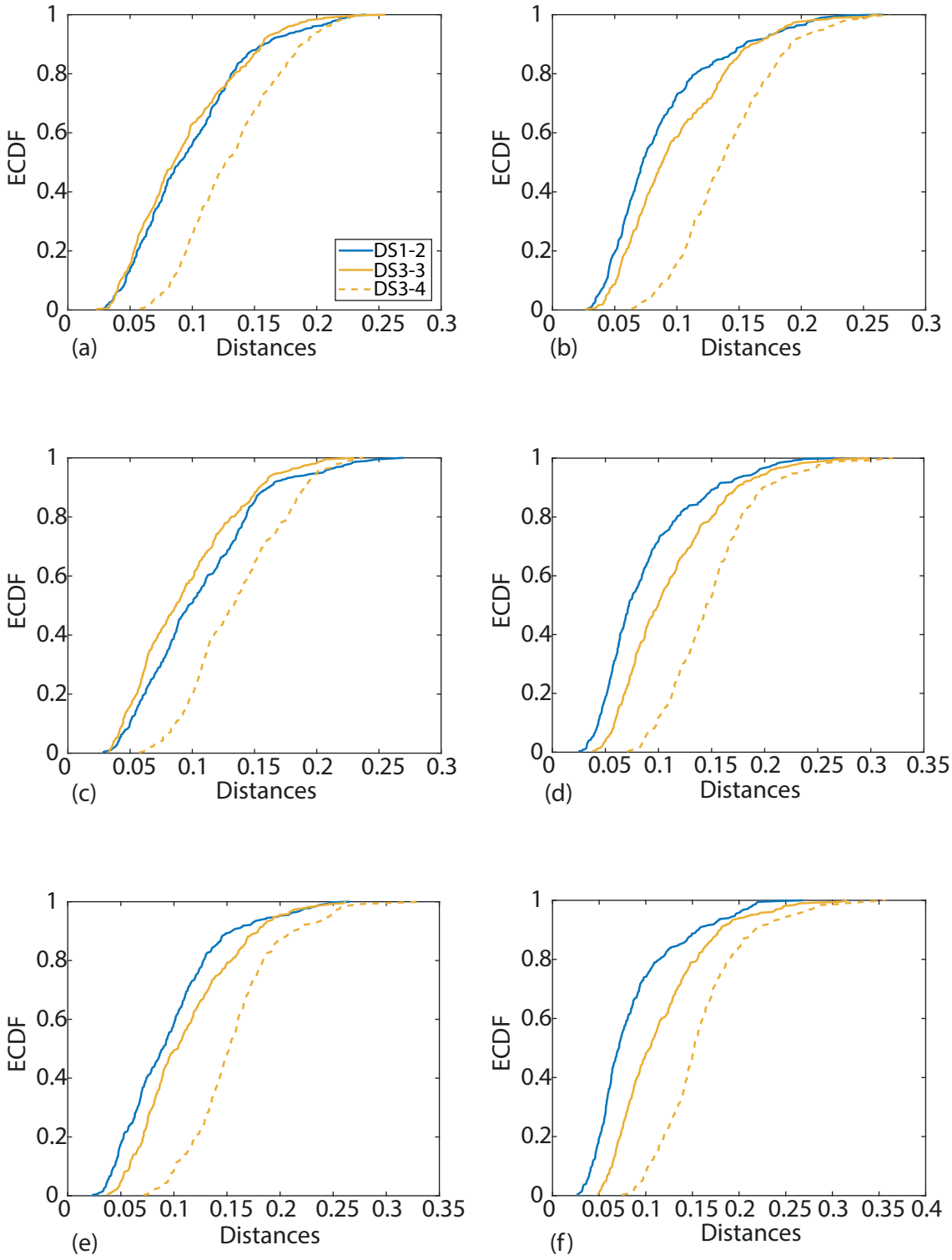

FIGURE C.13: ECDFs of the KS distances for accelerometers (a) 4, (b) 14, (c) 5, (d) 15, (e) 6, and (f) 16 for Test A in DS1-2, DS3-3, and DS3-4.

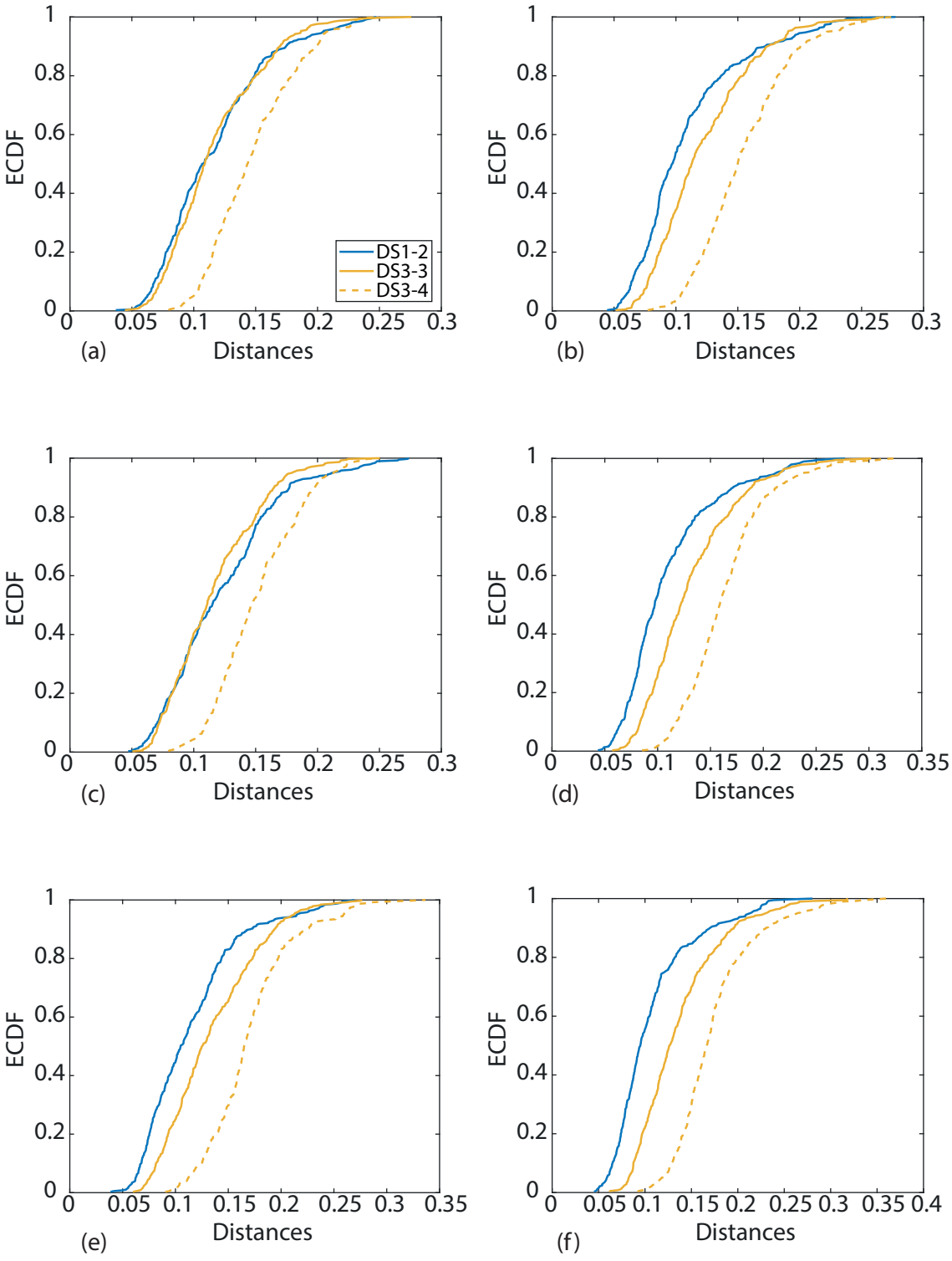

FIGURE C.14: ECDFs of the K distances for accelerometers (a) 4, (b) 14, (c) 5, (d) 15, (e) 6, and (f) 16 for Test A in DS1-2, DS3-3, and DS3-4.

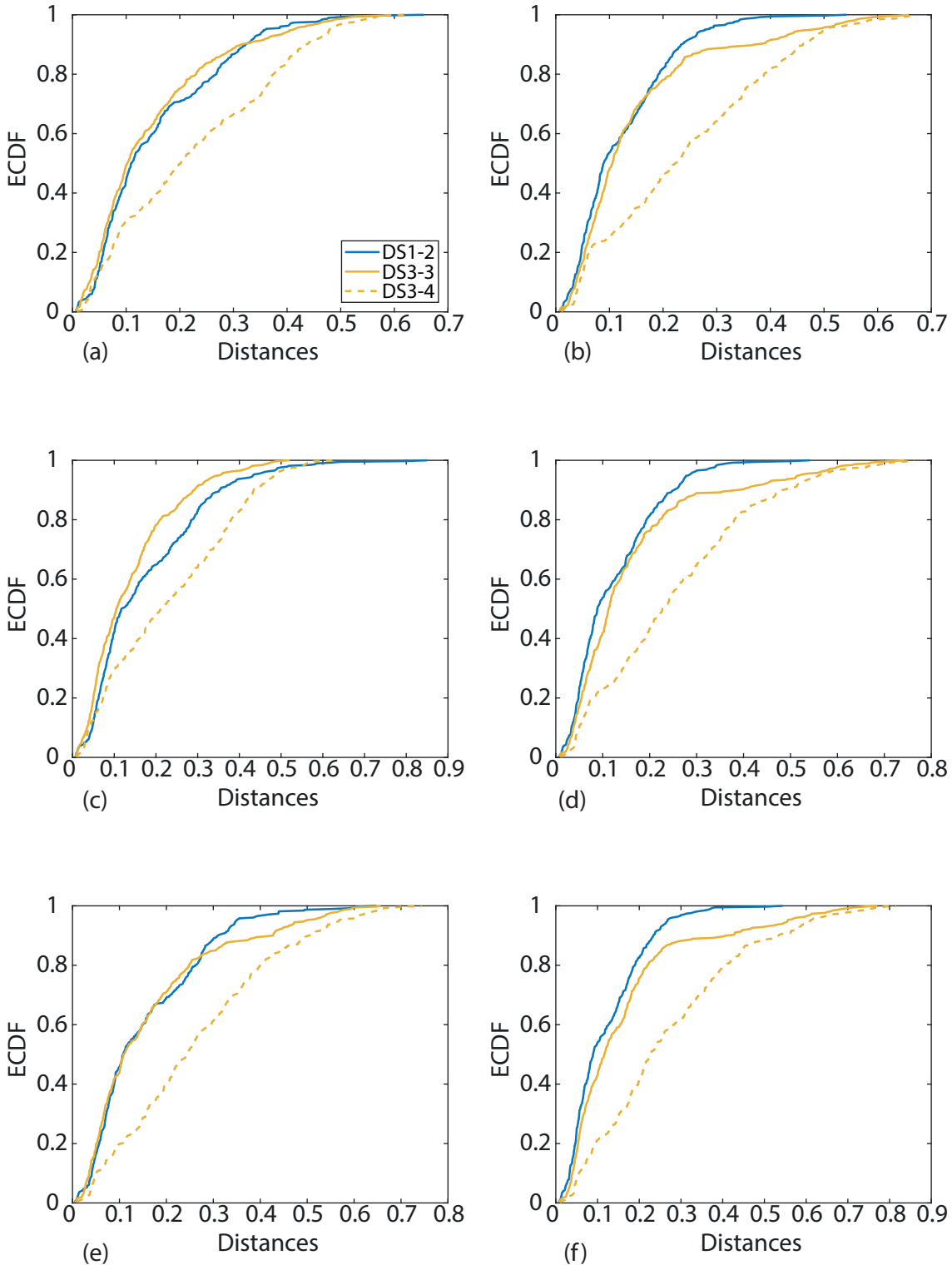

FIGURE C.15: ECDFs of the WAD distances for accelerometers (a) 4, (b) 14, (c) 5, (d) 15, (e) 6, and (f) 16 for Test A in DS1-2, DS3-3, and DS3-4.

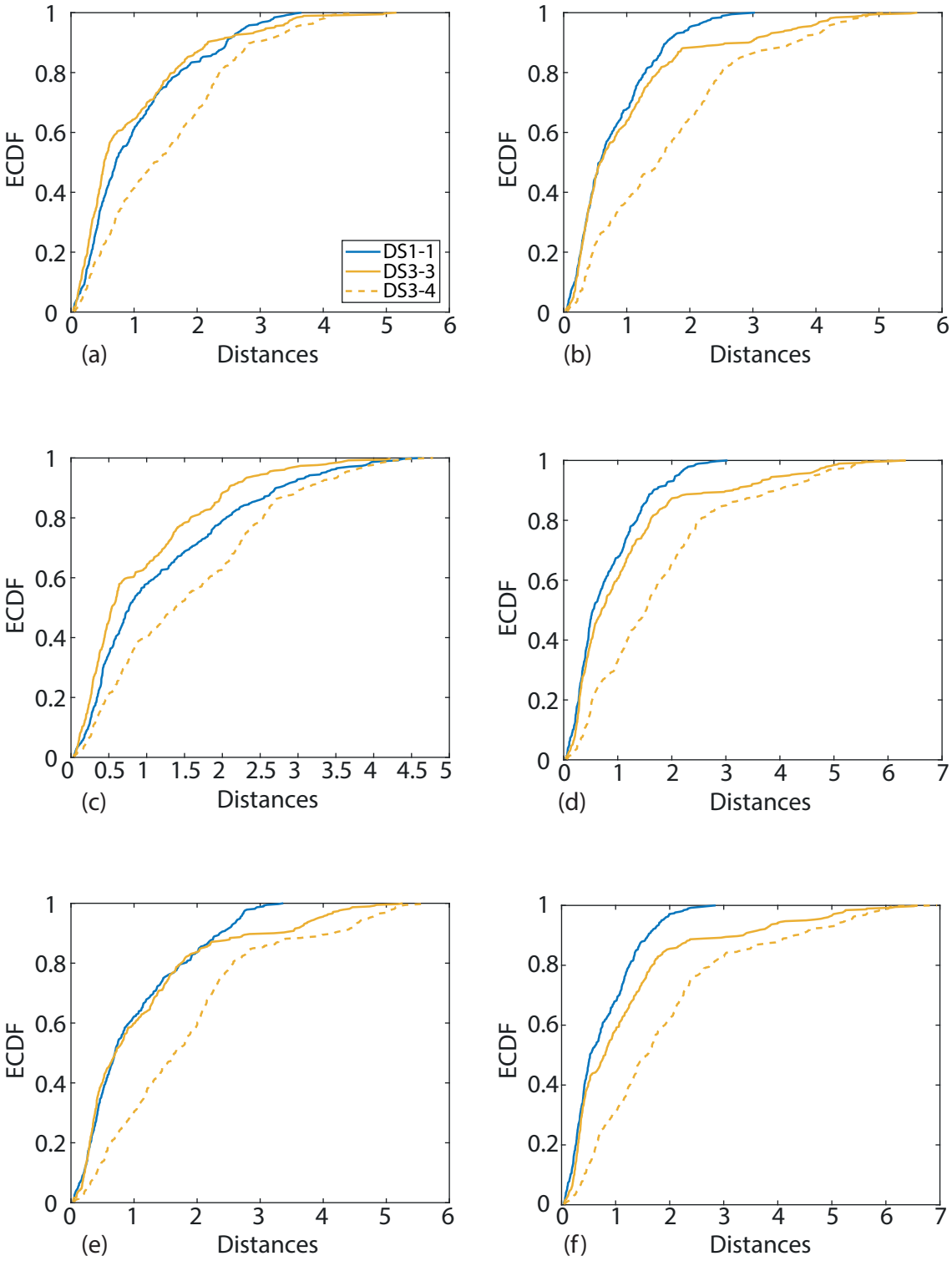

FIGURE C.16: ECDFs of the W distances for accelerometers (a) 4, (b) 14, (c) 5, (d) 15, (e) 6, and (f) 16 for Test A in DS1-2, DS3-3, and DS3-4.

C.2 With temperature compensation

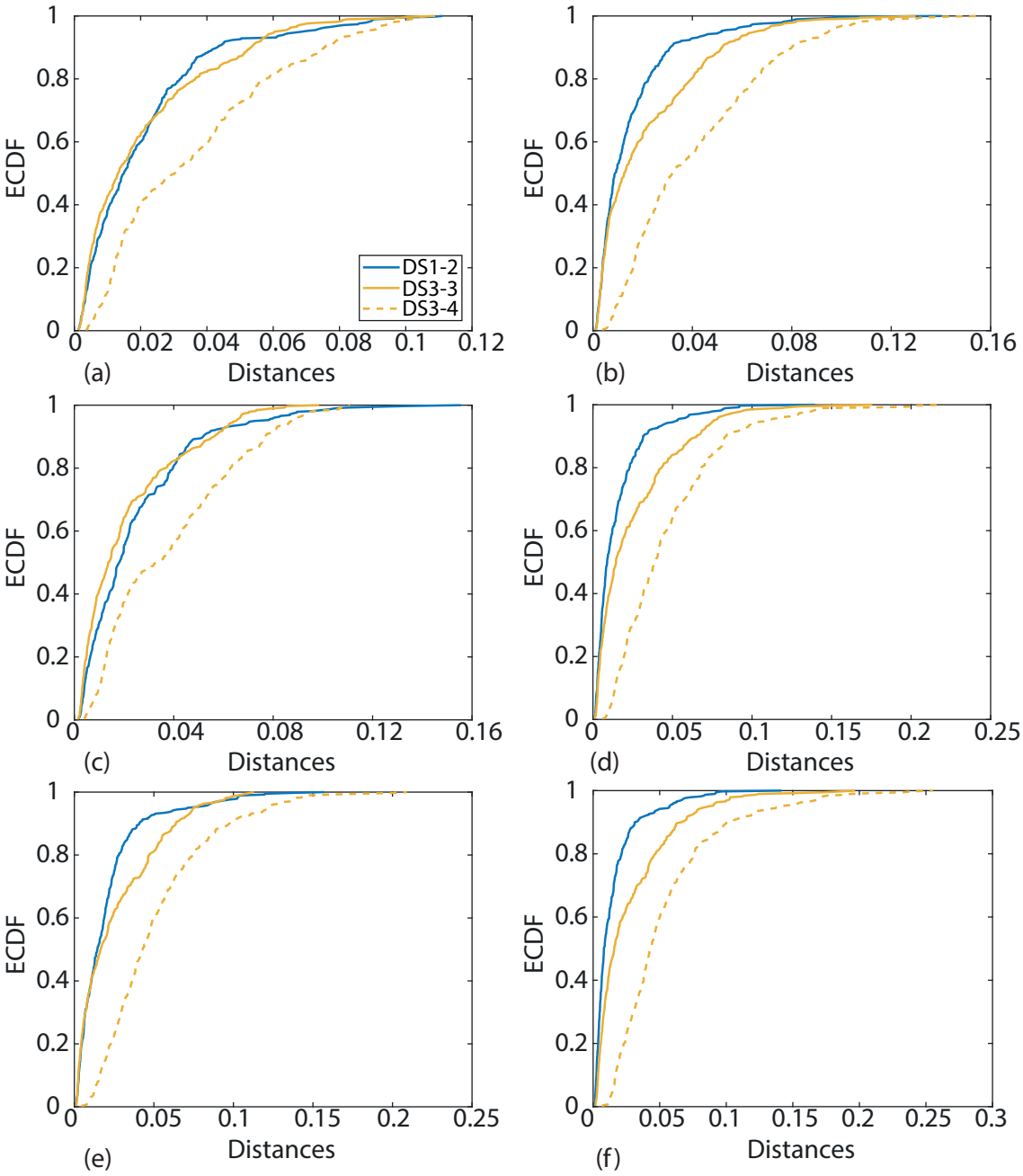

FIGURE C.17: ECDFs of the AD distances for accelerometers (a) 4, (b) 14, (c) 5, (d) 15, (e) 6, and (f) 16 for Test A in DS1-2, DS3-3, and DS3-4 with temperature compensation.

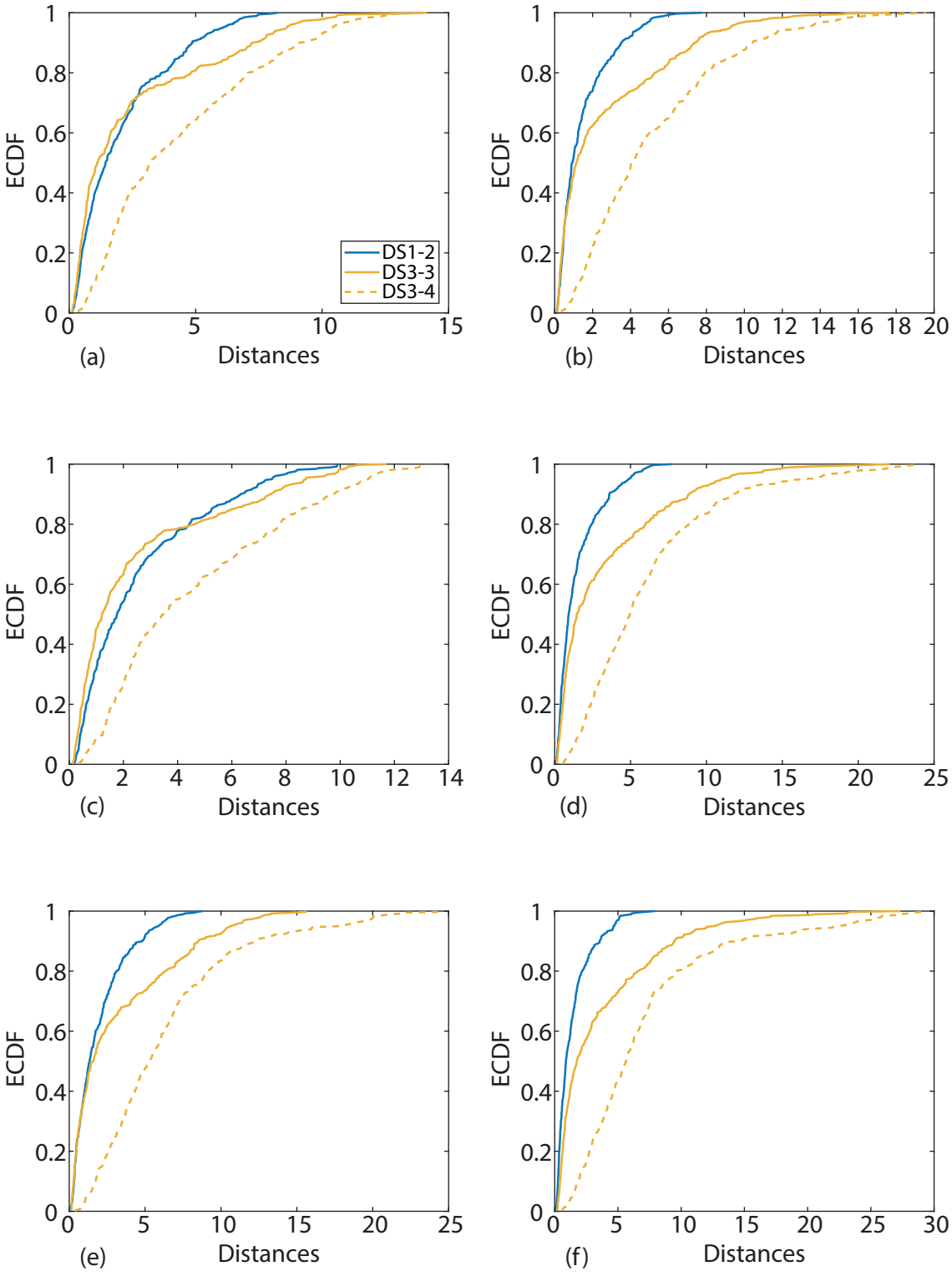

FIGURE C.18: ECDFs of the CVM distances for accelerometers (a) 4, (b) 14, (c) 5, (d) 15, (e) 6, and (f) 16 for Test A in DS1-2, DS3-3, and DS3-4 with temperature compensation.

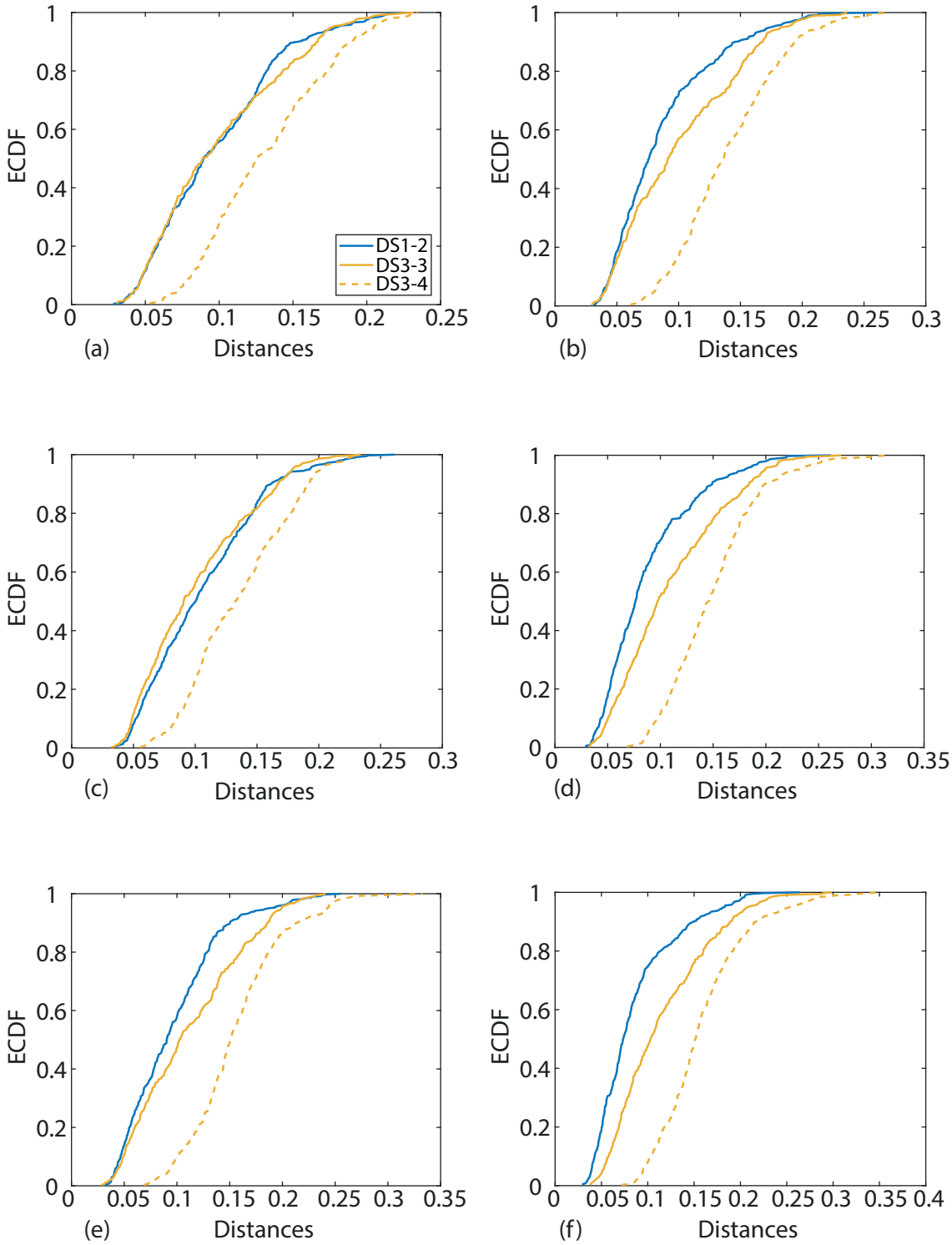

FIGURE C.19: ECDFs of the KS distances for accelerometers (a) 4, (b) 14, (c) 5, (d) 15, (e) 6, and (f) 16 for Test A in DS1-2, DS3-3, and DS3-4 with temperature compensation.

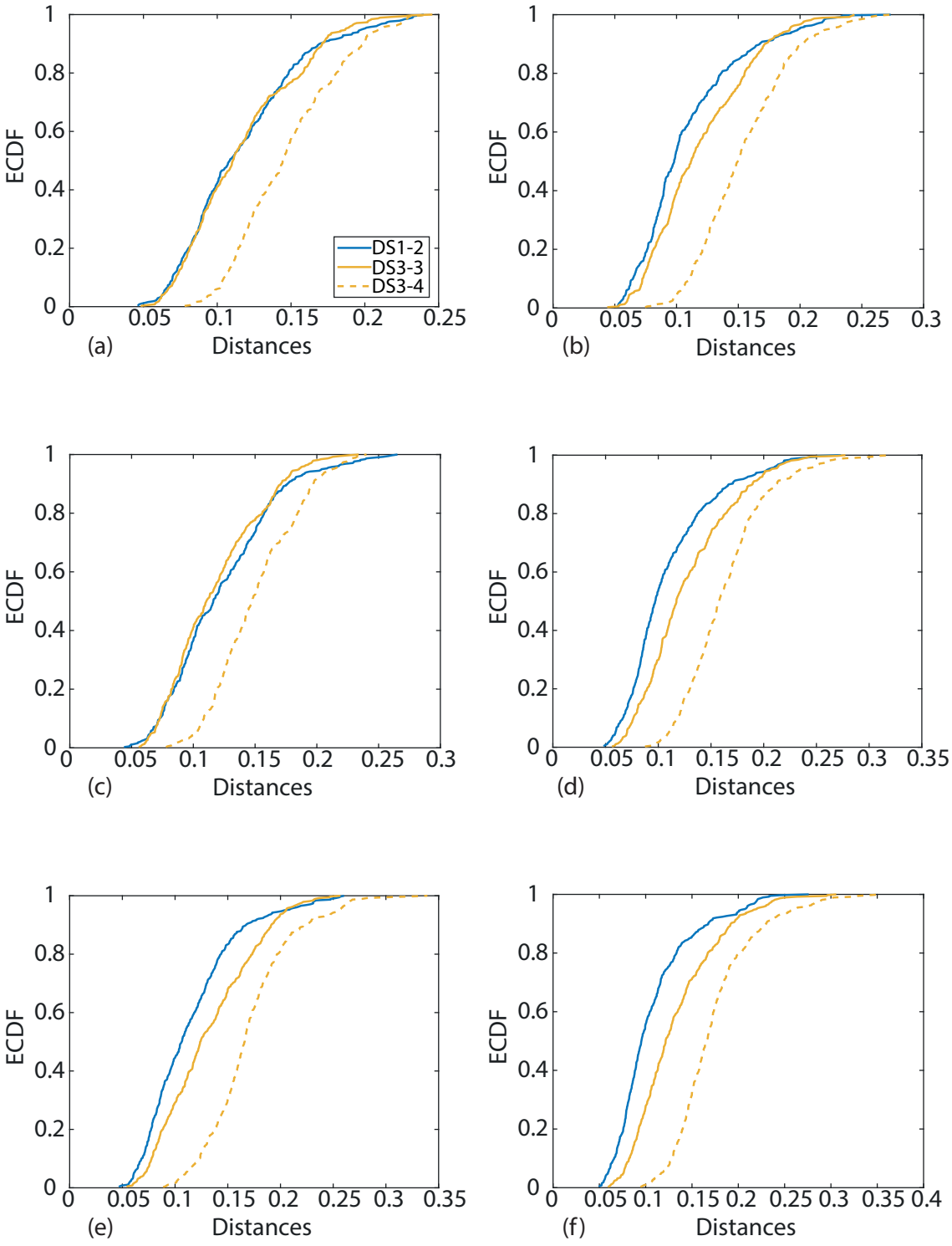

FIGURE C.20: ECDFs of the K distances for accelerometers (a) 4, (b) 14, (c) 5, (d) 15, (e) 6, and (f) 16 for Test A in DS1-2, DS3-3, and DS3-4 with temperature compensation.

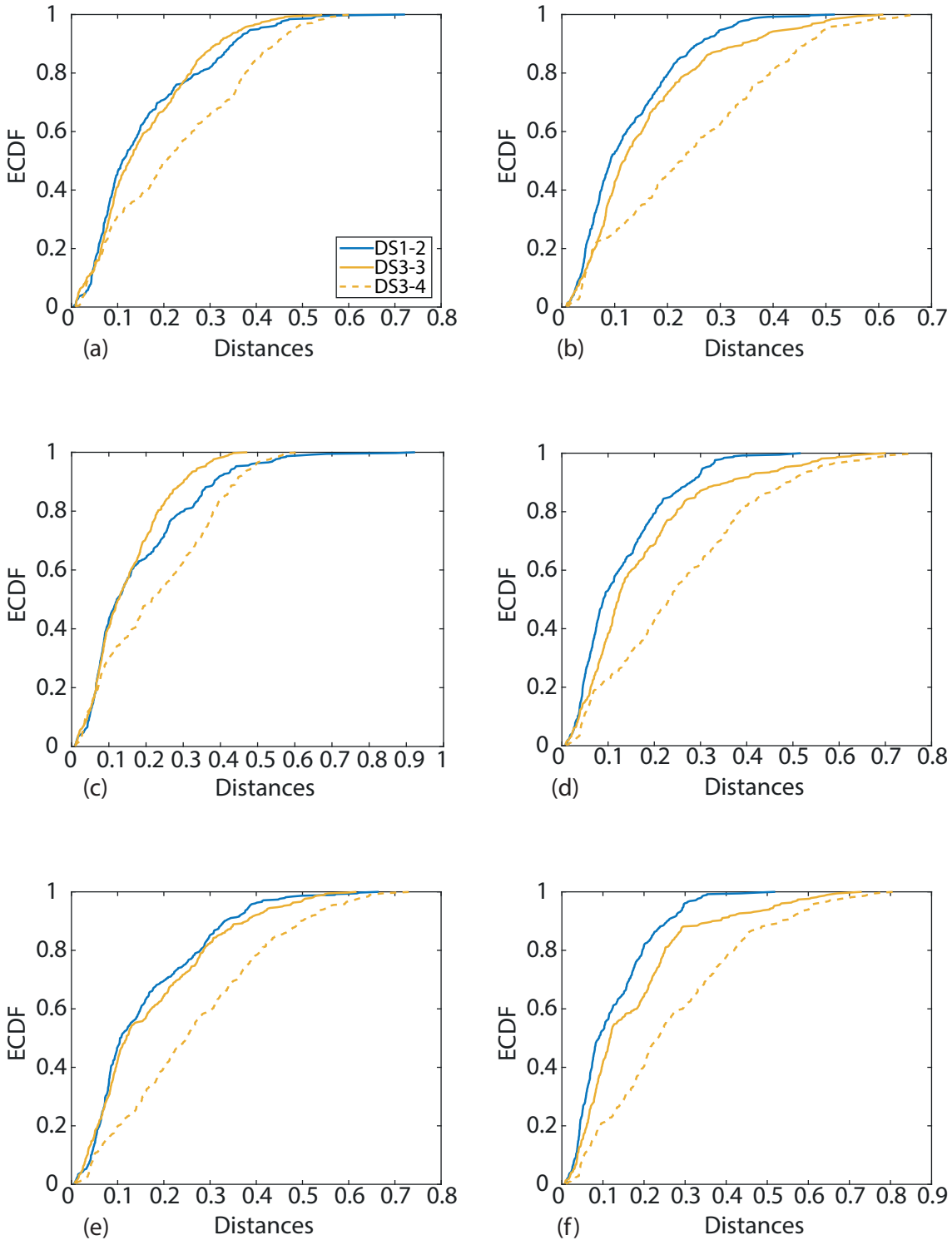

FIGURE C.21: ECDFs of the WAD distances for accelerometers (a) 4, (b) 14, (c) 5, (d) 15, (e) 6, and (f) 16 for Test A in DS1-2, DS3-3, and DS3-4 with temperature compensation.

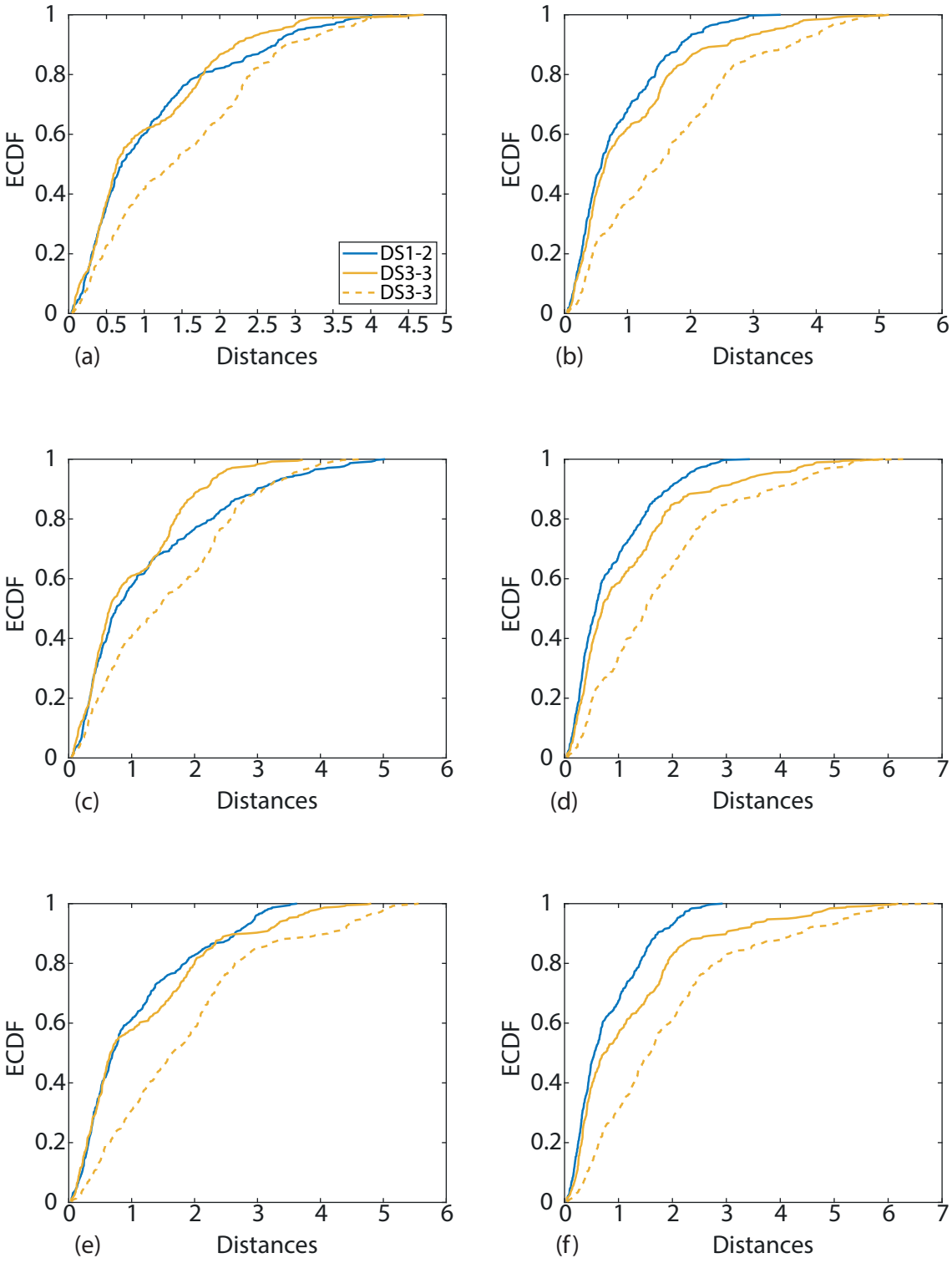

FIGURE C.22: ECDFs of the W distances for accelerometers (a) 4, (b) 14, (c) 5, (d) 15, (e) 6, and (f) 16 for Test A in DS1-2, DS3-3, and DS3-4 with temperature compensation.